

This is to certify that the
dissertation entitled

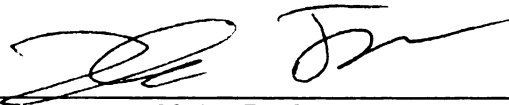
IONIC POLYMER-METAL COMPOSITE ARTIFICIAL
MUSCLES AND SENSORS: A CONTROL SYSTEMS
PERSPECTIVE

presented by

Zheng Chen

has been accepted towards fulfillment
of the requirements for the

Ph.D degree in Electrical Engineering



Major Professor's Signature

8/18/2009

Date

PLACE IN RETURN BOX to remove this checkout from your record.
TO AVOID FINES return on or before date due.
MAY BE RECALLED with earlier due date if requested.

DATE DUE	DATE DUE	DATE DUE

IONIC POLYMER-METAL COMPOSITE ARTIFICIAL MUSCLES AND SENSORS:
A CONTROL SYSTEMS PERSPECTIVE

By
Zheng Chen

A DISSERTATION

Submitted to
Michigan State University
in partial fulfillment of the requirements
for the degree of

DOCTOR OF PHILOSOPHY

Electrical Engineering

2009

ABSTRACT

IONIC POLYMER-METAL COMPOSITE ARTIFICIAL MUSCLES AND SENSORS: A CONTROL SYSTEMS PERSPECTIVE

By

Zheng Chen

Ionic polymer metal composites (IPMCs) form an important category of electroactive polymers (EAPs), also known as artificial muscles. IPMCs have many potential applications in robotics, biomedical devices, and micro/nano manipulation systems. In this dissertation, a systems perspective is taken to explore the potential of these novel materials in smart microsystems. In particular, this investigation includes modeling, control, compact sensing, and microfabrication techniques for IPMCs.

The starting point of this research is control-oriented modeling of IPMC sensors and actuators for obtaining faithful and practical mathematical models. The models are derived by exactly solving the governing partial differential equation in the Laplace domain with the consideration of distributed surface resistance. They are represented by infinite-dimensional transfer functions in terms of physical parameters and dimensions, which are scalable and amenable to model reduction. The actuation model of IPMC has been applied to develop a model for biomimetic robotic fish propelled by an IPMC actuator, which is useful in optimal design and control of the robotic fish. A nonlinear control-oriented model for IPMC has also been investigated to accommodate large deformation of IPMC under a relatively high voltage input.

Feedback control of IPMC actuators is often necessary in bio and micro applications. Since traditional sensors cannot be embedded into micro/bio systems, the second aspect of this research is to develop a compact sensing scheme for IPMC actuators. An integrated sensory actuator, IPMC/PVDF hybrid structure, utilizes an IPMC as actuator and one or two polyvinylidene fluoride (PVDF) films as sensors to implement simultaneous actuation and sensing. An IPMC/PVDF single-mode structure has been tested in open-loop microin-

jection of fruit-fly embryos. Feedback control of IPMC with integrated differential-mode sensors has been implemented in real-time, which shows accuracy and robustness of this sensory actuator.

Since microfabrication of IPMC is another challenge in realizing smart microsystems enabled by IPMCs, the third aspect of this research is to develop microfabrication techniques for IPMC. A monolithic microfabrication process for IPMC actuators capable of complex deformation has been developed. Two novel fabrication techniques have been introduced: 1) selectively thinning down Nafion with plasma etch, to make the passive areas thin and compliant; 2) impregnating Nafion film with platinum ions before the patterning step, which significantly increases the film stiffness and allows subsequent lithography and other steps. As the first application, an artificial pectoral fin has been fabricated using the developed process flow. It can generate bending, twisting, and cupping motions, which shows promise in robotic fish applications.

Copyright by

Zheng Chen

2009

DEDICATION

To Mom, Dad, and Wife

ACKNOWLEDGMENT

I am grateful to my advisor, Dr. Xiaobo Tan, for his enthusiastic encouragement and thoughtful guidance during the course of my PhD study. He inspired me with his vision and expertise and guided me with his patience in the exciting field of electroactive polymers. Besides providing technical guidance, he offered me invaluable advices on how to pursue my academic career.

I would like to thank my committee members, Dr. Hassan Khalil, Dr. Ning Xi, Dr. Ranjan Mukherjee, and Dr. Keith Promislow for providing insightful suggestions and comments. Thanks go to my colleagues for their help and discussion, in particular Yang Fang, Dr. Mart Anton, Dr. Yantao Shen, Ki-Yong Kwon, Alex Will, Ernest Mbemmo, and Stephan Shatara. Thanks also go to the staff and friends at the Keck Microfabrication Center and the ERC Clean Room at Michigan State University, in particular Dr. Baokang Bi, Karl Dersch, Dr. Hoyin Chan, and Yixing Wang, who gave me great help during my microfabrication research.

I am grateful for the financial support of my studies and research from the National Science Foundation (Grant No. ECCS 0547131) and the Office of Naval Research (Grant No. N000140810640).

I would like to thank my family for their patience, understanding and support during this study. I owe my greatest thanks to my parents for their support and sacrifice that enabled me to be here to pursue my Ph.D degree. Thanks also go to my brothers, Ningheng and Jian, and all my other relatives for their support. Special thanks go to my dear wife Ying for her understanding, support and sacrifice during the long time of study.

TABLE OF CONTENTS

List of Tables	x
List of Figures	xii
1 Introduction	1
1.1 Research Background	1
1.2 Research Objective	3
1.3 Contributions	4
1.3.1 Control-oriented modeling for IPMC actuators	4
1.3.2 Dynamic model for IPMC sensors	6
1.3.3 Modeling of IPMC-propelled biomimetic robotic fish	7
1.3.4 Nonlinear, control-oriented model for IPMC actuators	8
1.3.5 Compact sensing schemes for IPMC actuators	10
1.3.6 Monolithic fabrication of IPMC actuators for complex deformations	11
1.4 Organization of This Dissertation	15
2 A Dynamic Model for Ionic Polymer-Metal Composite Actuators	16
2.1 The Governing Partial Differential Equation	16
2.2 Electrical Impedance Model	19
2.2.1 Model ignoring the surface resistance	21
2.2.2 Model considering distributed surface resistance	22
2.3 Actuation Model	25
2.4 Model Reduction	27
2.5 Experimental Model Verification	29
2.5.1 Experimental setup	29
2.5.2 Identification of parameters in impedance model	29
2.5.3 Verification of the impedance model	31
2.5.4 Verification of the actuation model	33
2.6 Controller-Design Example: Model-based H_∞ Control	36
2.7 Chapter Summary	39
3 A Dynamic Model for Ionic Polymer-Metal Composite Sensors	43
3.1 A Dynamic Sensing Model	43
3.1.1 Model ignoring the surface resistance	46
3.1.2 Model considering distributed surface resistance	48
3.2 Model Reduction	53
3.3 Experimental Verification	57
3.3.1 Experimental setup	57

3.3.2	Parameter identification	57
3.3.3	Model verification	60
3.3.4	Impact of hydration level on sensing response	64
3.4	Chapter Summary	66
4	Modeling of Biomimetic Robotic Fish Propelled by An Ionic Polymer-Metal Composite Caudal Fin	69
4.1	Description of IPMC-propelled Robotic Fish	69
4.2	Model	70
4.2.1	Lighthill's theory of elongated-body propulsion	70
4.2.2	IPMC beam dynamics in fluid	73
4.2.3	Actuation model of the tail	76
4.2.4	Speed model of robotic fish	84
4.3	Experimental Verification and Parameter Identification	85
4.3.1	Drag coefficient identification	85
4.3.2	Fish tail model verification	86
4.3.3	Speed model verification	90
4.4	Chapter Summary	92
5	Nonlinear Control-oriented Model for Ionic Polymer-Metal Composite	97
5.1	Governing Nonlinear PDE	97
5.2	Analysis of the PDE at the Steady State	98
5.2.1	Numerical solution of the PDE at the steady state	99
5.2.2	Analytical solution of the PDE at the steady state	100
5.3	Nonlinear Circuit Model	106
5.3.1	Nonlinear capacitance of IPMC	106
5.3.2	Pseudocapacitance due to adsorption	108
5.3.3	Nonlinear DC resistance	109
5.3.4	Curvature output	109
5.3.5	Nonlinear control-oriented model	111
5.4	Experimental Verification	112
5.5	Chapter Summary	114
6	Integrated Sensing For IPMC Actuators Using PVDF Thin Films	117
6.1	IPMC/PVDF Single-Mode Sensory Actuator and Its Biological Application	117
6.1.1	Design of IPMC/PVDF single-model structure	117
6.1.2	Impact of the stiffening effect and design of the insulator thickness .	120
6.1.3	Electrical feedthrough coupling and model-based real-time compensation	126
6.1.4	Application to micro-injection of living drosophila embryos	134
6.2	IPMC/PVDF Differential-Mode Sensory Actuator and Its Validation in Feedback Control	140
6.2.1	Design of IPMC/PVDF differential-mode sensory actuator	140
6.2.2	Experimental verification of sensor robustness	148
6.2.3	Feedback control based on the integrated sensor	154

6.3	Chapter Summary	163
7	Monolithic Fabrication of Ionic Polymer Metal Composite Actuators Capable of Complex Deformations	165
7.1	Fabrication Process	165
7.1.1	Aluminum mask deposition	166
7.1.2	Plasma etching	168
7.1.3	Stiffening treatment	169
7.1.4	Patterning of Nafion surface	170
7.1.5	Electroless platinum plating and gold sputtering	170
7.1.6	Final membrane treatment	171
7.2	Impact of Stiffening Treatment	172
7.2.1	Stiffness change	172
7.2.2	Swelling capacity change	176
7.2.3	Impact of ion-exchange on lithography	177
7.3	Characterization of Fabricated Artificial Fins	177
7.3.1	Characterization method	177
7.3.2	Demonstration of twisting and cupping	179
7.3.3	Impact of the thickness in passive and active areas	180
7.3.4	Impact of actuation signals	183
7.3.5	DPIV study on MDOF IPMC actuation in water	185
7.4	Chapter Summary	188
8	Conclusions and Future Work	189
8.1	Conclusions	189
8.2	Future Work	190
A	Appendix for Chapter 2	191
A.1	Derivation of impedance model (2.31)	191
B	Appendix for Chapter 4	194
B.1	Derivation of $M(L, s)$, $F_c(L, s)$, $F_d(z, s)$ in Section 4.2.3	194
B.2	Derivation of $H_{fi}(s)$	195
B.3	Derivation of Actuation Model for Hybrid Tail	197
C	Appendix for Chapter 5	199
C.1	Proof of Proposition 1	199
C.2	Derivation of Eq. (5.17)	200
	Bibliography	202

LIST OF TABLES

2.1	Parameters for the impedance model.	30
2.2	Dimensions of three IPMC samples used for verification of model scalability.	32
3.1	Physical constants and directly-measured parameters.	59
3.2	Identified parameters through curve-fitting.	60
3.3	Dimensions of three IPMC samples used for verification of model scalability.	61
4.1	Parameters related to the drag force.	86
4.2	Parameters in IPMC beam dynamics.	89
4.3	Parameters related to the electrical dynamics of IPMC.	89
4.4	Dimensions of four tails (see Fig. 4.3 for the definitions of dimension variables).	92
5.1	Parameters in the model.	113
6.1	Dimension and spring constant of different beams.	124
6.2	Identified parameters in the circuit model.	129
6.3	Parameters identified for the IPMC/PVDF sensory actuator prototype (including force sensor).	144
7.1	Plasma etching with different recipes.	168
7.2	Spring constant, dimensions, and Young's moduli of the Nafion films in stiffness testing. The ion-exchanged films are identified with an asterisk.	174

7.3	Surface area changes of Nafion films in water and acetone. The ion-exchanged films are identified with an asterisk.	176
7.4	Thicknesses of MDOF IPMC actuators.	183
7.5	Actuation signals.	185

LIST OF FIGURES

1.1	(a) Structure of Nafion molecule; (b) illustration of the IPMC actuation mechanism due to the swelling force.	3
1.2	Smart microsystem enabled by IPMCs.	4
1.3	Pectoral fin of a bluegill sunfish undergoing sophisticated shape changes during maneuvering and locomotion [54].	13
2.1	Geometric definitions of an IPMC cantiliver beam.	20
2.2	Illustration of the IPMC impedance model with surface resistance.	23
2.3	Actuation model structure.	27
2.4	Experimental setup.	30
2.5	Comparison of experimental impedance responses with model predictions, with and without consideration of surface resistance.	32
2.6	Impedance model verification for the <i>Big</i> and <i>Slim</i> IPMC samples.	33
2.7	Impedance model verification for the <i>Slim</i> and <i>Short</i> IPMC samples.	34
2.8	Comparison of the measured actuation response with the proposed full and reduced models for the <i>Big</i> sample.	35
2.9	Schematic of the closed-loop control system for an IPMC actuator.	36
2.10	The modeling error and its bound $W_a(s)$	37
2.11	The feedback connection of $M_s(s)$ and $\Delta_a(s)$	38

2.12	Experimental and simulation results on tracking of IPMC actuator under H_∞ control.	40
2.13	Experimental and simulation results on tracking of IPMC actuator under PI control.	41
2.14	Comparison of controller outputs under H_∞ control and PI control.	42
3.1	Illustration of the distributed surface resistance for the IPMC sensing model.	49
3.2	(a) Schematic of the experimental setup; (b) picture showing a cantilevered IPMC under mechanical deformation.	58
3.3	Performance of the models with and without consideration of surface resistance.	61
3.4	Frequency responses of the sensing dynamics. (a) For the <i>Big</i> and <i>Slim</i> samples; (b) for the <i>Slim</i> and <i>Short</i> Samples.	63
3.5	The sensing response of the <i>Slim</i> sample under a decaying, oscillatory mechanical stimulus. (a) The tip displacement trajectory; (b) prediction of the sensing response versus experimental measurement.	65
3.6	The sensing response of the <i>Big</i> sample under a step stimulus. (a) The tip displacement trajectory; (b) prediction of the sensing response versus experimental measurement.	66
3.7	The sensing response at 6 Hz for the <i>Slim</i> IPMC sample over time.	67
3.8	Identified diffusion coefficient versus time.	67
4.1	(a) Schematic of the robotic fish; (b) prototype of the robotic fish.	71
4.2	The original moment in (a) is replaced by a distributed force density and a concentrated bending moment in (b).	78
4.3	Illustration of an IPMC beam with a passive fin. The lower schematic shows the definitions of dimensions.	80
4.4	Forces and moments acting on the hybrid tail.	82
4.5	Experimental setup for the drag force measurement.	85
4.6	Drag force versus velocity of the fish.	86

4.7	Experimental setup for identification and verification of IPMC actuation model in water.	87
4.8	Vibration of IPMC beam in water.	88
4.9	Validation of model for IPMC operating underwater. Shown in the figure are the Bode plots for (a) model $H_1(L, s)$ without passive fin; and (b) model $H_2(L_0, s)$ with passive fin.	91
4.10	Snapshot of robotic fish in swimming test.	92
4.11	Identified Γ_2 for <i>Tail1</i> and <i>Tail2</i>	93
4.12	Verification of motion model for the fish with <i>Tail1</i> and <i>Tail2</i> . (a) With <i>Tail1</i> ; (b) with <i>Tail2</i>	94
4.13	Verification of motion model for the fish with <i>Tail3</i> and <i>Tail4</i> . (a) With <i>Tail3</i> ; (b) with <i>Tail4</i>	95
5.1	Numerical solution of the nonlinear ODE for $V = 2.61\text{V}$: Charge density. .	101
5.2	Numerical solution of the nonlinear ODE for $V = 2.61\text{V}$: Electrical field. .	101
5.3	Numerical solution of the nonlinear ODE for $V = 2.61\text{V}$: Electrical potential.	102
5.4	Illustration of solving for p_1 and p_2	104
5.5	(a) Charge versus voltage at the steady state; (b) charge density at the boundaries versus voltage input.	107
5.6	Circuit model of IPMC.	108
5.7	Model structure.	111
5.8	Illustration of experimental setup.	112
5.9	(a) Initial current versus step voltage input; (b) DC current versus step voltage input.	114
5.10	Current response under a step voltage input of 1.0 V.	115
5.11	Current response under a sinusoid voltage input.	115
6.1	Design of the IPMC/PVDF composite structure.	118

6.2	Design of the charge amplifier.	119
6.3	(a) Charge output of the PVDF corresponding to the damped vibration; (b) charge output versus the bending displacement.	121
6.4	Bending of IPMC/PVDF composite beam.	123
6.5	(a) Experimental setup for spring constant measurement; (b) picture of the experimental setup.	125
6.6	Spring constant of IPMC/PVDF beams.	126
6.7	(a) Bending displacement detected by the laser sensor; (b) sensing output from the PVDF, showing the spikes from electrical feedthrough.	128
6.8	Circuit model of the IPMC/PVDF structure.	129
6.9	(a) V_{p+} , V_{p-} sensing signals; (b) extracted coupling signal V_c	131
6.10	Comparison of model prediction and experimental measurement. (a) Actuation current; (b) coupling signal.	132
6.11	Verification of the coupling dynamics.	133
6.12	Bode plots of coupling dynamics and actuation dynamics.	134
6.13	Diagram of the real-time compensation.	135
6.14	Comparison of displacement measurements by laser sensor and PVDF sensor.	135
6.15	Illustration of the IPMC/PVDF micro-force injector.	136
6.16	(a) Diagram of experimental setup for embryo injection; (b) picture of experimental setup.	137
6.17	(a) Snap shots captured during the embryo injection; (b) bending displacement during the injection measured by both the laser sensor and the integrated PVDF sensor.	139
6.18	Design of the IPMC/PVDF composite structure for sensing of bending output (force sensor not shown).	141
6.19	Differential charge amplifier for PVDF sensor.	142

6.20	Geometric definitions of IPMC/PVDF sensory actuator.	144
6.21	Design of the force sensor for the end-effector.	145
6.22	Geometric definitions of the PVDF sensor.	147
6.23	IPMC/PVDF sensory actuator and sensing circuits in shielding enclosures.	147
6.24	Distributed circuit model of IPMC/PVDF beam.	149
6.25	Experimental results showing elimination of feedthrough signal. (a) Raw PVDF sensing signals under a square-wave actuation input (2V, 0.1 Hz); (b) Comparison between the bending displacements obtained from the PVDF sensor and from the laser sensor.	151
6.26	(a) Sensing noise when IPMC/PVDF placed in open field; (b) sensing noise when IPMC/PVDF placed inside conductive shielding enclosure.	153
6.27	Self-compensation of asymmetric tension/compression sensing response. (a) Raw PVDF sensing signals under a sinusoidal actuation signal (0.2 Hz, amplitude 1 V); (b) Comparison between the bending displacements obtained from the PVDF sensor and from the laser sensor.	155
6.28	Comparison between the bending displacements obtained from the PVDF sensor and from the laser sensor, when a 2V step input is applied.	156
6.29	Closed-loop system for control of IPMC bending displacement.	156
6.30	Experimental results on feedback control of bending displacement using integrated PVDF sensor. (a) Bending displacement; (b) actuation voltage.	158
6.31	Measurement of the micro force in piercing soap bubbles. (a) Experimental setup; (b) PVDF sensor response during and after penetration.	160
6.32	Measured forces during penetration of soap bubble membranes.	161
6.33	Experimental results on bending feedback control with tip force measurement. (a) Displacement of the end-effector estimated based on the integrated PVDF bending sensor alone; (b) PVDF force sensor output.	162
6.34	Actuation voltage generated by the feedback controller.	163

6.35	Estimation of true end-effector displacement by combining the integrated bending and force sensors, and its comparison with the laser sensor measurement.	164
7.1	The process flow for monolithic fabrication of an MDOF IPMC actuator. . .	167
7.2	SEM picture of a plasma-etched Nafion film.	169
7.3	Nafion film fixed by an aluminum frame.	171
7.4	Patterned IPMC membrane. (a) Top view picture; (b) planar dimensions of the membrane; (c) SEM picture of the cross section.	173
7.5	Experimental setup for measuring the stiffness of a Nafion film.	174
7.6	Results of stiffness measurement. (a) Nafion-N1110; (b) Nafion-117.	175
7.7	Lithography results. (a) With pure Nafion; (b) with ion-exchanged Nafion. .	178
7.8	Experimental setup for characterizing MDOF IPMC actuators.	179
7.9	Snapshots of an actuated MDOF IPMC actuator, demonstrating the twisting motion.	181
7.10	(a) Definitions of the tip displacements and the twisting angle; (b) trajectories of the tip displacements and the twisting angle corresponding to the voltage inputs as in Fig. 7.9.	182
7.11	(a) Definition of the cupping angle; (b) the trajectory of the cupping angle for a sample with 85 μm thickness in both active and passive areas (voltages: 3 V, 0.3 Hz, 180°).	182
7.12	Twisting angles generated by different samples with 0.3 Hz, 3 V and 90° phase sinusoid voltage signals. (a) MDOF IPMC actuators with different thickness in both active areas and passive areas; (b) MDOF IPMC actuators with the same thickness in active areas (170 μm) but different thicknesses in passive areas.	184
7.13	(a) <i>S1</i> actuated by voltage signals with different amplitudes but the same frequency (0.3 Hz) and phase (90°); (b) <i>S5</i> actuated by voltage signals with the same amplitude (3 V) and frequency (0.3 Hz) but different phases. . . .	186

7.14 DPIV study of MDOF IPMC actuator operating in water. (a) Actuation of the actuator in water (the edge of the actuator is highlighted); (b) Velocity field of the fluid.	187
--	-----

Chapter 1

Introduction

1.1 Research Background

Electroactive polymers (EAPs) [8, 10, 9] are polymers whose shapes are changed when an electrical stimulus is applied. Since EAPs have built-in actuation and sensing capabilities, they can be used both as actuators and sensors. As actuators, because of the similarity to biological muscles in terms of achievable stress and strain, they are also called artificial muscles. There are many different types of EAPs, but they can be divided into two categories, electronic EAPs and ionic EAPs. Electronic EAPs are driven by electrostatic forces between the electrodes. Typical examples are dielectric elastomers [70]. They can generate large force but require high voltage (typically higher than 100 V). Ionic EAPs are driven by the ionic movement under a low voltage (1 or 2 V). Typical examples are ionic polymer-metal composites [79] and conjugated polymers [84]. They require low voltages and can work well under wet conditions, but can only generate relatively low forces.

Since EAPs are soft, resilient, and can generate large deformation, they have many potential applications in robotics [86], biomedical devices [80], and micro/nano manipulation [97]. In human-like robots, electronic EAPs can be used to move hands and fingers, and to generate face expression, such as happiness and sadness. In bio-inspired robots, ionic

EAPs can be used to propel biomimetic robotic fish under water. EAPs can also be potentially used as highly active flow sensors in many bio-inspired robotic applications. In biomedical devices, ionic EAPs can be potentially used to assist patients with heart problems [80]. Since they can convert mechanical energy into electricity, ionic EAPs can also be potentially used as energy harvesters to charge the implanted biomedical devices in human body.

Ionic polymer-metal composites (IPMCs) [79, 10] form an important category of ionic EAPs. An IPMC sample typically consists of a thin ion-exchange membrane (e.g., Nafion, shown in Fig. 1.1(a)), chemically plated on both surfaces with noble metals as electrodes [49]. With an ion-exchange process, positive hydrogen ions in the membrane are replaced by other cations, such as Na^+ , Li^{2+} , and Ca^{2+} . When IPMC is hydrated, the cations can move freely in the membrane. There are two possible physical forces which lead to actuation of IPMC. One is the fluid-induced swelling force [79]. When a voltage is applied across the IPMC, cations will move to the cathode side bringing with their water molecules and creates differential swelling across the polymer thickness. Consequently, the IPMC will bend to the anode side. The other force is the electrostatic force due to the imbalanced net charges in the polymer [64]. Under an electric field, the cations are redistributed, resulting in a locally imbalanced net charge density which produces internal stresses acting on the backbone of polymer. In the anion-rich region, the polymer chains relax, while in the cation-rich region, they further extend, which make the IPMC bend to the anode side. Fig. 1.1(b) illustrates the mechanism of IPMC actuation. On the other hand, if a mechanical force is applied to the IPMC and makes it bend, the ion movement will generate sensing charges on the electrodes. So an IPMC can be used both for sensing and actuation.

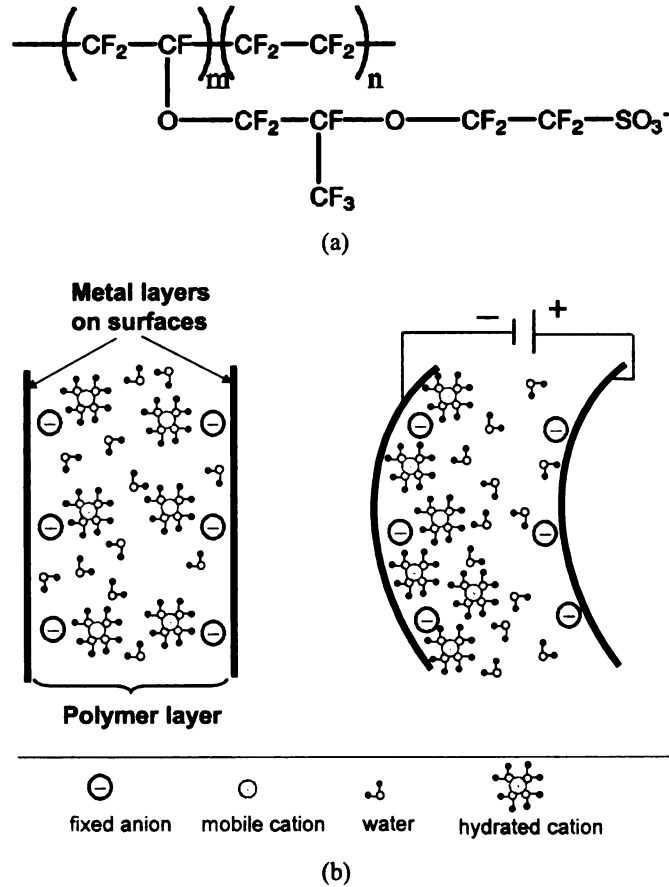


Figure 1.1: (a) Structure of Nafion molecule; (b) illustration of the IPMC actuation mechanism due to the swelling force.

1.2 Research Objective

It is intriguing to build smart microsystems with smart sensors, actuators, and energy harvesters, which can accomplish bio/micro manipulation, bio-sensing, and micro robotic tasks. Fig. 1.2 illustrates one example of our envisioned IPMC-based smart microsystems, where a micro gripper is trying to capture a cell and then do surgery at the cellular level. This research strives to bring us closer to the envisioned smart microsystems, and a systems perspective is taken to achieve this goal.

From a control system point of view, there are three challenges in building smart microsystems enabled by IPMCs. Since understanding of the actuation and sensing mech-

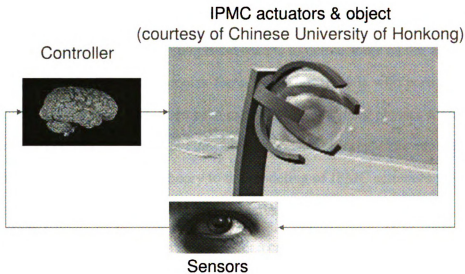


Figure 1.2: Smart microsystem enabled by IPMCs.

anism of these sophisticated materials is still underway, the first challenge is to obtain a faithful and practical mathematical model for IPMC. To achieve precise operation, a feedback control is often necessary in a smart microsystem. Since the traditional and separate sensors are hard to be embedded into microsystems, the second challenge is to develop compact sensing schemes for IPMC actuators. Since the traditional microfabrication processes cannot meet the special requirements in fabricating IPMCs, the third challenge arises from how to fabricate these materials for microsystem applications. This dissertation is focused on addressing these challenges.

1.3 Contributions

1.3.1 Control-oriented modeling for IPMC actuators

Current modeling work can be classified into three categories based on their complexity levels. Based purely on the empirical responses, *black-box* models, e.g., [45, 92], offer minimal insight into the governing mechanisms within the IPMC. While these models are simple in nature, they are often sample-dependent and not scalable in dimensions. As a

more detailed approach, *gray-box* models, e.g., [46, 67, 27], are partly based on physical principles while also relying on empirical results to define some of the more complex physical processes. In the most complex form, *white-box* models with partial differential equations (PDEs), e.g., [64, 85], attempt to explain the underlying physics for the sensing and actuation responses of IPMCs, but they are not practical for real-time control purposes. Del Bufalo *et al.* applied mixture theory to the modeling of IPMC actuators [17], but they only addressed the behavior under quasi-static actuation.

Farinholt derived the impedance response for a cantilevered IPMC beam under step and harmonic voltage excitations [33]. The derivation was based on a linear, one-dimensional PDE governing the internal charge dynamics, which was first developed by Nemat-Nasser and Li for studying the actuation response of IPMCs [64]. Farinholt analytically solved the PDE with some assumptions on the solution. These assumptions limit the model's applicability in real-time control where the model should work for arbitrary voltage inputs.

Our accomplished modeling work on IPMC actuation dynamics attempts to bridge the gap between physical models and empirical models. The starting point is the physical model developed by Nemat-Nasser [64], where the governing PDE describes the charge redistribution dynamics under electrostatic interactions, ionic diffusion, and ionic migration along the thickness direction. Field equations describe the relations among the electric field, the charge density, and the electric potential. Two assumptions are made in the modeling work. One is zero ion flux at the boundary. The other is that the generated stress is proportional to the charge density. To capture the effects of surface resistance on the electrodes [78, 74], we introduce a transmission line circuit model which leads to an integrodifferential equation serving as a boundary condition for the governing PDEs. We exactly solve the PDEs in Laplace domain with the boundary conditions. The derived model is an infinite-dimensional transfer function relating the output to the input. It is geometrically scalable, and amenable to model reduction for real-time control. Experiments have been conducted to validate the proposed dynamic model for IPMC actuators. Based

on the reduced model, an H_∞ controller is designed and then implemented in real-time. The experimental results have verified that the proposed model is faithful and practical in model-based control design.

1.3.2 Dynamic model for IPMC sensors

Comparing with the extensive work on modeling of IPMC actuators, research on IPMC sensing models has been relatively limited. De Gennes *et al.* proposed a static model based on linear irreversible thermodynamics to capture both actuation and sensing mechanisms of IPMCs [27]. Using an analogy to piezoelectric materials, Newbury and Leo presented a geometrically scalable *gray-box* model for IPMC sensors [65, 66]. The latter model was further elaborated and verified by Bonomo *et al.* [12]. Farinholt and Leo derived the charge sensing response for a cantilevered IPMC beam under a step change in tip displacement [32]. The derivation was based on a linear, one-dimensional partial differential equation governing the internal charge dynamics, which was first developed by Nemat-Nasser and Li for studying the actuation response of IPMCs [64]. A key assumption in [32] is that the initial charge density at the boundary is proportional to the applied step deformation. Farinholt and Leo then obtained an analytical but approximate solution by assuming that the solution is separable as a product of temporal and spatial components.

Our accomplished modeling work on IPMC sensing dynamics is an explicit, dynamic, physics-based, and practical model for IPMC sensors. With the same modeling approach as described in the modeling of IPMC actuators, we exactly solve the governing PDE in the Laplace domain with the consideration of surface resistance. The boundary condition is the same as the key assumption made in Farinholt's work [32]. The derived sensing model is an infinite-dimensional transfer function in terms of physical parameters and dimensions. It is easy to reduce the model into a low-order transfer function, which can be used to construct compensation circuits or algorithms for real-time conditioning of IPMC sensor signals. Experimental results show that considering the surface resistance leads to more accurate

predictions. The geometric scalability of the sensor model has also been confirmed without re-tuning of the identified physical parameters. Experiments for an IPMC sensor under a damped oscillatory deformation and a step deformation have further verified the reduced, low-order model. The influence of the IPMC hydration level on the sensing performance has also been studied.

1.3.3 Modeling of IPMC-propelled biomimetic robotic fish

Aquatic animals (e.g., fishes, cetaceans) are ultimate examples of superior swimmers as a result of millions of years of evolution, endowed with a variety of morphological and structural features for moving through water with speed, agility, and efficiency [53, 35]. Recent years have also witnessed significant effort in the development of aquatic robots, or robotic fish [88, 39, 40, 47, 86, 62, 5, 52]. IPMCs are attractive for aquatic robots because they are flexible and produce significant bending deformations under low voltages (several volts). IPMC-based robotic fish have been reported by several groups [39, 47, 6, 86, 44].

A faithful model is desirable for both optimal design [95] and control [96] of an underwater robot. For instance, Boyer *et al.* presented a dynamic model for 3D eel-like robot [15]. Morgansen *et al.* investigated geometric methods for modeling and control of free-swimming and rigid fin-actuated underwater vehicles [62]. There have been limited studies related to modeling of flexible fins. A finite-element method was adopted by Yim *et al.* to model the motion of an IPMC actuator underwater [94], where an empirical RC circuits was used to predict the bending moment of IPMC under actuation. The added-mass effect due to acceleration of surrounding water was ignored in modeling hydrodynamic interactions, and the authors presented only simulation results. Modeling of IPMC actuators in underwater operations was also studied by Brunetto and coworkers [16]. However, actuation dynamics of IPMC was captured by an empirical transfer function $d(s)$, which cannot indicate the fundamental physics in IPMC. Furthermore, the experimental results in [16] were limited to a clamped IPMC beam in water, and no attempt was made to validate the model

on a free-swimming robot. Recently Porfiri and coworkers investigated the hydrodynamics of an IPMC beam using numerical computation [1] and Digital Particle Image Velocimetry (DPIV) measurements [71]. Although their work was very interesting, it was limited to a clamped IPMC beam only and the actuation dynamics of IPMC was not considered.

In this research we present, to our best knowledge, the *first* model for IPMC-propelled robotic fish that captures the intrinsic actuation physics of IPMC and the complex hydrodynamic interactions between IPMC and fluid, and that is validated in experiments on a free-swimming robotic fish prototype. Inspired by biological fish fins, where passive, collagenous membranes are driven by muscle-controlled fin rays [53], we have attached a passive, plastic fin to the tip of IPMC to enhance propulsion. The model incorporates the interactions of the passive fin with both the IPMC actuator and the fluid, allowing us to capture simultaneously the passive fin's role in boosting propulsion and its loading effect on the IPMC beam. The model is used to predict the cruising speed of robotic fish, given a periodic actuation voltage to the IPMC fin. Experiments have been performed to identify model parameters and validate the model. It is found that the model can predict well the cruising speed of the robot at different operating frequencies, for different tail dimensions. Since most of the parameters in the model are expressed in terms of fundamental physical properties and geometric dimensions, the model will be instrumental for optimal design of the IPMC-propelled robotic fish to achieve good speed and efficiency.

1.3.4 Nonlinear, control-oriented model for IPMC actuators

A nonlinear model is desirable when a relatively high voltage is applied to the IPMC to generate large deformations. Nonlinear behaviors of IPMC have been reported in literature. Chen *et al.* [19] employed the Preisach operator to capture the hysteresis in IPMC. Bonomo *et al.* [13] reported a nonlinear circuit model of IPMC. However, it is an empirical nonlinear model and does not capture the fundamental physics in IPMC. Nemat-Nasser [63] captured a nonlinear capacitance of IPMC with an assumption that there is asymmet-

ric charge distribution along the thickness direction and that cation-depleted layer forms near the anode side when a relatively high voltage is applied. However, the region without cation depletion was still governed by the linear PDE. Porfiri [73] applied Poisson-Nernst-Planck equations to investigate charge dynamics in IPMC. He used matched asymptotic expansions to solve the nonlinear PDE and obtained a nonlinear circuit model for IPMC, which includes a nonlinear capacitance and a linear diffusion resistance. However, the circuit model does not accommodate electrochemical reaction near the electrodes and DC resistance of the polymer. Actuation model was not further derived based on the circuit model.

Our nonlinear model is based on the original nonlinear PDE, which can capture ion diffusion, ion migration, and electrostatic interactions in IPMC. The modeling work starts from the analysis of the equilibrium of IPMC under a step voltage input, which can be captured by a nonlinear ordinary differential equation (ODE). Numerical analysis of the nonlinear ODE demonstrates an asymmetric charge distribution along the thickness direction. The nonlinear term in the original PDE cannot be ignored when a moderate voltage (> 0.2 V) is applied. Since the nonlinear ODE cannot be explicitly solved, a systems perspective is taken to derive the analytical nonlinear mapping from the voltage to the charge. It is verified by the numerical solution, and is practically useful in real-time control. A nonlinear circuit model is employed to capture the electrical dynamics of IPMC. It incorporates nonlinear capacitance of IPMC derived from the nonlinear mapping function between the charge and the voltage, ion diffusion resistance [13, 73], pseudocapacitance due to the electrochemical process at the polymer-metal interface [3], and nonlinear DC resistance of the polymer [13]. Based on the electromechanical coupling effect, the curvature output can be obtained from the electrical dynamic model. The proposed model shows consistency with the linear model when the voltage is small [64]. With definitions of the state variable, input, and output, the model is further presented in the state space, which will be the starting point for nonlinear control design. Parameters are measured or identified through experiments.

The proposed model is validated in experiments.

1.3.5 Compact sensing schemes for IPMC actuators

Compact sensing methods are desirable for feedback control of IPMC actuators to ensure precise and safe operation without using bulky, separate sensors. Extensive work has been done in sensory actuators. It is intriguing to utilize the inherent sensory property of an IPMC to achieve simultaneous actuation and sensing, like the self-sensing scheme for piezoelectric materials [29]. However, this approach is difficult to implement due to the very small magnitude of the sensing signal compared to the actuation signal (millivolts versus volts) [79] and the nonlinear [14], dynamic [32] sensing responses. Newbury [66] explored the idea of using two IPMCs, mechanically coupled in a side-by-side or bilayer configuration, to perform actuation and sensing. The attempt was reported to be unsuccessful since the sensing signal was buried in the feedthrough signal from actuation [66].

In this research, a novel sensing scheme for IPMC actuators is proposed by bonding an IPMC actuator and PVDF (polyvinylidene fluoride) sensing films to achieve simultaneous sensing and actuation. Two versions of IPMC/PVDF sensory actuator have been developed. In the first version, a single-mode IPMC/PVDF sensory actuator has been built by bonding an IPMC and a PVDF thin film with an insulating layer in-between. The insulating layer thickness is properly designed to minimize the stiffness of the composite IPMC/PVDF structure while reducing the electrical feedthrough coupling between IPMC and PVDF. A distributed circuit model is developed to effectively represent the electrical coupling dynamics, which is then used in real-time compensation for extraction of the true sensing signal. Experimental results show that the developed IPMC/PVDF structure, together with the compensation algorithm, can perform effective, simultaneous actuation and sensing. As the first application, the single-mode IPMC/PVDF sensori-actuator has been successfully used for performing and monitoring open-loop micro-injection of living *Drosophila* embryos.

The second version of IPMC/PVDF structure adopts a differential configuration for PVDF sensors. Two complimentary PVDF films are bonded to an IPMC actuator in a sandwich fashion, and a differential charge sensing circuit is used to measure the sensor output. As analyzed and verified experimentally, this design has a number of advantages: 1) it allows shielding of capacitive coupling between IPMC and PVDF, and eliminates the fictitious, feedthrough sensing signal induced directly by the actuation signal; 2) it removes the influence of thermal fluctuation and other environmental noises, which is often the most challenging problem for PVDF sensors; 3) it compensates for asymmetric sensing responses of a single PVDF film under compression versus extension; and 4) it minimizes the internal stress at bonding interfaces, which could otherwise cause delamination of layers or spontaneous creep of the composite beam structure. The design of an IPMC actuator incorporates both bending and force feedback. A force sensor with μN resolution is designed by sandwiching a relatively rigid beam with two PVDF films. The force sensor is then bonded to the tip of the IPMC actuator, (which itself is sandwiched by PVDF for sensing of bending). The effectiveness of the proposed sensory actuator has been demonstrated in feedback control experiments. Precise position tracking of the end-effector is achieved through proportional-integral (PI) control based upon feedback from the integrated sensor. A laser distance sensor is used as an independent observer for validation purposes. The capability of simultaneous force measurement is shown in experiments of piercing soap bubbles. Interaction forces as low as μN are well captured.

1.3.6 Monolithic fabrication of IPMC actuators for complex deformations

Fabrication techniques for IPMCs have been developed by several research groups [79, 68] based on commercially available ion-exchange membranes such as Nafion. A casting process has been developed to fabricate thin (down to $20\ \mu\text{m}$) IPMC actuators [48, 69]. Kim

and Shahinpoor fabricated thick IPMCs (up to 2 mm) by baking the mixture of Nafion powder and solvent in a mold [50]. Plasma treatment was introduced to roughen the Nafion surface and improve the actuation performance of IPMC [51]. Chung *et al.* applied silver nano-powder in fabrication of IPMC to improve the adhesion between metal and polymer [22]. Akle *et al.* developed direct assembly plating method to make electrodes and produced high-strain IPMC [2].

IPMC produced with the aforementioned fabrication methods can only generate bending motions. However, actuators capable of complex deformation are highly desirable in many applications, such as contour control of space inflatable structures [90], biomimetic robots [52, 93], and tunable mirror membranes [61]. Fig. 1.3 shows an inspiring example from biology, where one can see that the pectoral fin of a sunfish produces sophisticated conformational changes to achieve efficient locomotion and maneuvering. The complex shape change is enabled by multiple muscle-controlled, relatively rigid fin rays that are connected via collagenous membrane. Several groups have assembled discrete components to make such multiple degree-of-freedom (MDOF) actuators [52, 93]. However, the performance of assembled actuators was limited by complex structure design, friction among the components, and low energy efficiency in force transmission. While MDOF IPMC actuators can be obtained by manually removing the metal electrode of IPMC in certain areas [28], this approach is time-consuming and not amenable to miniaturization and batch-fabrication. Monolithic fabrication of MDOF IPMC actuators with a simple structure will be essential to improve the performance, reduce the cost, and enable mass production.

Efforts have been made in fabrication of patterned IPMCs by Jeon and coworkers [41, 43, 42], where they combined electroplating with electroless plating to selectively grow platinum electrodes on a Nafion film. In their work, however, tapes were used as masks to achieve patterning, which would not be conducive to microfabrication or batch-fabrication. Lithography-based microfabrication of IPMC has also been pursued by several groups [89,

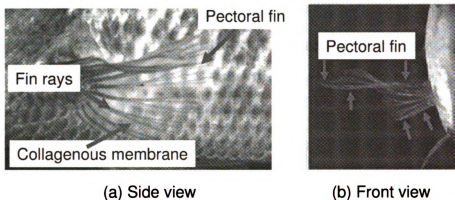


Figure 1.3: Pectoral fin of a bluegill sunfish undergoing sophisticated shape changes during maneuvering and locomotion [54].

97, 41], where metal layers are deposited directly on Nafion to form electrodes. Without the critical ion-exchange and electroless plating processes, IPMCs fabricated this way typically are not highly active, and the metal electrodes tend to peel off under large deformation because of the poor metal-polymer bonding. Feng *et al.* developed microfabrication-based IPMCs with arbitrarily defined shapes, where the ion-exchange and electroless plating steps were also incorporated [34]. However, the actuators fabricated with this approach have a single degree of freedom and can perform bending only.

The contribution of this research is a new process flow for lithography-based, monolithic fabrication of highly active, MDOF IPMC actuators. Inspired by the structure of the sunfish pectoral fin, we propose to achieve sophisticated three-dimension (3-D) deformation by creating multiple IPMC regions that are mechanically coupled through compliant, passive membrane. Both the IPMCs and the passive regions are to be formed from a same Nafion film. There are two major challenges in fabricating such actuators. First, the passive areas can substantially constrain the motion of the active areas. An effective, precise approach is needed for tailoring the stiffness of the passive areas. Second, Nafion films are highly swellable in a solvent. Large volume change results in poor adhesion of photoresist to Nafion and creates problems in photolithography and other fabrication steps.

To overcome these challenges, two novel fabrication techniques have been introduced: 1) selectively thinning down Nafion with plasma etch, to make the passive areas thin and compliant; 2) impregnating Nafion film with platinum ions, which significantly reduces the film swellability and allows subsequent lithography and other steps.

The developed fabrication process involves plasma etching, ion-exchange, lithography, physical vapor deposition (PVD), and electroless plating steps. Reactive ion etching (RIE) with oxygen and argon plasmas is used to selectively thin down the passive area of Nafion membrane with a patterned aluminum mask. An etch recipe has been developed to achieve a high etching rate of $0.58 \mu\text{m}/\text{min}$ without damaging the film. In IPMC fabrication, an ion-exchange step is usually performed immediately before electrode plating. However, we have found that impregnating Nafion with platinum ions through ion-exchange can also increase its stiffness by two to three times, and reduce its swellability in water and in acetone by over 20 times. This has proven critical in successful photolithography-based patterning in that it ensures good adhesion of photoresist to the Nafion film. A positive photoresist, AZ9260, is used in photolithography to create thick patterns which are used as the mask in the electroless plating process to selectively grow platinum electrodes in IPMC regions. After IPMC is formed, we treat the sample with hydrochloride acid (HCL) to undo the effect of the stiffening process, which softens the passive areas and enhances the actuation performance.

As a demonstration, we have applied the proposed method and fabricated artificial pectoral fins, each with three IPMC regions. A characterization system consisting of a CCD camera and image processing software has been set up to quantify the deformations generated by the fabricated samples. We have verified that, by controlling the phase differences between the voltage signals applied to the IPMC regions, each artificial fin can produce sophisticated deformation modes, including bending, twisting, and cupping. For example, a twisting angle of 16° peak-to-peak can be achieved with actuation voltages of 3 V at 0.3 Hz, when the top and bottom IPMCs lead the middle IPMC in phase by $\pm 90^\circ$. We have

investigated the impact of the thickness of passive area, and verified that the thinner the passive region, the larger the deformations. This has thus provided supporting evidence for our approach of modulating mechanical stiffness through plasma etching. We have further performed preliminary studies of the fabricated fins in underwater operation using a Digital Particle Image Velocimetry (DPIV) system. Interesting flow patterns are observed when the fin is actuated, which shows the promise of the fabricated fins in robotic fish applications.

1.4 Organization of This Dissertation

The remainder of this dissertation is organized as follows. Control-oriented modeling of IPMC actuator is presented in Chapter 2. Modeling of IPMC sensors is discussed in Chapter 3. Modeling of biomimetic robotic fish propelled by an IPMC actuator is shown in Chapter 4. Nonlinear control-oriented model for IPMC is discussed in Chapter 5. IPMC/PVDF sensory actuator is described in Chapter 6. Monolithic fabrication of the IPMC actuator to achieve complex deformations is presented in Chapter 7. Conclusions and future work are provided in Chapter 8.

Chapter 2

A Dynamic Model for Ionic Polymer-Metal Composite Actuators

The remainder of the chapter is organized as follows. The governing PDE is reviewed in Section 2.1. In Section 2.2, the electrical impedance model for IPMC actuator is derived by exactly solving the PDE, with and without considering the surface resistance. This lays the groundwork for deriving the full actuation model, which is described in Section 2.3. Model reduction is discussed in Section 2.4. Experimental validation of the proposed model is presented in Section 2.5. Model-based H_∞ controller design and its real-time implementation are reported in Section 2.6. Finally, concluding remarks are provided in Section 2.7.

2.1 The Governing Partial Differential Equation

The governing PDE for charge distribution in an IPMC was first presented in [64] and then used by Farinholt and Leo [32] for investigating the sensing response. Let \mathbf{D} , \mathbf{E} , ϕ , and ρ denote the electric displacement, the electric field, the electric potential, and the charge

density, respectively. The following equations hold:

$$\mathbf{E} = \frac{\mathbf{D}}{\kappa_e} = -\nabla\phi, \quad (2.1)$$

$$\nabla \cdot \mathbf{D} = \rho = F(C^+ - C^-), \quad (2.2)$$

where κ_e is the effective dielectric constant of the polymer, F is Faraday's constant, and C^+ and C^- are the cation and anion concentrations, respectively. The continuity equation that relates the ion flux vector \mathbf{J} to C^+ is given by,

$$\nabla \cdot \mathbf{J} = -\frac{\partial C^+}{\partial t}. \quad (2.3)$$

Since the thickness of an IPMC is much smaller than its length or width, one can assume that, inside the polymer, \mathbf{D} , \mathbf{E} , and \mathbf{J} are all restricted to the thickness direction (x -direction). This enables one to drop the boldface notation for these variables. The ion flux consists of diffusion, migration, and convection terms:

$$J = -d \left(\nabla C^+ + \frac{C^+ F}{RT} \nabla \phi + \frac{C^+ \Delta V}{RT} \nabla p \right) + C^+ v, \quad (2.4)$$

where d is the ionic diffusivity, R is the gas constant, T is the absolute temperature, p is the fluid pressure, v the free solvent velocity field, and ΔV is the volumetric change which demonstrates how much the polymer volume swells after taking water. From (2.2), C^+ can be written as

$$C^+ = \frac{1}{F} \rho + C^-, \quad (2.5)$$

where C^- is homogeneous in space and time-invariant since anions are fixed to the polymer backbone. Taking the gradient with respect to x on both sides of (2.5) and using (2.1) and (2.2), one gets

$$\nabla C^+ = \frac{\kappa_e}{F} \nabla^2 \phi. \quad (2.6)$$

Darcy's Law [26] is used to relate the fluid velocity v to the pressure gradient ∇p [38],

$$v = k'(C^- FE - \nabla p), \quad (2.7)$$

where k' denotes the hydraulic permeability coefficient. Neglecting the convection term [32], i.e., assuming $v = 0$, leads to

$$\nabla p = C^- FE. \quad (2.8)$$

Substituting (2.5), (2.6), and (2.8) into the original ion flux equation (2.4) and using $\nabla \phi = -E$, one can rewrite J as

$$J = -d \left(\frac{\kappa_e}{F} \nabla^2 E - \frac{\kappa_e (1 - C^- \Delta V)}{RT} \nabla E \cdot E - \frac{FC^- (1 - C^- \Delta V)}{RT} E \right). \quad (2.9)$$

Assuming $\kappa_e \nabla E \ll C^- F$ (see [63] for justification), the nonlinear term involving $\nabla E \cdot E$ in (2.9) is dropped, resulting in

$$J = -d \left(\frac{\kappa_e}{F} \nabla^2 E - \frac{FC^-}{RT} (1 - C^- \Delta V) E \right). \quad (2.10)$$

Next writing

$$\frac{\partial C^+}{\partial t} = \frac{1}{F} \frac{\partial \rho}{\partial t} = \frac{\kappa_e}{F} \frac{\partial (\nabla E)}{\partial t} = \frac{\kappa_e}{F} \frac{\partial^2 E}{\partial x \partial t},$$

and using (2.3), one obtains the following equation involving E :

$$\frac{\kappa_e}{F} \frac{\partial^2 E}{\partial x \partial t} = d \left(\frac{\kappa_e}{F} \frac{\partial^3 E}{\partial x^3} - \frac{FC^-}{RT} (1 - C^- \Delta V) \frac{\partial E}{\partial x} \right). \quad (2.11)$$

Expressing (2.11) in terms of $\rho = \kappa_e \nabla E = \kappa_e \frac{\partial E}{\partial x}$, we can get

$$\frac{\partial \rho}{\partial t} - d \frac{\partial^2 \rho}{\partial x^2} + \frac{F^2 d C^-}{\kappa_e RT} (1 - C^- \Delta V) \rho = 0, \quad (2.12)$$

which is the governing PDE for the charge density ρ inside the polymer. Nemat-Nasser and Li [64] assumed that the induced stress is proportional to the charge density:

$$\sigma = \alpha_0 \rho , \quad (2.13)$$

where α_0 is the coupling constant.

Farinholt [33] investigated the current response of a cantilevered IPMC beam when the base is subject to step and harmonic actuation voltages. A key assumption is that the ion flux at any point on the IPMC electrodes is zero. This assumption, which serves as a boundary condition for the governing PDEs, leads to

$$\left(\frac{\partial^3 \phi}{\partial x^3} - \frac{F^2 C^-}{\kappa_e R T} \frac{\partial \phi}{\partial x} \right) \Big|_{x = \pm h} = 0 . \quad (2.14)$$

The work of Farinholt was based on obtaining an analytical but approximate solution $\rho(x, t)$ to (2.12) with some assumptions on the solution. For the step response, the solution is assumed to take a separable form $\rho(x, t) = P(x)Q(t)$. For the harmonic response, the solution is assumed to be the sum of forced and resonant components. These assumptions limit the model's applicability in real-time control where the model should work for arbitrary voltage inputs.

2.2 Electrical Impedance Model

From (2.13), the stress induced by the actuation input is directly related to the charge density distribution ρ . Therefore, as a first step in developing the actuation model, we will derive the electrical impedance model in this section. While the latter is of interest in its own right, one also obtains the explicit expression for ρ as a byproduct of the derivation.

Consider Fig. 2.1, where the beam is clamped at one end ($z = 0$), and is subject to an actuation voltage producing the tip displacement $w(t)$ at the other end ($z = L$). The neutral

axis of the beam is denoted by $x = 0$, and the upper and lower surfaces are denoted by $x = h$ and $x = -h$, respectively. To ease the presentation, define the aggregated constant

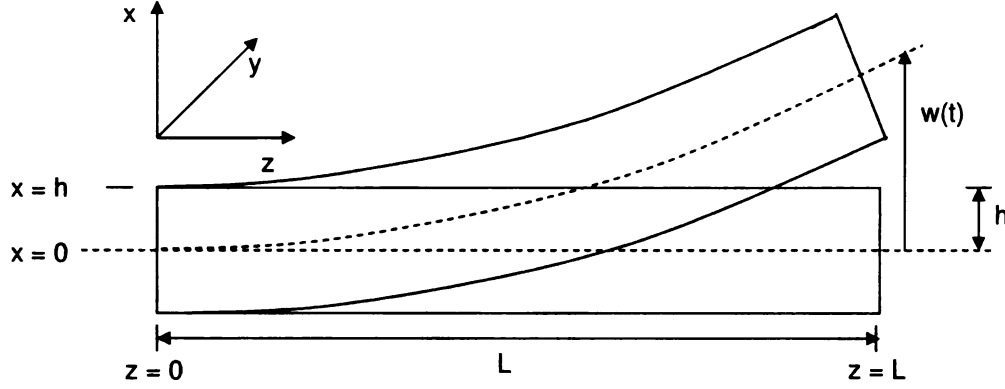


Figure 2.1: Geometric definitions of an IPMC cantiliver beam.

$$K \triangleq \frac{F^2 d C^-}{\kappa_e R T} (1 - C^- \Delta V) . \quad (2.15)$$

Performing Laplace transform for the time variable of $\rho(x, z, t)$ (noting the independence of ρ from the y coordinate), one converts (2.12) into the Laplace domain:

$$s\rho(x, z, s) - d \frac{\partial^2 \rho(x, z, s)}{\partial x^2} + K\rho(x, z, s) = 0 , \quad (2.16)$$

where s is the Laplace variable. Define $\beta(s)$ such that $\beta^2(s) = \frac{s+K}{d}$. With an assumption of symmetric charge distribution about $x = 0$, a generic solution to (2.16) can be obtained as

$$\rho(x, z, s) = 2c_2(z, s) \sinh(\beta(s)x) , \quad (2.17)$$

where $c_2(z, s)$ depends on the boundary condition of the PDEs. Using (2.17) and the field equations (2.1) and (2.2), one can derive the expressions for the electric field E and then

for the electric potential ϕ in the Laplace domain:

$$E(x, z, s) = 2c_2(z, s) \frac{\cosh(\beta(s)x)}{\kappa_e \beta(s)} + a_1(z, s), \quad (2.18)$$

$$\phi(x, z, s) = -2c_2(z, s) \frac{\sinh(\beta(s)x)}{\kappa_e \beta^2(s)} - a_1(z, s)x + a_2(z, s), \quad (2.19)$$

where $a_1(z, s)$ and $a_2(z, s)$ are appropriate functions to be determined based on the boundary conditions on ϕ . Two different boundary conditions are discussed next, one ignoring the surface electrode resistance and the other considering the resistance. In both cases it will be shown that the final actuation current is proportional to the applied voltage input $V(s)$, and thus a transfer function for the impedance model can be derived.

2.2.1 Model ignoring the surface resistance

First consider the case where the surface electrodes are perfectly conducting, as was assumed by Farinholt [33]. The electric potential is uniform across both surfaces $x = \pm h$, and without loss of generality, the potential is set to be:

$$\phi(\pm h, z, s) = \pm \frac{V(s)}{2}. \quad (2.20)$$

Combining (2.19), (2.20) with (2.14), one can solve for $a_1(z, s)$, $a_2(z, s)$, and $c_2(z, s)$, and then obtain $E(h, z, s)$ from (2.18):

$$E(h, z, s) = -\frac{V(s)}{2h} \frac{\gamma(s)(s+K)}{(s\gamma(s) + K \tanh(\gamma(s)))}, \quad (2.21)$$

where $\gamma(s) \triangleq \beta(s)h$. The total charge is obtained by integrating the electrical displacement D on the boundary $x = h$:

$$Q(s) = \int_0^W \int_0^L D(h, z, s) dz dy = \int_0^W \int_0^L \kappa_e E(h, z, s) dz dy. \quad (2.22)$$

Plugging (2.21) into (2.22), one can derive $Q(s)$, which is linear with respect to the external stimulus $V(s)$. The actuation current $i(t)$ is the time-derivative of the charge $Q(t)$, and hence $I(s) = sQ(s)$ in the Laplace domain. The impedance is then derived as:

$$Z_1(s) = \frac{V(s)}{I(s)} = \frac{s + K \frac{\tanh(\gamma(s))}{\gamma(s)}}{Cs(s + K)}, \quad (2.23)$$

where $C = \kappa_e \frac{WL}{2h}$ can be regarded as the apparent capacitance of the IPMC.

2.2.2 Model considering distributed surface resistance

The surface electrode of an IPMC typically consists of aggregated nanoparticles formed during chemical reduction of noble metal salt (such as platinum salt) [49]. The surface resistance is thus non-negligible and has an influence on the sensing and actuation behavior of an IPMC [78]. In this chapter the effect of distributed surface resistance is incorporated into the impedance model, as illustrated in Fig. 2.2. Let the electrode resistance per unit length be r_1 in z direction and r_2 in x direction. One can further define these quantities in terms of fundamental physical parameters: $r_1 = r'_1/W$, $r_2 = r'_2/W$, with r'_1 and r'_2 representing the surface resistance per {unit length · unit width} in z and x directions, respectively. In Fig. 2.2, $i_p(z, s)$ is the distributed current per unit length going through the polymer due to the ion movement, $i_k(z, s)$ represents the leaking current per unit length, and $i_s(z, s)$ is the surface current on the electrodes. R_p denotes the through-polymer resistance per unit length, which can be written as $R_p = R'_p/W$, with R'_p being the polymer resistance per {unit length · unit width}. Note that by the continuity of current, the current $i_s(z, s)$ on the top surface equals that on the bottom surface but with an opposite direction. The surface current $i_s(0, s)$ at $z = 0$ is the total actuation current $i(s)$.

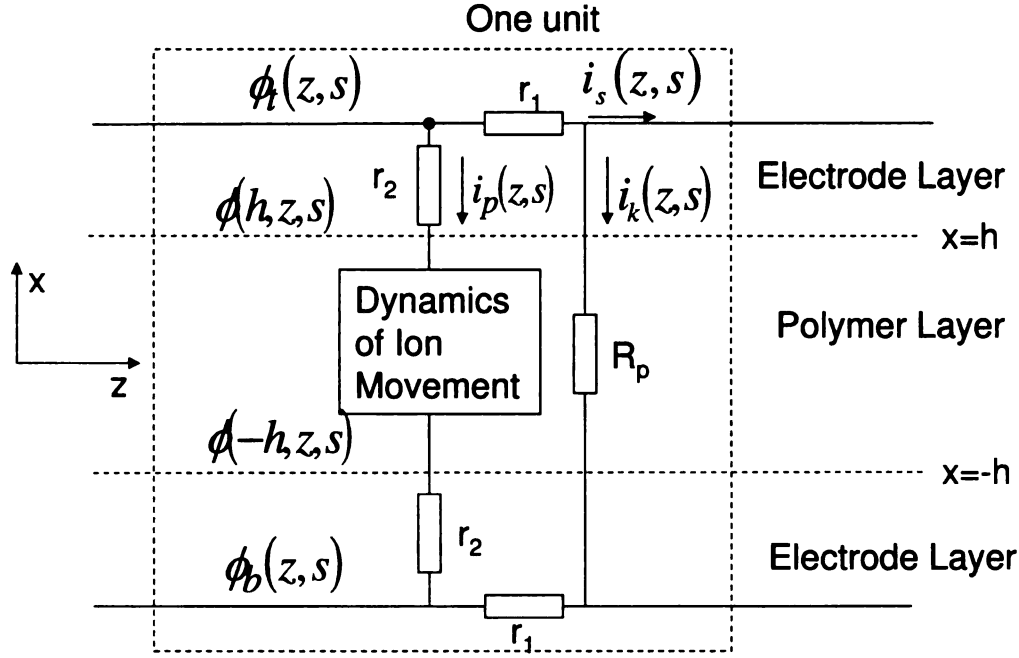


Figure 2.2: Illustration of the IPMC impedance model with surface resistance.

The following equations capture the relationships between $i_s(z,s)$, $i_p(z,s)$, $i_k(z,s)$, $\phi_{\pm}(z,s)$:

$$\frac{\partial \phi_{\pm}(z,s)}{\partial z} = \mp \frac{r'_1}{W} i_s(z,s) , \quad (2.24)$$

$$\frac{\partial i_s(z,s)}{\partial z} = -(i_p(z,s) + i_k(z,s)) . \quad (2.25)$$

From the potential condition at $z = 0$, i.e., $\phi_{\pm}(0,s) = \pm \frac{V(s)}{2}$, the boundary conditions for (2.19) are derived as:

$$\phi(\pm h,z,s) = \phi_{\pm}(z,s) \mp i_p(z,s)r'_2/W . \quad (2.26)$$

With (2.24) and (2.26), one gets

$$\phi(\pm h,z,s) = \frac{\pm V(s)}{2} \mp \int_0^z \frac{r'_1}{W} i_s(\tau,s) d\tau - \frac{r'_2}{W} i_p(z,s) , \quad (2.27)$$

Combining (2.27) with (2.19), one can solve for the functions $a_1(z,s)$ and $a_2(z,s)$ in the generic expression for $\phi(x,z,s)$. With consideration of the boundary condition (2.14), one

can solve for $c_2(z, s)$. With $a_1(z, s)$, $a_2(z, s)$ and $c_2(z, s)$, one obtains $E(h, z, s)$ from (2.18):

$$E(h, z, s) = -\frac{\phi(h, z, s)}{h} \frac{\gamma(s)(s+K)}{\gamma(s)s + K \tanh(\gamma(s))}. \quad (2.28)$$

Define the actuation current along the negative x -axis direction to be positive. The current i_p due to the ion movement can be obtain as

$$i_p(z, s) = -sWD(h, z, s) = -sW\kappa_e E(h, z, s). \quad (2.29)$$

The leaking current i_k can be obtained as

$$i_k(z, s) = \frac{\phi_+(z, s) - \phi_-(z, s)}{R'_p/W}. \quad (2.30)$$

With (2.28), (2.29) and (2.30), one can solve the PDE (2.25) for the surface current $i_s(z, s)$ with the boundary condition $i_s(L, s) = 0$. The total actuation current $I(s) = i_s(0, s)$ can be obtained, from which the transfer function for the impedance can be shown to be

$$Z_2(s) = \frac{V(s)}{I(s)} = \frac{2\sqrt{B(s)}}{A(s) \tanh(\sqrt{B(s)}L)}, \quad (2.31)$$

where

$$A(s) \triangleq \frac{\theta(s)}{(1 + r'_2 \theta(s)/W)} + \frac{2W}{R'_p}, \quad (2.32)$$

$$B(s) \triangleq \frac{r'_1}{W} A(s), \quad (2.33)$$

$$\theta(s) \triangleq \frac{sW\kappa_e \gamma(s)(s+K)}{h(s\gamma(s) + K \tanh(\gamma(s)))}. \quad (2.34)$$

See Appendix A.1 for the detailed derivation.

One can show that $Z_2(s)$ is consistent with $Z_1(s)$, (2.23), when $r'_1 \rightarrow 0$, $r'_2 \rightarrow 0$ and $R'_p \rightarrow \infty$.

2.3 Actuation Model

First we derive the transfer function $H(s)$ relating the free tip displacement of an IPMC beam, $w(L, s)$, to the actuation voltage $V(s)$, when the beam dynamics (inertia, damping, etc.) is ignored. From (2.13) and (2.17), one obtains the generic expression for the stress $\sigma(x, z, s)$ generated due to actuation:

$$\sigma(x, z, s) = 2\alpha_0 c_2(z, s) \sinh(\beta(s)x). \quad (2.35)$$

Note that $c_2(z, s)$ is available from the derivation of the impedance model. When considering the surface resistance, the bending moment $M(z, s)$ is obtained as

$$\begin{aligned} M(z, s) &= \int_{-h}^h x \sigma(x, z, s) W dx \\ &= \int_{-h}^h 2\alpha_0 W x c_2(z, s) \sinh(\beta(s)x) dx \\ &= -\frac{2\alpha_0 K W \kappa_e (\gamma(s) - \tanh(\gamma(s))) \phi(h, z, s)}{(s\gamma(s) + K \tanh(\gamma(s)))}. \end{aligned} \quad (2.36)$$

From the linear beam theory [37],

$$\begin{aligned} \frac{\partial^2 w(z, s)}{\partial z^2} &= \frac{M(z, s)}{YI} \\ &= -\frac{2\alpha_0 K W \kappa_e (\gamma(s) - \tanh(\gamma(s))) \phi(h, z, s)}{YI(s\gamma(s) + K \tanh(\gamma(s)))} \\ &= -\frac{\alpha_0 K W \kappa_e (\gamma(s) - \tanh(\gamma(s)))}{YI(s\gamma(s) + K \tanh(\gamma(s)))} \\ &\quad \cdot \frac{V(s) - 2 \int_0^z \frac{r'_1}{W} i_s(\tau, s) d\tau}{1 + r'_2 \theta(s)/W}, \end{aligned} \quad (2.37)$$

where the last equality follows from (2.27) and (A.1), Y is the effective Young's modulus of the IPMC, and $I = \frac{2}{3} W h^3$ is the moment of inertia of the IPMC. Solving (2.37) with

boundary conditions $w(0,s) = 0$ and $w'(0,s) = 0$, one can get

$$w(L,s) = -\frac{1}{2} \frac{\alpha_0 W}{YI} \frac{K \kappa_e (\gamma(s) - \tanh(\gamma(s)))}{(\gamma(s)s + K \tanh(\gamma(s)))} \cdot \frac{V(s)L^2 - 4 \int_0^L \int_0^z \int_0^{z'} \frac{r'_1}{W} i_s(\tau,s) d\tau dz' dz}{1 + r'_2 \theta(s)/W}.$$

Using (A.7) and (A.8), one can show

$$V(s)L^2 - 4 \int_0^L \int_0^z \int_0^{z'} \frac{r'_1}{W} i_s(\tau,s) d\tau dz' dz = 2L^2 X(s)V(s),$$

where $X(s)$ is defined as:

$$X(s) \triangleq -\frac{1 - \operatorname{sech}(\sqrt{B(s)}L) - \tanh(\sqrt{B(s)}L) \sqrt{B(s)}L}{B(s)L^2}. \quad (2.38)$$

One thus obtains the transfer function $H(s) = \frac{w(L,s)}{V(s)}$:

$$H(s) = -\frac{L^2 \alpha_0 W}{2YI} \frac{K \kappa_e (\gamma(s) - \tanh(\gamma(s)))}{(\gamma(s)s + K \tanh(\gamma(s)))} \left(\frac{2X(s)}{1 + r'_2 \theta(s)/W} \right). \quad (2.39)$$

$H(s)$ for the case where the surface resistance is ignored can be derived in an analogous and simpler manner, and it is omitted here for brevity. Note that the blocking force output $F(s)$ at the tip can be derived via $F(s) = w(L,s)K_0$, where $K_0 = \frac{3YI}{L^3}$ denotes the spring constant of the beam.

Back to the free bending case, in order to accommodate the vibration dynamics of the beam, we cascade $G(s)$ to $H(s)$, as illustrated in Fig. 2.3. As the output of $G(s)$ represents the bending displacement (as that of $H(s)$ does), $G(s)$ will have a DC gain of 1. Since the actuation bandwidth of an IPMC actuator is relatively low (under 10 Hz), it often suffices to

capture the mechanical dynamics $G(s)$ with a second-order system (first vibration mode):

$$G(s) = \frac{\omega_n^2}{s^2 + 2\xi\omega_n s + \omega_n^2}, \quad (2.40)$$

where ω_n is the natural frequency of the IPMC beam, and ξ is the damping ratio. The natural frequency ω_n can be further expressed in terms of the beam dimensions and mechanical properties [91].

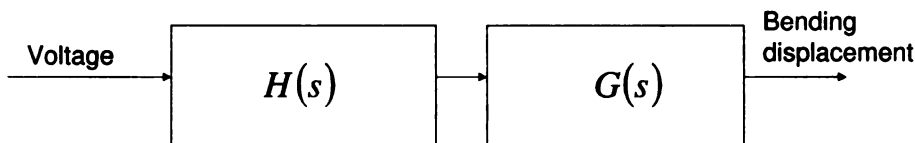


Figure 2.3: Actuation model structure.

2.4 Model Reduction

An important motivation for deriving a transfer function-type actuation model is its potential use for real-time feedback control. For practical implementation of feedback control design, the model needs to be finite-dimensional, i.e., being a finite-order, rational function of s . However, in the actuation model derived earlier, $H(s)$ is infinite-dimensional since it involves non-rational functions including $\sinh(\cdot)$, $\cosh(\cdot)$, $\sqrt{\cdot}$, etc. A systematic approach to model reduction is Padé approximation [7], where one can approximate $H(s)$ with a rational function of specified order. However, the computation involved is lengthy and the resulting coefficients for the reduced model can be complex. Therefore, in this chapter a much simpler, alternative approach is proposed for model reduction by exploiting the knowledge of physical parameters and specific properties of hyperbolic functions.

For ease of presentation, decompose $H(s)$ as

$$H(s) = f(s) \cdot g(s) \cdot X(s), \quad \text{where}$$

$$f(s) = -\frac{L^2 \alpha_0 W K \kappa_e (\gamma(s) - \tanh(\gamma(s)))}{2YI (\gamma(s)s + K \tanh(\gamma(s)))}, \quad (2.41)$$

$$g(s) = \frac{2}{1 + r'_2 \theta(s)/W}. \quad (2.42)$$

Based on the physical parameters (see Table 2.1 in Section 2.5), $|\gamma(s)| \gg 10$, and $K \gg 10^6$, which allows one to make the approximation in the low frequency range (< 100 Hz):

$$\tanh(\gamma(s)) \approx 1, \quad (2.43)$$

$$\gamma(s) \approx h\sqrt{\frac{K}{d}} =: \gamma. \quad (2.44)$$

With (2.43) and (2.44), one can simplify $f(s)$, $\theta(s)$ and $g(s)$ as

$$f(s) \approx -\frac{L^2 \alpha_0 W K \kappa_e (\gamma - 1)}{2YI (\gamma s + K)}, \quad (2.45)$$

$$\theta(s) \approx \frac{sW \kappa_e \gamma (s + K)}{h(\gamma s + K)}, \quad (2.46)$$

$$g(s) \approx \frac{2h(\gamma s + K)}{r'_2 \gamma \kappa_e s (s + K) + h(\gamma s + K)}. \quad (2.47)$$

The Taylor series expansions of $\sinh(a)$ and $\cosh(a)$ will be used for approximating $X(s)$:

$$X(s) \approx \frac{1 + \sum_{n=0}^m \left(\frac{a^{2n+2}}{(2n+1)!} - \frac{a^{2n}}{(2n)!} \right)}{\sum_{n=0}^m \frac{a^{2n+2}}{(2n)!}}, \quad (2.48)$$

with $a = \sqrt{B(s)}L$, for some finite integer m . When $|s|$ is small (low-frequency range) and $\frac{2r'_1}{R'_p}$ is small (which is indeed the case, see parameters in Table 2.1), $|\sqrt{B(s)}L|$ is small and (2.48) approximates $X(s)$ well with a small integer m . Note that only even-degree terms appear in (2.48), and hence (2.48) is a function of $B(s)L^2$ instead of $\sqrt{B(s)}L$. Finally, since

$B(s)$ is a rational function of $\theta(s)$ and $\theta(s)$ is approximated by a rational function (2.46), one can obtain an approximation to $X(s)$ by a rational function of s .

Combining (2.45), (2.47), and the approximation to $X(s)$, one gets a rational approximation to $H(s)$. Since the mechanical dynamics $G(s)$ is already rational, one obtains a finite-dimensional actuation model. Note that a reduced model is still a physical model. In particular, it is described in terms of fundamental physical parameters and is thus geometrically scalable. This represents a key difference from other low-order, black-box models, in which case the parameters have no physical meanings and one would have to re-identify the parameters empirically for every actuator.

2.5 Experimental Model Verification

2.5.1 Experimental setup

Fig. 2.4 shows the experimental setup. An IPMC sample is dipped in water and clamped at one end. The IPMC is subject to voltage excitation generated from the computer (through dSPACE DS1104 and ControlDesk). A laser displacement sensor (OADM 20I6441/S14F, Baumer Electric) with precision set to $\pm 0.02\text{mm}$ is used to measure the bending displacement $w(t)$. The IPMC actuation current is measured with a current-amplifier circuit.

2.5.2 Identification of parameters in impedance model

Table 2.1 lists the parameters obtained for the impedance model. Among them some are physical constants (gas constant R and Faraday's constant F), some can be measured directly (absolute temperature T , effective Young's modulus Y [18], actuator dimensions, surface resistance r_1 in z direction and through-polymer resistance R_p), and the others need to be identified through curve-fitting. Since $|C^-\Delta V| \ll 1$ [64], we take $1 - C^-\Delta V \approx 1$. The IPMC materials used in this work were obtained from Environmental Robots Inc., and

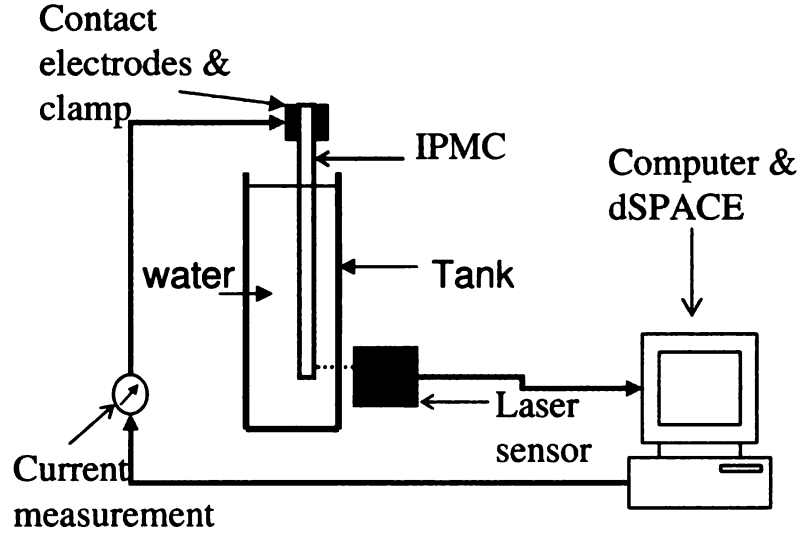


Figure 2.4: Experimental setup.

the sample dimensions reported have an accuracy of ± 0.5 mm in the length and width directions and ± 0.5 μm in the thickness direction.

Table 2.1: Parameters for the impedance model.

F	R	T	R'_p
96487 C/mol	8.3143 J/mol · K	300 K	$0.37 \Omega \cdot \text{m}^2$
Y [18]	h	r'_1	r'_2
5.71×10^8 Pa	180 (μm)	22.3 Ω	$1.8 \times 10^{-5} \Omega \cdot \text{m}$
d	C^-	κ_e	
1.38×10^{-9} m ² /s	1091 mol/m ³	1.34×10^{-6} F/m	

A nonlinear fitting process is used to identify the diffusion coefficient d , the anion concentration C^- , the dielectric constant κ_e , and the surface resistance density r'_2 in x direction, based upon the empirical impedance response of an IPMC actuator with dimensions 37.0×5.5 mm. In particular, the impedance model $Z_2(j2\pi f)$ predicts the magnitude and phase response of the actuator at frequency f , as a nonlinear function of the parameters. The Matlab function *fminsearch* can be used to find the parameters that minimize the squared error between the empirical frequency response and the model prediction. The identified parameters are listed in Table 2.1, where the values of d and C^- are close to what were reported in the literature [63, 33]. The value of κ_e , however, differs from those

reported in [63, 33] by several orders of magnitude. This could be attributed to different materials and experimental conditions (e.g., in water versus in air). It should be noted that the value of κ_e in the relevant literature was also obtained through model fitting instead of direct physical measurement. It is thus of interest to examine more direct measurement of these parameters in the future.

For independent verification of the proposed model, the identified parameters will be used in predicting impedance behaviors of other IPMC actuators with different dimensions, as will be seen in Section 2.5.3.

2.5.3 Verification of the impedance model

Impedance model verification will be conducted on two aspects. First, it will be shown that the model considering the surface resistance is more accurate than the model ignoring the resistance, by comparing them with the measured frequency response of an IPMC actuator. Second, the geometric scalability of the proposed model will be confirmed by the agreement between model predictions and experimental results for IPMC actuators with different dimensions.

Effect of surface resistance

In order to examine the difference between the impedance models $Z_1(s)$ and $Z_2(s)$, their model parameters were identified separately through the nonlinear fitting process described in Section 2.5.2. The experimental data were obtained for an IPMC actuator with dimensions $37.0 \times 5.5 \times 0.360 \text{ mm}^3$. Fig. 2.5 compares the predicted frequency response (both magnitude and phase) by each model with the measured frequency response. It is clear that the model considering the surface resistance shows better agreement than the one ignoring the resistance. This indicates that the model incorporating the surface resistance is more effective in capturing the actuation dynamics of IPMC, and thus it will be used for the remainder of this chapter.

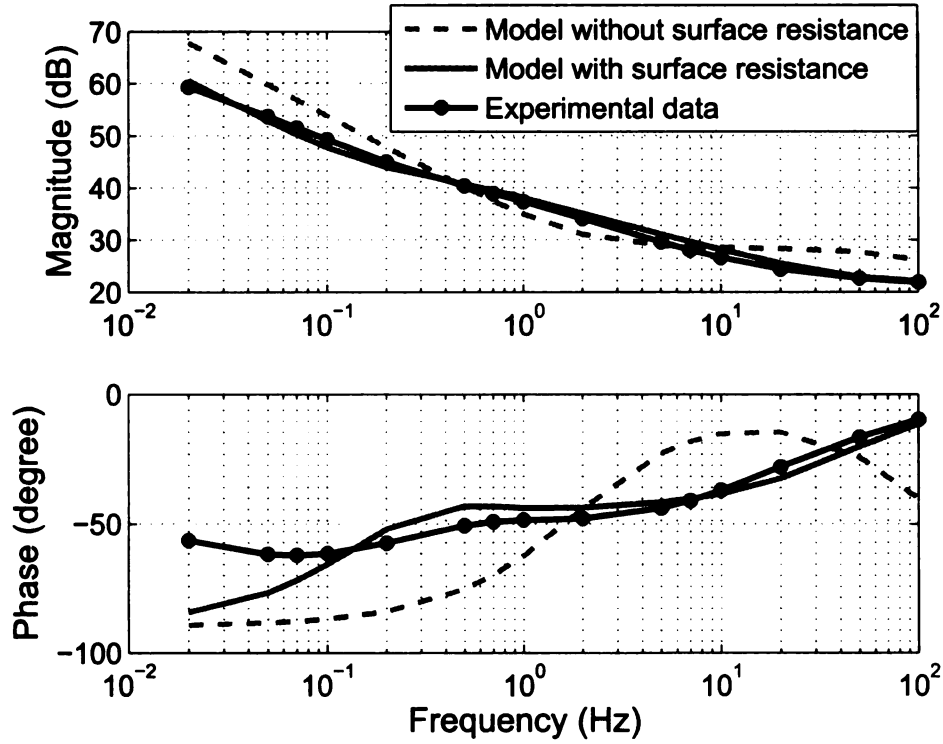


Figure 2.5: Comparison of experimental impedance responses with model predictions, with and without consideration of surface resistance.

Geometric scalability of the dynamic model.

Three samples with different dimensions (see Table 2.2) were cut from one IPMC sheet, and were labeled as *Big*, *Slim*, and *Short* for ease of referencing. The model parameters were first identified for the *Slim* sample, as discussed in Section 2.5.2. Without re-tuning, these parameters (except geometric dimensions) were plugged into (2.31), i.e., the model $Z_2(s)$, for predicting the frequency response for the *Big* and *Short* samples.

Table 2.2: Dimensions of three IPMC samples used for verification of model scalability.

IPMC beam	length (mm)	width (mm)	thickness (μm)
<i>Big</i>	39.0	11.0	360
<i>Slim</i>	37.0	5.5	360
<i>Short</i>	27.0	5.5	360

Fig. 2.6 shows the Bode plots of the frequency responses for the *Slim* and *Big* samples. It can be seen that for both samples, good agreement between the model prediction and the experimental data is achieved. Fig. 2.7 compares the frequency responses of the *Slim* and *Short* samples. Reasonable match between the model predictions and the empirical curves is again achieved for both samples. These figures show that the model is geometrically scalable.

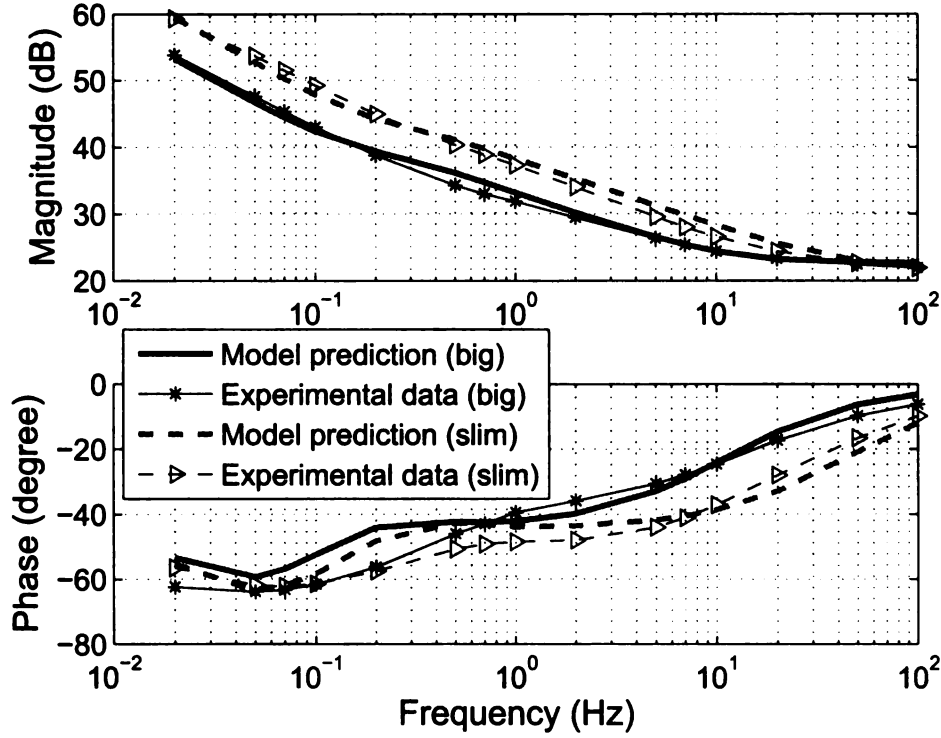


Figure 2.6: Impedance model verification for the *Big* and *Slim* IPMC samples.

2.5.4 Verification of the actuation model

The actuation model has two modules serially connected, as shown in Fig. 2.3. All parameters of $H(s)$ have been identified during identification of the impedance model except the stress-charge coupling constant α_0 . The natural frequency ω_n and the damping ratio ξ in $G(s)$ can be identified based on the measurement of damped oscillations of the IPMC

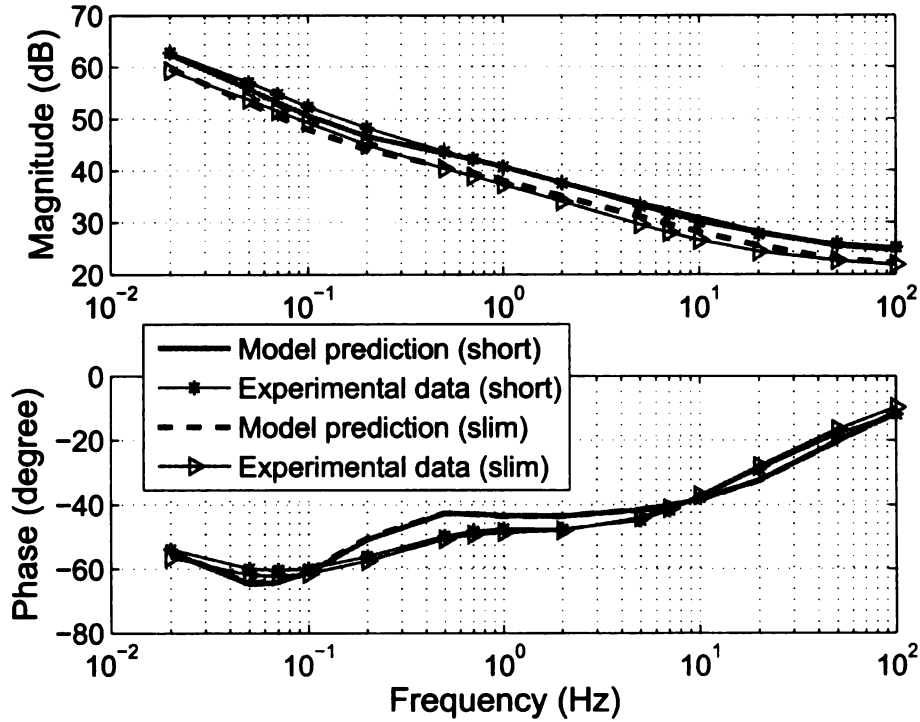


Figure 2.7: Impedance model verification for the *Slim* and *Short* IPMC samples.

beam in the passive state. For the *Big* sample, we obtained $\omega_n = 28.9$ rad/s, and $\xi = 0.1$. Finally, α_0 , which is simply a gain parameter in the actuation model, was identified to be $\alpha_0 = 0.129$ J/C using the magnitude of actuation response measured under a sinusoidal voltage input.

The whole actuation model was verified in experiments by applying sinusoidal actuation signals $V(t)$ with amplitude 0.2 V and frequency from 0.02 Hz to 20 Hz. The laser sensor was used to measure the bending displacement $w(t)$ at the free end of the *Big* sample. The magnitude gain and phase shift from the input $V(s)$ to the output $w(s)$ were obtained, which show good agreement with the model prediction; see Fig. 2.8. Note that, from the empirical Bode plot, the natural frequency of the IPMC beam in the active state (under actuation) is about 30 rad/s, and thus slightly higher than that measured in the passive state. It indicates that the effective stiffness of an IPMC is influenced by the actuation input. How-

ever, such an effect is not significant for relatively low actuation voltages, and a detailed discussion on this would be beyond the scope of the current chapter.

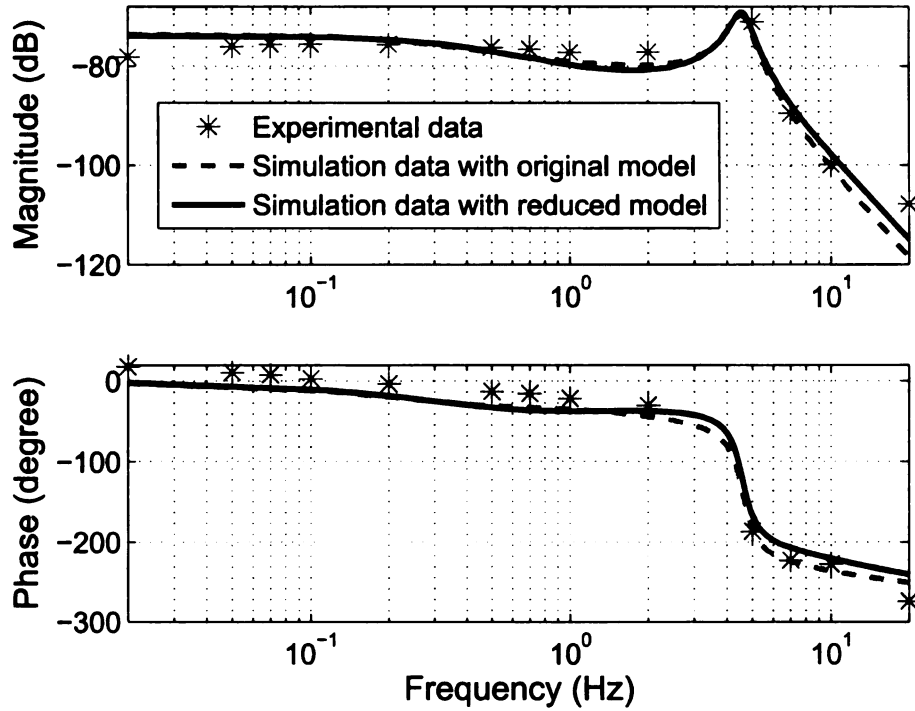


Figure 2.8: Comparison of the measured actuation response with the proposed full and reduced models for the *Big* sample.

Model reduction was then carried out for $H(s)$ using the techniques discussed in Section 2.4, where $m = 2$ was used. This resulted in a seventh-order model $\hat{H}_1(s)$ for approximating $H(s)$. The Matlab command *reduce* was further used to reduce $\hat{H}_1(s)$ to a second-order function $\hat{H}(s)$, which leads to a fourth-order reduced model for the overall actuation response for the *Big* sample:

$$P(s) = \hat{H}(s) \cdot G(s) = \frac{0.005s + 0.043}{s^2 + 78s + 204} \cdot \frac{835}{s^2 + 5.78s + 835} . \quad (2.49)$$

From Fig. 2.8, the reduced model also matches closely the empirical response. It will be used for model-based controller design in the next section.

2.6 Controller-Design Example: Model-based H_∞ Control

In this section we provide an example to illustrate the use of the proposed model in model-based controller design. While other control design methodologies can be adopted, H_∞ control has been chosen to accommodate multiple considerations, including stability in the presence of uncertainty, attenuation of the effect of sensing noise, and minimization of control effort.

Consider Fig. 2.9, where the IPMC is represented by some nominal model $P(s)$ with an additive uncertainty Δ_a . Let $P(s)$ be the reduced model (2.49) for the *Big* sample. Then Δ_a represents the error between the full actuation model and $P(s)$ plus the unmodeled nonlinearities. The signals d_1 and d_2 denote the actuation noise and the sensing noise, respectively. One is interested in designing a controller $K(s)$ which ensures closed-loop stability and robust tracking performance in the presence of Δ_a and the noises d_1 and d_2 while taking into account the consumed control effort. Standard H_∞ control techniques [98] are used in the following controller design.

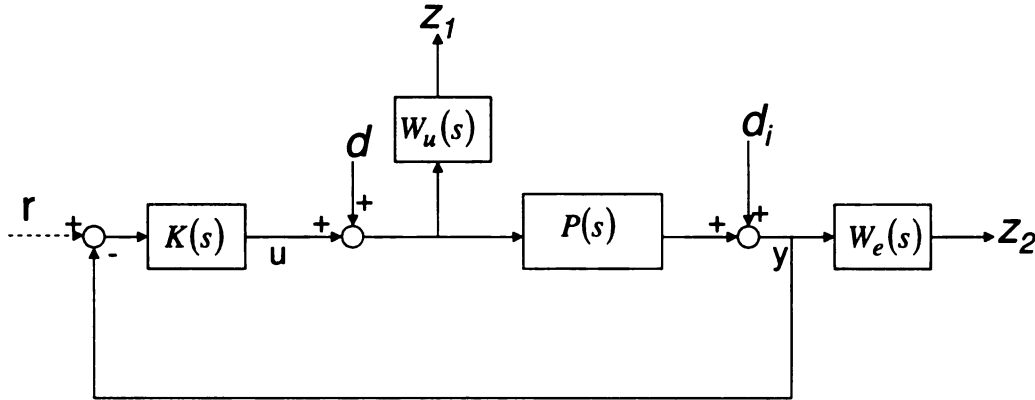


Figure 2.9: Schematic of the closed-loop control system for an IPMC actuator.

To ensure the closed-loop stability in the presence of Δ_a , one needs to first obtain the bound $\|\Delta_a\|_\infty$. Fig. 2.10 shows the modeling error - the difference between the measured

response and $P(s)$, as well as a bound $W_a(s)$ on the error, where

$$W_a(s) = \frac{0.15}{s^2 + 37s + 1318} . \quad (2.50)$$

Then $\|\Delta_a\|_\infty \leq \|W_a(s)\|_\infty = 1.65 \times 10^{-4}$.

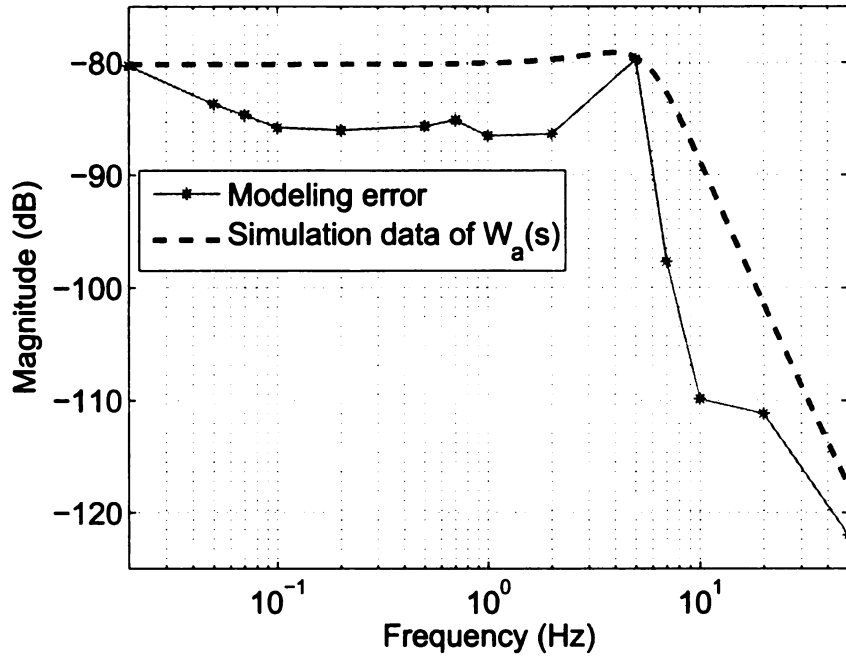


Figure 2.10: The modeling error and its bound $W_a(s)$.

The closed-loop system in Fig. 2.9 can be regarded as the feedback connection of Δ_a and $M_s(s)$, as illustrated in Fig. 2.11. $M_s(s)$ can be obtained by computing the transfer function from the output of Δ_a to the input of Δ_a in Fig. 2.9:

$$M_s(s) = \frac{K(s)}{1 + P(s)K(s)} . \quad (2.51)$$

From the small gain theorem [98], a sufficient condition for internal stability is

$$\|M_s(s)\|_\infty < \frac{1}{\|W_a(s)\|_\infty} = 6038 . \quad (2.52)$$

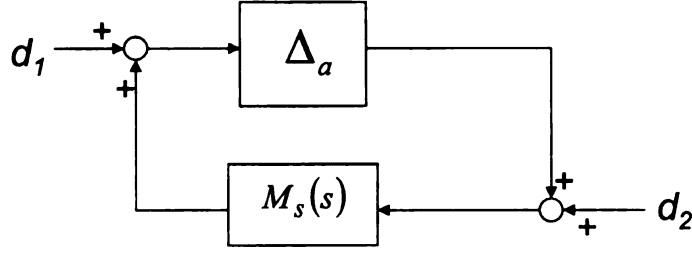


Figure 2.11: The feedback connection of $M_s(s)$ and $\Delta_a(s)$.

To proceed with the controller design, define two artificial outputs z_1 and z_2 as in Fig. 2.9, where the performance weight $W_e(s)$ and the control weight $W_u(s)$ are chosen to be

$$W_e(s) = \frac{s + 124}{4(s + 3.1 \times 10^{-3})}, \quad W_u(s) = \frac{100(s + 0.24)}{s + 3.4 \times 10^5}.$$

See [98] for guidelines on choosing these weight functions. Now ignore the Δ_a block, and design $K(s)$ to minimize the H_∞ norm of the transfer function from $\{d_1, d_2\}^T$ to $\{z_1, z_2\}^T$. This would minimize the effect of the noises on the tracking performance and the control effort. The resulting controller is

$$K(s) = \frac{29527(s + 2.569)}{(s + 0.00314)(s + 4.952)}.$$

From (2.51), one can calculate $\|M_s(s)\|_\infty = 5395$, which satisfies the internal stability condition (2.52) under the uncertainty.

The designed H_∞ controller was implemented for tracking control of the *Big* IPMC sample, where the reference r used was

$$r(t) = 0.133 \sin(0.02\pi t) + 0.0665 \sin(0.06\pi t) \text{ mm}.$$

The laser sensor for measuring the tip displacement has a noise level of ± 0.02 mm. For

comparison purposes, a PI controller

$$K_1(s) = 3000\left(1 + \frac{1}{s}\right)$$

was also implemented together with a low-pass filter

$$F(s) = \frac{961}{s^2 + 62s + 961}$$

for the output measurement. Note that a PID controller was explored for IPMC actuators by Richardson et al. [75].

Fig. 2.12 shows the IPMC tracking performance under model-based H_∞ control and Fig. 2.13 shows the tracking performance under PI control. Simulation results under both PI control and H_∞ control are also shown in the figures. It can be seen that the tracking error under H_∞ control is almost at the level of sensing noise, while the error under PI control is about twice as large. The agreement between experimental and simulation results has further validated the reduced model. Fig. 2.14 compares the controller output under H_∞ control and PI control in the experiments, which shows that the H_∞ control requires lower control effort. Therefore, controller design based on the reduced model is effective.

2.7 Chapter Summary

In this chapter a dynamic model for IPMC actuators was developed by solving the physics-governing PDE analytically in the Laplace domain. It is distinguished from existing modeling work of IPMC actuators in that it is amenable to model reduction and control design while capturing fundamental physics. The modeling work bridges the traditional gap between the physics-based perspective and the system-theoretic perspective on these novel but sophisticated materials. The model also incorporates the effect of surface electrode resistance in an integrative manner. The compact, explicit, transfer-function representation of

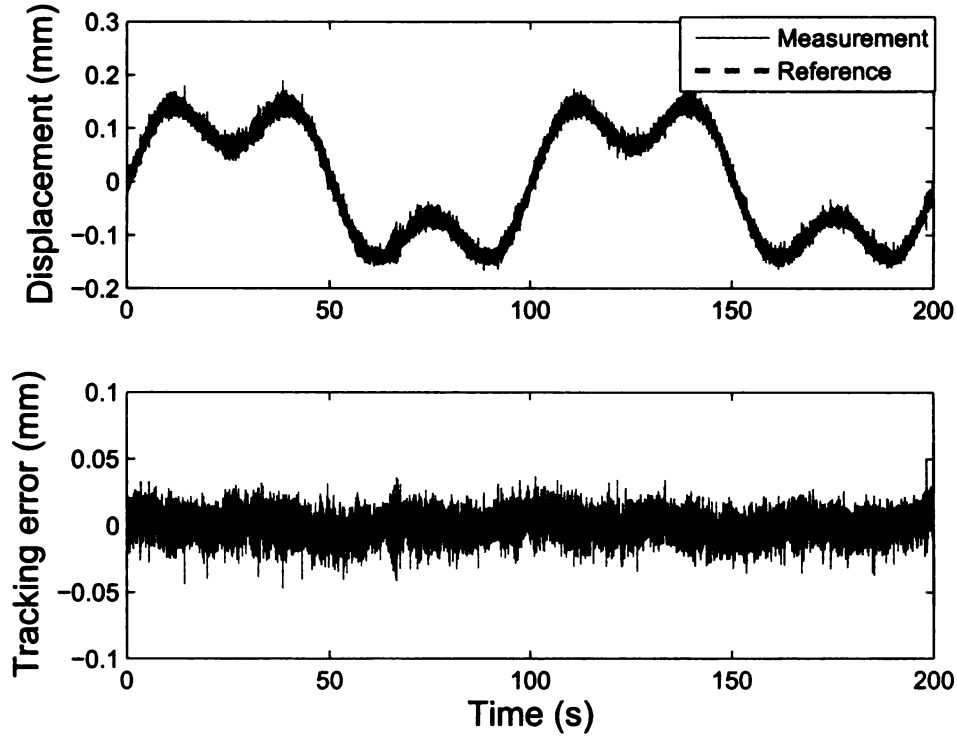


Figure 2.12: Experimental and simulation results on tracking of IPMC actuator under H_∞ control.

the physics-based model can be reduced to low-order models for real-time feedback control purposes. A number of experimental results were presented to demonstrate the geometric scalability of the model. Due to the physical nature of the model, the agreement between model predictions and experimental results also provides insight into the underlying actuation mechanisms of IPMC materials. An H_∞ controller based on the reduced low-order model has been designed and implemented in real-time tracking experiments. Experimental results have proven that the proposed model is faithful and suitable for control design. Note that while this chapter is focused on a particular class of smart materials, pursuing physics-based and control-oriented models could be a valuable approach to the design and control of a variety of materials and manufacturing systems (see, e.g., [55]).

Future work will be focused on two aspects. First, the proposed actuation model will be extended to incorporate material nonlinearities which become pronounced at large ac-

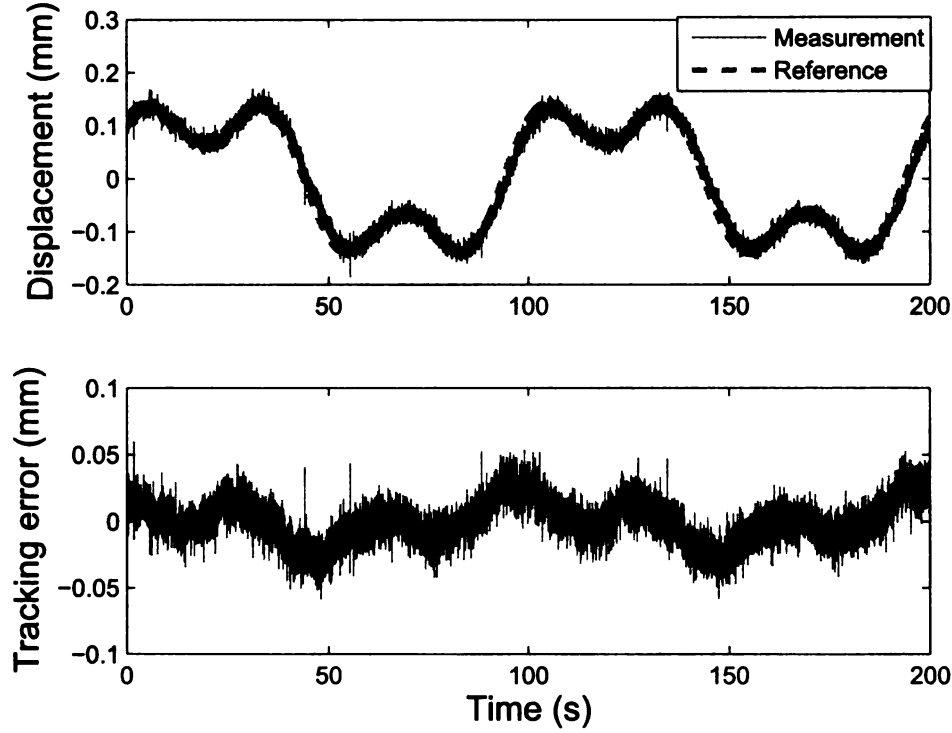


Figure 2.13: Experimental and simulation results on tracking of IPMC actuator under PI control.

tuation levels. The nonlinearities include nonlinear elasticity, hysteresis [19], and the dependence of parameters (such as surface resistance) on the curvature output [74]. The actuation model in this chapter was assumed to be a cascade of stress-generation module $H(s)$ and linear beam dynamics $G(s)$. However, the two-way coupling effects existing between the stress-generation module and the beam dynamics module, as indicated by the curvature-dependent electrical parameters, introduce challenging nonlinearities in modeling and control of IPMC materials that require further study. The second direction of future work is the application of the proposed modeling approach to control of micromanipulation [18] and biomimetic robots [86, 58]. There the model has to be extended to account for force interactions with external objects.

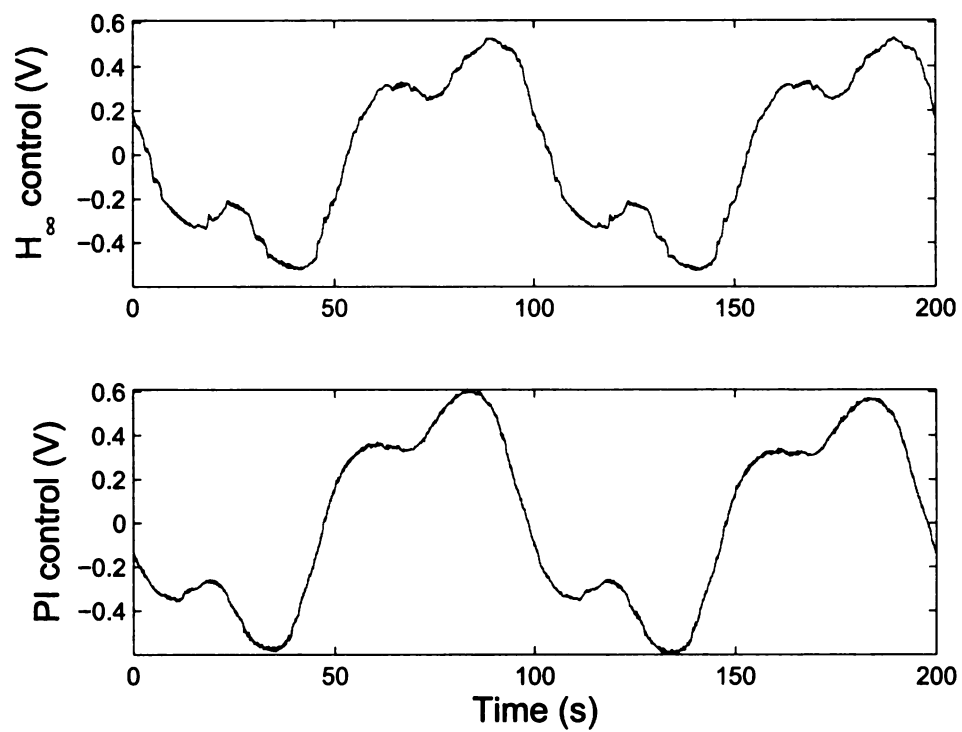


Figure 2.14: Comparison of controller outputs under H_∞ control and PI control.

Chapter 3

A Dynamic Model for Ionic Polymer-Metal Composite Sensors

This chapter is organized as follows. In Section 3.1 the exact solution and thus the model are derived, with and without considering the surface resistance. Model reduction is discussed in Section 3.2. Experimental validation results are presented in Section 3.3. Finally, concluding remarks are provided in Section 3.4.

3.1 A Dynamic Sensing Model

The governing PDE of sensing model is the same PDE as described in the modeling of actuation (See Section 2.1). Farinholt and Leo investigated the short-circuit current (and charge) sensing response of a cantilevered IPMC beam when the tip is subject to a step displacement [32], as illustrated in Fig. 2.1. Their work is based on obtaining an analytical but approximate solution $\rho(x, t)$ to (2.12), which is assumed to take a separable form $\rho(x, t) = P(x)Q(t)$. A key assumption in [32] is that the initial charge density at any point on the IPMC surface along the length direction (denoted as z -direction) is proportional to the induced stress at the same point. This assumption, which serves as an initial/boundary

condition for (2.12), is made based upon that a similar assumption was used in modeling the actuation response of IPMCs [64], and that IPMCs demonstrate reciprocity between sensing and actuation [66]. Note that the solution $\rho(x, t)$ has implicit dependence on the length coordinate z due to the nonuniform stress profile on the surface.

The objective of this modeling work is to derive a sensing model for IPMCs that accommodate arbitrary mechanical stimuli (including step deformations as a special case). While Farinholt and Leo assume perfectly-conducting surface electrodes [32], we also incorporate the distributed surface resistance into the proposed model, which will be shown to produce more accurate predictions in experiments. The model is based upon the exact solution to (2.12) subject to appropriate boundary conditions, which is made possible by converting it to the Laplace domain. The latter also makes transfer function a natural representation for the model.

Consider Fig. 2.1, where the beam is clamped at one end ($z = 0$), and is subject to an external force $F(t)$ at the other end ($z = L$) producing the tip displacement $w(t)$. The neutral axis of the beam is denoted by $x = 0$, and the upper and lower surfaces are denoted by $x = h$ and $x = -h$, respectively. Performing Laplace transform for the time variable of $\rho(x, t)$, one converts (2.12) into the Laplace domain:

$$s\rho(x, s) - d\frac{\partial^2 \rho(x, s)}{\partial x^2} + K\rho = 0, \quad (3.1)$$

where s is the Laplace variable. After rearranging, (3.1) becomes

$$\frac{\partial^2 \rho(x, s)}{\partial x^2} = \frac{(s + K)}{d}\rho(x, s). \quad (3.2)$$

Define $\beta(s)$ such that $\beta^2(s) = \frac{s + K}{d}$. A generic solution to (3.2) is obtained as

$$\rho(x, s) = c_1(s)e^{-\beta(s)x} + c_2(s)e^{\beta(s)x}, \quad (3.3)$$

for some appropriate functions $c_1(s)$ and $c_2(s)$. An assumption, analogous to the one in [32], will be made to determine $c_1(s)$ and $c_2(s)$. In particular, it is assumed that the charge density $\rho(\pm h, s)$ at the boundary $x = \pm h$ is proportional to the induced stress $\sigma(\pm h, s)$:

$$\sigma(\pm h, s) = \alpha_0 \rho(\pm h, s), \quad (3.4)$$

where α_0 is the charge-stress coupling constant. From $\sigma(h, s) = -\sigma(-h, s)$, one gets

$$\rho(h, s) + \rho(-h, s) = 0,$$

which implies $c_1(s) = -c_2(s)$ and thus

$$\rho(x, s) = 2c_2(s) \sinh(\beta(s)x). \quad (3.5)$$

One can further relate $\sigma(h, s)$ to the external stimuli. In the time domain,

$$\sigma(h, t) = \frac{M(t)h}{I}, \quad (3.6)$$

where $M(t)$ is the bending moment, and $I = \frac{2}{3}Wh^3$ is the moment of inertia with W being the beam width (refer to Fig. 2.1). $M(t)$ is related to the external force $F(t)$ at $z = L$ by

$$M(t) = F(t)(L - z), \quad (3.7)$$

where L is the beam length. The out-of-plane deflection $w(t)$ at the tip can be related to the force $F(t)$ [72] by

$$w(t) = \frac{L^3 F(t)}{3YI}, \quad (3.8)$$

where Y denotes the Young's modulus of the beam. Combining (3.6), (3.7), and (3.8) yields

$$\sigma(h, t) = \frac{3Yh(L-z)}{L^3} w(t). \quad (3.9)$$

Transforming (3.9) into the Laplace domain and combining with (3.4), one gets

$$\rho(h, s) = \frac{3Yh(L-z)}{\alpha_0 L^3} w(s), \quad (3.10)$$

which, together with (3.5), implies

$$c_2(s) = \frac{3Yh(L-z)}{2\alpha_0 L^3 \sinh(\beta(s)h)} w(s). \quad (3.11)$$

Note that $c_2(s)$ depends implicitly on the length coordinate z .

Using (3.5) and the field equations (2.1) and (2.2), one can derive the expressions for the electric field E and then for the electric potential ϕ in the Laplace domain:

$$E(x, s) = 2 c_2(s) \frac{\cosh(\beta(s)x)}{\kappa_e \beta(s)} + a_1(s), \quad (3.12)$$

$$\phi(x, s) = -2 c_2(s) \frac{\sinh(\beta(s)x)}{\kappa_e \beta^2(s)} - a_1(s)x + a_2(s), \quad (3.13)$$

where $a_1(s)$ and $a_2(s)$ are appropriate functions to be determined based on boundary conditions on ϕ . Two different boundary conditions are discussed next, one ignoring the surface electrode resistance and the other considering the resistance. In both cases it will be shown that the final sensing current is proportional to the applied deformation $w(s)$, and thus a transfer function relating the sensor output to the deformation input can be derived.

3.1.1 Model ignoring the surface resistance

First consider the case where the surface electrodes are perfectly conducting, as was assumed by Farinholt and Leo [32]. In the short-circuit current (or charge) sensing mode, the

electric potential is uniform across both surfaces $x = \pm h$, and without loss of generality, the potential is set to be zero:

$$\phi(h, z, s) = \phi(-h, z, s) = 0. \quad (3.14)$$

Note that the z -dependence of ϕ is made explicit in (3.14) for clarity (but with abuse of notation). Combining (3.14) with (3.13), one can solve for $a_1(s)$ and $a_2(s)$:

$$a_1(s) = -2c_2(s) \frac{\sinh(\beta(s)h)}{hk_e\beta^2(s)}, \quad (3.15)$$

$$a_2(s) = 0. \quad (3.16)$$

The total induced sensing charge is obtained by integrating the electrical displacement D on the boundary $x = h$:

$$Q(s) = \int_0^W \int_0^L D(h, z, s) dz dy = \int_0^W \int_0^L \kappa_e E(h, z, s) dz dy. \quad (3.17)$$

Note that, again, the z -dependence of D and E (through $c_2(s)$) is made explicit in (3.17) by putting z as the second argument of D or E . All field variables (ϕ , D , and E), on the other hand, have no dependence on the width variable y . From (3.17), one gets

$$\begin{aligned} Q(s) &= \int_0^W \int_0^L \kappa_e \left[2c_2(s) \frac{\cosh(\beta(s)h)}{\kappa_e\beta(s)} - 2c_2(s) \frac{\sinh(\beta(s)h)}{h\kappa_e\beta^2(s)} \right] dz dy \\ &= \frac{2W(\beta(s)h \cosh(\beta(s)h) - \sinh(\beta(s)h))}{h\beta^2(s)} \int_0^L c_2(s) dz \\ &= \frac{2W(\beta(s)h \cosh(\beta(s)h) - \sinh(\beta(s)h))}{h\beta^2(s)} \int_0^L \frac{3Yh(L-z)w(s)}{2\alpha_0 L^3 \sinh(\beta(s)h)} dz \\ &= \frac{3YW(\beta(s)h \coth(\beta(s)h) - 1)w(s)}{\alpha_0 L^3 \beta^2(s)} \int_0^L (L-z) dz \\ &= \frac{3YW(\beta(s)h \coth(\beta(s)h) - 1)}{2\alpha_0 L \beta^2(s)} w(s). \end{aligned}$$

In the above the first equality is from (3.12) and (3.15), the second equality follows from

the independence of $c_2(s)$ from y , and the third equality is from (3.11). The short-circuit current $i(t)$ is the time-derivative of the charge $Q(t)$, and hence $i(s) = sQ(s)$ in the Laplace domain. The transfer function from the mechanical input $w(s)$ to the sensing output $i(s)$ is then derived as

$$H_1(s) = \frac{i(s)}{w(s)} = \frac{3sYW(\beta(s)h \coth(\beta(s)h) - 1)}{2\alpha_0 L \beta^2(s)} \quad (3.18)$$

with $\beta(s) = \sqrt{\frac{s+K}{d}}$.

3.1.2 Model considering distributed surface resistance

The surface electrode of an IPMC typically consists of aggregated nanoparticles formed during chemical reduction of noble metal salt (such as platinum salt) [49]. The surface resistance is thus non-negligible and has an influence on the sensing and actuation behavior of an IPMC [78]. In this modeling work, the effect of distributed surface resistance is incorporated into the sensing model, as illustrated in Fig. 3.1. An IPMC beam is clamped at one end ($z = 0$) and is subject to an applied displacement $w(s)$ at the other end ($z = L$). Let the resistance per unit length be $r = r_0/W$, with r_0 representing the surface resistance per unit length and unit width (a parameter independent of IPMC dimensions). For each section Δz of the IPMC, a current $i_p(z,s)\Delta z$ is generated inside the polymer and then joins the surface current $i_s(z,s)$. Note that by the continuity of current, the current $i_s(z,s)$ on the top surface equals that on the bottom surface but with an opposite direction. The surface current $i_s(0,s)$ collected at $z = 0$, where $\phi(h,0,s) = \phi(-h,0,s) = 0$, is the short-circuit sensing current $i(s)$.

The following equations capture the relationships between the surface current $i_s(z,s)$, the current density $i_p(z,s)$ within the polymer, and the electric potential $\phi(\pm h,z,s)$ on the

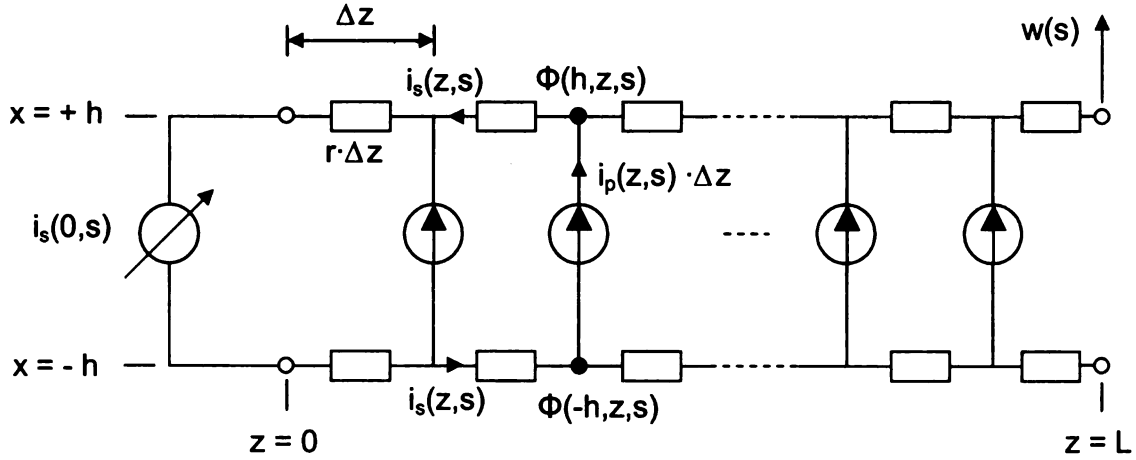


Figure 3.1: Illustration of the distributed surface resistance for the IPMC sensing model.

surfaces:

$$\frac{\partial \phi(h, z, s)}{\partial z} = r i_s(z, s) = \frac{r_0}{W} i_s(z, s), \quad (3.19)$$

$$\frac{\partial \phi(-h, z, s)}{\partial z} = -r i_s(z, s) = -\frac{r_0}{W} i_s(z, s), \quad (3.20)$$

$$\frac{\partial i_s(z, s)}{\partial z} = -i_p(z, s). \quad (3.21)$$

From the short-circuit condition at $z = 0$, i.e., $\phi(h, 0, s) = \phi(-h, 0, s) = 0$, the boundary conditions for (3.13) are derived as:

$$\phi(h, z, s) = \int_0^z \frac{r_0}{W} i_s(\tau, s) d\tau, \quad (3.22)$$

$$\phi(-h, z, s) = -\int_0^z \frac{r_0}{W} i_s(\tau, s) d\tau. \quad (3.23)$$

Combining (3.22) and (3.23) with (3.13), one can solve for the functions $a_1(s)$ and $a_2(s)$ in the generic expression for $\phi(x, z, s)$:

$$a_1(s) = -\frac{\int_0^z r_0 i_s(\tau, s) d\tau}{hW} - 2 c_2(s) \frac{\sinh(\beta(s)h)}{h\kappa_e \beta^2(s)}, \quad (3.24)$$

$$a_2(s) = 0. \quad (3.25)$$

Next we will eliminate $i_p(z, s)$ in (3.21) so that the equation involves $i_s(z, s)$ only, which can then be solved for the sensing output $i_s(0, s)$. Note that the generated sensing charge on a Δz section can be expressed as $D(h, z, s)W\Delta z$, i.e.,

$$\frac{i_p(z, s)\Delta z}{s} = D(h, z, s)W\Delta z = \kappa_e E(h, z, s)W\Delta z,$$

implying

$$i_p(z, s) = s\kappa_e E(h, z, s)W. \quad (3.26)$$

Evaluating $E(h, z, s)$ using (3.12) with (3.11) and (3.24) plugged in for $c_2(s)$ and $a_1(s)$, respectively, one gets (after simplification):

$$i_p(z, s) = A(s)(L - z) - B(s) \int_0^z i_s(\tau, s) d\tau, \quad (3.27)$$

where

$$A(s) = \frac{3sYW(\beta(s)h \coth(\beta(s)h) - 1)}{\alpha_0 L^3 \beta^2(s)} w(s), \quad (3.28)$$

$$B(s) = \frac{s\kappa_e r_0}{h}. \quad (3.29)$$

Plugging (3.27) into (3.21), one obtains an integro-differential equation for $i_s(z, s)$:

$$\frac{\partial i_s(z, s)}{\partial z} = -A(s)(L - z) + B(s) \int_0^z i_s(\tau, s) d\tau. \quad (3.30)$$

Eq. (3.30) can be solved analytically through (yet another) Laplace transform, this time for the z variable.

We introduce the unilateral Laplace transform for functions of the length coordinate z . The new Laplace variable will be denoted as p since s has already been used for the

transform of time functions. For instance, the transform of $i_s(z, s)$ will be defined as

$$I_s(p, s) \triangleq \int_0^\infty i_s(z, s) e^{-pz} dz.$$

Now perform the Laplace transform with respect to the z variable on both sides of (3.30).

Using properties of Laplace transforms [23, 36], one gets

$$pI_s(p, s) - i_s(0, s) = -A(s) \left(\frac{L}{p} - \frac{1}{p^2} \right) + B(s) \frac{I_s(p, s)}{p}. \quad (3.31)$$

Solving for $I_s(p, s)$, one obtains

$$I_s(p, s) = \frac{p}{p^2 - B(s)} i_s(0, s) - \frac{pL - 1}{p(p^2 - B(s))} A(s), \quad (3.32)$$

which can be rewritten through partial fraction expansion as:

$$I_s(p, s) = \frac{1}{2} \left(\frac{1}{p - \sqrt{B(s)}} + \frac{1}{p + \sqrt{B(s)}} \right) i_s(0, s) + \left(\frac{q_1(s)}{p} + \frac{q_2(s)}{p - \sqrt{B(s)}} + \frac{q_3(s)}{p + \sqrt{B(s)}} \right) A(s), \quad (3.33)$$

with

$$q_1(s) = -\frac{1}{B(s)}, \quad q_2(s) = \frac{1 - L\sqrt{B(s)}}{2B(s)}, \quad q_3(s) = \frac{1 + L\sqrt{B(s)}}{2B(s)}.$$

The surface current $i_s(z, s)$ is then obtained from (3.33) using the inverse Laplace transform

of $I_s(p, s)$:

$$\begin{aligned}
i_s(z, s) &= \frac{e^{\sqrt{B(s)}z} + e^{-\sqrt{B(s)}z}}{2} i_s(0, s) + \\
&\quad \left(-\frac{1}{B(s)} + \frac{1 - \sqrt{B(s)}L}{2B(s)} e^{\sqrt{B(s)}z} + \frac{1 + \sqrt{B(s)}L}{2B(s)} e^{-\sqrt{B(s)}z} \right) A(s) \\
&= \cosh(\sqrt{B(s)}z) i_s(0, s) + \\
&\quad \left(-1 + \cosh(\sqrt{B(s)}z) - \sqrt{B(s)}L \sinh(\sqrt{B(s)}z) \right) \frac{A(s)}{B(s)}. \tag{3.34}
\end{aligned}$$

Refer to Fig. 3.1. Since the circuit is open at $z = L$, the following holds:

$$i_s(L, s) = 0. \tag{3.35}$$

Plugging $z = L$ into (3.34) and using (3.35), one obtains the sensing current $i_s(0, s)$ as

$$i_s(0, s) = \frac{A(s) \left(1 - \cosh(\sqrt{B(s)}L) + \sqrt{B(s)}L \sinh(\sqrt{B(s)}L) \right)}{B(s) \cosh(\sqrt{B(s)}L)}. \tag{3.36}$$

In particular, the short-circuit sensing current $i(s) = i_s(0, s)$ is obtained as

$$\begin{aligned}
i(s) &= \frac{3sYW (\beta(s)h \coth(\beta(s)h) - 1)}{\alpha_0 L^3 \beta^2(s)} \cdot \\
&\quad \frac{\left(1 - \cosh(\sqrt{B(s)}L) + \sqrt{B(s)}L \sinh(\sqrt{B(s)}L) \right)}{B(s) \cosh(\sqrt{B(s)}L)} w(s). \tag{3.37}
\end{aligned}$$

The transfer function from the mechanical input $w(s)$ to the sensor output $i(s)$ is then

$$\begin{aligned}
H_2(s) = \frac{i(s)}{w(s)} &= \frac{3sYW (\beta(s)h \coth(\beta(s)h) - 1)}{\alpha_0 L^3 \beta^2(s)} \cdot \\
&\quad \frac{\left(1 - \cosh(\sqrt{B(s)}L) + \sqrt{B(s)}L \sinh(\sqrt{B(s)}L) \right)}{B(s) \cosh(\sqrt{B(s)}L)}, \tag{3.38}
\end{aligned}$$

where $B(s)$ is as defined by (3.29).

Note that the model $H_2(s)$ incorporating surface resistance is consistent with the model $H_1(s)$ ignoring surface resistance. Indeed, $H_2(s)$ degenerates to $H_1(s)$ when the resistance $r_0 \rightarrow 0$. To see this, from (3.18) and (3.38), one can write

$$H_2(s) = \frac{2}{L^2} \cdot \frac{\left(1 - \cosh(\sqrt{B(s)}L) + \sqrt{B(s)}L \sinh(\sqrt{B(s)}L)\right)}{B(s) \cosh(\sqrt{B(s)}L)} \cdot H_1(s).$$

When $r_0 \rightarrow 0$, $\sqrt{B(s)} = \sqrt{s\kappa_e r_0/h} \rightarrow 0$. From l'Hôpital's rule,

$$\lim_{a \rightarrow 0} \left(\frac{a}{\tanh(a)} \right) = 1 \quad (3.39)$$

Taking $\sqrt{B(s)}$ to be a in (3.39), one obtains

$$\lim_{r_0 \rightarrow 0} H_2(s) = \frac{2}{L^2} \cdot \frac{L^2}{2} \cdot H_1(s) = H_1(s).$$

3.2 Model Reduction

An important motivation for deriving a transfer function-type sensing model $H(s)$ is its potential use for real-time feedback control and for sensor signal conditioning. In the case of feedback control, knowing the sensor dynamics is essential to the controller design [36]. For pure sensing applications (such as structural health monitoring), the knowledge of sensor dynamics allows one to correctly reconstruct the original mechanical stimulus $w(s)$ based on the sensor output $i(s)$, either online or offline. This can be done through inversion of the sensor dynamics:

$$w(s) = H_{inv}(s)i(s), \quad (3.40)$$

where $H_{inv}(s)$ represents the inverse dynamics

$$H_{inv}(s) = \frac{1}{H(s)}. \quad (3.41)$$

For practical implementation of sensor conditioning or feedback control design, the model $H(s)$ needs to be finite-dimensional, i.e., being a finite-order, rational function of s . However, the sensing models derived earlier, $H_1(s)$ and $H_2(s)$ ((3.18) and (3.38)), are infinite-dimensional since they involve non-rational functions including $\sinh(\cdot)$, $\cosh(\cdot)$, $\sqrt{\cdot}$, etc. A systematic approach to model reduction is to use Padé approximation [7], where one can approximate $H_1(s)$ or $H_2(s)$ by a finite-dimensional transfer function with any specified order.

In the following we discuss reduction of the IPMC sensing models by exploiting their specific properties. The method is less general than Padé approximation, but it is also simpler. The discussion will be focused on $H_2(s)$ since it covers $H_1(s)$ as a special case. For ease of presentation, decompose $H_2(s)$ as

$$H_2(s) = f(s) \cdot g(s),$$

with

$$f(s) = \frac{3sYW(\beta(s)h \coth(\beta(s)h) - 1)}{\alpha_0 \beta^2(s)L^3}, \quad (3.42)$$

$$g(s) = \frac{1 - \cosh(\sqrt{B(s)}L) + \sqrt{B(s)}L \sinh(\sqrt{B(s)}L)}{B(s) \cosh(\sqrt{B(s)}L)}. \quad (3.43)$$

Based on the physical parameters (see Table 3.1 and Table 3.2 in Section 3.3), the composite constant $\frac{K}{d}$ is in the order of 10^{12} , which implies

$$|\beta(s)| = \left| \frac{s+K}{d} \right| > 10^6,$$

for $s = j\omega$, where ω denotes the angular frequency of any sinusoidal input. Since the

thickness h of an IPMC is typically bigger than 1×10^{-4} m, it can be seen that

$$|\beta(s)h| \gg 10,$$

which allows one to make the approximation

$$\coth(\beta(s)h) \approx 1. \quad (3.44)$$

With (3.44), one can simplify (3.42) as

$$\begin{aligned} f(s) &\approx \frac{3sYW(\beta(s)h-1)}{\alpha_0\beta^2(s)L^3} = \frac{3sYWd}{\alpha_0L^3} \cdot \frac{\sqrt{\frac{s+K}{d}}h-1}{s+K} \\ &= \frac{3sYW\sqrt{d}\left(\sqrt{s+K}h-\sqrt{d}\right)}{\alpha_0L^3(s+K)}. \end{aligned}$$

One can further approximate $\sqrt{s+K}$ by its Taylor series about $s=0$. For instance, considering up to the second-order terms results in the following approximation to $f(s)$:

$$f(s) \approx \frac{3sYW\sqrt{d}\left(h\sqrt{K}\left(1+\frac{s}{2K}\right)-\sqrt{d}\right)}{\alpha_0L^3(s+K)}. \quad (3.45)$$

The following Taylor series expansions of $\sinh(a)$ and $\cosh(a)$ will be used for $g(s)$:

$$\begin{aligned} \sinh(a) &= a + \frac{a^3}{3!} + \frac{a^5}{5!} + \cdots, \\ \cosh(a) &= 1 + \frac{a^2}{2!} + \frac{a^4}{4!} + \cdots, \end{aligned}$$

with $a = \sqrt{B(s)}L$. This results in

$$g(s) = \frac{\left(1 - \frac{1}{2!}\right) B(s)L^2 + \left(\frac{1}{3!} - \frac{1}{4!}\right) B^2(s)L^4 + \left(\frac{1}{5!} - \frac{1}{6!}\right) B^3(s)L^6 + \dots}{B(s) \left(1 + \frac{B(s)L^2}{2!} + \frac{B^2(s)L^4}{4!} + \dots\right)}. \quad (3.46)$$

Recall $B(s) = \frac{s\kappa_e r_0}{h}$.

Truncation of the series in (3.46) leads to a finite-order approximation. For example, keeping the first three terms in each series yields

$$g(s) \approx \frac{\left(1 - \frac{1}{2!}\right) B(s)L^2 + \left(\frac{1}{3!} - \frac{1}{4!}\right) B^2(s)L^4 + \left(\frac{1}{5!} - \frac{1}{6!}\right) B^3(s)L^6}{B(s) \left(1 + \frac{B(s)L^2}{2!} + \frac{B^2(s)L^4}{4!}\right)}. \quad (3.47)$$

Combining (3.45) and (3.46) leads to a fourth-order model for IPMC sensors:

$$\hat{H}(s) = \frac{3sYW\sqrt{d} \left(h\sqrt{K} \left(1 + \frac{s}{2K}\right) - \sqrt{d} \right)}{\alpha_0 L^3 (s+K)} \cdot \frac{\left(1 - \frac{1}{2!}\right) B(s)L^2 + \left(\frac{1}{3!} - \frac{1}{4!}\right) B^2(s)L^4 + \left(\frac{1}{5!} - \frac{1}{6!}\right) B^3(s)L^6}{B(s) \left(1 + \frac{B(s)L^2}{2!} + \frac{B^2(s)L^4}{4!}\right)}. \quad (3.48)$$

Although $\hat{H}(s)$ is an improper rational function, i.e., the numerator is of higher order than the denominator, it is not a concern for feedback or sensing applications. This is because the inverse dynamics (3.41), which is what matters in implementation, will be proper.

Note that a reduced model like (3.48) is still a physical model. In particular, it is described in terms of fundamental physical parameters and is thus geometrically scalable. This represents a key difference from other low-order, black-box models, in which case the parameters have no physical meanings and one would have to re-identify the parameters empirically for every sensor.

3.3 Experimental Verification

3.3.1 Experimental setup

An experimental setup was built to produce periodic mechanical stimulus with controllable frequency. The schematic of the setup is shown in Fig. 3.2(a), while Fig. 3.2(b) shows its picture. A crank-slider mechanism is used to convert the rotational motion generated by a DC motor (GM8724S009, Pittman) into the linear, oscillatory motion of the slider, which slides on a fixed rail. A rigid bar connects the slider and the rotating disk, and by changing the distance from the bar end to the disk center, the amplitude of translational motion can be adjusted. The oscillation frequency is controlled by tuning the voltage input to the motor, and it is measured through an optical switch. The setup can provide periodic excitation from 1 to 20 Hz.

The free end of a cantilevered IPMC beam is constrained to a slit in the slider, which correlates the slider motion directly with the tip-bending deformation $w(t)$ of the IPMC. In particular, $w(t)$ can be calculated explicitly based on the bar-disk configuration and the optical switch signal. A differential current-amplifier circuit is used to measure the IPMC sensing current generated under the mechanical stimulus. Data acquisition and processing are performed through a PC running on a real-time Linux kernel.

3.3.2 Parameter identification

In the dynamic sensing models $H_1(s)$ and $H_2(s)$, some parameters are physical constants (gas constant R and Faraday's constant F), some can be measured directly (absolute temperature T , Young's modulus Y , sensor dimensions, and surface resistance density r_0), and the others need to be identified through curve-fitting. Table 3.1 lists the physical constants and the parameters obtained through direct measurement. Since $|C^-\Delta V| \ll 1$ [64], we take $1 - C^-\Delta V = 1$. The IPMC materials used in this work were obtained from Environmental

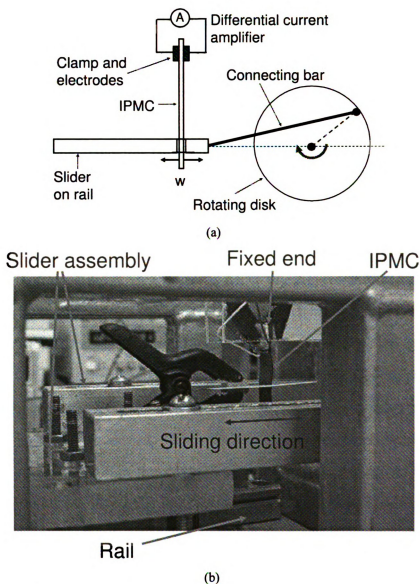


Figure 3.2: (a) Schematic of the experimental setup; (b) picture showing a cantilevered IPMC under mechanical deformation.

Robots Inc., and the thickness is $360 \mu\text{m}$, i.e., $h = 180 \mu\text{m}$. For an IPMC that is 22 mm long and 7 mm wide, the surface resistance was measured to be 19Ω , corresponding to $r_0 = 6.05 \Omega$.

The parameters that remain to be determined include the diffusion coefficient d , the anion concentration C^- , the dielectric constant κ_e , and the charge-stress coupling constant α_0 . The empirical frequency response of an IPMC sensor with dimensions $22 \times 7 \text{ mm}^2$

Table 3.1: Physical constants and directly-measured parameters.

F	R	T	Y [18]	h	r_0
96487 C_{mol}	8.3143 $J_{\text{mol}}\cdot K$	300 K	5.71×10^8 Pa	180 (μm)	6.05 Ω

was used to identify the remaining parameters through a nonlinear curve-fitting process, as described next.

Fix an excitation frequency f , and acquire the mechanical deformation $w(t)$ and the IPMC sensor output $i(t)$. Fast Fourier transforms are then performed on $w(t)$ and $i(t)$ to extract their amplitudes and phases, based on which one can compute the magnitude gain and the phase shift of the sensor dynamics (from the mechanical input to the sensing output) at that particular frequency. Repeat this process for other excitation frequencies that are available from the experimental setup (1-20 Hz), which produces the empirical Bode plots for the frequency response. Extra care is required to ensure consistent experimental conditions at different frequencies. This is because the sensing behavior of an IPMC depends on the hydration level of the material, and the latter decreases over time when the sensor is operated in air. To handle this problem, the IPMC sample is soaked in water for several minutes to get fully hydrated, and is then mechanically excited in air for ten minutes to get rid of excessive water before collecting data for each frequency.

One can then tune the unknown parameters of the sensor model $H_2(s)$ to fit the empirical frequency response. In particular, $H_2(j2\pi f)$ predicts the magnitude and phase response of the sensor at frequency f , and it is a nonlinear function of the parameters. The Matlab function *fminsearch* can be used to find the parameters that minimize the squared error between the empirical frequency response and the model prediction. The identified parameters are listed in Table 3.2, which are close to the values reported in literature [64, 32]. For independent verification of the proposed model, the identified parameters will be used in predicting behaviors of other IPMC sensors with different dimensions, as will be seen in Section 3.3.3.

Table 3.2: Identified parameters through curve-fitting.

d	C^-	κ_e	α_0
$3.32 \times 10^{-11} \text{ m}^2/\text{s}$	$1091 \text{ mol}/\text{m}^3$	$1.88 \times 10^{-3} \text{ F}/\text{m}$	$104 \text{ }^\circ\text{C}$

3.3.3 Model verification

Model verification will be conducted on three aspects. First, it will be shown that the model considering the surface resistance is more accurate than the model ignoring the resistance, by comparing them with the measured frequency response of an IPMC sensor. Second, the geometric scalability of the proposed model will be confirmed by the agreement between model predictions and experimental results for IPMC sensors with different dimensions. Third, the performance of the reduced model will be illustrated through its prediction of the time-domain sensing responses under a damped, oscillatory excitation and a step deformation, respectively.

Effect of surface resistance.

In order to examine the difference between the models $H_1(s)$ and $H_2(s)$, their model parameters were identified separately through the nonlinear fitting process described in Section 3.3.2. The experimental data were obtained for an IPMC sensor with dimensions $22 \times 7 \times 0.36 \text{ mm}^3$. Fig. 3.3 compares the predicted frequency response (both magnitude and phase) by each model with the measured frequency response. Both models show good agreement with the experimental data on the magnitude plot. On the phase plot, however, it is clear that the model considering the surface resistance shows better agreement than the one ignoring the resistance. This indicates that the model incorporating the surface resistance is more effective in capturing the sensing dynamics of IPMC, and thus it will be used for the remainder of this chapter.

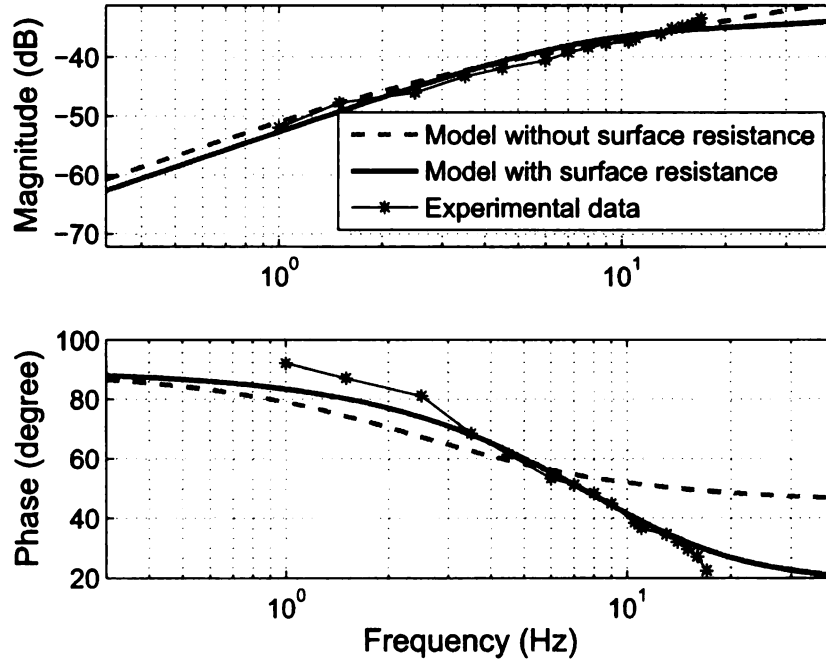


Figure 3.3: Performance of the models with and without consideration of surface resistance.

Geometric scalability of the dynamic model.

Three samples with different dimensions (see Table 3.3) were cut from one IPMC sheet, and were labeled as *Big*, *Slim*, and *Short* for ease of referencing. The model parameters were first identified for the *Slim* sample, as discussed in Section 3.3.2. Without re-tuning, these parameters (except geometric dimensions) were plugged into (3.38), i.e., the model $H_2(s)$, for predicting the frequency response for the *Big* and *Short* samples.

Table 3.3: Dimensions of three IPMC samples used for verification of model scalability.

IPMC beam	length (mm)	width (mm)	thickness (μm)
<i>Big</i>	22	14	360
<i>Slim</i>	22	7	360
<i>Short</i>	11	7	360

Fig. 3.4 (a) shows the Bode plots of the frequency responses for the *Slim* and *Big* samples. It can be seen that for both samples, good agreement between the model prediction

and the experimental data is achieved. Furthermore, since the two samples differ only in width, the model (3.38) predicts that their magnitude responses will differ by $20 \log 2 = 6$ dB uniformly in frequency, while their phase responses will be the same. Both predictions are confirmed in the figure: the experimentally measured magnitude responses are parallel to each other with a difference about 6 dB, and the measured phase responses overlap well.

Fig. 3.4 (b) compares the frequency responses of the *Slim* and *Short* samples. Reasonable match between the model predictions and the empirical curves is again achieved for both samples. The figure also indicates the need to incorporate the surface resistance in modeling. Since the two samples differ only in length, the model ignoring the surface resistance (3.18) will predict that the magnitude responses of the two samples would differ just by a constant while their phase responses would be identical. But the empirical magnitude curve for the *Slim* sample rises with frequency by approximately 14 dB per decade, while that for the *Short* sample rises by roughly 18 dB per decade. Moreover, the empirical phase curves clearly do not overlap. All these subtle trends, however, are captured well by the model considering the surface resistance, as can be seen in Fig. 3.4.

Verification of the reduced model.

Experiments were further conducted to verify the effectiveness of the model reduction approach presented in Section 3.2. Two mechanical stimuli, which were different from periodic signals, were used to demonstrate the wide applicability of the proposed model. In the first experiment the cantilevered *Slim* IPMC sample was allowed to freely vibrate upon an initial perturbation on the tip. In the second experiment the tip of the cantilevered *Big* sample was subject to a step displacement and then held there. A laser displacement sensor (OADM 20I6441/S14F, Baumer Electric) was used to record the tip displacement trajectory $w(t)$. The fourth-order reduced model (3.48) was adopted to predict the short-circuit current sensing response for each case, where the model parameters from the identification

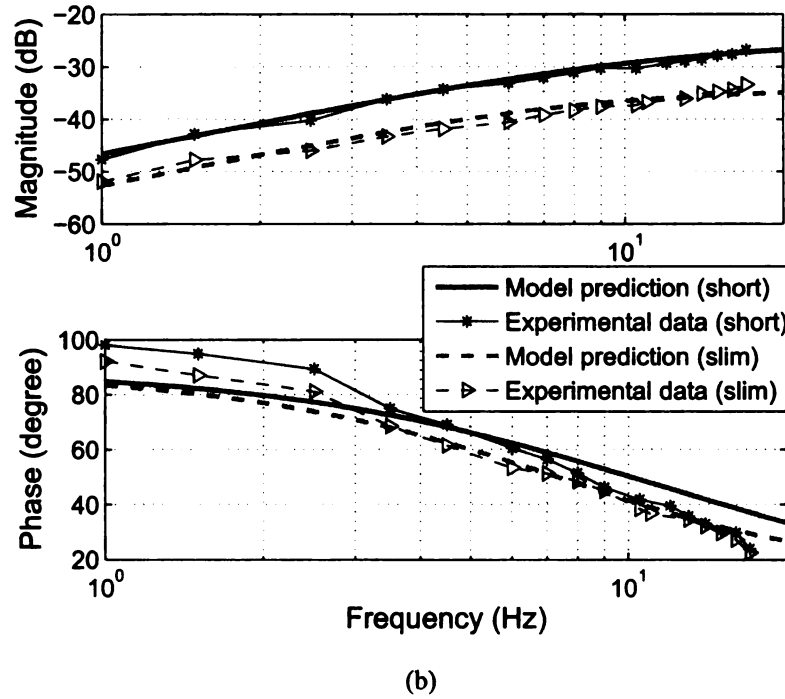
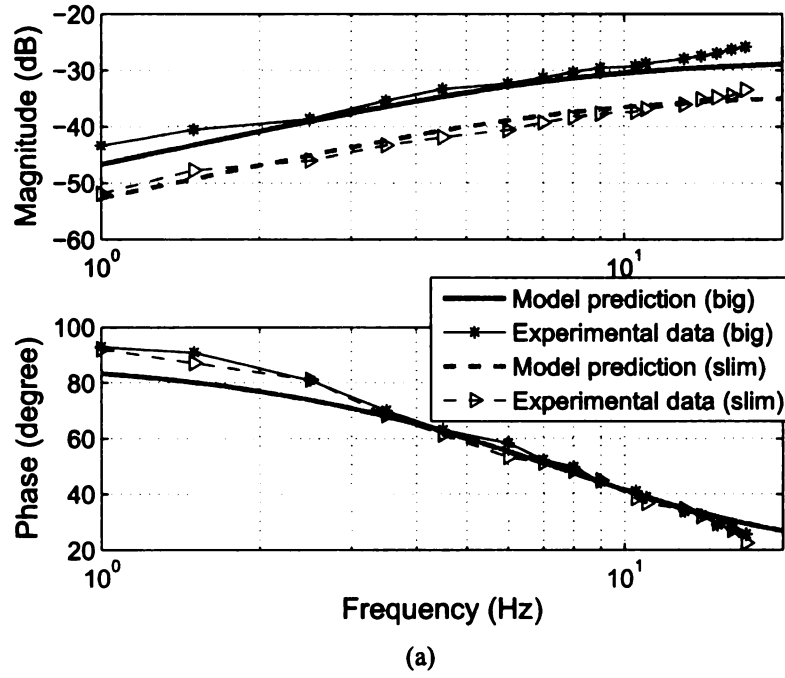


Figure 3.4: Frequency responses of the sensing dynamics. (a) For the *Big* and *Slim* samples; (b) for the *Slim* and *Short* Samples.

experiment in Section 3.3.2 were used directly.

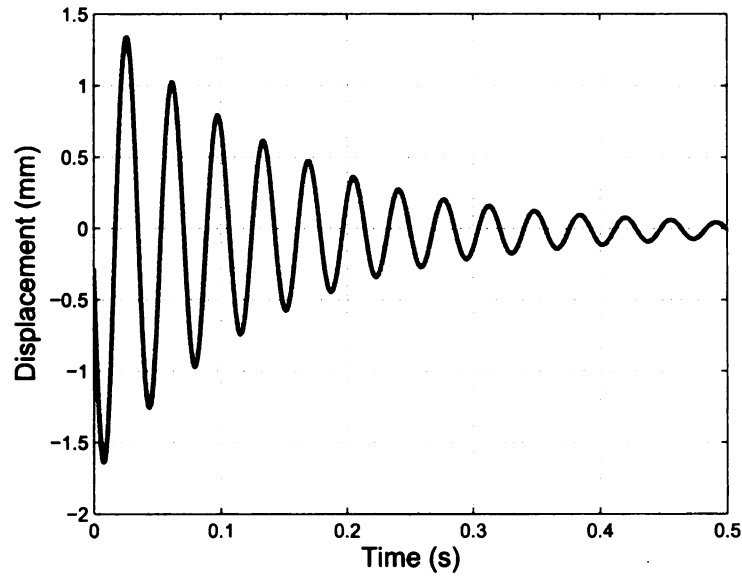
Fig. 3.5 compares the predicted sensing response with the experimental measurement

under the damped, oscillatory stimulus. The beam has a natural frequency of about 30 Hz, which is outside the frequency range of the signals used in parameter identification, yet the reduced model is able to predict the sensor output well. Fig. 3.6 shows the model prediction of the sensing response against the experimental data for the case of a step tip-deformation. It can be seen that satisfactory agreement between the predicted and the measured curves is again achieved.

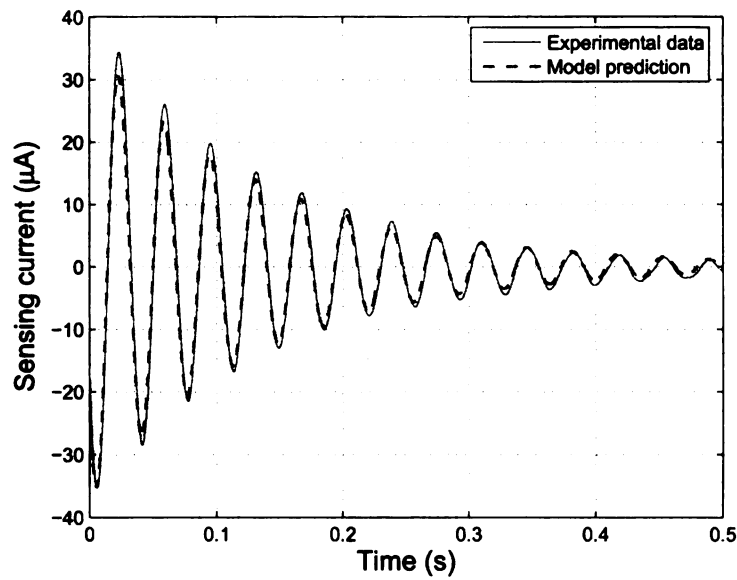
3.3.4 Impact of hydration level on sensing response

Finally, the proposed dynamic model is explored to gain insight into the dependence of IPMC sensing response on the hydration level of the sample. Such dependence is clearly seen from the experimental curve in Fig. 3.7. In this experiment the *Slim* IPMC sample was first soaked in water, and then subject to continuous, 6 Hz periodic mechanical excitation in air. Data (both the stimulus and the sensor output) were collected for about 40 minutes. The frequency response of the sensor at 6 Hz at each minute was then extracted from the data, including the magnitude gain and the phase shift. The evolution of this response is plotted in Fig. 3.7 (note the horizontal axis represents time instead of frequency), showing that the sensor output gets weaker over time.

The time-varying response is believed to arise from the water evaporation of the IPMC sample. In order to correlate this phenomenon with the proposed model (3.38), we assume that all parameters except the diffusion coefficient d are constant over time. Taking the values identified in Section 3.3.2 for these fixed parameters, we identify the evolving value of d by fitting the measured magnitude and phase response at each minute. The dashed line curves in Fig. 3.7 show the results of model fitting with a time-dependent d . The time-trajectory of the identified d is plotted in Fig. 3.8, and its decaying trend is consistent with the decreasing hydration level. This might suggest that the hydration level impacts the sensing behavior of an IPMC through its influence on the ion diffusivity. However, since d cannot be measured directly to confirm the identified trajectory in Fig. 3.8, more research



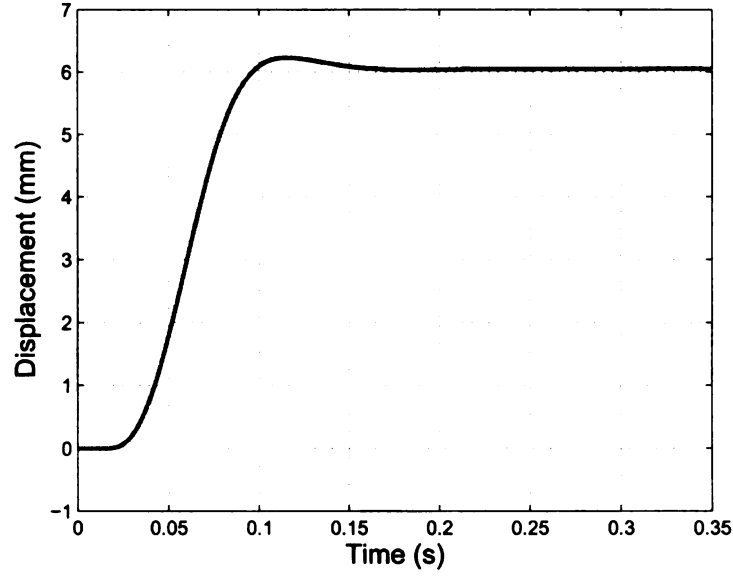
(a)



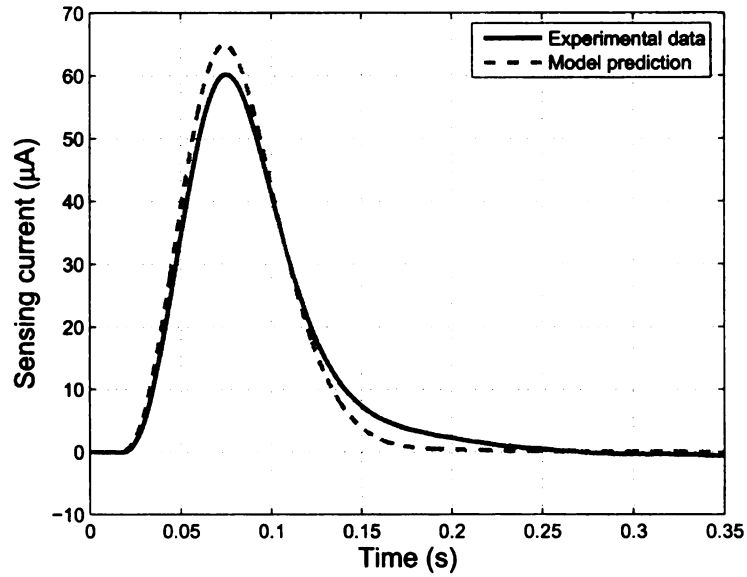
(b)

Figure 3.5: The sensing response of the *Slim* sample under a decaying, oscillatory mechanical stimulus. (a) The tip displacement trajectory; (b) prediction of the sensing response versus experimental measurement.

is needed before a conclusive statement can be made.



(a)



(b)

Figure 3.6: The sensing response of the *Big* sample under a step stimulus. (a) The tip displacement trajectory; (b) prediction of the sensing response versus experimental measurement.

3.4 Chapter Summary

In this chapter, a dynamic model for IPMC sensors has been developed by solving the physics-governing PDE analytically in the Laplace domain. The model accommodates

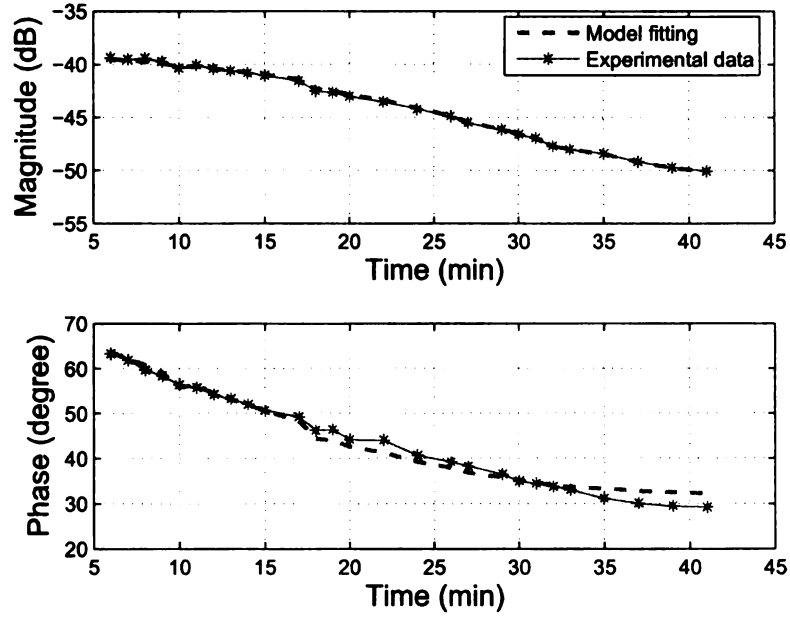


Figure 3.7: The sensing response at 6 Hz for the *Slim* IPMC sample over time.

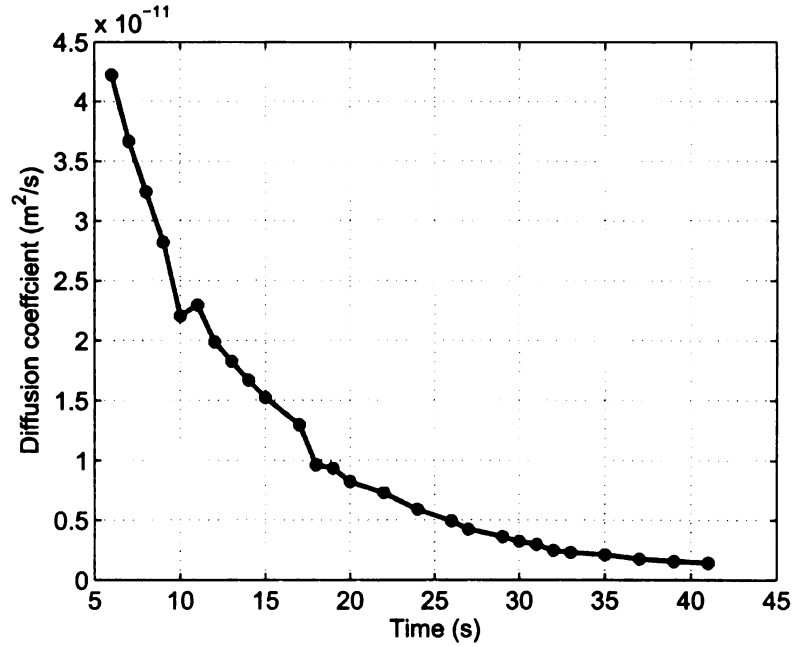


Figure 3.8: Identified diffusion coefficient versus time.

the surface electrode resistance in an integrative manner. The mechanical stimulus enters as a boundary condition for the PDE, and the sensing output is related to the mechani-

cal input linearly. This leads to a compact, explicit, transfer-function representation of the physics-based model, which can be further reduced to low-order models for real-time sensing and feedback control purposes. A number of experimental results were presented to demonstrate the geometric scalability of the model, as well as its applicability to arbitrary mechanical inputs. Due to the physical nature of the model, the agreement between model predictions and experimental results also provides insight into the underlying sensing mechanisms of IPMC materials.

Chapter 4

Modeling of Biomimetic Robotic Fish Propelled by An Ionic Polymer-Metal Composite Caudal Fin

This chapter is organized as follows. The robotic fish is described in Section 4.1. The proposed model is presented in Section 4.2. Experimental results on model validation are presented in Section 4.3. Finally, concluding remarks are provided in Section 4.4.

4.1 Description of IPMC-propelled Robotic Fish

Fig. 4.1 shows a prototype of the robotic fish, which is an upgraded version from that reported in [86]. The fish is designed to be fully autonomous and serve as a mobile, aquatic sensing platform. It consists of a rigid body and an IPMC caudal fin. Two gold-coated copper electrodes are used for IPMC to reduce corrosion of the electrodes in water. Corrosion of the electrodes results in high resistance of the contact, which would reduce the actuation performance of the IPMC tail and consume more electrical power. The IPMC actuator is further covered by a passive plastic fin to enhance propulsion. The rigid shell

of the fish was custom-made to reduce the wetted surface while having enough interior room to house rechargeable batteries and various electronic components for control, sensing, wireless communication, and navigation. All of these components are contained in a water-proof packaging with necessary wires and pins exposed for charging batteries and driving IPMC actuator. Without the tail, the fish is about 20 cm in length and 5.7 cm in diameter. Total volume is about 180 cm^3 . The fish body is in a water drop shape, which is expected to lead to good hydrodynamic efficiency. The Reynolds number of the swimming robotic fish is given by UD_0/ν , where U is the speed of the robot, D_0 is the body diameter, and $\nu = 10^{-6} \text{ m}^2/\text{s}$ is the kinematic viscosity of water. With a speed U of about 0.02 m/s (see Section 4.3.3), the Reynolds number of the robot is at the order of 1000. The total weight of the robotic fish is about 290 g. The shape and configuration of the robot put it into the category of carangiform fish.

4.2 Model

In this section we first review Lighthill's theory on elongated-body propulsion (Section 4.2.1). IPMC beam dynamics in fluid is discussed next, considering general force and moment inputs (Section 4.2.2). This is followed by detailed consideration of actuation-induced bending moment in the model, as well as the load contribution to the IPMC beam from the passive fin (Section 4.2.3). Finally, the model for computing the speed of IPMC-propelled robotic fish is obtained by merging Lighthill's theory and the hybrid tail dynamics (Section 4.2.4).

4.2.1 Lighthill's theory of elongated-body propulsion

A body is considered elongated if its cross-sectional area changes slowly along its length. The robotic fish described in Section 4.1 is thus elongated and Lighthill's theory [56] applies.

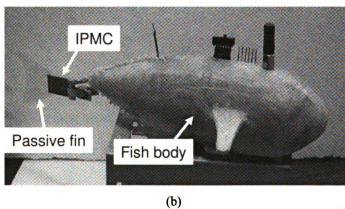
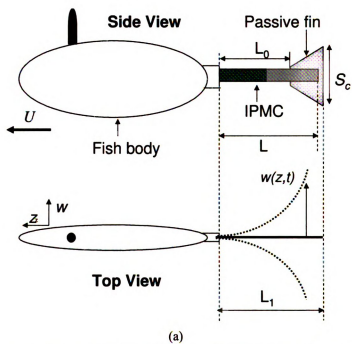


Figure 4.1: (a) Schematic of the robotic fish; (b) prototype of the robotic fish.

Suppose that the tail is bending periodically with the bending displacement at z denoted by $w(z, t)$. Refer to Fig. 4.1(a) for notation. At the steady state, the fish will achieve a periodic, forward motion with some mean speed U . In the discussion here, the word “mean” refers to the average over one period. The mean thrust \bar{T} produced by the tail can be calculated as

$$\bar{T} = \left[\frac{m}{2} \left(\overline{\left(\frac{\partial w(z, t)}{\partial t} \right)^2} - U^2 \overline{\left(\frac{\partial w(z, t)}{\partial z} \right)^2} \right) \right]_{z=L}, \quad (4.1)$$

where $z = L$ denotes the end of tail, $\overline{(\cdot)}$ denotes the *mean* value, m is the virtual mass density at $z = L$, expressed as

$$m = \frac{1}{4} \pi S_c^2 \rho_w \beta. \quad (4.2)$$

In (4.2), S_c is the width of the tail at the end $z = L$, ρ_w is the fluid density, and β is a non-dimensional parameter close to 1. Eq. (4.1) indicates that the mean thrust depends only on the lateral velocity $\frac{\partial w}{\partial t}$ and the slope $\frac{\partial w}{\partial z}$ at the tail end. A cruising fish, under inviscid flow conditions, will experience a drag force F_D :

$$F_D = \frac{C_D \rho_w U^2 S}{2}, \quad (4.3)$$

where S is the wetted surface area, and C_D is the drag coefficient. At the steady state, the mean thrust \bar{T} is balanced by the drag F_D , from which one can solve the cruising speed U :

$$U = \left[\frac{\overline{m \left(\frac{\partial w(z, t)}{\partial t} \right)^2}}{\sqrt{C_D \rho_w S + \overline{m \left(\frac{\partial w(z, t)}{\partial z} \right)^2}}} \right]_{z=L}. \quad (4.4)$$

Since the speed of the fish is related to the lateral velocity and the slope of the trailing edge, one needs to fully understand the actuation dynamics of the tail.

4.2.2 IPMC beam dynamics in fluid

In order to obtain the full actuation model of IPMC, we start with a fourth-order PDE for the dynamic deflection function $w(z, t)$ [24]

$$YI \frac{\partial^4 w(z, t)}{\partial z^4} + C \frac{\partial w(z, t)}{\partial t} + \rho_m A \frac{\partial^2 w(z, t)}{\partial t^2} = f(z, t), \quad (4.5)$$

where Y , I , C , ρ_m , and A denote the effective Young's modulus, the area moment of inertia, the internal damping ratio, the density, and the cross-sectional area of the IPMC beam, respectively, and $f(z, t)$ is the distributed force density acting on the beam.

Converting (4.5) into the Laplace domain, we get

$$YI \frac{\partial^4 w(z, s)}{\partial z^4} + C s w(z, s) + \rho_m A s^2 w(z, s) = F(z, s). \quad (4.6)$$

The force on the beam consists of two components, the hydrodynamic force F_{hydro} from water, and the driving force F_{drive} due to the actuation of IPMC:

$$F(z, s) = F_{\text{hydro}}(z, s) + F_{\text{drive}}(z, s). \quad (4.7)$$

The hydrodynamic force acting on the IPMC beam can be expressed as [76]:

$$F_{\text{hydro}}(z, s) = -\rho_w \frac{\pi}{4} W^2 s^2 \Gamma_1(\omega) w(z, s), \quad 0 \leq z \leq L, \quad (4.8)$$

W is the width of the IPMC beam, $\Gamma_1(\omega)$ is the hydrodynamic function for the IPMC beam subject to an oscillation with radial frequency ω , and ρ_w is the density of fluid. The hydrodynamic function for a rectangular beam can be represented as [76]:

$$\Gamma_1(\omega) = \Omega(R_e) \left[1 + \frac{4iK_1(-i\sqrt{iR_e})}{\sqrt{iR_e}K_0(-i\sqrt{iR_e})} \right], \quad (4.9)$$

where the Reynolds number

$$R_e = \frac{\rho_w W^2 \omega}{4\eta},$$

K_0 and K_1 are modified Bessel functions of the third type, $\Omega(R_e)$ is the correction function associated with the rectangular beam cross-section [76], η is the viscosity of fluid, and W is the width of the IPMC beam.

With (4.7) and (4.8), the beam dynamics equation (4.6) can be written as:

$$YI \frac{\partial^4 w(z,s)}{\partial z^4} + C_s w(z,s) + (\mu_m + m_d \Gamma_1) s^2 w(z,s) = F_{\text{drive}}(z,s), \quad (4.10)$$

where $m_d = \rho_w \frac{\pi}{4} W^2$ is the added mass and $\mu_m = \rho_m A$ is the mass of IPMC per unit length.

Under harmonic oscillation with frequency ω , we can denote

$$\mu_v = \mu_m + m_d \text{Re}(\Gamma_1), \quad (4.11)$$

$$C_v = C - m_d \omega \text{Im}(\Gamma_1), \quad (4.12)$$

where μ_v is the equivalent mass of IPMC per unit length in water, and C_v is the equivalent damping coefficient of IPMC in water. $\text{Re}(\cdot)$ and $\text{Im}(\cdot)$ are the functions that get the real part and the imaginary part from a complex value, respectively. Eq. (4.12) means that the damping of IPMC vibration in water includes both the internal damping in IPMC and the frequency-dependent external damping caused by fluid. With (4.11) and (4.12), Eq. (4.10) can be written as [16]:

$$YI \frac{\partial^4 w(z,s)}{\partial z^4} + C_v s w(z,s) + \mu_v s^2 w(z,s) = F_{\text{drive}}(z,s). \quad (4.13)$$

According to the mode analysis method, we can express the solution to (4.13) as the

sum of different modes [57]:

$$w(z, s) = \sum_{i=1}^{\infty} \varphi_i(z) q_i(s), \quad (4.14)$$

where $\varphi_i(z)$ is the beam shape for the i -th mode, and $q_i(s)$ is the corresponding generalized coordinate. The mode shape $\varphi_i(z)$ takes the form

$$\varphi_i(z) = \cosh(\lambda_i z) - \cos(\lambda_i z) - \beta_i (\sinh(\lambda_i z) - \sin(\lambda_i z)), \quad (4.15)$$

where λ_i can be obtained by solving

$$1 + \cos(\lambda_i L) \cosh(\lambda_i L) = 0,$$

and

$$\beta_i = \frac{\sinh(\lambda_i L) - \sin(\lambda_i L)}{\cosh(\lambda_i L) + \cos(\lambda_i L)}.$$

The generalized coordinate $q_i(s)$ can be represented as

$$q_i(s) = f_i(s) Q_i(s), \quad (4.16)$$

where $f_i(s)$ is the generalized force,

$$Q_i(s) = \frac{1}{s^2 + 2\xi_i \omega_i s + \omega_i^2}, \quad (4.17)$$

and the natural frequency ω_i and the damping ratio ξ_i for the i -th mode are

$$\omega_i = \frac{C_i^2}{L^2} \sqrt{\frac{YI}{\mu_v(\omega_i)}}, \quad (4.18)$$

$$\xi_i = \frac{C_v(\omega_i)}{2\mu_v(\omega_i)\omega_i}, \quad (4.19)$$

$C_i = \lambda_i L$. Noting that $\Gamma_1(\omega)$ is almost a constant value in the frequency region around ω_i , one can consider $\mu_v(\omega_i)$ as a constant in Eq. (4.18). So ω_i can be obtained approximately. Then with ω_i , ξ_i can be obtained from Eq. (4.19). The generalized force $f_i(s)$ is obtained from F_{drive} :

$$f_i(s) = \frac{1}{M_i} \int_0^L F_{\text{drive}}(z, s) \varphi_i(z) dz,$$

where M_i is the generalized mass

$$M_i(s) = \int_0^L \mu_v \varphi_i^2(z) dz = \mu_v L. \quad (4.20)$$

The next step is to derive the generalized force $f_i(s)$ from the moment generated by IPMC actuation, and from the hydrodynamic force acting on the passive fin but transmitted to the IPMC beam.

4.2.3 Actuation model of the tail

In our earlier work [21], we fully investigated the electrical dynamics of IPMC to obtain the moment generated within IPMC, but there the beam dynamics in water was not considered. In the following we will incorporate both electrical dynamics and hydrodynamic interactions into a full actuation model for IPMC hybrid tail in water.

The ion movement inside an IPMC, under the influence of an applied electric field, leads to a distribution of net charge density along the thickness direction of IPMC. A physics-based model for IPMC proposed by Nemat-Nasser and Li [64] relates the actuation-induced (axial) stress proportionally to the charge density, through electromechanical coupling. Variation of the actuation-induced stress along the thickness direction thus results in a bending moment at each point along the length direction. Our work on physics-based, control-oriented modeling of IPMC actuators [21] further incorporates the effect of distributed surface resistance. The latter leads to non-uniform potential difference along the

length direction, which in turn leads to actuation-induced bending moment that varies along the length direction, referred to as distributed bending moment in this section.

As shown in Section 2.3, with distributed surface resistance, we can relate the actuation-induced internal bending moment $M_{\text{IPMC}}(z, s)$ at point z to the actuation voltage $V(s)$ by an infinite-dimensional transfer function [21]:

$$M_{\text{IPMC}}(z, s) = \frac{\alpha_0 W K k_e (\gamma(s) - \tanh(\gamma(s)))}{(s\gamma(s) + K \tanh(\gamma(s)))} \cdot \frac{\cosh(\sqrt{B(s)}z) - \sinh(\sqrt{B(s)}z) \tanh(\sqrt{B(s)}L)}{1 + r_2 \theta(s)} V(s), \quad (4.21)$$

with

$$\begin{aligned} \theta(s) &\triangleq \frac{W k_e s \gamma(s) (s + K)}{h (s \gamma(s) + K)}, \\ B(s) &\triangleq \sqrt{r_1 \left(\frac{\theta(s)}{(1 + r_2 \theta(s))} + \frac{2}{R_p} \right)}, \\ \gamma(s) &\triangleq \sqrt{\frac{s + K}{d}}, \\ K &\triangleq \frac{F^2 d C^-}{\kappa_e R T} (1 - C^- \Delta V), \end{aligned}$$

where α_0 is an electromechanical coupling constant, d is the ionic diffusivity, R is the gas constant, F is Faraday's constant, T is the absolute temperature, C^- is the anion concentration, ΔV is the volumetric change, x is the coordinate defined in the thickness direction, κ_e is the effective dielectric constant of the polymer, r_1 is the electrode resistance per unit length in the length direction, r_2 is the electrode resistance per unit length in the thickness direction, and R_p is the through-polymer resistance per unit length. W , L , h are the width, length, and half thickness of the IPMC beam, respectively.

We replace the moment $M_{\text{IPMC}}(z, s)$ induced by actuation by three components: a dis-

tributed force density $F_d(z,s)$ acting along the length, a concentrated force $F_c(L,s)$, and a concentrated moment $M(L,s)$ acting at the IPMC tip $z = L$, where

$$\begin{aligned} F_c(L,s) &= -\frac{\partial M_{\text{IPMC}}(z,s)}{\partial z} \Big|_{z=L}, \\ F_d(z,s) &= \frac{\partial^2 M_{\text{IPMC}}(z,s)}{\partial z^2}, \end{aligned} \quad (4.22)$$

$$M(L,s) = M_{\text{IPMC}}(L,s). \quad (4.23)$$

The rationale of this replacement is that these components can generate the same bending moment as $M_{\text{IPMC}}(z,s)$. See Appendix B.1 for the details of this justification. With (4.21), it can be verified that $F_c(L,s) \equiv 0$. Then the generalized force can be obtained as [57]:

$$f_{1i}(s) = \frac{1}{M_i} \left(\int_0^L F_d(z,s) \phi_i(z) dz + M(L,s) \phi_i'(L) \right). \quad (4.24)$$

Fig. 4.2 shows that the original moment is replaced by a distributed force density and a concentrated moment. With the above replacement, we can derive the models for the

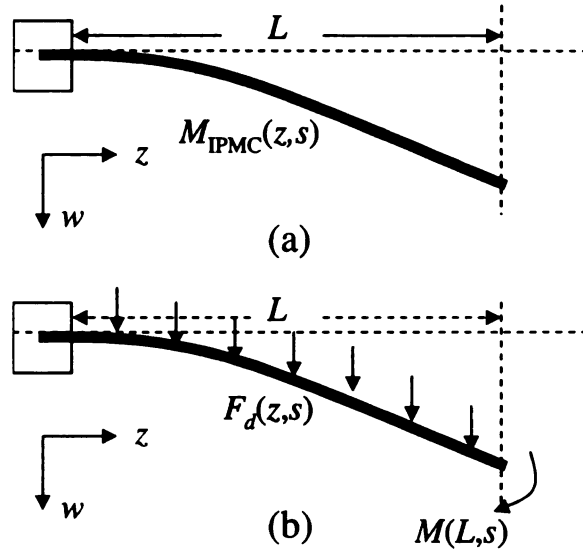


Figure 4.2: The original moment in (a) is replaced by a distributed force density and a concentrated bending moment in (b).

IPMC tail only case and the hybrid tail case.

With IPMC tail only

With (4.22) and (4.23), the generalized force (4.24) can be written as

$$f_{1i}(s) = H_{fi}(s) V(s), \quad (4.25)$$

where

$$H_{fi}(s) = \frac{1}{2M_i} \begin{pmatrix} (a-b)(a_L + b_L - c_L - d_L) \\ -\beta_i(a-b)(a_L - b_L + jc_L - jd_L) \end{pmatrix} + \frac{\alpha_0 W K k_e (\gamma(s) - \tanh(\gamma(s)))}{M_i (s\gamma(s) + K \tanh(\gamma(s)))} \frac{\phi'_i(L)}{(1 + r_2 \theta(s)) \cosh(cL)}, \quad (4.26)$$

and

$$a = \frac{\alpha_0 W K k_e (\gamma(s) - \tanh(\gamma(s)))}{(s\gamma(s) + K \tanh(\gamma(s)))} \frac{B(s)}{1 + r_2 \theta(s)}, \quad (4.27)$$

$$b = a \tanh(\sqrt{B(s)}L), \quad c = \sqrt{B(s)}, \quad (4.28)$$

$$a_L = \frac{\sinh((c + \lambda_i)L)}{c + \lambda_i}, \quad b_L = \frac{\sinh((c - \lambda_i)L)}{c - \lambda_i}, \quad (4.29)$$

$$c_L = \frac{\sinh((c + j\lambda_i)L)}{c + j\lambda_i}, \quad d_L = \frac{\sinh((c - j\lambda_i)L)}{c - j\lambda_i}. \quad (4.30)$$

See Appendix B.2 for the derivation of $H_{fi}(s)$.

From (4.14), one can then get the transfer function $H_1(z, s)$ relating $w(z, s)$ to $V(s)$:

$$H_1(z, s) = \frac{w(z, s)}{V(s)} = \sum_{i=1}^{\infty} \phi_i(z) H_{fi}(s) Q_i(s). \quad (4.31)$$

We can also derive the transfer function $H_{1d}(z, s)$ relating the slope of the beam $\frac{\partial w(z, s)}{\partial z}$

to the input voltage $V(s)$:

$$H_{1d}(z, s) = \frac{\frac{\partial w(z, s)}{\partial z}}{V(s)} = \sum_{i=1}^{\infty} \phi_i'(z) H_{fi}(s) Q_i(s). \quad (4.32)$$

Hybrid Tail

From (4.1) and (4.2), the tail width S_c at the end has a significant impact on the speed U . One could increase S_c by simply using a wider IPMC beam. Due to the IPMC actuation mechanism, however, a too wide beam (i.e., plate) will produce curling instead of bending motion and is thus not desirable. Therefore, it has been chosen to increase the edge width by attaching a passive plastic piece, as illustrated in Fig. 4.3. While such a hybrid tail is expected to increase the thrust, one has to also consider that the extra hydrodynamic force on the passive fin adds to the load of IPMC and may reduce the bending amplitude. Therefore, it is necessary to model these interactions carefully.

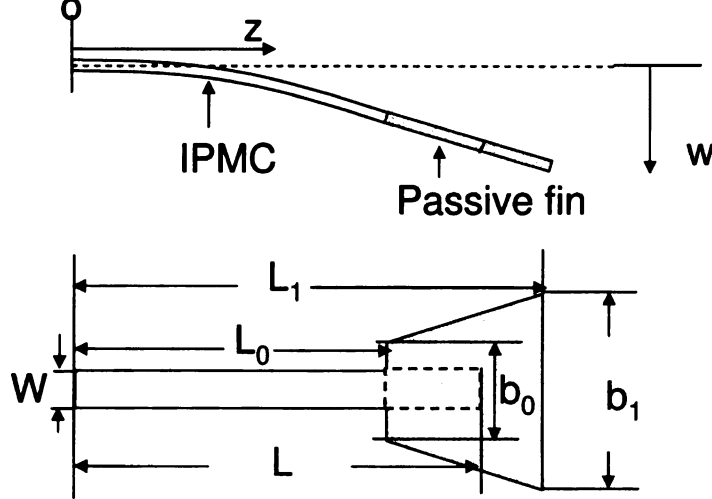


Figure 4.3: Illustration of an IPMC beam with a passive fin. The lower schematic shows the definitions of dimensions.

The hydrodynamic force acting on the passive fin can be written as [76]

$$f_{\text{tail}}(z, s) = -\frac{\pi}{4} \rho_w s^2 b(z)^2 \Gamma_2(\omega) w(z, s), \quad L_0 \leq z \leq L_1, \quad (4.33)$$

where $\Gamma_2(\omega)$ is the hydrodynamic function of the passive fin. Note that the hydrodynamic force acting on the active IPMC beam has been incorporated in (4.10), so only the hydrodynamic force on the passive fin needs to be considered here. Since the passive fin used is very light, its inertial mass is negligible compared to the propelled virtual fluid mass and is thus ignored in the analysis here. Considering that the passive fin is rigid compared to IPMC, its width $b(z)$ and deflection $w(z, s)$ can be expressed as

$$b(z) = \frac{b_1 - b_0}{L_1 - L_0} (z - L_0) + b_0, \quad (4.34)$$

$$w(z, s) = w(L_0, s) + \frac{\partial w(L_0, s)}{\partial z} (z - L_0), \quad (4.35)$$

where b_0, b_1, L, L_0, L_1 are as defined in Fig. 4.3. Then one can calculate the moment introduced by the passive fin: for $L_0 \leq z \leq L_1$,

$$\begin{aligned} M_{\text{fin}}(z, s) &= \int_{L_0}^{L_1} f_{\text{tail}}(\tau, s) (\tau - z) d\tau \\ &= \int_{L_0}^{L_1} f_{\text{tail}}(\tau, s) (\tau - L_0) d\tau + (L_0 - z) \int_{L_0}^{L_1} f_{\text{tail}}(\tau, s) d\tau. \end{aligned} \quad (4.36)$$

If we define

$$M_{\text{tail}}(s) = \int_{L_0}^{L_1} f_{\text{tail}}(\tau, s) (\tau - L_0) d\tau, \quad F_{\text{tail}}(s) = \int_{L_0}^{L_1} f_{\text{tail}}(\tau, s) d\tau, \quad (4.37)$$

then (4.36) can be written as

$$M_{\text{fin}}(z, s) = M_{\text{tail}}(s) + F_{\text{tail}}(s) (L_0 - z). \quad (4.38)$$

Fig. 4.4 shows the forces and moments acting on the hybrid tail.

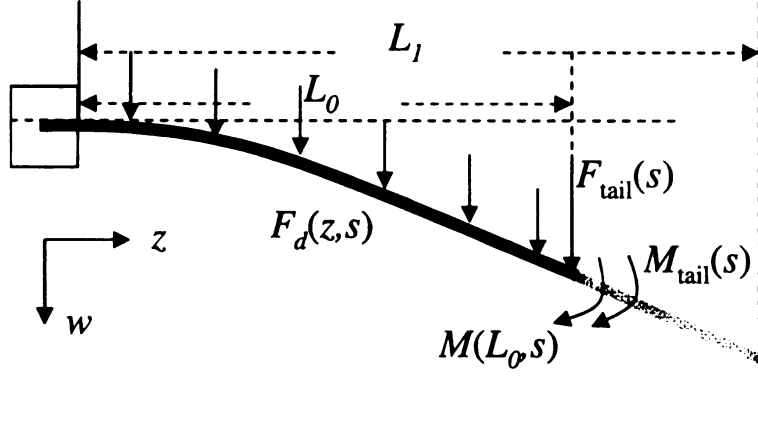


Figure 4.4: Forces and moments acting on the hybrid tail.

One can get the generalized force as:

$$f_{2i}(s) = \frac{1}{M_i} \left(\int_0^{L_0} F_d(z, s) \varphi_i(z) dz + \varphi_i(L_0) F_{\text{tail}}(s) \right) + \frac{(M_{\text{tail}}(s) + M(L_0, s)) \varphi_i'(L_0)}{M_i}, \quad (4.39)$$

where M_{tail} and F_{tail} are defined in (4.37), $F_d(z, s)$ and $M(L_0, s)$ are defined in (4.22) and (4.23).

Then the transfer function relating $w(L_0, s)$ to $V(s)$ and that relating $w'(L_0, s) \triangleq \frac{\partial w(L_0, s)}{\partial z}$ to $V(s)$ can be found as

$$H_2(L_0, s) = \frac{(1 + F_s) A_s - B_s E_s}{(1 + C_s)(1 + F_s) - B_s J_s}, \quad (4.40)$$

$$H_{2d}(L_0, s) = \frac{(1 + C_s) E_s - A_s J_s}{(1 + C_s)(1 + F_s) - B_s J_s}, \quad (4.41)$$

where

$$A_s = H_1(L_0, s), \quad E_s = H_{1d}(L_0, s), \quad (4.42)$$

$$D = L_1 - L_0, \quad k = \frac{b_1 - b_0}{D}, \quad M_s = \frac{\pi}{4} s^2 \Gamma_2(\omega) \rho_w, \quad (4.43)$$

$$B_s = \sum_{i=1}^{\infty} \frac{\varphi_i(L_0) Q_i(s)}{M_i} M_s \left[\varphi_i'(L_0) k_a + \varphi_i(L_0) k_b \right], \quad (4.44)$$

$$C_s = \sum_{i=1}^{\infty} \frac{\varphi_i(L_0) Q_i(s)}{M_i} M_s \left[\varphi_i'(L_0) k_b + \varphi_i(L_0) k_c \right], \quad (4.45)$$

$$F_s = \sum_{i=1}^{\infty} \frac{\varphi_i'(L_0) Q_i(s)}{M_i} M_s \left[\varphi_i'(L_0) k_a + \varphi_i(L_0) k_b \right], \quad (4.46)$$

$$J_s = \sum_{i=1}^{\infty} \frac{\varphi_i'(L_0) Q_i(s)}{M_i} M_s \left[\varphi_i'(L_0) k_b + \varphi_i(L_0) k_c \right], \quad (4.46)$$

and

$$\begin{aligned} k_a &= \frac{k^2 D^5}{5} + \frac{2k b_0 D^4}{4} + \frac{b_0^2 D^3}{3}, \\ k_b &= \frac{k^2 D^4}{4} + \frac{2k b_0 D^3}{3} + \frac{b_0^2 D^2}{2}, \\ k_c &= \frac{k^2 D^3}{3} + k b_0 D^2 + b_0^2 D. \end{aligned} \quad (4.47)$$

See Appendix B.3 for the detailed derivation. From (4.35), (4.40) and (4.41), one can obtain the transfer functions relating the bending displacement and the slope at $z = L_1$ to the voltage input $V(s)$ as follows:

$$\begin{aligned} H_3(L_1, s) &\triangleq \frac{w(L_1, s)}{V(s)} = H_2(L_0, s) + H_{2d}(L_0, s) D, \\ H_{3d}(L_1, s) &\triangleq \frac{w'(L_0, s)}{V(s)} = H_{2d}(L_0, s). \end{aligned} \quad (4.48)$$

4.2.4 Speed model of robotic fish

Given a voltage input $V(t) = A_m \sin(\omega t)$ to the IPMC actuator, the bending displacement and the slope of the IPMC at the tip $z = L$ can be written as,

$$w(L, t) = A_m |H(j\omega)| \sin(\omega t + \angle H(j\omega)), \quad (4.49)$$

$$\frac{\partial w(z, t)}{\partial z} \Big|_{z=L} = A_m |H_d(j\omega)| \sin(\omega t + \angle H_d(j\omega)), \quad (4.50)$$

where $\angle(\cdot)$ denotes the phase angle and $H(s)$ and $H_d(s)$ are the transfer functions relating the bending displacement $w(L, s)$ and the slope $w'(L, s)$ to the voltage input $V(s)$, respectively, which can be obtained as in Section 4.2.3. From (4.4), one can then obtain the steady-state speed U of the robotic fish under the actuation voltage $V(t) = A_m \sin(\omega t)$ as

$$U = \sqrt{\frac{mA_m^2 \omega^2 |H(j\omega)|^2}{2C_D \rho_w S + mA_m^2 |H_d(j\omega)|^2}}. \quad (4.51)$$

One can easily extend (4.51) to periodic signals of other forms. For instance, the prototype in Fig. 4.1(b) uses square-wave voltage signals for ease of implementation. To derive the speed U , we can write out the Fourier series of a square wave. Then the velocity of the fish actuated under a square wave voltage with amplitude A_m can then be obtained as

$$U = \sqrt{\frac{m \cdot \frac{8\omega^2 A_m^2}{\pi^2} \cdot \sum_{n=1,3,5,\dots}^{\infty} |H(jn\omega)|^2}{C_D \rho_w S + m \cdot \frac{8A_m^2}{\pi^2} \cdot \sum_{n=1,3,5,\dots}^{\infty} \frac{|H_d(jn\omega)|^2}{n^2}}}. \quad (4.52)$$

Derivation of (4.52) is omitted here due to the space limitation.

4.3 Experimental Verification and Parameter Identification

In this section, three different types of experiments have been carried out for model identification and validation: 1) drag coefficient identification (Section 4.3.1); 2) identification and validation of the actuation model for IPMC underwater with and without the passive fin (Section 4.3.2); and finally, 3) validation of the model for fish motion with different tail dimensions (Section 4.3.3).

4.3.1 Drag coefficient identification

The most important parameter related to the fish body is the drag coefficient C_D , which depends on the Reynolds number, the fitness ratio of the body, and the properties of the fish surface and fluid. In order to identify C_D , the fish was pulled with different velocities, and metric spring scales were used to measure the drag force F_D . With the measured drag force, velocity, and surface area of the fish, the drag coefficient C_D was calculated from (4.3). Fig. 4.5 illustrates the experimental setup for drag force measurement.

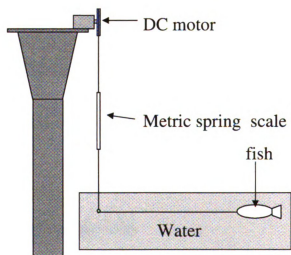


Figure 4.5: Experimental setup for the drag force measurement.

Through drag force measurement, one can get the plot of the drag force versus velocity. Based on (4.3), one can fit the experimental data with simulation data through the least squares method to identify the drag coefficient. Fig. 4.6 shows the drag force versus the velocity of the fish. Table 4.1 shows the parameters related to the drag force.

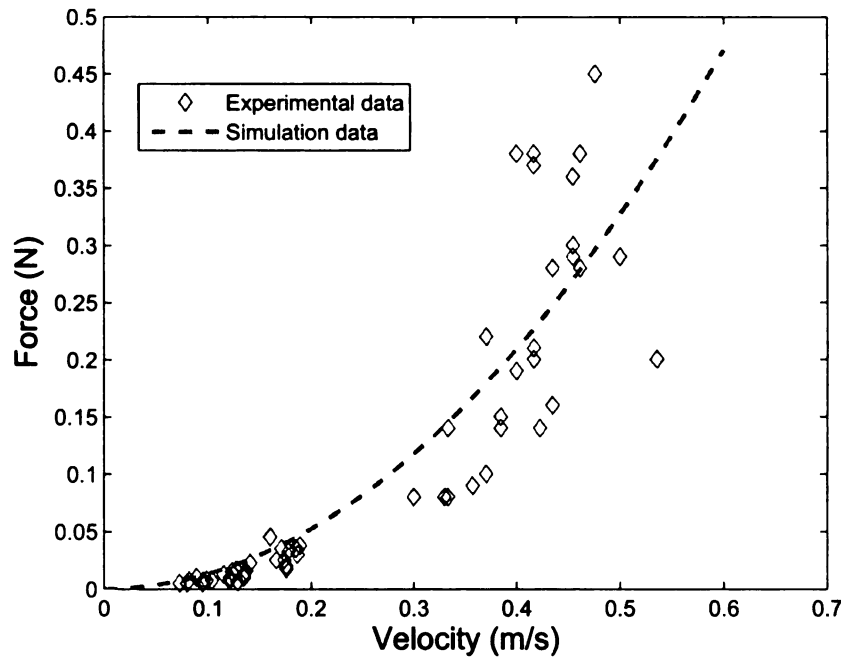


Figure 4.6: Drag force versus velocity of the fish.

Table 4.1: Parameters related to the drag force.

S	ρ_w	C_D
$218 \times 10^{-4} \text{m}^2$	1000 kg/m^3	0.12

4.3.2 Fish tail model verification

To investigate the parameters related to the IPMC beam dynamics, the natural vibrations of IPMC in water and in air were measured without an actuation voltage applied to the IPMC.

They were also used to verify $Q_1(s)$ for the first mode vibration. To investigate the hydrodynamic effect of passive fin on the IPMC beam, the frequency responses of the tail subject to voltage input were measured for both without and with the plastic fin. They were also used to verify the actuation models of IPMC. Fig. 4.7 shows the schematic of experimental setup. In the natural vibration testing, the tail was fixed in water and a mechanical impulse was applied at the tip to make the beam vibrate. The first-mode vibration was measured by a laser sensor (OADM 20I6441/S14F, Baumer Electric). In the frequency response testing, the fish tail was fixed in the water by a frame arm and a sequence of sinusoid voltages with amplitude 3.3 V and frequency ranging from 0.05 Hz to 10 Hz were applied to the IPMC. The lateral displacement of the IPMC beam was captured by a laser sensor and actuation voltage was measured by a dSpace system (DS1104, dSPACE).

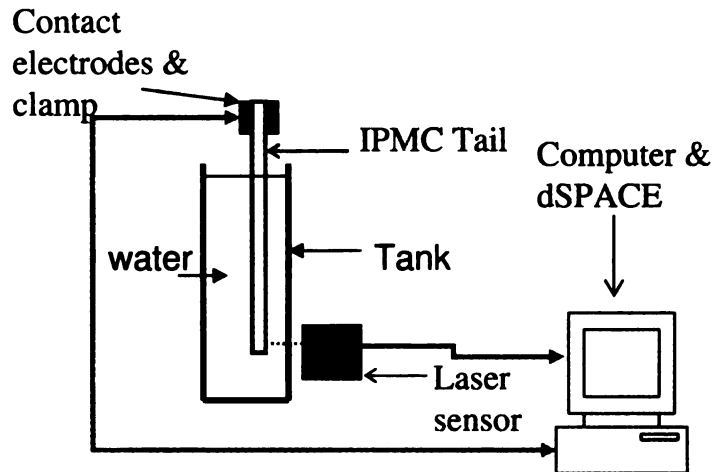


Figure 4.7: Experimental setup for identification and verification of IPMC actuation model in water.

Beam dynamics identification

Since the actuation bandwidth of IPMC actuators is relatively low (up to a few Hz), it suffices to consider the first mode of the beam motion. The parameters related to the beam dynamics can be identified through passive vibration tests of IPMC in water. The first mode

vibration related to the step response of the second-order system $Q_1(s)$ (see Eq. (4.17)) is

$$y(t) = y(0) e^{-\xi_1 \omega_1 t} \cos \left(\omega_1 t \sqrt{1 - \xi_1^2} \right).$$

In the experiment, we tapped the tip of the cantilevered IPMC beam (submerged in water) and recorded the tip trajectory with the laser sensor as the beam underwent passive, damped oscillations. Fig 4.8 shows both the simulation data and the experimental data on the tip displacement of the vibrating IPMC beam, where the beam dimensions were $L = 23$ mm, $W = 15$ mm.

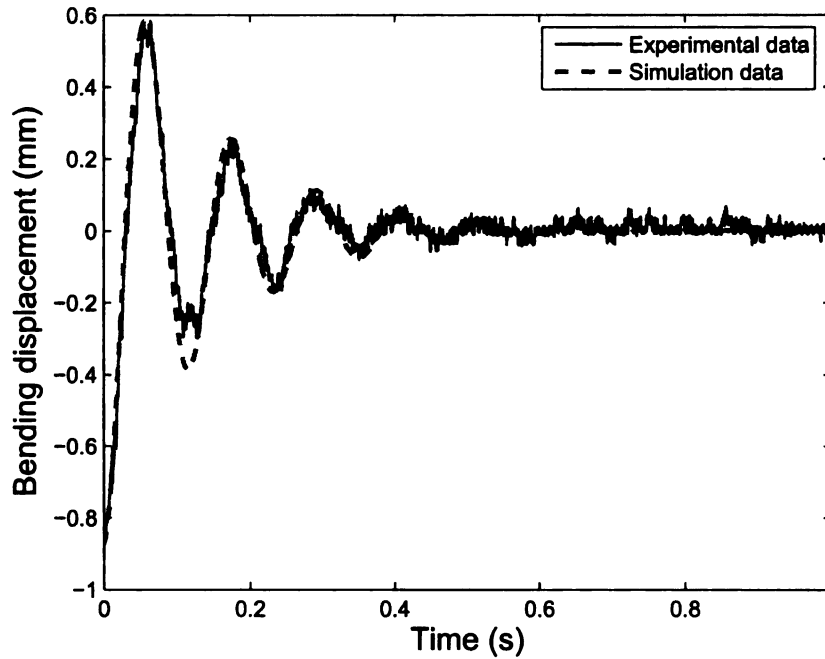


Figure 4.8: Vibration of IPMC beam in water.

From Fig. 4.8, the natural frequency and damping ratio in water were identified to be $\omega_1 = 54$ rad/sec, $\xi_1 = 0.14$. Hydrodynamic function of IPMC beam $\Gamma_1(\omega)$ can be simulated based on (4.9). The correction function $\Omega(\omega)$ for rectangular shape beam reported in [76] is used in the simulation. Around the natural frequency, one can pick $\text{Re}(\Gamma_1) = 1.07$ and $\text{Im}(\Gamma_1) = 0.04$. Based on (4.11), one can get μ_v . Based on (4.18), (4.19), one can

obtain Y and C_v . Table 4.2 shows all the parameters related to the beam dynamics.

Table 4.2: Parameters in IPMC beam dynamics.

C_v	μ_v	W	L
3.17	0.2 kg/m	15 mm	23 mm
h	C_1	Y	Γ_1
115 μm	1.8751	$2.91 \times 10^8 \text{ Pa}$	1.07+0.04j

Fish tail model identification

In the fish tail model, some parameters can be directly measured, such as dimensions, temperature, resistance, and density of IPMC. Some parameters are physical constants, such as R , F , and ρ_w . Since $|C^- \Delta V| \ll 1$ [64], we take $1 - C^- \Delta V = 1$. Some parameters, such as k_e , α_0 , r_2 , need to be identified through fitting the frequency responses with model simulation, which was discussed in [21]. Γ_2 can be identified through fitting the frequency response of hybrid tail with simulation data. Table 4.3 shows the parameters related to the electrical dynamics of IPMC. The dimensions of IPMC-only tail are shown in Table 4.2. The dimensions of hybrid tail *Tail1* are shown in Table 4.3.3.

Table 4.3: Parameters related to the electrical dynamics of IPMC.

F	T	R	C^-
96487 C/mol	300 K	8.3143 J/mol · K	1091 mol/m ³
r_1	r_2	d	κ_e
210 Ω/m	0.04 $\Omega \cdot \text{m}$	$5.39 \times 10^{-9} \text{ m/s}$	$2.48 \times 10^{-5} \text{ F/m}$
R_p	α_0		
38 $\Omega \cdot \text{m}$	0.08 J/C		

The actuation model of IPMC with and without passive fin is verified. We applied sinusoidal voltage signals with amplitude 3.3 V and different frequencies to IPMC. Both the voltage input and the bending displacement output at the tail tip were measured to obtain the empirical frequency responses. In the case of an IPMC beam only, the displacement

measurement was made at the beam tip; in the case of a hybrid tail, the displacement was measured at the tip of passive fin. In the simulation of the actuation models, only the first mode was taken into account, because the frequencies used were below or close to the first-mode resonant frequency. Fig. 4.9(a) compares the Bode plot of $H_1(L, s)$ (Eq. (4.31) in Section 4.2) with its empirical counterpart, and the agreement is good in both magnitude and phase. The cut-off frequency is estimated to be about 8.6 Hz, which is consistent with the IPMC beam's natural frequency in water, as identified from the free vibration experiment shown in Fig. 4.8. Fig. 4.9(b) compares the Bode plot of $H_3(L_1, s)$ (Eq. (4.48) in Section 4.2) and the measured frequency response from voltage input to the tail tip displacement for the hybrid tail. As can be seen in the figure, the cut-off frequency of the hybrid tail is much lower than that of an IPMC alone. This can be explained by the additional mass effect at the IPMC tip, introduced by the fluid pushed by the passive fin.

4.3.3 Speed model verification

To validate the speed model of the robotic fish, the velocities of the fish propelled by the IPMC under square-wave voltage inputs with amplitude 3.3 V and different frequencies were measured. In this experiment, the robotic fish swam freely in a tank marked with start and finish lines, and a timer recorded the time it took for the fish to travel the designated range after it reached the steady state. Fig. 4.10 shows a snapshot of fish swimming in the tank.

The capability of the model in predicting cruising speed was verified for different operating frequencies, for different tail dimensions. The speed model for square wave input (Eq.(4.52)) was applied to the robotic fish as described in Section 4.1. In the simulation of (4.52), we took the first three terms in each infinite series, which provided a good approximation to the sum of infinite series. Four different hybrid tails were investigated, shown in Table 4.3.3. The identified hydrodynamic functions Γ_2 are shown for *Tail1* and *Tail2* in Fig 4.11. It can be seen that, while the hydrodynamic functions are qualitatively close to

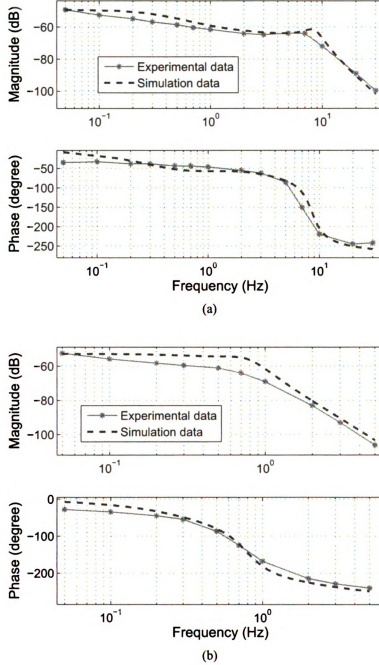


Figure 4.9: Validation of model for IPMC operating underwater. Shown in the figure are the Bode plots for (a) model $H_1(L, s)$ without passive fin; and (b) model $H_2(L_0, s)$ with passive fin.

each other, they are shape-dependent. The predicted speeds match the experimental data well, as shown in Fig. 4.12 and Fig 4.13. Intuitively, within the actuation bandwidth of

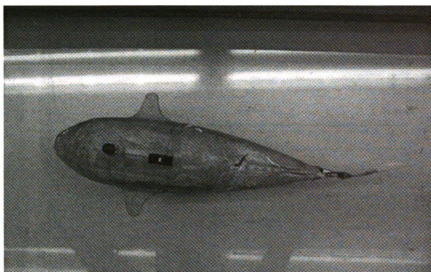


Figure 4.10: Snapshot of robotic fish in swimming test.

IPMC, the speed achieved increases with the actuation frequency. As the frequency gets relatively high, the bending amplitude of IPMC decreases. Thus for each tail, there is an optimal frequency under which the fish reaches the highest speed. Both the optimal frequency and the corresponding highest speed depend on the dimensions of both IPMC and passive fin, which can be predicted by the speed model.

Table 4.4: Dimensions of four tails (see Fig. 4.3 for the definitions of dimension variables).

	$L_0(\text{mm})$	$L(\text{mm})$	$W(\text{mm})$	$b_0(\text{mm})$	$b_1(\text{mm})$	$D(\text{mm})$
<i>Tail1</i>	18	23	15	20	40	40
<i>Tail2</i>	18	23	15	20	50	30
<i>Tail3</i>	18	23	20	20	65	25
<i>Tail4</i>	18	23	20	20	50	30

4.4 Chapter Summary

In this chapter, the modeling of steady-state cruising motion was presented for an IPMC-propelled robotic fish. The model incorporates both IPMC actuation dynamics and hydrodynamic interactions, and it further considers the effect of a passive fin on the robot

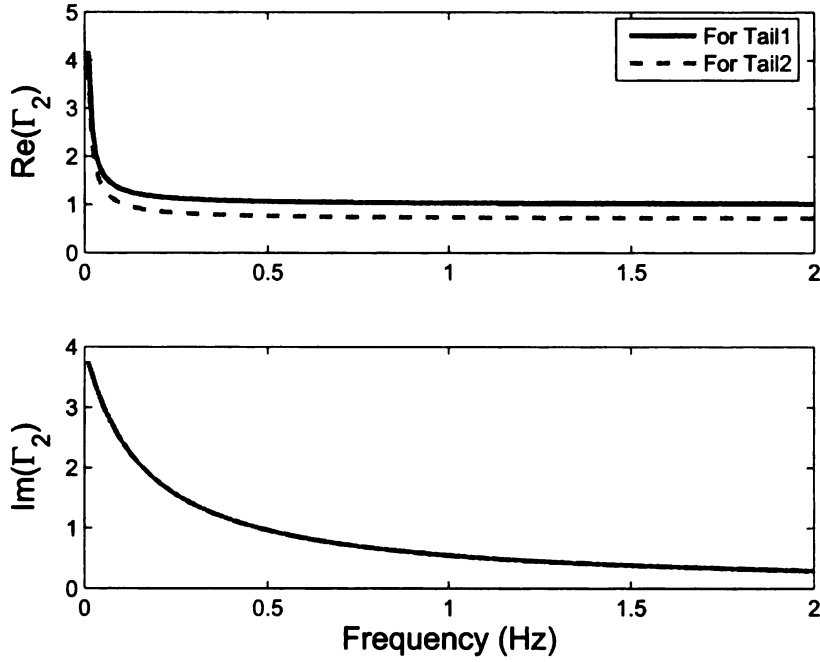
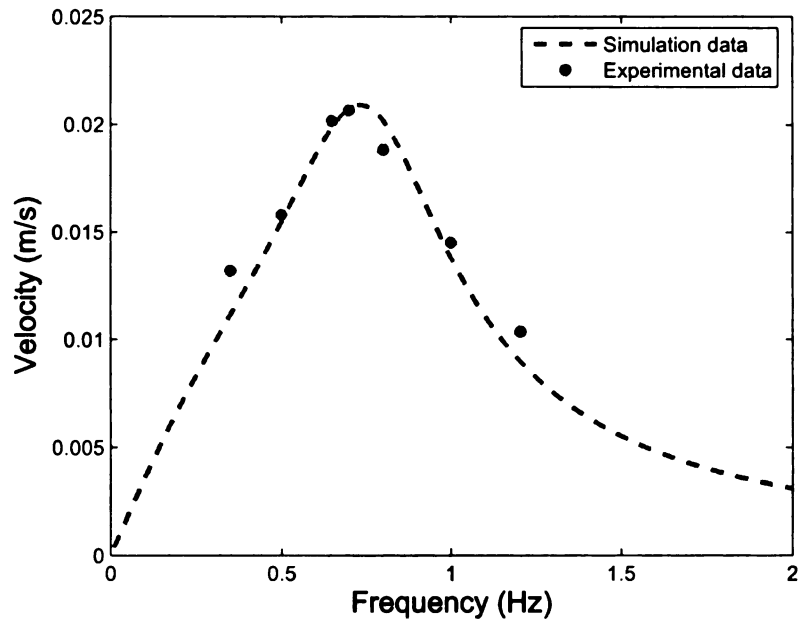


Figure 4.11: Identified Γ_2 for *Tail1* and *Tail2*.

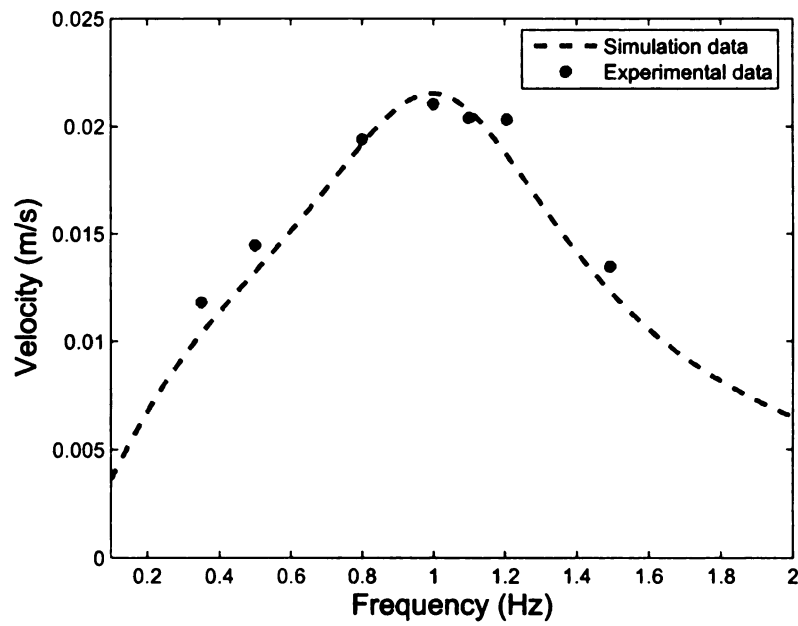
performance. The model was verified in experiments for robotic fish with different tail dimensions. The model will be useful for design and control of the robot to meet the tradeoff between locomotion speed and energy consumption.

Although a focus of the modeling work here is to understand how the steady-state speed of the robot depends on the fin design and actuation input, the approach to modeling IPMC fins in underwater operation holds promise for understanding general motions and maneuvers of the robotic fish. We will extend the presented model to investigate steady turning motion under periodic but asymmetric (left versus right) actuation of the IPMC, as well as unsteady motions such as the acceleration and deceleration of the robot. Path planning and control of the robotic fish will also be examined. In addition, we are exploring the use of IPMC as flow sensors for robotic fish control.

We note that other ionic-type electroactive polymers, in particular, conjugated polymers, have also been explored as propelling mechanisms for robotic fish [87, 4, 59]. The

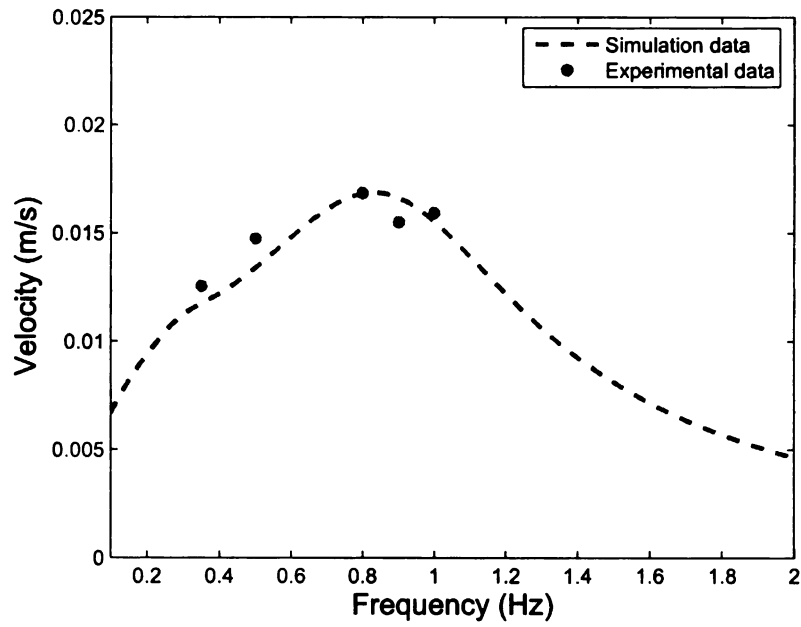


(a)

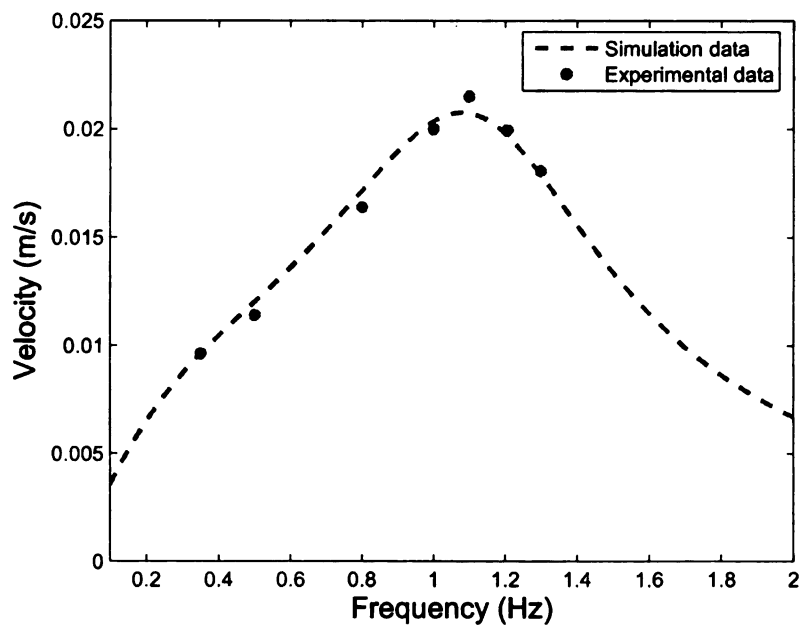


(b)

Figure 4.12: Verification of motion model for the fish with *Tail1* and *Tail2*. (a) With *Tail1*; (b) with *Tail2*.



(a)



(b)

Figure 4.13: Verification of motion model for the fish with *Tail3* and *Tail4*. (a) With *Tail3*; (b) with *Tail4*.

focus of the current chapter is on incorporating both IPMC actuation dynamics and hydrodynamics into modeling. The comparison of IPMC-enabled robotic fish with those of conjugated polymer-enabled ones is outside of the scope of this work, although a clear distinction is that a conjugated polymer fin needs either to be encapsulated or to work in electrolyte for long-term operation [59]. However, the presented approach to coupling actuation and hydrodynamic effects can be potentially extended to conjugated polymer-enabled robotic fish by using corresponding actuation models, e.g., [31].

Chapter 5

Nonlinear Control-oriented Model for Ionic Polymer-Metal Composite

This chapter is organized as follows. The governing nonlinear PDE is reviewed in Section 5.1. Section 5.2 shows numerical and analytical analysis of the nonlinear PDE at the steady state. In Section 5.3, a nonlinear circuit model is introduced to capture the electrical dynamics of IPMC. The derivation of curvature output of IPMC and a nonlinear control-oriented model are also shown in Section 5.3. Experimental validation of the proposed model is presented in Section 5.4. Finally, concluding remarks are provided in Section 5.5.

5.1 Governing Nonlinear PDE

Many papers [64, 63, 33] have mentioned that the nonlinear term $\frac{k_e}{RT}(1 - C^- \Delta V) \frac{\partial E}{\partial x} \cdot E$ can be ignored in the flux (2.9), based on the assumption

$$\rho(x) = k_e \frac{\partial E}{\partial x} \ll C^- F, \quad (5.1)$$

which would result in the linear PDE (2.12). However, this assumption will not hold when a relatively high voltage is applied, as to be shown later in this chapter. Without any can-

cellation of nonlinear term, the original nonlinear governing PDE for charge distribution in an IPMC is:

$$\frac{\partial^2 E}{\partial t \partial x} = d \left(\frac{\partial^3 E}{\partial x^3} - \frac{F(1 - C^- \Delta V)}{RT} \left[\frac{\partial^2 E}{\partial x^2} \cdot E + \left(\frac{\partial E}{\partial x} \right)^2 \right] - \frac{F^2 C^- (1 - C^- \Delta V)}{RT \kappa_e} \frac{\partial E}{\partial x} \right). \quad (5.2)$$

5.2 Analysis of the PDE at the Steady State

A key component in the proposed model is the capacitance of the IPMC. The first step in our modeling work is to analyze the nonlinear PDE (5.2) at the equilibrium when a step voltage is applied, and find the mapping function from voltage to charge. At equilibrium, $J = 0$. Eq. (2.9) then implies

$$E'' - \frac{(1 - C^- \Delta V)}{FRT} E' \cdot E - \frac{F^2 C^-}{\kappa_e RT} (1 - C^- \Delta V) E = 0, \quad (5.3)$$

where $E'(x) = \frac{dE(x)}{dx}$ and $E''(x) = \frac{d^2 E(x)}{dx^2}$. Define

$$\begin{aligned} a &\triangleq \frac{F(1 - C^- \Delta V)}{RT}, \\ b &\triangleq \frac{F^2 C^- (1 - C^- \Delta V)}{RT \kappa_e}. \end{aligned}$$

Then (5.3) becomes

$$E''(x) - aE'(x)E(x) - bE(x) = 0. \quad (5.4)$$

The following two conditions hold for the ODE:

- 1) The overall charge-balance condition leads to

$$\int_{-h}^h \rho(x) dx = 0.$$

Since $E'(x) = \frac{\rho(x)}{\kappa_e}$,

$$\frac{1}{\kappa_e} \int_{-h}^h \rho(x) dx = E(h) - E(-h) = 0, \quad (5.5)$$

which implies $E(h) = E(-h)$.

2) The potential difference is equal to the applied voltage

$$\int_{-h}^h E(x) dx = V. \quad (5.6)$$

Note that $x = -h$ is defined as the anode and $x = h$ is defined as the cathode in this section, so $V \geq 0$.

There are two approaches to solving the nonlinear ODE (5.4), numerical solution and analytical solution. The numerical solution can show the charge distribution, electrical field, and electrical potential along x direction. The analytical solution can provide a mapping function from the voltage to the charge, leading to the nonlinear capacitance of IPMC. These two approaches will be discussed next.

5.2.1 Numerical solution of the PDE at the steady state

In order to numerically solve the second-order ODE (5.3), one needs to know the boundary condition $E(-h)$ and $E'(-h)$, or $E(h)$ and $E'(h)$. However, these conditions are unknown. So we change the initial point to $x = x_0$, where x_0 is defined as the zero charge density point, $\rho(x_0) = \kappa_e E'(x_0) = 0$. Note that x_0 will also depend on the applied voltage. In order to satisfy the conditions (5.5) and (5.6), we run the following steps recursively:

Step 1: Assign a value to x_0 such that $-h < x_0 < +h$, and a very small value to $E(x_0) = E_0$;

Step 2: Integrate ODE (5.3) forward from $x = x_0$ to $x = h$ and backward from $x = x_0$ to $x = -h$, separately, to get $E(x)$ and $E'(x)$;

Step 3: If $|E(-h) - E(h)| \leq \varepsilon$, go to Step 4; If $E(-h) - E(h) > \varepsilon$, decrease $x_0 = x_0 - \varepsilon_1$

and go to Step 2; if $E(-h) - E(h) < -\varepsilon$, increase $x_0 = x_0 + \varepsilon_1$ and go to Step 2;

Step 4: Do integration $-\int_{-h}^x E(x) dx$ to get $\phi(x)$ with $\phi(-h) = 0$;

Step 5: If $|\phi(h) - V| < \varepsilon_2$, then go to Step 6; If $\phi(h) - V > \varepsilon_2$, then increase $E_0 = E_0 + \varepsilon_3$ and go to Step 1; If $\phi(h) - V < -\varepsilon_2$, then decrease $E_0 = E_0 - \varepsilon_3$ and go to Step 1;

Step 6: Calculate $\rho(x) = \kappa_e E'(x)$ and do integration $Q = \int_{x_0}^h \rho(x) S dx$, then stop.

In the steps above, ε , ε_1 , ε_2 , ε_3 are small positive constants, $S = WL$ is the surface area of IPMC. All the physical parameters in the PDE are listed in Table 5.1 in Section 5.4. Fig. 5.1, Fig. 5.2, and Fig. 5.3 show the numerical simulation results when $V = 2.61V$. Fig 5.1 shows the asymmetric charge distribution along the thickness direction. Two inset figures show the details at the turning points of the curve. The negative charge density near the anode approaches the saturation value $C^- F$. The charge density distribution also shows that (5.1) will not hold in the region close to the boundaries. In other words, the linear PDE will not hold when a high voltage is applied.

Numerical solution offers us insight into the charge distribution, electrical field and electrical potential along the thickness direction for a given step voltage, but it does not provide us an overall picture of the induced charge versus applied voltage. Moreover, the numerical solution takes recursive steps to find proper initial conditions, and requires much computation which is not practical for control purposes. An analytical solution is practical in real-time implementation. It is also the starting point in the derivation of nonlinear capacitance of IPMC.

5.2.2 Analytical solution of the PDE at the steady state

Define $y \triangleq E$ and $p \triangleq E'$. Eq. (5.4) becomes

$$\frac{pdp}{(ap+b)} = ydy. \quad (5.7)$$

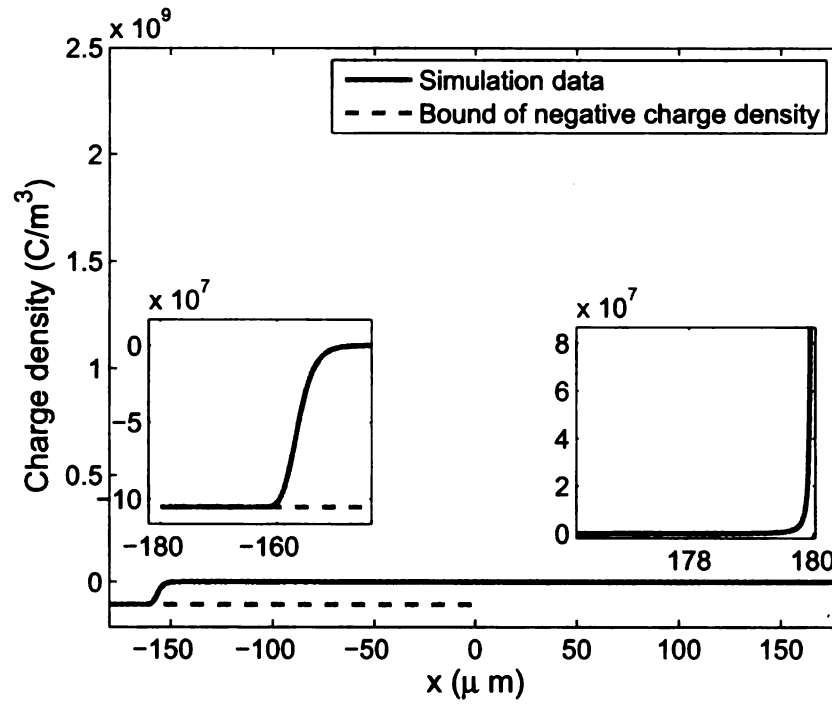


Figure 5.1: Numerical solution of the nonlinear ODE for $V = 2.61\text{V}$: Charge density.

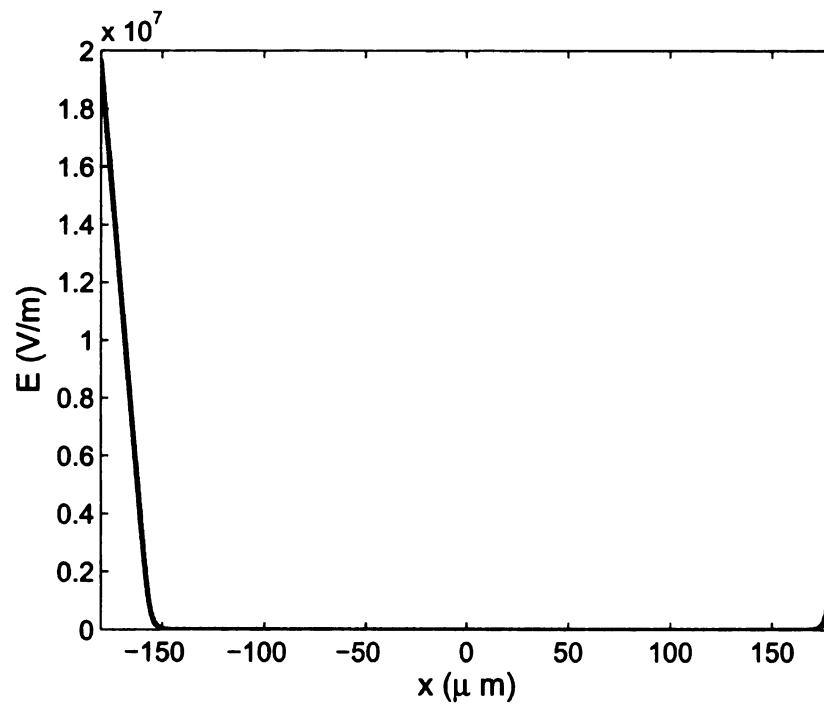


Figure 5.2: Numerical solution of the nonlinear ODE for $V = 2.61\text{V}$: Electrical field.

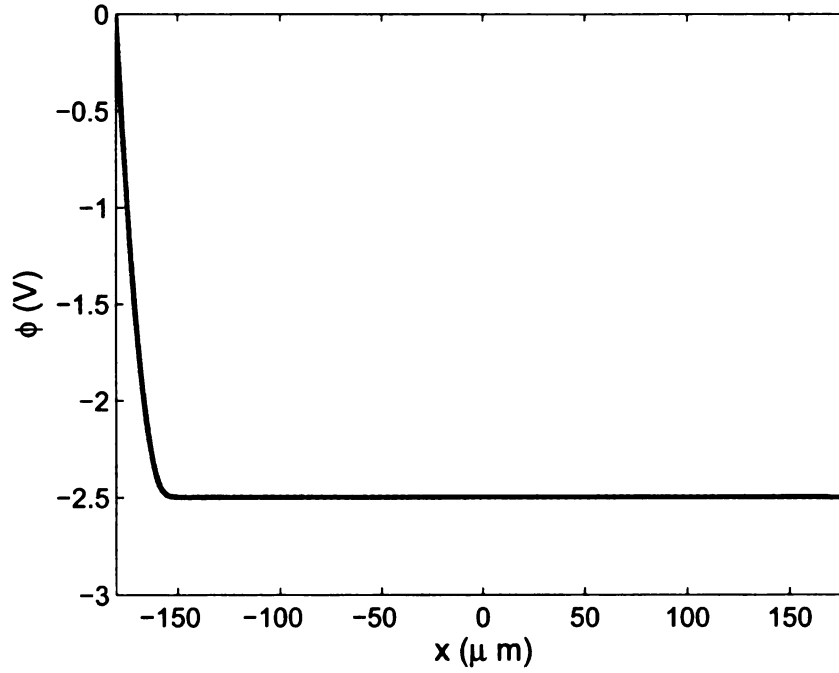


Figure 5.3: Numerical solution of the nonlinear ODE for $V = 2.61\text{ V}$: Electrical potential.

We integrate both sides of (5.7). On the left-hand side we integrate from $p(x_0)$ to p , while on the right-hand side, we integrate from $E(x_0)$ to y :

$$\frac{p}{a} - \frac{b}{a^2} \ln\left(\frac{a}{b}p + 1\right) = \frac{1}{2}y^2 - \frac{E(x_0)^2}{2}. \quad (5.8)$$

Let

$$y \triangleq g(p) = \sqrt{2\left(\frac{p}{a} - \frac{b}{a^2} \ln\left(\frac{a}{b}p + 1\right)\right) + E(x_0)^2}. \quad (5.9)$$

Since it is difficult to get an explicit function of $p = g^{-1}(y)$, one cannot continue to solve the ODE equation to get an explicit function $E(x)$. We will take a systems perspective to solve this problem. What we are really concerned about is how the total charge is analytically related to the input voltage, so it is not necessary to know the explicit function $E(x)$.

By integrating both sides of (5.3) from $x = -h$ to $x = h$, we get

$$\int_{-h}^h E''(x) dx - \int_{-h}^h aE'(x)E(x) dx - \int_{-h}^h bE(x) dx = 0. \quad (5.10)$$

With (5.6), Eq. (5.10) can be written as

$$E'(h) - E'(-h) - \frac{a}{2}(E^2(h) - E^2(-h)) - bV = 0. \quad (5.11)$$

From (5.5) and (5.11), one can get

$$V = \frac{1}{b}(E'(h) - E'(-h)). \quad (5.12)$$

The total charge Q can be obtained by integrating $\rho(x)$ from $x = x_0$ to $x = h$, where $\rho(x_0) = 0$:

$$\int_{x_0}^h \rho(x) S dx = Q = (E(h) - E(x_0)) S \kappa_e. \quad (5.13)$$

In Section 5.2.1, Fig. 5.2 shows that $E(x_0) \ll E(h)$ ($E(x_0) = 1.5 \times 10^{-23}$ V/m and $E(h) = 2 \times 10^7$ V/m). So (5.13) can be written as

$$E(h) = E(-h) = \frac{Q}{S \kappa_e}. \quad (5.14)$$

Note that $E'(h)$ and $E'(-h)$ are the positive root and negative root of (5.8), respectively, when $y = E(h)$.

Define

$$k \triangleq \frac{1}{2} \left(\frac{Q}{S \kappa_e} \right)^2. \quad (5.15)$$

Then (5.8) can be written as

$$\frac{p}{a} - k = \frac{b}{a^2} \ln \left(\frac{a}{b} p + 1 \right). \quad (5.16)$$

Proposition 1. *If $k > 0$, there exist two roots (p_1, p_2) for (5.16) such that $-\frac{b}{a} < p_1 < 0$ and $p_2 > 0$. Furthermore, if $k = 0$, then $p_1 = p_2 = 0$.*

See Appendix C.1 for the proof of Proposition 1.

In order to get the mapping function from V to Q , we need find out how k is related to the distance of two roots $|p_1 - p_2|$. As shown in Fig 5.4, the roots of (5.16) are the intersection points (p_1 and p_2) of the following two curves:

$$\begin{aligned}\eta &= \frac{b}{a^2} \ln \left(\frac{a}{b} p + 1 \right) = f(p), \\ \eta &= \frac{p}{a} - k = \lambda(p).\end{aligned}$$

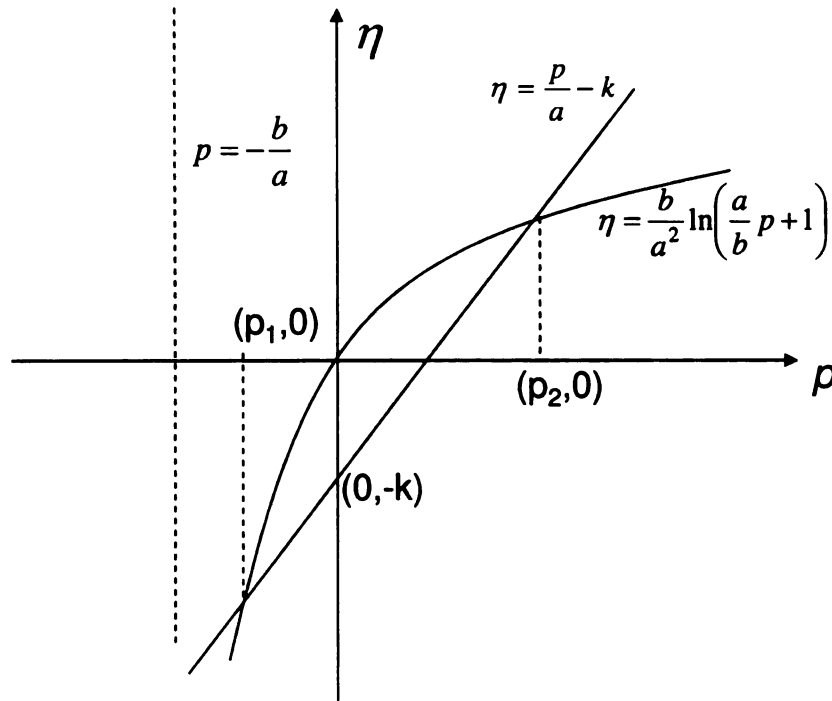


Figure 5.4: Illustration of solving for p_1 and p_2 .

From Fig. 5.4, the negative root p_1 will never hit the line $p = -\frac{b}{a}$ because $p = -\frac{b}{a}$ is the asymptote of the logarithmic function of $\eta = \ln(\frac{b}{a}p + 1)$. The physical explanation of

this is the following. Since the negative ions cannot move and the negative ion density are uniform in IPMC, $\frac{b}{a\kappa_e} = C^-F$ is the bound of the negative charge density. So $p > -\frac{b}{a}$ implies that the layer of depleted positive charges will not form, although the positive charge density can be very close to zero.

Finally, we can write k in terms of the voltage input V

$$k = \bar{\Gamma}(V) \triangleq \begin{cases} \Gamma(V), V > 0 \\ 0, V = 0 \end{cases} \quad (5.17)$$

where

$$\Gamma(V) \triangleq \frac{b}{a^2} \left(\frac{aV}{e^{aV} - 1} - \ln \left(\frac{aV}{e^{aV} - 1} \right) - 1 \right), \quad (5.18)$$

and Γ is continuous at $V = 0$. See Appendix C.2 for the derivation of (5.17). With (5.15) and (5.17), one can get the total charge Q as a function of V :

$$Q = S\kappa_e \sqrt{2\bar{\Gamma}(V)}. \quad (5.19)$$

Note that the nonlinear mapping function from input voltage is similar to the one reported in [73], which Porfiri obtained by solving the nonlinear PDE with matched asymptotic expansions.

When $V \rightarrow 0$, one can approximate $\bar{\Gamma}(V)$ using its Taylor series expansion around $V = 0$,

$$\bar{\Gamma}(V) \approx \frac{b|V|^2}{8}. \quad (5.20)$$

Then $Q \approx \frac{\sqrt{b}VS\kappa_e}{2}$, which is consistent with the charge generated in the linear case [64].

Fig. 5.5(a) shows the simulation results of charge versus voltage at the steady state. It includes the results based on the analytical solution of the nonlinear ODE, the numerical solution of the nonlinear ODE, and the numerical solution of the linear ODE (which ignores the nonlinear term), respectively. One can see that the analytical solution matches well the

numerical solution of the nonlinear ODE. When the voltage is small, one can ignore the nonlinear term in the nonlinear PDE. However, if a relatively large voltage ($> 0.2V$) is applied, the error between the nonlinear model and the linear one becomes significant. Fig. 5.5(b) shows the charge densities at the boundaries of IPMC based on the analytical solution. Note that these densities correspond to the solutions p_1 and p_2 of (5.16), which can be analytically obtained as shown in Appendix C.2. The figure shows that $\rho(-h)$ cannot go lower than $-C^-F$, but $\rho(h)$ can go arbitrarily high. The inset figure shows the zoom-in view around the turning corner where the negative charge density approaches saturation. It is consistent with the numerical simulation results in Fig. 5.1. The voltage corresponding to the turning corner is about 0.2 V. The above analytical analysis of PDE at the steady state will be helpful for deriving the nonlinear capacitance of IPMC, which will be discussed next.

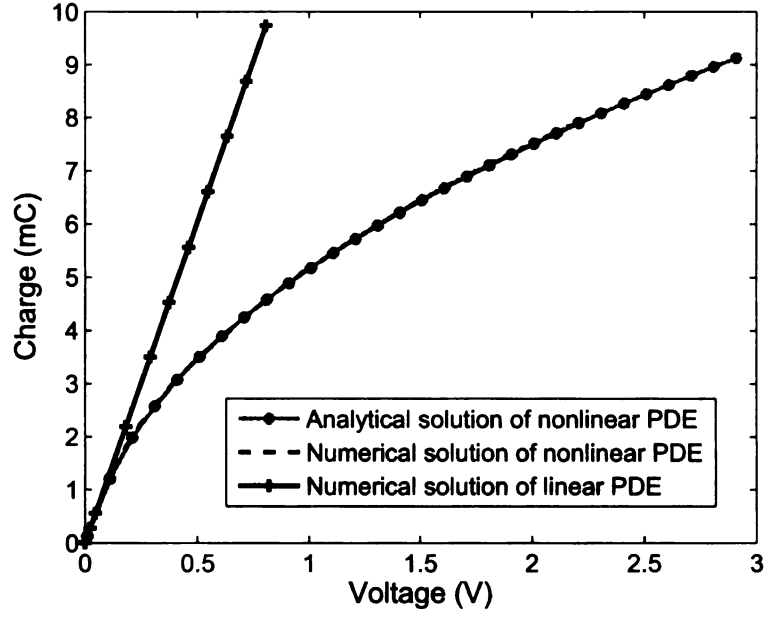
5.3 Nonlinear Circuit Model

The above analysis can only capture the nonlinear capacitance of IPMC. A dynamic model needs to capture the transient processes in IPMC as well. We propose a nonlinear circuit model, as shown in Fig. 5.6. It incorporates the nonlinear capacitance of IPMC C_1 , pseudocapacitance C_a due to the electrochemical adsorption process at the polymer-metal interface, ion diffusion resistance R_c , electrode resistance R_a , and nonlinear DC resistance of polymer R_{dc} .

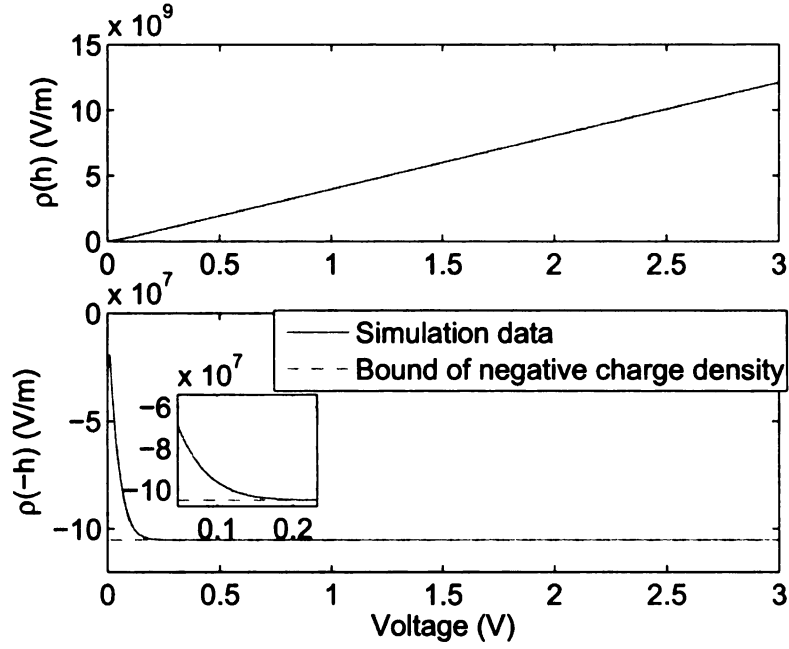
5.3.1 Nonlinear capacitance of IPMC

The nonlinear capacitance can be obtained by taking derivative of (5.19),

$$C_1(V) = \frac{dQ}{dV} = S\kappa_e \frac{\Gamma'(V)}{\sqrt{2\Gamma(V)}}, \quad (5.21)$$



(a)



(b)

Figure 5.5: (a) Charge versus voltage at the steady state; (b) charge density at the boundaries versus voltage input.

where $\Gamma'(V)$ is the first derivative of $\Gamma(V)$. From (5.18),

$$\Gamma'(V) = \frac{b}{a} \left(1 - \frac{e^{aV} - 1}{aV} \right) \frac{e^{aV} - 1 - aVe^{aV}}{(e^{aV} - 1)^2}. \quad (5.22)$$

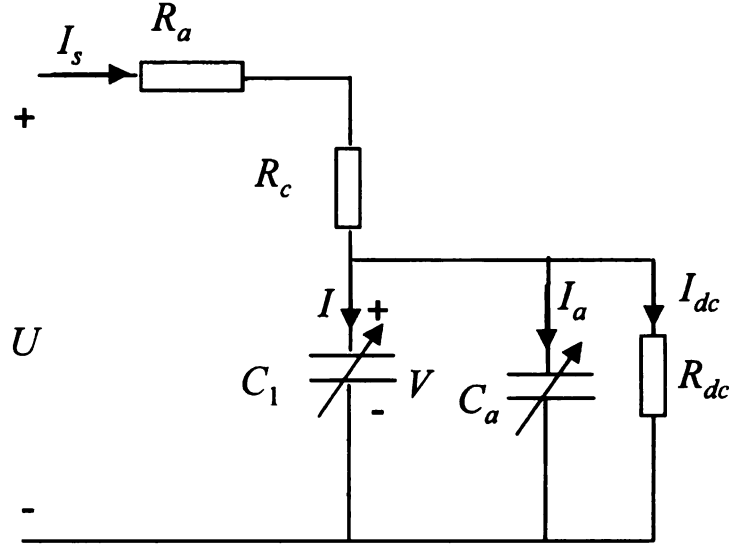
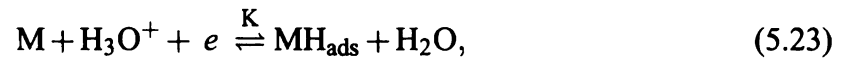


Figure 5.6: Circuit model of IPMC.

The proposed analytical solution of nonlinear capacitance captures the fundamental physics in the IPMC. It is represented by a function in terms of physical parameters and dimensions, and is geometrically scalable.

5.3.2 Pseudocapacitance due to adsorption

For an electrochemical surface process, e.g., the so-called underpotential deposition of H [25], the following holds:



where M is the substrate (usually a noble metal, Pt, Rh, Ru or Ir). Since IPMC has Pt as electrode and some electrolyte in the polymer, the underpotential deposition process should be incorporated into the model [3]. The adsorption current due to this electrochemical process can be represented by [25]:

$$I_a = C_a(V_a) \frac{dV_a}{dt}, \quad (5.24)$$

where

$$C_a(V_a) \triangleq \frac{q_1 SF}{RT} \frac{K_1 c^{H^+} e^{-\frac{V_a F}{RT}}}{\left(K_1 c^{H^+} + e^{-\frac{V_a F}{RT}} \right)^2}, \quad (5.25)$$

V_a is the voltage on the pseudocapacitance, q_1 is some constant (For H on polycrystalline Pt, $q_1 = 210 \mu\text{C}/\text{cm}^2$ [25]), $K_1 = \frac{k_1}{k_{-1}}$, k_1, k_{-1} are the chemical rate constants for forward and reverse directions of (5.23), and c^{H^+} is the concentration of H^+ .

5.3.3 Nonlinear DC resistance

The current response under a step voltage input will not vanish at the steady state [13] because of the DC resistance of polymer. One can approximate the DC current by a series of polynomial functions $Y(V)$. In this modeling work, we use a third-order polynomial function:

$$I_{dc} = Y(V) \triangleq \text{sign}(V)(Y_1|V| + Y_2|V|^2 + Y_3|V|^3). \quad (5.26)$$

Note that I_{dc} is supposed to be an odd function of V . That is why $\text{sign}(V)$ appears in (5.26).

5.3.4 Curvature output

The induced stress is proportional to the charge density [64]:

$$\sigma = \alpha_0 \rho, \quad (5.27)$$

where α_0 is the coupling constant. The moment generated by IPMC can be written by:

$$M = \int_{-h}^h \sigma x W dx = \int_{-h}^h W \alpha_0 x \rho(x) dx. \quad (5.28)$$

Since $\rho(x) = \kappa_e \frac{dE}{dx}$,

$$\begin{aligned} M &= \int_{-h}^h W \alpha_0 \kappa_e x dE \\ &= W \alpha_0 \kappa_e \left(xE \Big|_{-h}^h - \int_{-h}^h E dx \right). \end{aligned} \quad (5.29)$$

Since $E(-h) = E(h) = \frac{Q}{S\kappa_e}$, with (5.19) and $\int_{-h}^{+h} E dx = V$, (5.29) can be written as

$$M = W \alpha_0 \kappa_e \left(\text{sign}(V) 2h \sqrt{2\Gamma(|V|)} - V \right). \quad (5.30)$$

If one takes $V \rightarrow 0$,

$$M \rightarrow W \alpha_0 \kappa_e V \left(h\sqrt{b} - 1 \right) \approx W \alpha_0 \kappa_e V h\sqrt{b}, \quad (5.31)$$

which is consistent with the moment reported in the linear case [64]. One can then obtain the curvature output via

$$\kappa = \frac{M}{Y_e I}, \quad (5.32)$$

where $I = \frac{2}{3} W h^3$ is the moment inertia and Y_e is the equivalent Young's modulus of IPMC.

With (5.30), Eq. (5.32) can be written as

$$\kappa = \Psi(V) \triangleq \frac{3\alpha_0 \kappa_e \left(\text{sign}(V) 2h \sqrt{2\Gamma(|V|)} - V \right)}{2Y_e h^3}. \quad (5.33)$$

We note that one could also use nonlinear elasticity theory to model the mechanical output under large deformation [30]. This is outside of the scope of the current work.

5.3.5 Nonlinear control-oriented model

The objective of this work is to derive a control-oriented nonlinear model which can be used in controller design. Based on the circuit model (Fig. 5.6) and the curvature output (5.30), the model structure is shown in Fig. 5.7.

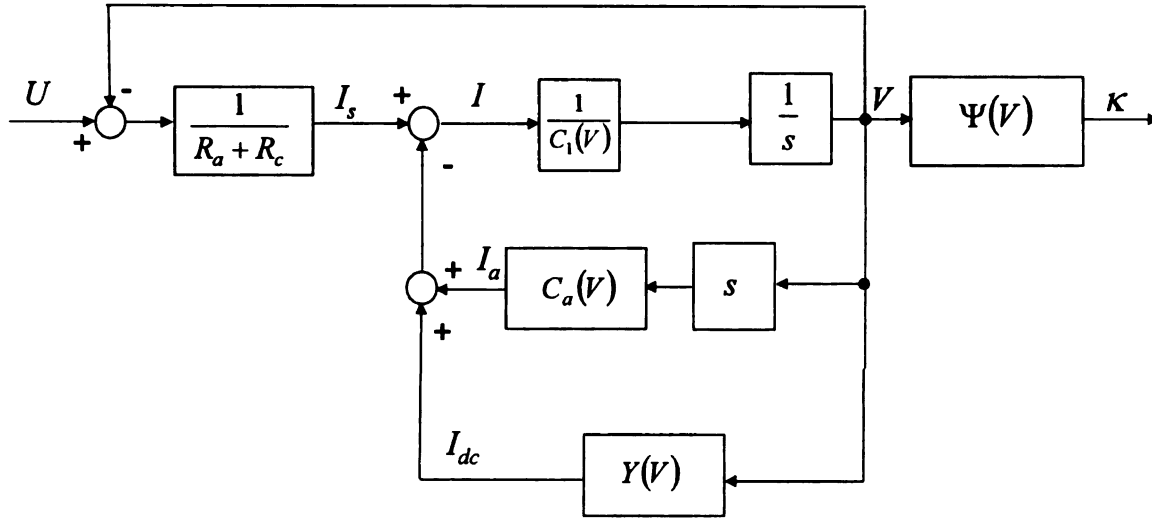


Figure 5.7: Model structure.

From (5.24) and (5.26), one can get

$$\frac{dV}{dt} = \frac{\frac{U - V}{R_a + R_c} - Y(V)}{C_1(V) + C_a(V)}. \quad (5.34)$$

Defining the state variable $x = V$, the control input $u = U$, and the system output $y = \kappa$, one can obtain a first-order nonlinear dynamic model in the state space:

$$\begin{aligned} \dot{x} &= -\frac{x + Y(x)(R_a + R_c) - u}{(C_1(x) + C_a(x))(R_a + R_c)}, \\ y &= \Psi(x). \end{aligned} \quad (5.35)$$

5.4 Experimental Verification

Some physical parameters can be directly measured through the experiments, such as the temperature T , the dimensions L , W , h , the equivalent Young's modulus of IPMC Y_e , and the electrodes resistance R_a . Some parameters are physical constants, such as R , F , q_1 . Other parameters ($Y_1, Y_2, Y_3, R_c, K_1, C^-, \kappa_e, \alpha_0$) can be identified by a model fitting process. To ignore the distributed resistance effect of the electrode on the impedance of IPMC, we clamped the IPMC sample with two aluminum electrodes which short circuit the electrode resistance R_a . To measure the current, we added another small resistance $R_i = 18 \Omega$ which is serially connected with IPMC. By measuring the voltage V_i , one can obtain $I_s = \frac{V_i}{R_i}$. Fig 5.8 illustrates the configuration of experimental setup. In the rest of this section, R_a is replaced by R_i .

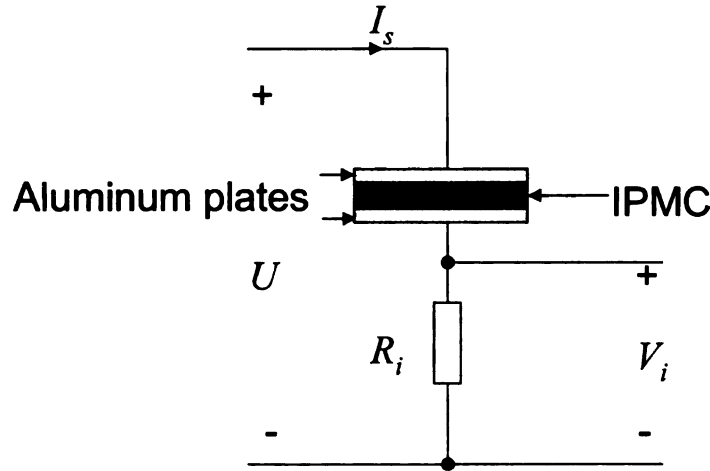


Figure 5.8: Illustration of experimental setup.

The current responses under a series of step voltage inputs are measured in order to identify those unmeasured parameters. Fig. 5.9 shows the initial current I_{s0} and the DC current $I_{s\infty}$ under step voltage inputs. The initial current I_{s0} is the current when the capacitors are uncharged ($V = 0$). The DC current $I_{s\infty}$ is the current when the capacitors have been fully charged. Since the polymer resistance R_{dc} is much larger than R_c , when $V = 0$,

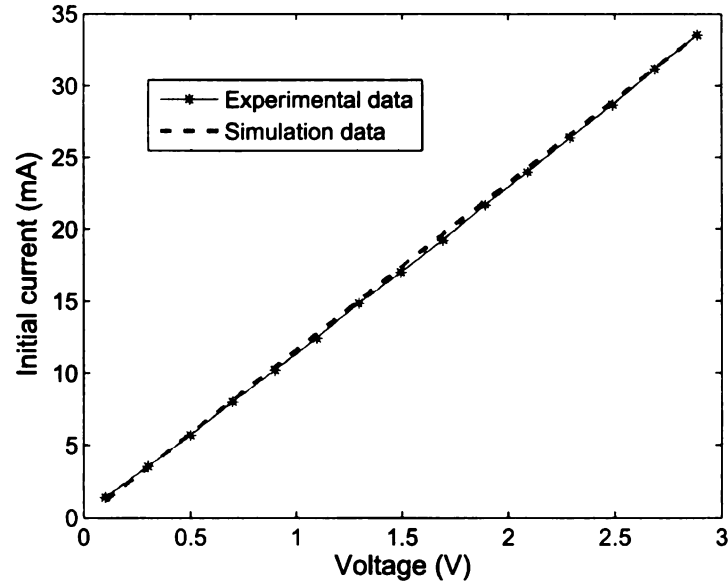
one can get (see Fig. 5.6)

$$I_{s0} \approx \frac{U}{R_i + R_c}. \quad (5.36)$$

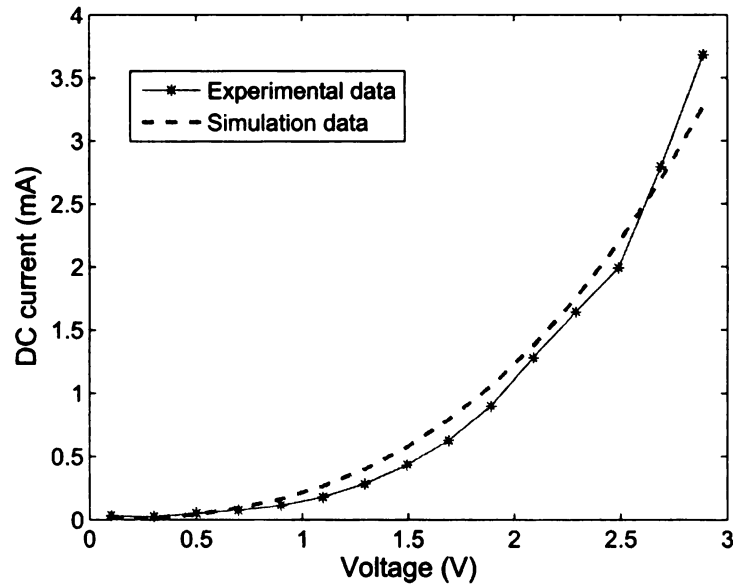
Fig. 5.9(a) shows that the initial current is a linear function of the step voltage. One can obtain the linear resistance $R_i + R_c$ by calculating the slope of I_{s0} versus U . Fig. 5.9(b) shows that the DC current can be approximated by a third-order polynomial function of V (5.26), thus the coefficients Y_1, Y_2, Y_3 can be identified. c^{H+}, K_1, κ_e can be tuned to fit the transient process. Fig. 5.10 shows the current responses under a step input of 1.0 V, suggesting that the proposed model can capture both the transient process and the steady state in current responses under a step voltage input. Identification of α_0 was reported in [21]. Table 5.1 shows all the parameters in the model. The model is further verified through an experiment to examine the current response under a sinusoid voltage input with frequency 0.01 Hz and amplitude 3 V. Fig. 5.11 shows that the model can predict the current response well.

Table 5.1: Parameters in the model.

F	R	T	R_i
96487 C/mol	8.3143 J/mol · K	300 K	18 Ω
R_c	L	W	h
48 Ω	22 mm	10 mm	100 μm
C^-	κ_e	c^{H+}	K_1
1091 mol/m ³	1.34×10^{-6} F/m	1×10^{-6} mol/m ³	4×10^5
α_0	Y_e	q_1	
0.129 J/C [21]	0.56 GPa [21]	210 μC/cm ² [25]	
Y_1	Y_2	Y_3	
1×10^{-5} A/V	1×10^{-4} A/V ²	1×10^{-4} A/V ³	



(a)



(b)

Figure 5.9: (a) Initial current versus step voltage input; (b) DC current versus step voltage input.

5.5 Chapter Summary

In this chapter, a nonlinear control-oriented model is proposed for IPMC actuation. It was derived based on the nonlinear dynamics-governing PDE. Numerical analysis of the

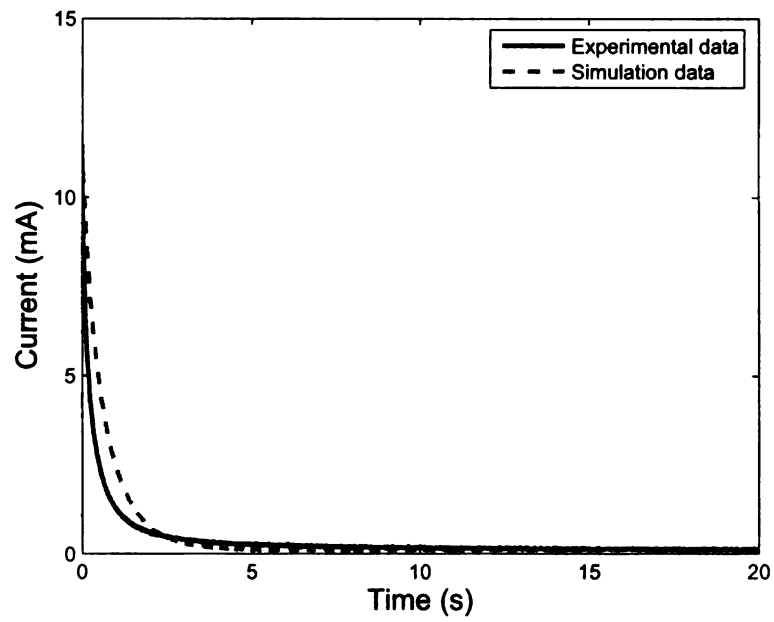


Figure 5.10: Current response under a step voltage input of 1.0 V.

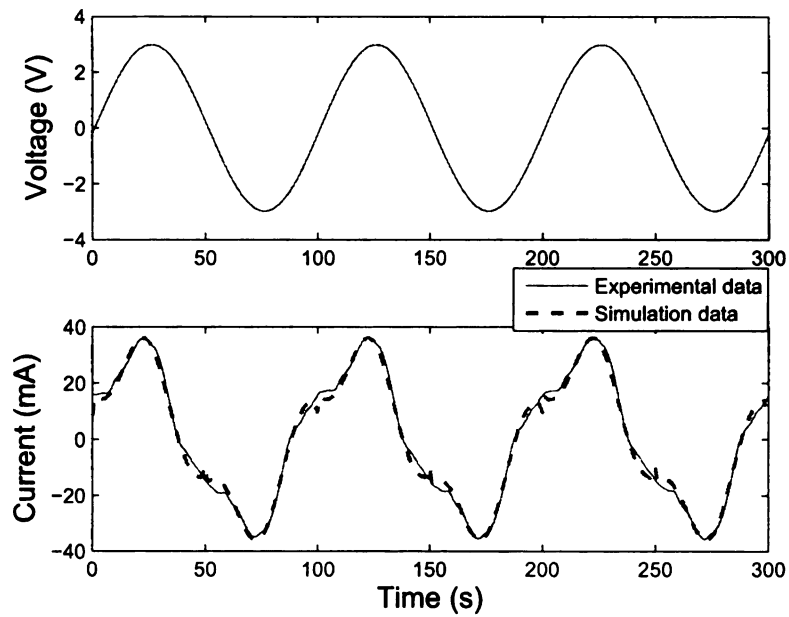


Figure 5.11: Current response under a sinusoid voltage input.

nonlinear PDE at the steady state shows an asymmetric charge distribution along the thickness. A systems perspective was taken in analytical analysis of nonlinear PDE to obtain a nonlinear mapping from the voltage to the induced charge, which represents the nonlinear capacitance of IPMC. A nonlinear circuit model is employed to capture the electrical dynamics of IPMC, including the nonlinear capacitance of IPMC, the ion diffusion resistance, the pseudocapacitance due to the electrochemical process at the polymer-metal interface, and nonlinear DC resistance of polymer. The curvature output is obtained from the circuit model. The proposed model is described in the state space, which will be the starting point of nonlinear control of IPMC. The proposed model is validated experimentally by the electrical responses of IPMC.

Chapter 6

Integrated Sensing For IPMC Actuators Using PVDF Thin Films

Compact sensing methods are desirable for ionic polymer-metal composite (IPMC) actuators in microrobotic and biomedical applications. In this chapter, a novel sensing scheme for IPMC actuators is proposed by integrating IPMC and PVDF (polyvinylidene fluoride) thin films. This chapter is organized as follows. Section 6.1 introduces the IPMC/PVDF with single mode sensing configuration and its biological application. Section 6.2 discusses an IPMC/PVDF structure with differential configurations and its validation in feedback control. Finally, concluding remarks are provided in Section 6.3.

6.1 IPMC/PVDF Single-Mode Sensory Actuator and Its Biological Application

6.1.1 Design of IPMC/PVDF single-model structure

To construct the IPMC/PVDF sensori-actuator, a PVDF film (30 μm thick, Measurement Specialties Inc.) is bonded to an IPMC (340 μm thick, Environmental Robotics Inc.) with

an insulating layer (Polyvinyl chloride PVC film, 30 μm thick) in between. The Fast-Cure Elastic Epoxy (Polysciences Inc., Warrington, PA) is used in bonding. The design of the IPMC/PVDF structure is illustrated in Fig. 6.1, where a picture of the IPMC/PVDF prototype is shown at the bottom.

An IPMC using water as solvent needs to be hydrated to work in air. For the IPMC/PVDF structure, it is not recommended to immerse the sample in water due to the presence of the PVDF. Instead, one can place a damp paper towel on top of the IPMC side of the structure and at the same time apply a uniform compressive stress. This will facilitate uniform hydration of the IPMC while preventing the delamination of the layers. The effect of the humidity level on PVDF sensing is not appreciable [60]. The hydrating procedure is not required if one adopts IPMC samples that use ionic fluids [11] or other non-water-based solvents.

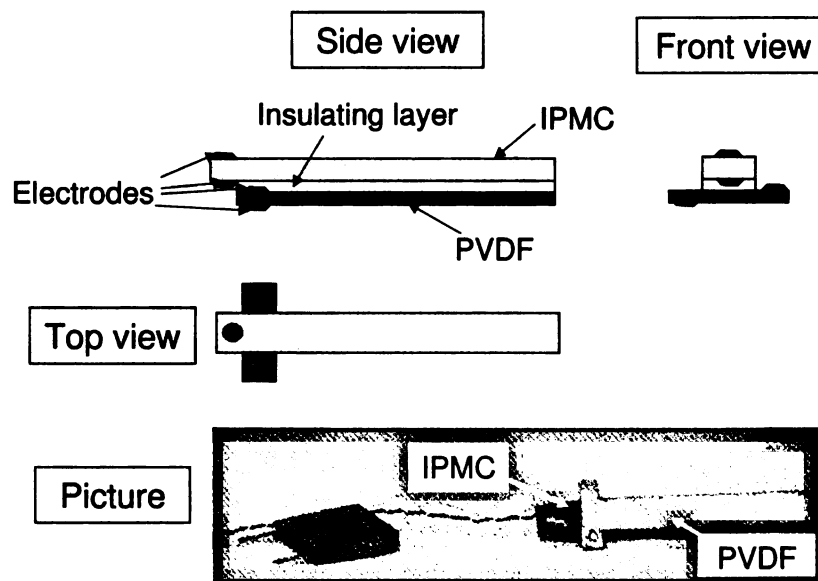


Figure 6.1: Design of the IPMC/PVDF composite structure.

When the IPMC/PVDF structure is bent due to IPMC actuation or external forces, charges are generated on the PVDF, which can be measured by a charge amplifier. Fig. 6.2 shows a differential charge amplifier which can minimize the common-mode noise. The

transfer function of the charge amplifier is described by:

$$\frac{V_o(s)}{Q(s)} = \frac{2R_1s}{1 + R_1C_1s} \frac{R_3}{R_2}, \quad (6.1)$$

which is a high-pass filter. As $R_1 \rightarrow \infty$, the transfer function $\frac{V_o(s)}{Q(s)} \rightarrow \frac{2R_3}{C_1R_2}$. However, in the circuit implementation, R_1 cannot be infinitely large because the bias current of the operational amplifier will saturate the signal output. To accommodate the actuation bandwidth of IPMC (typically below 10 Hz), the R_1 and C_1 values in the circuit are properly chosen so that the cutoff frequency of the charge amplifier is sufficiently low. By picking $R_1 = 5000 \text{ M}\Omega$ and $C_1 = 1350 \text{ pF}$, a cutoff frequency of 0.023 Hz is achieved.

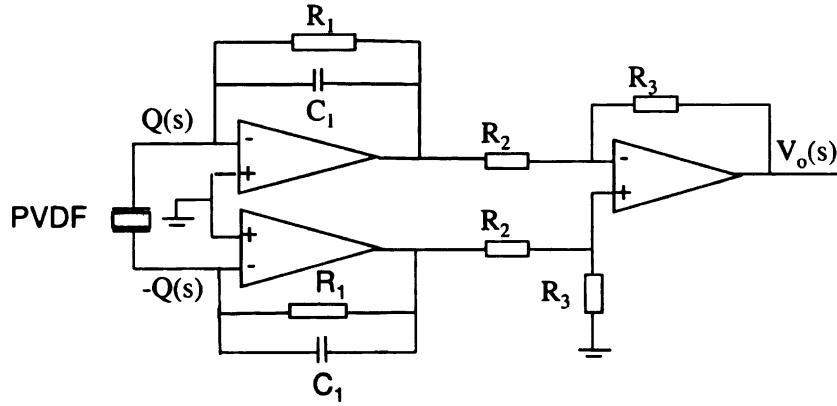


Figure 6.2: Design of the charge amplifier.

Basically, the charge $Q(s)$ generated by the PVDF is proportional to the bending displacement $Z(s)$ of the beam [82]:

$$Q(s) = GZ(s), \quad (6.2)$$

where the constant G depends on the transverse piezoelectric coefficient d_{31} , the geometry of the composite beam, and the Young's moduli of individual layers. By combining (6.1) and (6.2), one can obtain the transfer function from $Z(s)$ to $V_o(s)$. A laser displacement sensor (OADM 20I6441/S14F, Baumer Electric) is used for both calibration of the PVDF

sensor and validation of the sensing approach. In order to test the charge amplifier circuit, the IPMC/PVDF beam with one end fixed is tapped and then the laser sensor is used to detect the damped vibration of the beam. The measured vibration frequency is 42 Hz, which is much higher than the cutoff frequency of the charge amplifier. Fig. 6.3(a) shows the charge output of PVDF corresponding to the damped vibration, and Fig. 6.3(b) demonstrates that the charge signal is almost linear with respect to the bending displacement. These experimental results have validated the performance of the charge amplifier circuit.

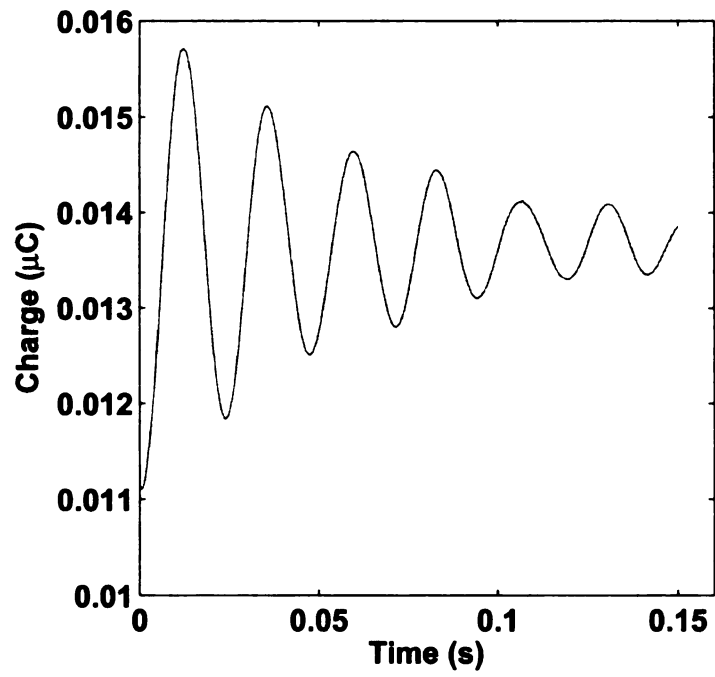
6.1.2 Impact of the stiffening effect and design of the insulator thickness

The additional PVDF and insulating layers make the composite beam stiffer than the IPMC layer itself. It is of interest to understand the impact of this stiffening effect on the bending performance since this will be useful for the optimal IPMC/PVDF structure design. The investigation is conducted by combining analytical modeling, finite element computation, and experiments. Design optimization here is concentrated on the thickness of the insulating layer, but the approach can be used for the design of other parameters, such as the type of material for the insulating layer and the dimensions for IPMC and PVDF.

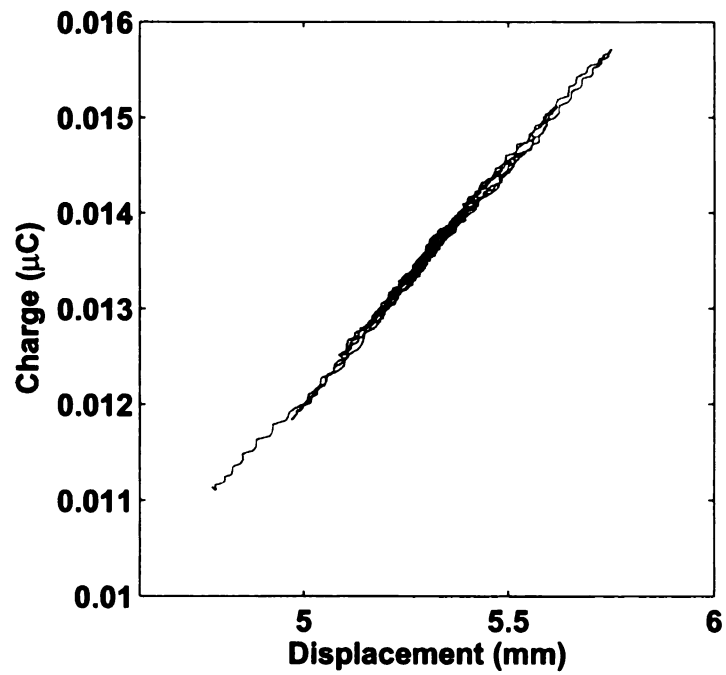
Fig. 6.4 illustrates the schematic of the IPMC/PVDF structure and the used notation in the following discussion. The beam stiffness can be characterized by its spring constant

$$K = \frac{F}{z_{max}}, \quad (6.3)$$

where F is a quasi-static transverse force applied at the free end of the cantilever beam and z_{max} is the corresponding displacement at the acting point. The spring constant can be calculated analytically using composite beam theory [37]. In Fig. 6.4, the position of the



(a)



(b)

Figure 6.3: (a) Charge output of the PVDF corresponding to the damped vibration; (b) charge output versus the bending displacement.

mechanical neutral axis of the composite beam is given by:

$$h_0 = \frac{\sum_{i=1}^3 E_i H_i C_i}{\sum_{i=1}^3 E_i H_i}. \quad (6.4)$$

Here E_1 , E_2 and E_3 are the Young's moduli of IPMC, insulating layer, and PVDF, respectively. H_1 , H_2 and H_3 are the thicknesses of those layers. C_1 , C_2 and C_3 are the positions of the central axes of the layers, which can be calculated as:

$$C_1 = H_1/2, C_2 = H_1 + H_2/2, C_3 = H_1 + H_2 + H_3/2. \quad (6.5)$$

The distance between the central axis and the neutral axis can be written as:

$$d_i = |C_i - h_0|, \quad \text{for } i = 1, 2, 3. \quad (6.6)$$

The moment of inertia of each layer is:

$$I_i = \frac{1}{12} W H_i^3 + W H_i d_i^2, \quad \text{for } i = 1, 2, 3. \quad (6.7)$$

From the moment balance equation [37],

$$M = \frac{\sum_{i=1}^3 E_i I_i}{\rho(x)} = F(L - x), \quad (6.8)$$

where $\rho(x)$ is the radius of curvature. For small bending, the radius of curvature can be given by:

$$\frac{1}{\rho(x)} = \frac{d^2 z}{dx^2}, \quad (6.9)$$

where $z(x)$ denotes the deflection of the beam along the length x . With the boundary con-

dition $z(0) = 0$ and $\dot{z}(0) = 0$, one gets

$$z(x) = \frac{F}{\sum_{i=1}^3 E_i I_i} \left(\frac{Lx^2}{2} - \frac{x^3}{6} \right). \quad (6.10)$$

Evaluating z at $x = L$ yields the expression of spring constant

$$K = \frac{F}{z_{\max}} = \left(\frac{3 \sum_{i=1}^3 E_i I_i}{L^3} \right). \quad (6.11)$$

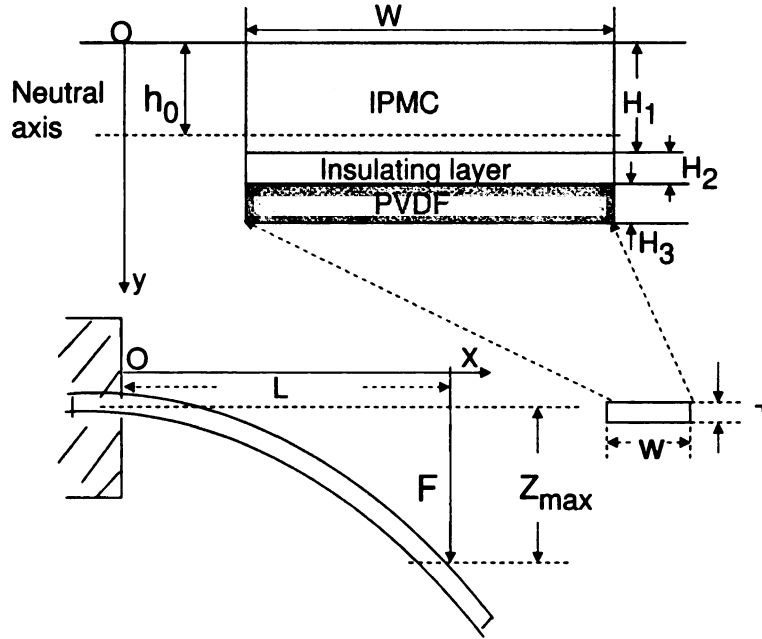


Figure 6.4: Bending of IPMC/PVDF composite beam.

Experiments are conducted to measure and compare the spring constants of the IPMC and IPMC/PVDF beams. The IPMC or IPMC/PVDF beam is clamped at one end and is pushed by the tip of a calibrated micro-force sensor which is mounted on a linear actuator. The sensitivity of the micro-force sensor is $9.09 \text{ mV}/\mu\text{N} \pm 6.5\%$ and its spring constant is 0.264 N/m . A laser displacement sensor measures the bending displacement of the beam z_{\max} under the pushing force F . A 20X microscope (FS60, Mitutoyo) is used to monitor the experiments. Fig. 6.5(a) illustrates the diagram of the experimental setup, while

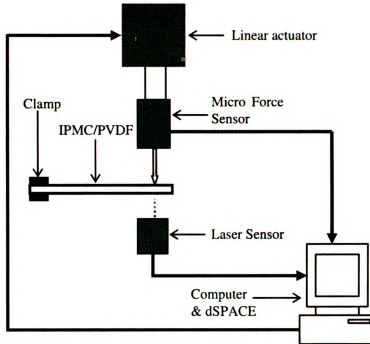
Fig. 6.5(b) shows the actual picture. Measurements are conducted for an IPMC beam and two IPMC/PVDF beams which have insulating layers in different thickness (IPMC/PVDF1 and IPMC/PVDF2). Detailed beam dimensions can be found in Table 6.1. Fig. 6.6 shows the measured displacement versus force data and the linear approximations, from which the spring constants can be calculated. From the experimental data, the Young's moduli of individual layers can be identified using (6.11): $E_1 = 0.571$ GPa, $E_2 = 0.73$ GPa, $E_3 = 1.96$ GPa. These values are within the ranges reported in the literature [83, 77].

Table 6.1: Dimension and spring constant of different beams.

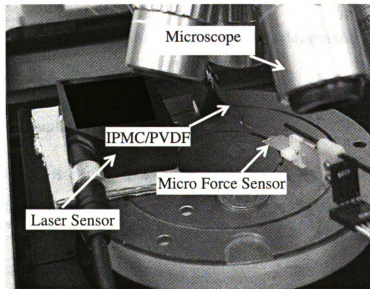
Beams	IPMC	IPMC/PVDF1	IPMC/PVDF2
W (mm)	7.3	8.2	7.6
L (mm)	37.2	36.0	33.0
H_1 (μm)	355	340	350.0
H_2 (μm)		30.0	100.0
H_3 (μm)		30.0	30.0
K_{mea} (N/m)	0.906	2.283	4.676
K_{FEA} (N/m)	0.908	2.286	4.647

To validate the linear analysis above, more accurate finite-element computation is conducted using CoventorWare, where the identified parameters are used together with the given geometric dimensions. The spring constants are calculated based on the free-end deflection of beams when they are subjected to an external force $F = 20 \mu\text{N}$ at the tip. Table 6.1 lists the spring constants obtained through experimental measurement (K_{mea}) and finite element analysis (K_{FEA}), for the different beams. The close agreement between K_{mea} and K_{FEA} validates the model and analysis.

As shown in Table 6.1, the thicker the insulator, the stiffer the IPMC/PVDF structure. In order to optimize the bending performance of the IPMC/PVDF structure, one should select the elastic insulating layer as soft and thin as possible. However, thinner insulating layer may result in stronger electrical feedthrough coupling. In our design, the thickness of the insulating layer is chosen to be $30 \mu\text{m}$ to achieve tradeoff between the two considerations.



(a)



(b)

Figure 6.5: (a) Experimental setup for spring constant measurement; (b) picture of the experimental setup.

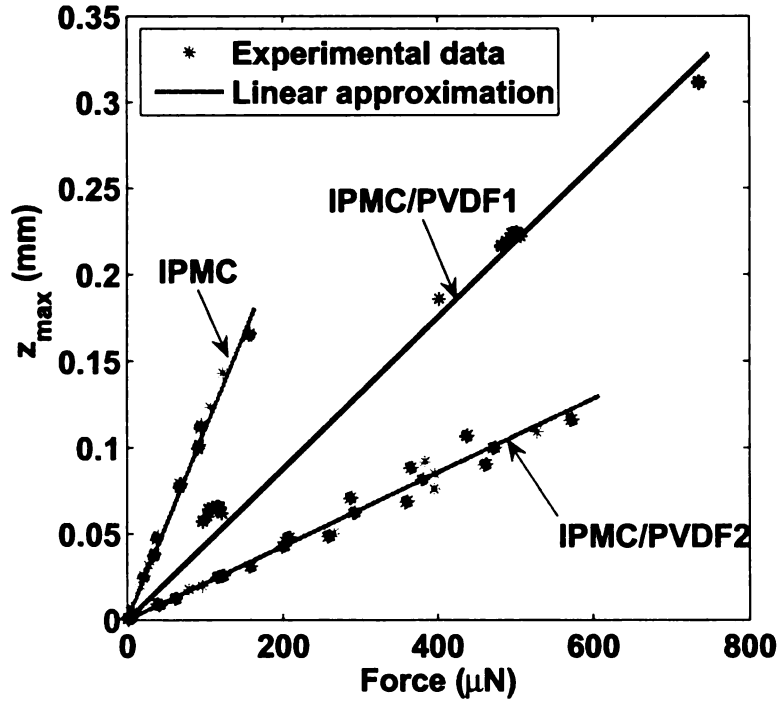


Figure 6.6: Spring constant of IPMC/PVDF beams.

6.1.3 Electrical feedthrough coupling and model-based real-time compensation

The feedthrough coupling effect

Since the PVDF film is closely bonded to the IPMC with a very thin insulating PVC film, the coupling capacitance between the IPMC and the PVDF results in the electrical feedthrough effect during simultaneous actuation and sensing. When the actuation signal is applied to the IPMC, the actuation voltage generates coupling current going through the insulating layer and then induces coupling charge on the PVDF. As a result, the charge amplifier gathers both the sensing and coupling charges from the PVDF. The presence of feedthrough coupling is illustrated by applying a 0.4 Hz square-wave actuation input (peak-to-peak 1.4 V). In the experiment, the humidity is 34% and the temperature is 23 °C. Fig. 6.7(a) shows the bending displacement detected by the laser sensor, while Fig. 6.7(b)

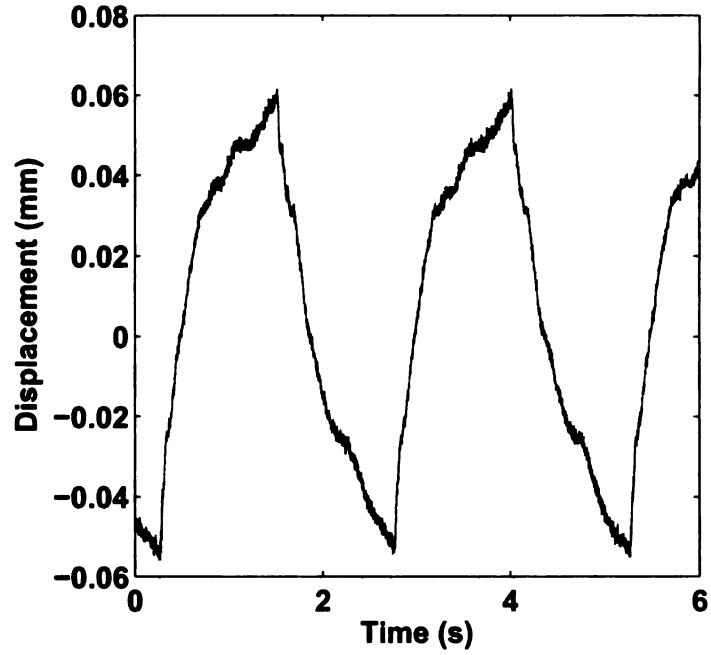
shows the output from the charge amplifier. The spikes in the PVDF sensor output arise from the capacitive coupling between the IPMC and PVDF layers when the actuation voltage jumps.

Modeling of the coupling effect

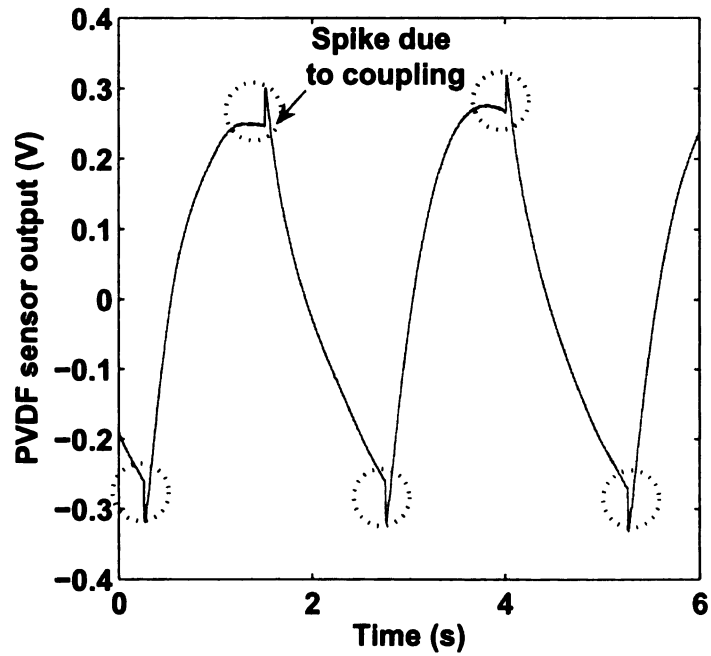
A complete circuit model of the IPMC/PVDF structure is developed to understand and capture the feedthrough coupling dynamics. As shown in Fig. 6.8, the model includes the equivalent circuits for individual layers and their natural couplings. Due to the nonnegligible resistances resulted from the porous surface electrodes of the IPMC, the voltage potential is not uniform along the IPMC length. A distributed transmission-line type model is thus proposed. The overall circuit model is broken into discrete elements along its length for parameter identification and simulation purposes. In this work, the circuit model is chosen to have four sections of identical elements. The surface resistance of IPMC is represented by R_{s1} , while other key electrodynamic processes (e.g., ionic transport, polymer polarization, and internal resistances) are reflected in the shunt element consisting of resistor R_{c1} and capacitor C_{p1} . The polymer resistance is described by R_{p1} . In the circuit model of the insulating layer, R_{p2} , C_{p2} , R_{c2} are resistances and capacitances between the IPMC and PVDF. In the circuit model of the PVDF, R_{s3} is the surface resistance of PVDF and R_{p3} , C_{p3} represent the resistance and capacitance between the electrodes of the PVDF.

In order to identify the circuit parameters, the impedances are measured at multiple frequencies. The impedances of each layer are nonlinear functions of the resistances and capacitances involved. The parameters are identified using the Matlab command *nlinear fit*, which estimates the coefficients of a nonlinear function using least squares. Table 6.2 lists the identified parameters.

The proposed circuit model will be validated by comparing its prediction of the feedthrough coupling signal with experimental measurement. We first explain a simple method for measuring the coupling signal. We observe that, due to the low surface resistance of PVDF (see



(a)



(b)

Figure 6.7: (a) Bending displacement detected by the laser sensor; (b) sensing output from the PVDF, showing the spikes from electrical feedthrough.

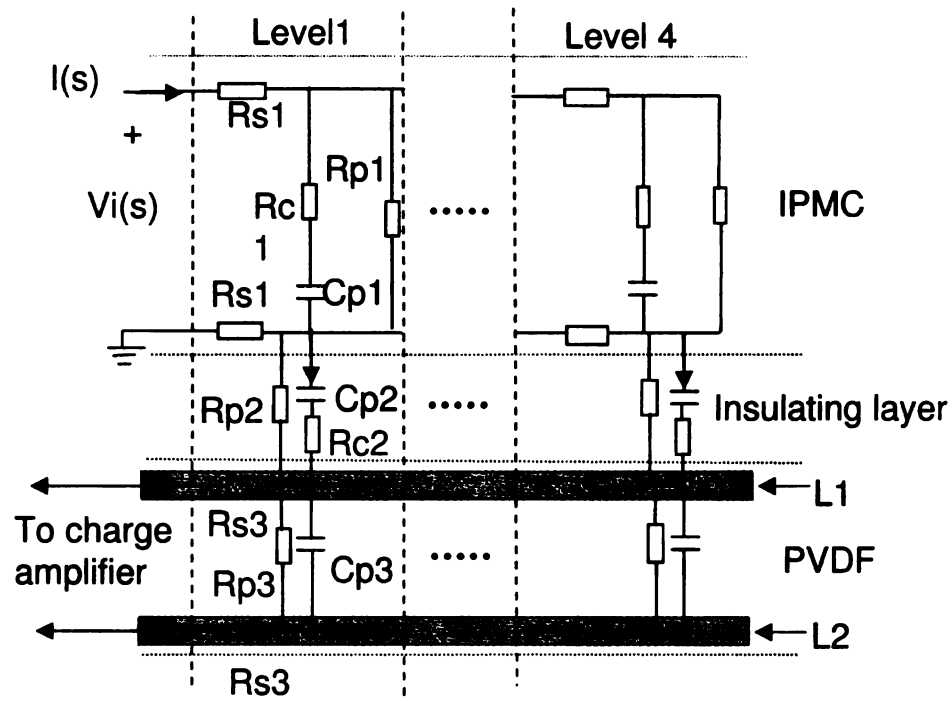


Figure 6.8: Circuit model of the IPMC/PVDF structure.

Table 6.2: Identified parameters in the circuit model.

IPMC layer		Insulating Layer		PVDF layer	
R_{s1}	17 Ω	R_{p2}	500 M Ω	R_{s3}	0.1 Ω
R_{c1}	30 Ω	C_{p2}	42 pF	R_{p3}	600 M Ω
C_{p1}	3 mF	R_{c2}	4.5 M Ω	C_{p3}	290 pF
R_{p1}	25 K Ω				

Table 6.2), the electrode layer L_1 in Fig. 6.8 shields the coupling current from reaching the electrode layer L_2 . This means that the feedthrough coupling signal does not exist in V_{p-} , which is related to the charge from the layer L_2 . This statement is supported by the measurement, shown in Fig. 6.9(a), where spikes only appear in V_{p+} . Since only V_{p+} has the coupling component while the sensing components in V_{p-} and V_{p+} have a phase shift of 180° , the coupling signal is obtained as:

$$V_c = V_{p+} + V_{p-}. \quad (6.12)$$

Fig. 6.9(b) shows the extracted coupling signal.

Fig. 6.10 compares the Pspice simulation results based on the circuit model with experimental results when a 1 Hz square-wave actuation voltage is applied. Good agreement is achieved for both the actuation current in IPMC (Fig. 6.10(a)) and the coupling voltage V_c (Fig. 6.10(b)).

The transfer function from the actuation voltage to the coupling voltage can be derived from the circuit model. Since there are 14 capacitors in the circuit model, the transfer function will be 14th-order, which is not easy to implement in real time. After an order-reduction process, the transfer function of the coupling dynamics can be approximated by a 5th-order system:

$$T_c = \frac{-(509s^4 + 72s^3 + 1.5 \times 10^4 s^2 + 2203s)}{s^5 + 9525s^4 + 1.5 \times 10^4 s^3 + 2.9 \times 10^5 s^2 + 4.5 \times 10^5 s + 6 \times 10^4}. \quad (6.13)$$

To further verify the coupling model, a sequence of sinusoidal voltage signals with frequency ranging from 0.01 Hz to 20 Hz are applied to the IPMC. Actuation voltages are measured and coupling signals are effectively extracted from V_{p+} and V_{p-} for the purpose of obtaining the empirical Bode plots of coupling dynamics. Fig. 6.11 shows that the Bode plots of the derived transfer function (6.13) match up well with the measured Bode plots.

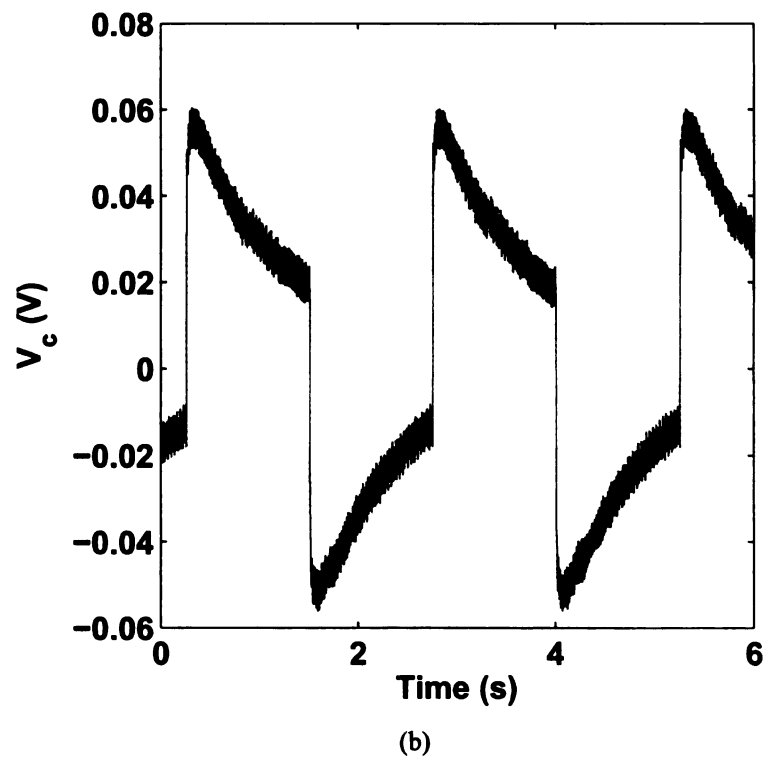
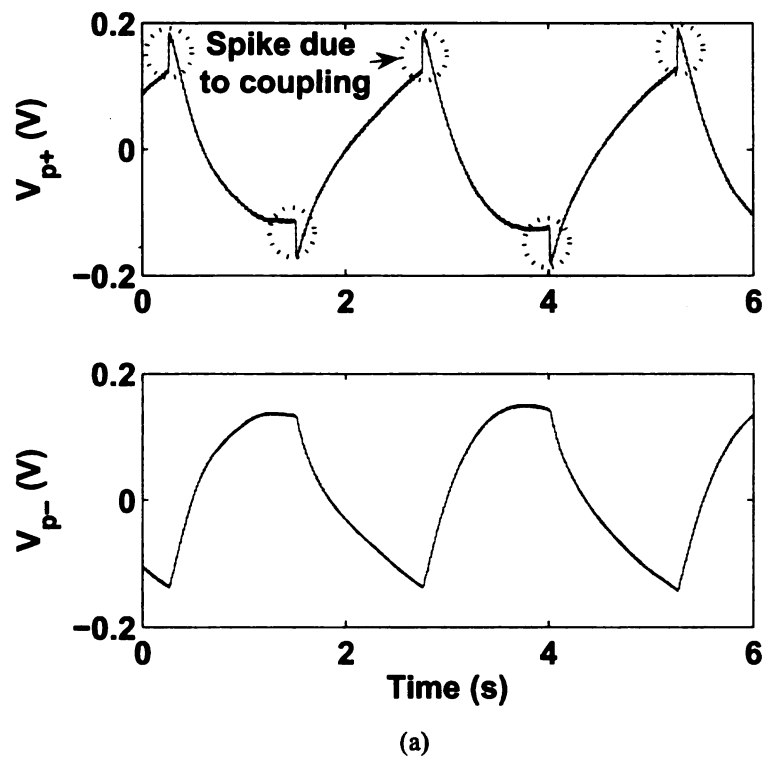
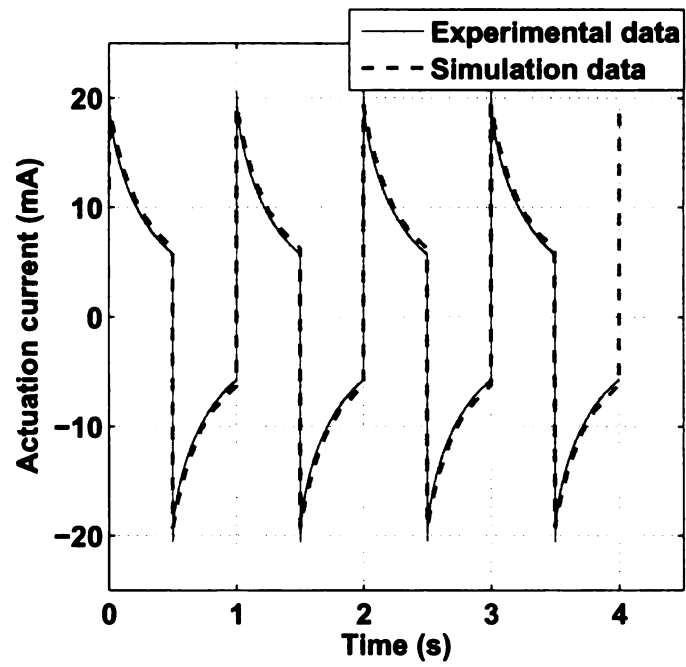
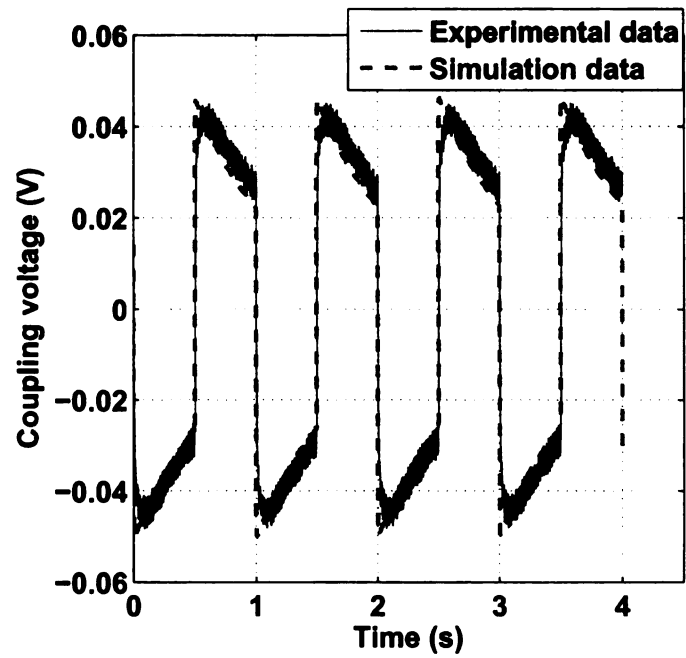


Figure 6.9: (a) V_{p+} , V_{p-} sensing signals; (b) extracted coupling signal V_c .



(a)



(b)

Figure 6.10: Comparison of model prediction and experimental measurement. (a) Actuation current; (b) coupling signal.

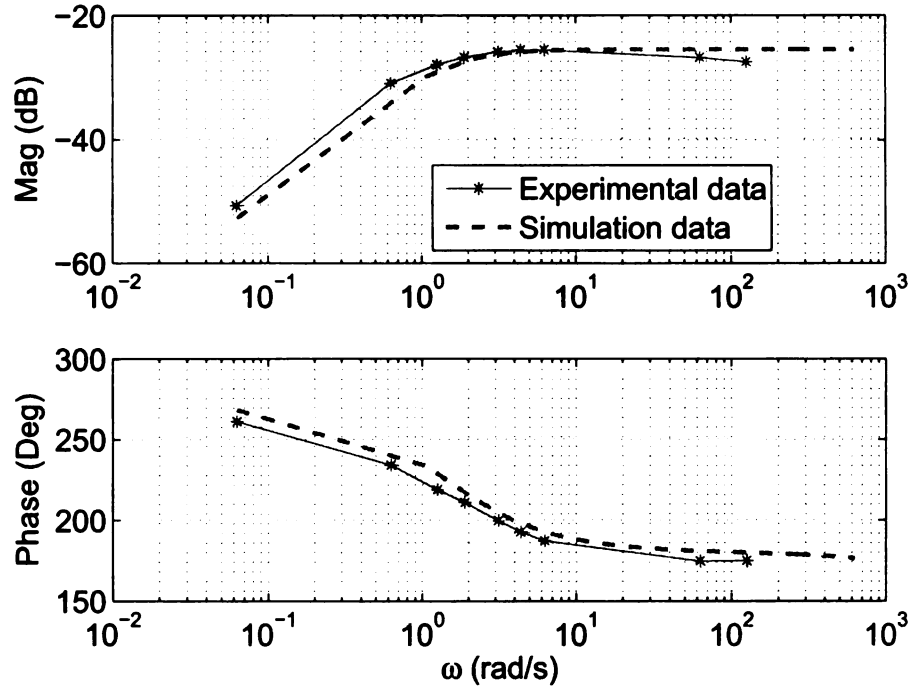


Figure 6.11: Verification of the coupling dynamics.

Real-time compensation in simultaneous actuation and sensing

There are several possible schemes to get rid of the coupling signal. Inserting another conductive layer between the IPMC and PVDF to shield the feedthrough coupling is one potential solution, but at the cost of increased stiffness and fabrication complexity. Another solution is to just use V_{p-} as the sensing signal, but this single-mode sensing scheme is sensitive to the common-mode noise in practice. Since the coupling dynamics has high-pass characteristics, one might also try to eliminate the coupling component with low-pass filtering. However, the relatively low cut-off frequency of the coupling dynamics, comparing to the actuation bandwidth (See Fig. 6.12), makes this approach infeasible.

In this research, a model-based real-time compensation scheme is proposed to remove the feedthrough coupling component. The coupling charge is calculated from the coupling circuit model (6.13). By subtracting it from the measured charge of the PVDF, the sensing charge can be extracted. Fig. 6.13 illustrates the compensation scheme. Fig. 6.14 compares the displacement measurement obtained from the PVDF sensor with that from the laser

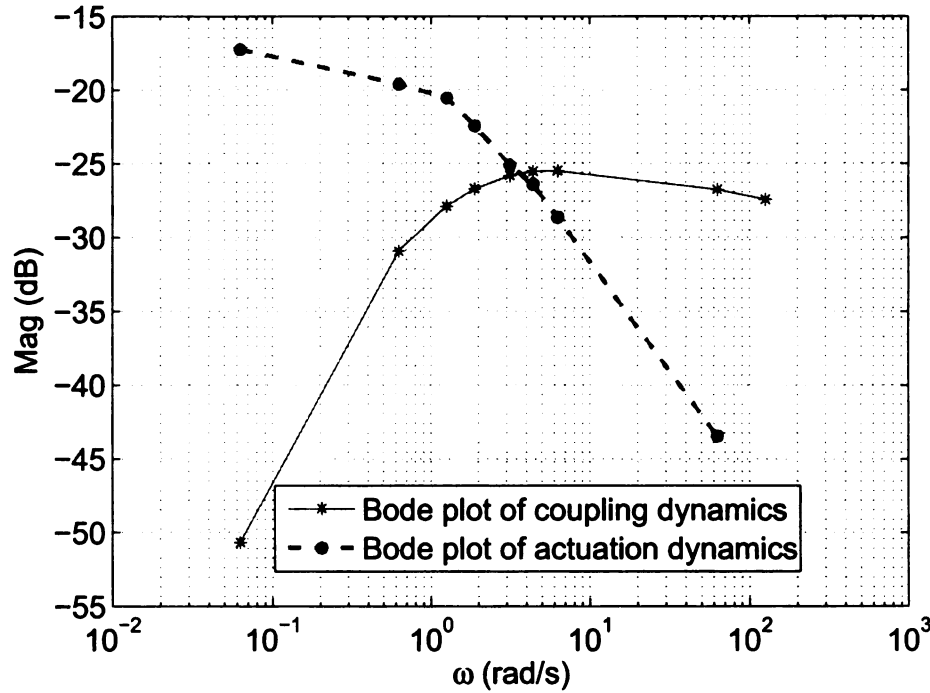


Figure 6.12: Bode plots of coupling dynamics and actuation dynamics.

sensor when a 0.4 Hz square-wave actuation input is applied. It is seen that the spike related to the electrical coupling is removed by the compensation scheme. Although there is about 12% error shown in Fig. 6.14, the amplitudes and the phases agree well. Investigation is under way to further improve the measurement accuracy of the PVDF sensor.

6.1.4 Application to micro-injection of living drosophila embryos

The developed IPMC/PVDF sensori-actuator is applied to the micro-injection of living *Drosophila* embryos. Such operations are important in embryonic research for genetic modification. Currently this process is implemented manually, which is time-consuming and has low success rate due to the lack of accurate control on the injection force, the position, and the trajectory. The IPMC/PVDF structure is envisioned to provide accurate force and position control in the micro-injection of living embryos, and thus to automate this process with a high yield rate. In this research, an open-loop injection experiment with

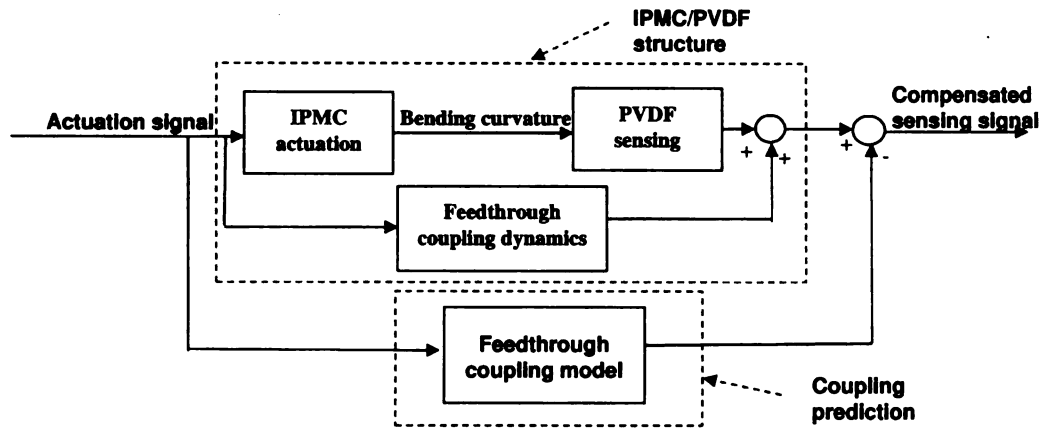


Figure 6.13: Diagram of the real-time compensation.

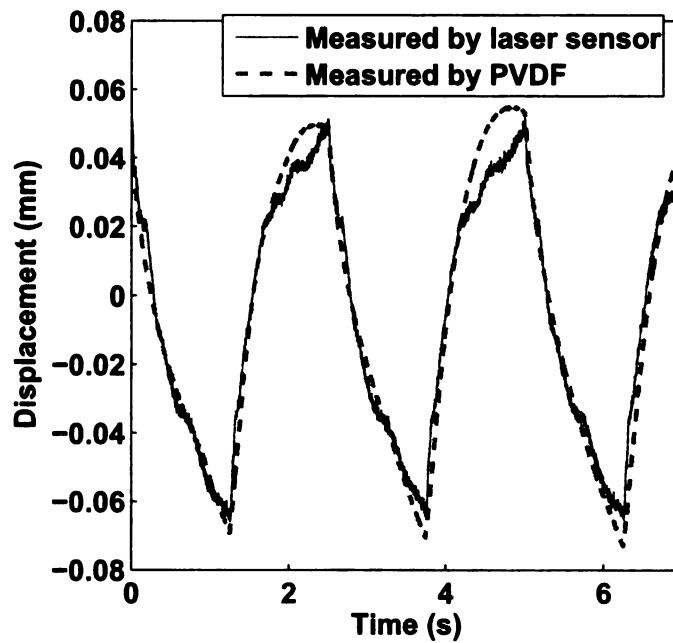


Figure 6.14: Comparison of displacement measurements by laser sensor and PVDF sensor.

the IPMC/PVDF sensori-actuator is conducted, and the process of the injection behavior is captured by the PVDF sensor.

The developed IPMC/PVDF micro-force injector is illustrated in Fig. 6.15. A micropipette with an ultra-sharp tip ($1.685\ \mu\text{m}$ in diameter and 2.65° in angle), is mounted at the end point of a rigid tip attached to the IPMC/PVDF structure. The *Drosophila*

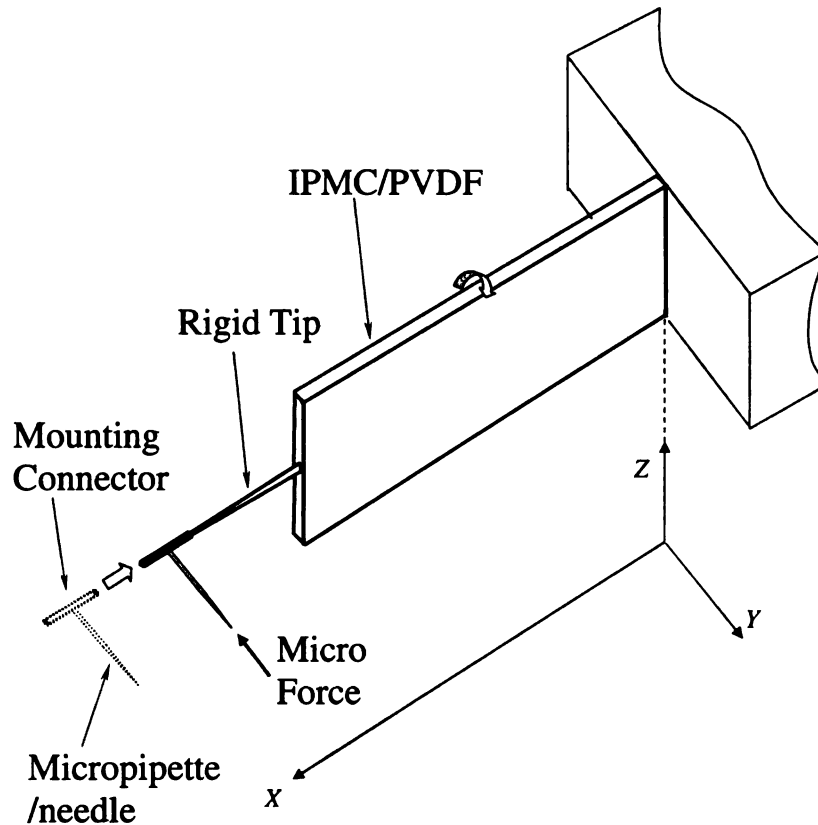


Figure 6.15: Illustration of the IPMC/PVDF micro-force injector.

embryos are prepared as described in [81]. The dimensions of the embryos are variable with an average length of $500\ \mu\text{m}$ and a diameter of about $180\ \mu\text{m}$. Fig. 6.16(a) shows the diagram of the experimental setup for embryo injection, while Fig. 6.16(b) shows the photo. A 3-D precision probe station (CAP-945, Signatone), which is controlled by a 3-D joystick, moves the needle close to an embryo and then a ramp voltage, which starts from 0 V and saturates at 2 V, is applied to the IPMC. The IPMC drives the beam with the needle to approach the embryo. After the needle gets in contact with the membrane of the embryo,

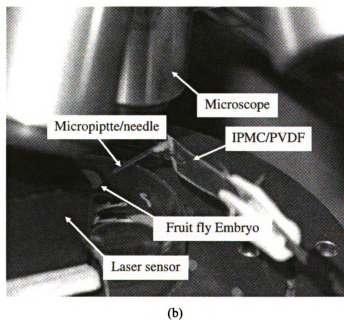
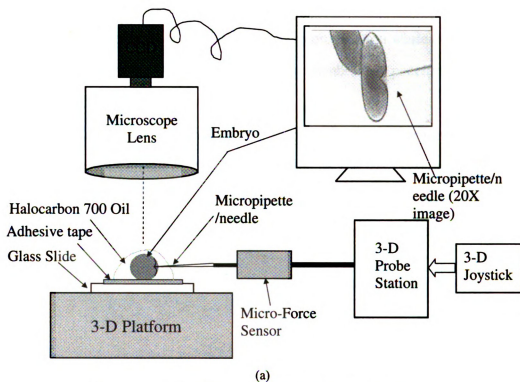
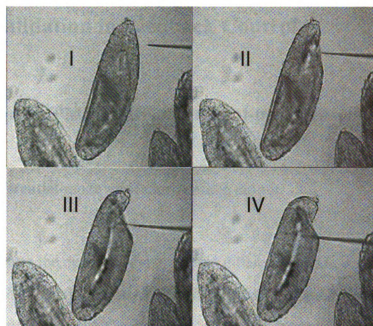


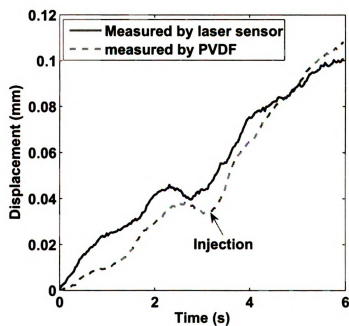
Figure 6.16: (a) Diagram of experimental setup for embryo injection; (b) picture of experimental setup.

the latter will be deformed but not penetrated due to its elasticity. At this stage, the needle is still moving until the reaction force between the needle and embryo reaches the penetration force. The needle stops at the penetration moment for a while (about 0.2 ms) due to temporary force balance. After that, the embryo membrane is penetrated and the needle moves freely into the embryo.

Fig. 6.17(a) shows the snapshots of the successful injection progress. Fig. 6.17(b) shows both the displacement of the needle detected by the laser sensor and by the compensated PVDF sensing signal. It is concluded that the predicted displacement reflects the movement of the needle, and the process of injection can be monitored by the PVDF.



(a)



(b)

Figure 6.17: (a) Snap shots captured during the embryo injection; (b) bending displacement during the injection measured by both the laser sensor and the integrated PVDF sensor.

6.2 IPMC/PVDF Differential-Mode Sensory Actuator and Its Validation in Feedback Control

6.2.1 Design of IPMC/PVDF differential-mode sensory actuator

Integrated differential-mode sensor for bending output

Fig. 6.18 illustrates the design of the integrated differential mode bending sensor for an IPMC actuator. Two complementary PVDF films, placed in opposite poling directions, are bonded to both sides of an IPMC with insulating layers in between. In our experiments, we have used 30 μm thick PVDF film from Measurement Specialties Inc., and 200 μm thick IPMC from Environmental Robots Inc. The IPMC uses non-water-based solvent and thus operates consistently in air, without the need for hydration. Scrapbooking tape (double-sided adhesive tape, 70 μm thick) from 3M Scotch Ltd. is used for both insulating and bonding purposes. A picture of a prototype is shown at the bottom of Fig. 6.18. Since we are focused on demonstrating the proof of the concept in this work, the materials used are chosen mainly based on convenience. However, the models to be presented later will allow one to optimize the geometry design and material choice based on applications at hand.

The differential charge amplifier, shown in Fig. 6.19, is used to measure the PVDF sensor output. In particular, the inner sides of two PVDF films are connected to the common ground, while the outer sides are fed to the amplifiers. Let $Q_1(s)$ and $Q_2(s)$ be the charges generated on the upper PVDF and the lower PVDF, respectively, represented in the Laplace domain. The signals V_p^+ and V_p^- in Fig. 6.19 are related to the charges by

$$V_p^+(s) = -\frac{R_1 s}{1 + R_1 C_1 s} Q_1(s), \quad V_p^-(s) = -\frac{R_1 s}{1 + R_1 C_1 s} Q_2(s),$$

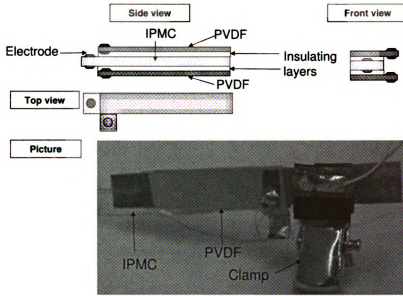


Figure 6.18: Design of the IPMC/PVDF composite structure for sensing of bending output (force sensor not shown).

and the sensor output V_o equals

$$V_o(s) = \frac{R_1 R_3 s}{R_2 (1 + R_1 C_1 s)} (Q_1(s) - Q_2(s)). \quad (6.14)$$

Let the bending-induced charge be $Q(s)$ for the upper PVDF, and the common noise-induced charge be $Q_n(s)$. If the sensor response is symmetric under compression versus tension (more discussion on this in Section 6.2.2), one has $Q_1(s) = Q(s) + Q_n(s)$, $Q_2(s) = -Q(s) + Q_n(s)$, which implies

$$V_o(s) = \frac{2R_1 R_3 s}{R_2 (1 + R_1 C_1 s)} Q(s), \quad (6.15)$$

and the effect of common noises (such as thermal drift and electromagnetic interference) is eliminated from the output. The charge amplifier (6.15) is a high-pass filter. To accommodate the actuation bandwidth of IPMC (typically below 10 Hz), the R_1 and C_1 values in the circuit are properly chosen so that the cutoff frequency of the charge amplifier is sufficiently low. By picking $R_1 = 5000 \text{ M}\Omega$, $C_1 = 1350 \text{ pF}$ and $R_2 = R_3 = 10 \text{ k}\Omega$, a cutoff

frequency of 0.023 Hz is achieved.

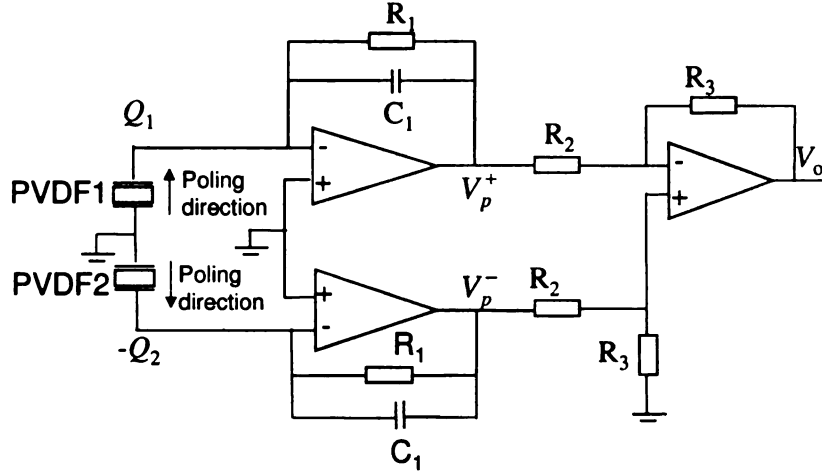


Figure 6.19: Differential charge amplifier for PVDF sensor.

A model is developed for predicting the sensitivity of the bending sensor in terms of the design geometry and material properties. Refer to Fig. 6.20 for the definition of geometric variables. Suppose that the IPMC/PVDF beam has a small uniform bending curvature with tip displacement z_1 ; without external force, the force sensor beam attached at the end of IPMC/PVDF appears straight with tip displacement z_2 . One would like to compute the sensitivity $\frac{Q}{z_2}$, where Q represents charges generated in one PVDF layer given the end-effector displacement z_2 . With the assumption of small bending for IPMC/PVDF beam, the curvature can be approximated by [19]

$$\frac{1}{\rho} \approx \frac{2z_1}{L_1^2}, \quad (6.16)$$

where ρ represents the radius of curvature. As $H_3 \ll 0.5H_1 + H_2$, we assume the stress inside the PVDF to be uniform and approximate it by the value at the center line of this layer:

$$\sigma_s = E_3 \varepsilon = E_3 \frac{0.5H_1 + H_2 + 0.5H_3}{\rho} \quad (6.17)$$

where E_3 is the Young's modulus of the PVDF. The electric displacement on the surface of

PVDF is

$$D_s = d_{31}\sigma_s. \quad (6.18)$$

where d_{31} is the transverse piezoelectric coefficient. The total charge generated on the PVDF is then

$$Q = \int D_s dS = D_s L_1 W_1. \quad (6.19)$$

With (6.16), (6.17), (6.18) and (6.19), one can get

$$Q = \frac{2d_{31}E_3W_1(0.5H_1 + H_2 + 0.5H_3)z_1}{L_1}. \quad (6.20)$$

The end-effector displacement z_2 is related to z_1 by

$$z_2 = z_1 + L_2 \sin\left(\arctan\left(\frac{2z_1}{L_1}\right)\right) \approx z_1\left(1 + \frac{2L_2}{L_1}\right), \quad (6.21)$$

Combining (6.20) and (6.21), one can get the sensitivity

$$S = \frac{Q}{z_2} = \frac{2d_{31}E_3W_1(0.5H_1 + H_2 + 0.5H_3)}{L_1 + 2L_2}. \quad (6.22)$$

Table 6.3 lists the parameters measured or identified for our prototype. The sensitivity is predicted to be 1830 pC/mm, while the actual sensitivity is characterized to be 1910 pC/mm using a laser distance sensor (OADM 20I6441/S14F, Baumer Electric). With the charge amplifier incorporated, the sensitivity $\frac{V_o}{z_2}$ at frequencies of a few Hz or higher is measured to be 2.75 V/mm, compared to a theoretical value of 2.71 V/mm.

Force Sensor for End-effector

The structure of the force sensor is similar to that of IPMC/PVDF sensory actuator. As illustrated in Fig. 6.21, two PVDF films are bonded to the both sides of a relatively rigid beam. In our experiments, we have used 200 μm thick Polyester from Bryce Corp. for the

Table 6.3: Parameters identified for the IPMC/PVDF sensory actuator prototype (including force sensor).

W_1	L_1	H_1	H_2	H_3
10 mm	40 mm	200 μm	65 μm	30 μm
W_2	L_2	h_1	h_2	h_3
6 mm	30 mm	200 μm	65 μm	30 μm
E_1	E_2	E_3	d_{31}	
5 GPa	0.4 GPa	2 GPa	28 pC/N	

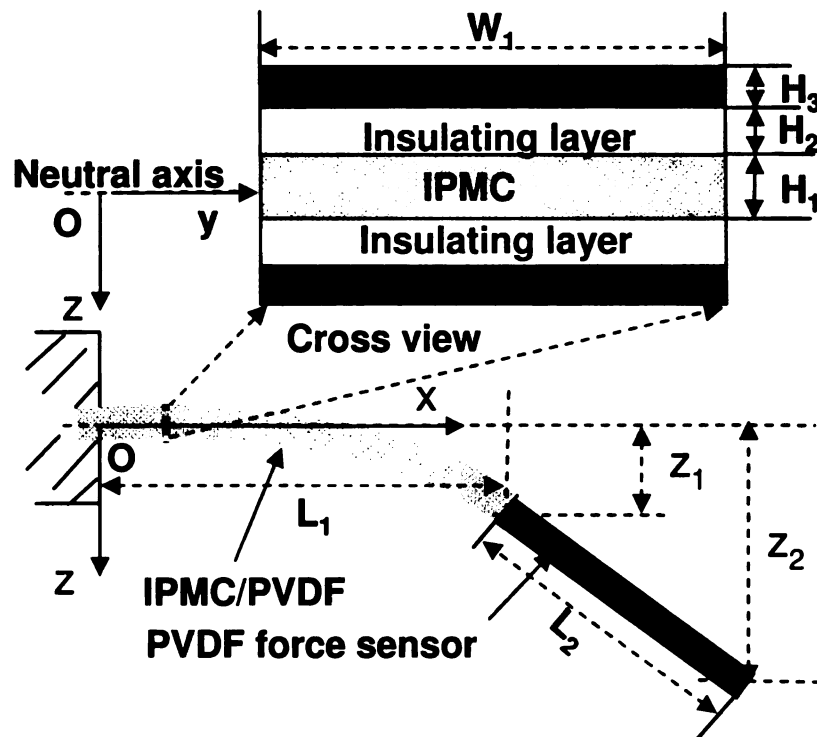


Figure 6.20: Geometric definitions of IPMC/PVDF sensory actuator.

beam. An end-effector, e.g., a glass needle in microinjection applications, is bonded the tip of the force sensor. An external force experienced by the end-effector will cause the composite beam to bend, which produces charges on the PVDF films. Another differential charge amplifier as in Fig. 6.19 is used for the force sensor. The whole force-sensing beam is attached to the front end of the IPMC/PVDF beam.

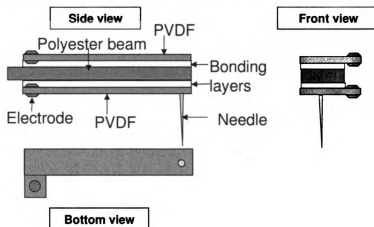


Figure 6.21: Design of the force sensor for the end-effector.

Refer to Fig. 6.22. The sensitivity model for force sensing, $\frac{Q_f}{F}$, is provided below. Here Q_f represents the charges generated in one PVDF in response to the force F exerted by the end-effector. The beam curvature can be written as

$$\frac{1}{\rho(x)} = \frac{F(L_2 - x)}{\sum_{i=0}^3 E_i I_i}, \quad (6.23)$$

where $\rho(x)$ denotes the radius of curvature at x , E_1 , E_2 , E_3 are the Young's moduli of the Polyester film, the bonding layer, and PVDF respectively. I_1 , I_2 and I_3 are the moments of inertia for those layers, which are given by

$$\begin{aligned} I_1 &= \frac{1}{12} W_2 h_1^3, \\ I_2 &= \frac{1}{6} W_2 h_2^3 + \frac{W_2 h_2 (h_1 + h_2)^2}{2}, \\ I_3 &= \frac{1}{6} W_2 h_3^3 + \frac{W_2 h_3 (h_1 + 2h_2 + h_3)^2}{2}. \end{aligned}$$

The stress generated in the PVDF is approximately

$$\sigma_3(x) = E_3 \varepsilon_3(x) = E_3 \frac{h_1 + 2h_2 + h_3}{2\rho(x)}. \quad (6.24)$$

With (6.18), (6.23) and (6.24), one can get the electric displacement in PVDF,

$$D_3(x) = d_{31} \sigma_3(x) = E_3 d_{31} \frac{h_1 + 2h_2 + h_3}{2} \frac{F(L_2 - x)}{\sum_{i=0}^3 E_i I_i}. \quad (6.25)$$

The total charge generated in the PVDF can be written as

$$Q_f = \int_0^{L_2} D_3(x) W_2 dx = \frac{d_{31} E_3 W_2 L_2^2 (h_1 + 2h_2 + h_3)}{4 \sum_{i=0}^3 E_i I_i} F \quad (6.26)$$

Then the sensitivity of the force sensor is

$$S_f = \frac{Q_f}{F} = \frac{d_{31} E_3 W_2 L_2^2 (h_1 + 2h_2 + h_3)}{4 \sum_{i=0}^3 E_i I_i}. \quad (6.27)$$

Relevant parameters for the force sensor in our prototype can be found in Table 6.3. Theoretical value of S_f is computed to be $0.456 \text{ pC}/\mu\text{N}$, which is close to the actual value $0.459 \text{ pC}/\mu\text{N}$ from measurement. With the charge amplifier circuit, the sensitivity of the overall force sensor $\frac{V_{0f}}{F}$ at high frequencies (several Hz and above) is characterized to be $0.68 \text{ mV}/\mu\text{N}$, compared to the model prediction of $0.67 \text{ mV}/\mu\text{N}$.

The integrated IPMC/PVDF sensory actuator and the charge sensing circuits are placed in conductive plastic enclosures (Hammond Manufacturing) to shield electromagnetic interference (EMI) and reduce air disturbance and thermal drift. A slit is created on the side of the shielding box enclosing IPMC/PVDF so that the end-effector protrudes out for manipulation purposes. Fig. 6.23 shows the picture of the overall system.

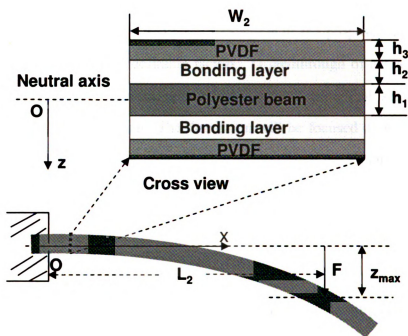


Figure 6.22: Geometric definitions of the PVDF sensor.

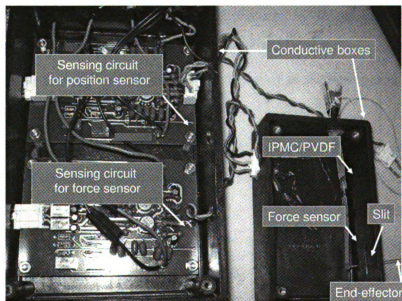


Figure 6.23: IPMC/PVDF sensory actuator and sensing circuits in shielding enclosures.

6.2.2 Experimental verification of sensor robustness

In this section we experimentally verify the robustness of the proposed sensory actuator with respect to the following undesirable factors: 1) feedthrough of actuation signal, 2) thermal drift and other environmental noises, and 3) asymmetric PVDF sensing responses during compression versus tension. The discussion will be focused on the PVDF sensor for IPMC bending output, since the problems associated with the PVDF force sensor are similar and actually simpler (no need to worry about actuation feedthrough).

Feedthrough Coupling

Close proximity between IPMC and PVDF results in capacitive coupling between the two. Fig. 6.24 illustrates the distributed circuit model for the composite IPMC/PVDF beam. Suppose an actuation signal $V_i(s)$ is applied to IPMC. If one connects both sides of a single PVDF film to a differential charge amplifier, as done typically in Section 6.1, the output will pick up a signal that is induced by the actuation signal via electrical coupling. Fig. 6.7 in Section 6.1 illustrates the traditional feedthrough problem. While one can attempt to model the feedthrough coupling and cancel it through feedforward compensation, the complexity of such algorithms and the varying behavior of coupling make this approach unappealing to real applications.

In the new charge sensing scheme proposed in this design, the inner sides of the two PVDF sensors are connected to a common ground (see Fig. 6.19). Since the surface electrode resistances of PVDF films are very low ($< 0.1\Omega$), the inner layers L_2 and L_3 in Fig. 6.24 will effectively play a shielding role and eliminate the feedthrough coupling signals. This analysis is verified experimentally, where a square-wave actuation voltage with amplitude 2 V and frequency 0.1 Hz is applied to the IPMC. Fig. 6.25(a) shows that the charge amplifier output V_o contains no feedthrough-induced spikes. The definitions for V_o , V_p^+ , and V_p^- in the figure can be found in Fig. 6.19. Furthermore, the bending displacement

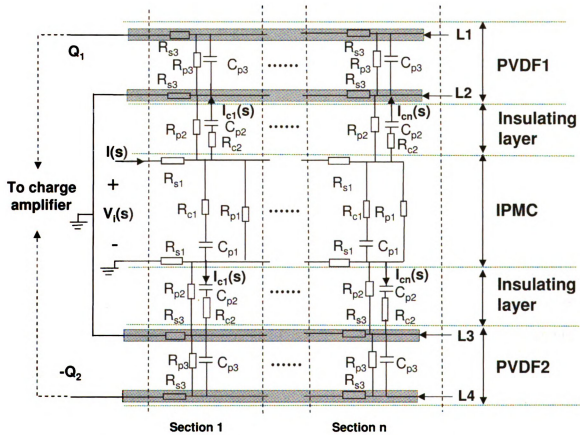


Figure 6.24: Distributed circuit model of IPMC/PVDF beam.

obtained from the PVDF output V_o correlates well with the actual bending displacement measured by the laser distance sensor, as shown in Fig. 6.25(b). Note that the PVDF output V_o is related to the bending displacement z_1 through the charge amplifier dynamics (6.15) and the proportional relationship (6.20). Since (6.15) represents a high-pass filter, at relatively high frequencies (determined by the cut-off frequency), the correlation between V_o and z_1 can be approximated by a constant; however, at lower frequencies (including the step input, in particular), the dynamics (6.15) has to be accommodated to obtain the displacement trajectory from the raw PVDF signal V_o . The latter has been adopted throughout the chapter, whether the inverse of the charge amplifier dynamics is implemented digitally to retrieve z_1 .

Thermal Drift and Environmental Noises

PVDF sensors are very sensitive to ambient temperatures and electromagnetic noises. Such environmental noises could significantly limit the use of PVDF bending/force sensors, especially when the operation frequency is low (comparing with the fluctuation of ambient conditions). Refer to Fig. 6.19. Let noise-induced charges be Q_{n_1} and Q_{n_2} for PVDF1 and PVDF2, respectively. Suppose that no actuation signal is applied, and thus bending-induced charge $Q(s) = 0$. The voltage signals can then be expressed as

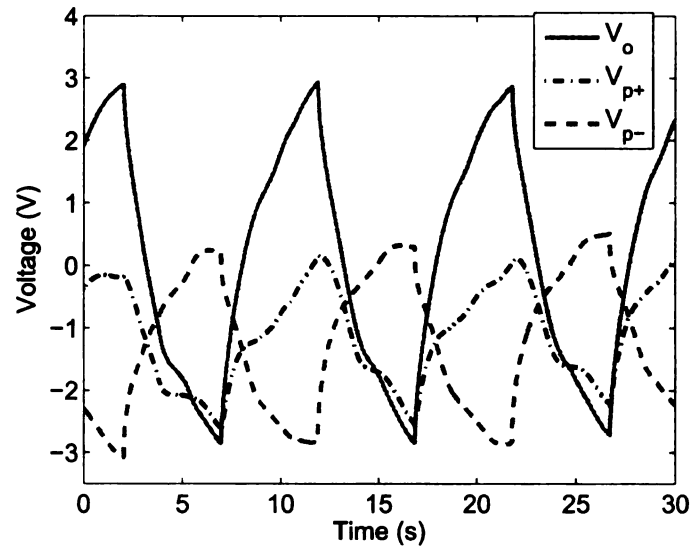
$$V_p^+(s) = -\frac{R_1 s}{1 + R_1 C_1 s} Q_{n_1}(s), \quad (6.28)$$

$$V_p^-(s) = -\frac{R_1 s}{1 + R_1 C_1 s} Q_{n_2}(s), \quad (6.29)$$

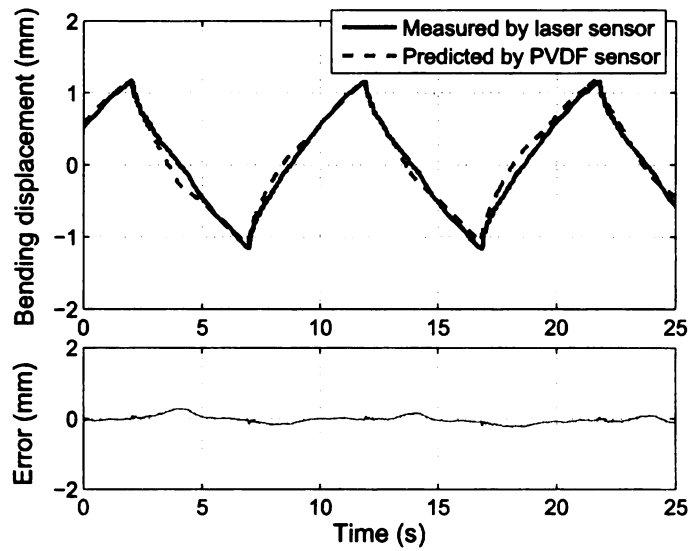
$$V_o(s) = \frac{R_1 R_3 s}{R_2 (1 + R_1 C_1 s)} (Q_{n_1}(s) - Q_{n_2}(s)). \quad (6.30)$$

Inside a conductive shielding enclosure, thermal and EMI conditions are relatively steady and uniform. This implies $Q_{n_1}(s) \approx Q_{n_2}(s)$ and the influence of environmental noises on the sensor output V_o is negligible.

Two experiments have been conducted to confirm the above analysis. In order to isolate



(a)



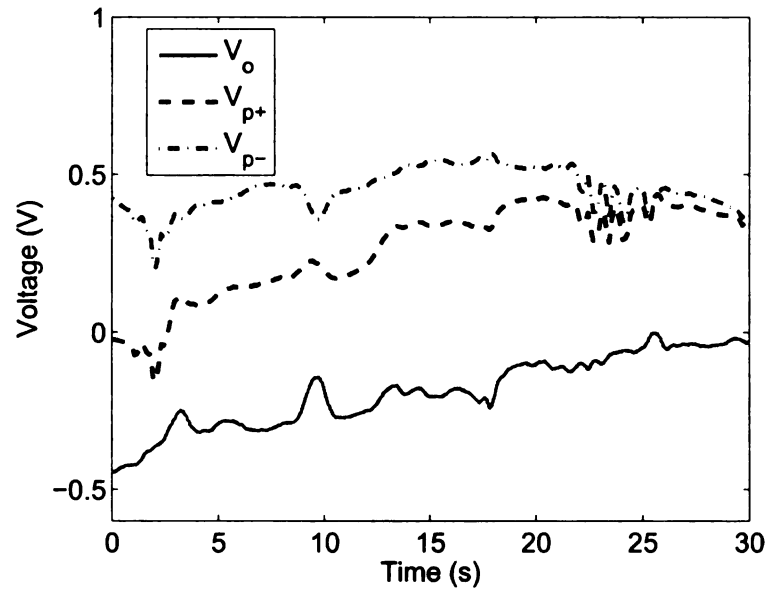
(b)

Figure 6.25: Experimental results showing elimination of feedthrough signal. (a) Raw PVDF sensing signals under a square-wave actuation input (2V, 0.1 Hz); (b) Comparison between the bending displacements obtained from the PVDF sensor and from the laser sensor.

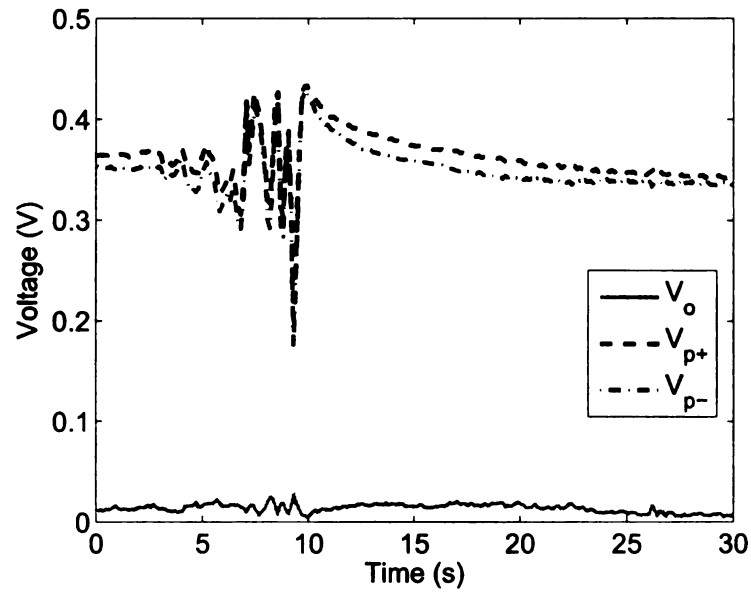
the effect of noises, no actuation signal is applied. In the first experiment, the IPMC/PVDF beam was exposed to ambient air flows and electromagnetic noises. Fig. 6.26(a) shows the complementary sensing outputs V_p^+ and V_p^- and the resulting charge amplifier output V_o . From (6.28)-(6.30), the discrepancy between V_p^+ and V_p^- indicates that the noise-induced charges Q_{n1} and Q_{n2} on the two PVDF layers can be significantly different, leading to relatively large sensing noise in V_o . In contrast, Fig. 6.26(b) shows the results from the second experiment, where the IPMC/PVDF sensory actuator was placed inside the conductive shielding enclosure. In this case, while V_p^+ and V_p^- could still vary over time individually, their trajectories are highly correlated and close to each other. Consequently, V_o remained under 1 mV, compared to about 20 mV in the first case. These experiments have confirmed that the proposed differential sensing scheme, together with the shielding enclosure, can effectively minimize the effect of thermal drift and other common noises.

Asymmetric Sensing Response during Extension versus Compression

Because of its compliant nature, a single PVDF film does not produce symmetric charge responses when it is under tension versus compression. In particular, it is difficult to effectively introduce compressive normal stress into the flexible film. As a result, the charge response of a PVDF layer under extension can faithfully capture the beam motion while the response under compression cannot. This is illustrated by experimental results shown in Fig. 6.27(a): each of the sensing signals V_p^+ and V_p^- from the two PVDF layers is asymmetric under a symmetric, sinusoidal actuation input. With the differential configuration of two PVDF films, however, the asymmetric responses of individual PVDF films combine to form a symmetric output V_o , as seen in Fig. 6.27(a). This is because when one film is in compression, the other is in tension. Fig. 6.27(b) shows that the bending displacement obtained based on the PVDF signal V_o agrees well with the laser sensor measurement. We have further examined the performance of the proposed integrated sensing scheme under other types of actuation inputs, including the step inputs. From Fig. 6.28, the bending



(a)



(b)

Figure 6.26: (a) Sensing noise when IPMC/PVDF placed in open field; (b) sensing noise when IPMC/PVDF placed inside conductive shielding enclosure.

trajectory under a step input (2V) can be captured well by the PVDF sensor.

Another advantage of adopting two complementary PVDF films is that it alleviates the effect of internal stresses at bonding interfaces. When bonding a single PVDF to IPMC, mismatch of internal stresses at the PVDF/IPMC interface could lead to delamination and/or spontaneous creep of the composite beam. While this problem could be lessened by using appropriate bonding technologies, it was found that the proposed scheme can effectively maintain the structural stability of the composite beam, without stringent requirements on bonding.

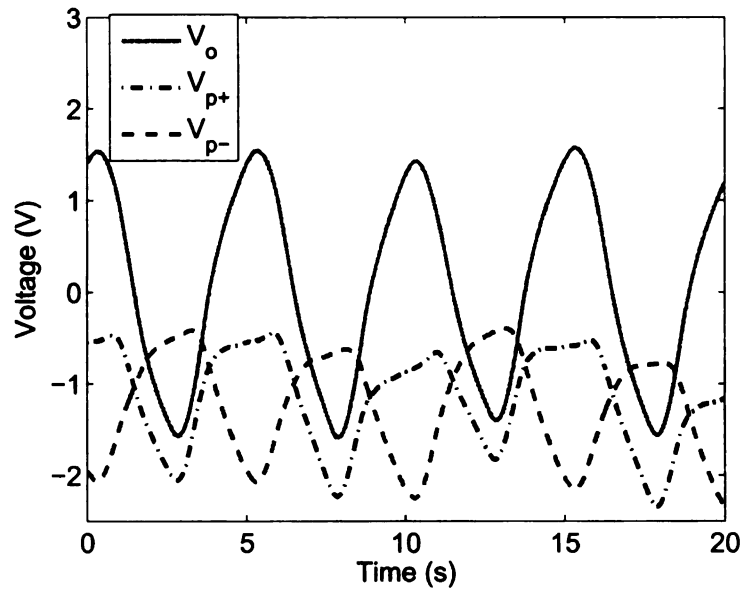
6.2.3 Feedback control based on the integrated sensor

The practical utility of the proposed IPMC/PVDF sensory actuator has been demonstrated in feedback control experiments. Trajectory tracking experiments are first performed, where no tip interaction force is introduced. Simultaneous trajectory tracking and force measurement are then conducted to examine both integrated bending and force sensors.

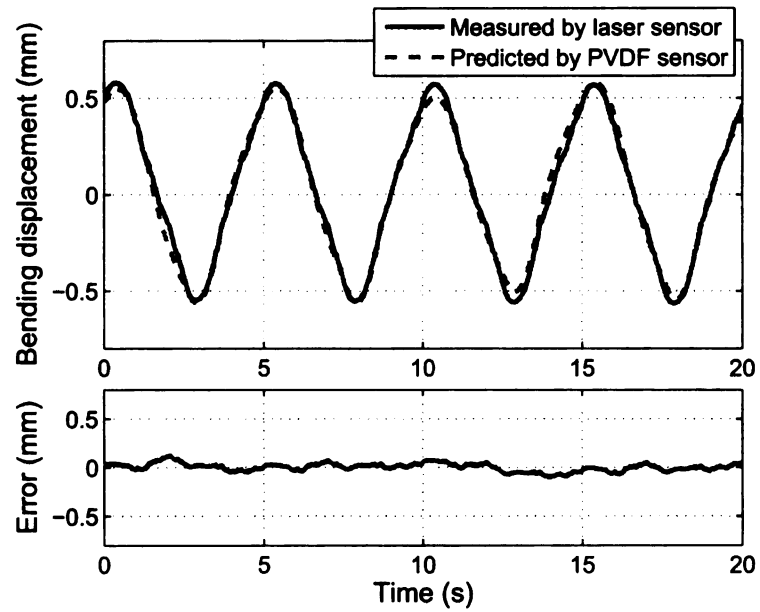
Feedback control of bending displacement

Fig. 6.29 illustrates the closed-loop system for the control of IPMC bending displacement. Here $P(s)$ represents the actuation dynamics for the IPMC/PVDF composite structure, $H(s)$ is the bending sensor dynamics, $K(s)$ is the controller, r is the reference input, u is the actuation voltage, and z_2 is the bending displacement of the end-effector. In experiments data acquisition and control calculation are performed by a dSPACE system (DS1104, dSPACE Inc.); for real applications such tasks can be easily processed by embedded processors, e.g., microcontrollers. A laser sensor is used as an external, independent observer for verification purposes.

In general $K(s)$ can be designed based on a nominal model of the plant $P(s)$ and various objectives and constraints. An example of H_∞ control design can be found in [20], where a physics-based, control-oriented model is also developed for IPMC actuators. Since IPMC



(a)



(b)

Figure 6.27: Self-compensation of asymmetric tension/compression sensing response. (a) Raw PVDF sensing signals under a sinusoidal actuation signal (0.2 Hz, amplitude 1 V); (b) Comparison between the bending displacements obtained from the PVDF sensor and from the laser sensor.

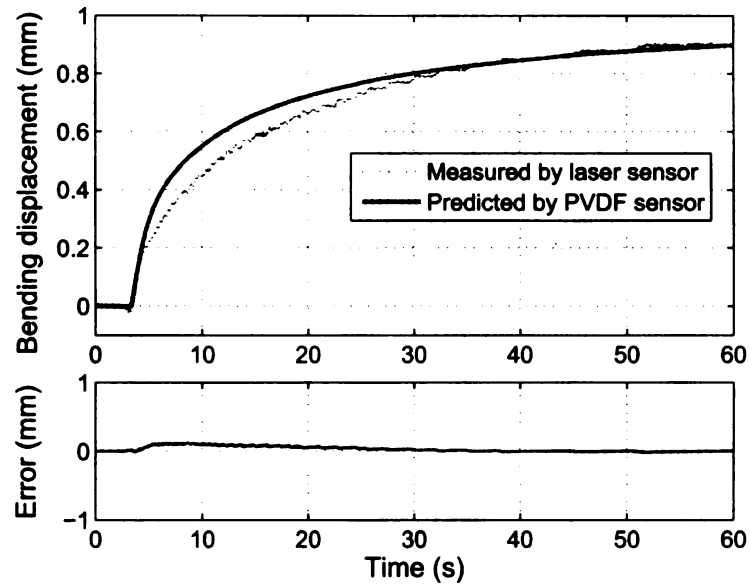


Figure 6.28: Comparison between the bending displacements obtained from the PVDF sensor and from the laser sensor, when a 2V step input is applied.

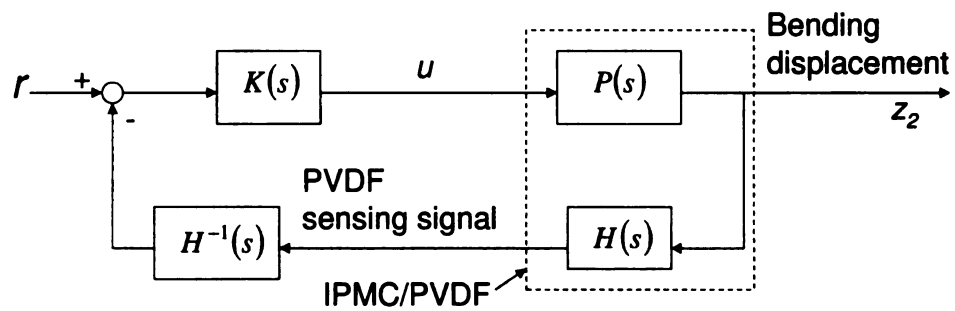


Figure 6.29: Closed-loop system for control of IPMC bending displacement.

modeling and control design are not the focus of this chapter, we have identified the plant model $P(s)$ empirically and used a simple proportional-integral (PI) controller for $K(s)$ to validate the integrated sensing scheme. In particular, the empirical frequency response of the IPMC/PVDF sensory actuator has been obtained by applying a sequence of sinusoidal actuation inputs (amplitude 0.2 V, frequency 0.01 Hz to 10 Hz) and measuring the corresponding bending response. It has been found that the measured dynamic behavior could be approximated by a second order system, the parameters of which have been further determined using the Matlab command “fitsys”. The resulting $P(s)$ is

$$P(s) = \frac{2.7s + 20}{1000(s^2 + 33.4s + 18.9)}.$$

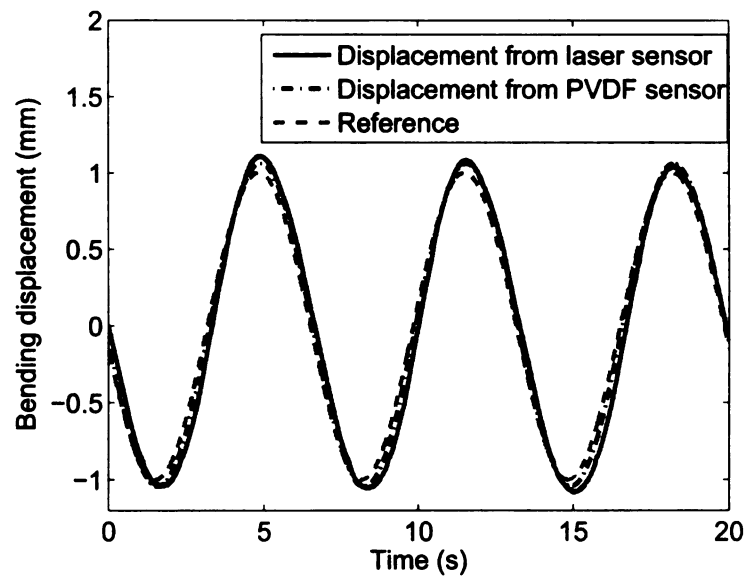
The sensing model is obtained from (6.15) and (6.20):

$$H(s) = \frac{18150s}{6.57s + 1}.$$

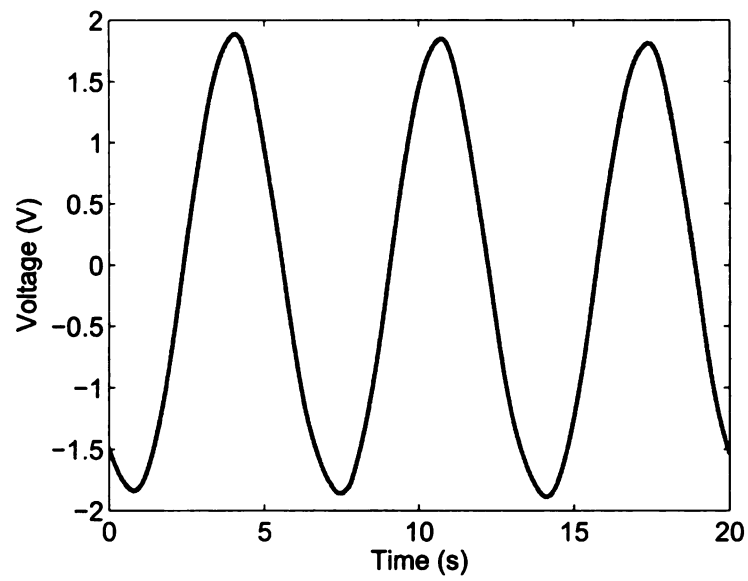
The following reference trajectory is used: $r(t) = \sin(0.3\pi t)$ mm. Based on the models and the reference, a PI controller $K(s) = 1000 \left(40 + \frac{30}{s} \right)$ is designed to achieve good tracking performance while meeting the constraint $|u| < 2$ V. Fig. 6.30(a) shows the experimental results of tracking the bending reference. It can be seen that the PVDF sensor output tracks the reference well; furthermore, the actual bending displacement, as observed by the laser sensor, has close agreement with the PVDF output. The actuation voltage u , shown in Fig. 6.30(b), falls within the limit $[-2, 2]$ V.

Feedback bending control with simultaneous force measurement

It is desirable in many applications to have both displacement and force feedback. With the proposed IPMC/PVDF sensory actuator, one can perform feedback control of the displacement while monitoring the force output, as well as perform feedback control of the force



(a)



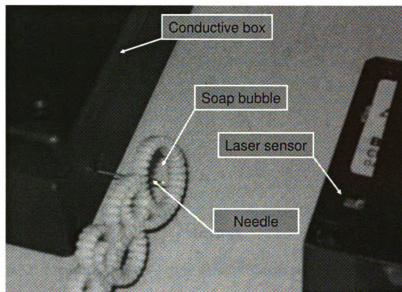
(b)

Figure 6.30: Experimental results on feedback control of bending displacement using integrated PVDF sensor. (a) Bending displacement; (b) actuation voltage.

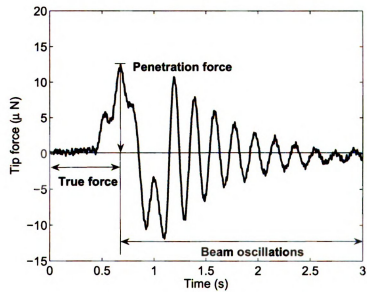
output while monitoring the displacement. In the following experiment we will demonstrate the feedback bending control with simultaneous force measurement.

To mimic the force level often encountered in bio and micromanipulation applications, we have attached a sharp glass needle as an end-effector at the tip of force-sensing beam and used it to pierce soap bubbles. Fig. 6.31(a) shows the experimental setup. A number of bubble-penetrating experiments were conducted to get an estimate of the rupture force by moving a bubble manually toward the needle until it breaks, when no actuation voltage was applied. Fig. 6.31(b) shows the force sensor response during a typical run. It can be seen that the response first rises from zero to a peak value, and then starts decayed oscillations. Since the PVDF sensor measures essentially the bending of the passive beam, its output can be interpreted as an interaction force only when the end-effector is in contact with a foreign object. Thus for the response in Fig. 6.31(b), only the first rising segment truly represents the force, after which the membrane ruptures and the beam starts oscillating. Hence we take the peak value of such responses as the penetration force. Fig. 6.32 shows the penetration force measured in 26 independent experiments. Overall the measurements are consistent with an average of $11 \mu\text{N}$. The variation is believed due to the randomly created bubbles that might have different thicknesses. Note that for many real applications, such as microinjection of embryos or cells [18], the end-effector will maintain contact with the object under manipulation, in which case the output of PVDF force sensor would truly represent the interaction force at all times.

A feedback bending control experiment with force monitoring has been conducted, where the reference for the end-effector displacement $r(t) = 0.2 \sin(0.4\pi t)$ mm. During the experiment, the end-effector penetrated two soap bubbles at $t = 9.32$ and $t = 15.72$ seconds, respectively. Fig. 6.33(a) shows the estimated end-effector displacement based on the integrated PVDF bending sensor (sandwiching IPMC), under the assumption that the force-sensing PVDF beam is not deflected. The estimated displacement trajectory follows closely the reference, with slight perturbations at the moments when penetrations occur,



(a)



(b)

Figure 6.31: Measurement of the micro force in piercing soap bubbles. (a) Experimental setup; (b) PVDF sensor response during and after penetration.

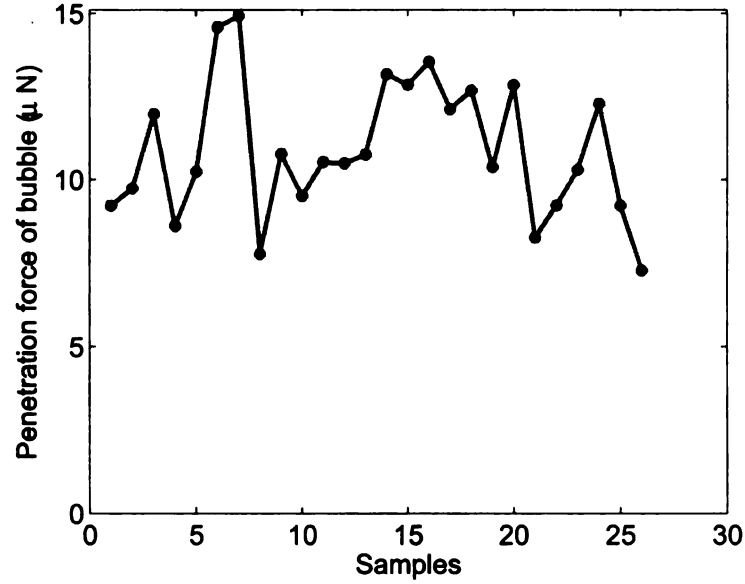


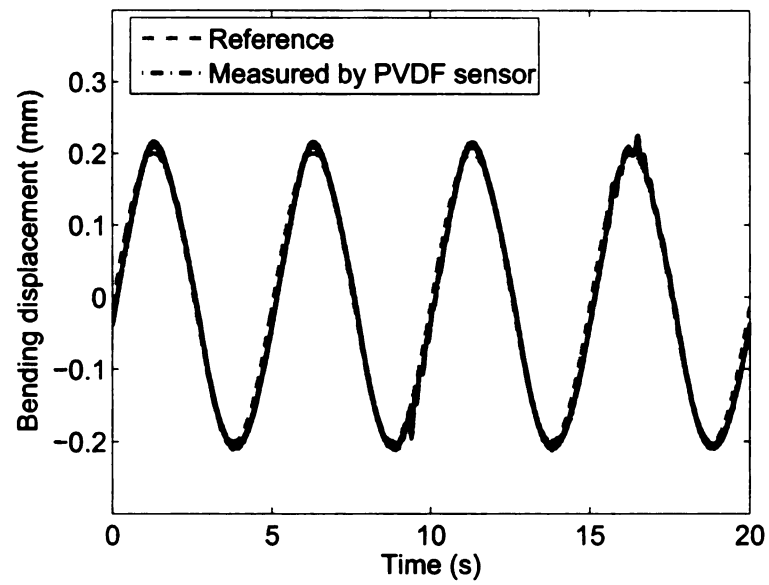
Figure 6.32: Measured forces during penetration of soap bubble membranes.

indicating that the feedback control was in effect. Fig. 6.33(b) shows the output of the integrated force sensor, where the two penetrations were captured clearly. Note that, as explained earlier and illustrated in Fig. 6.31(b), only the first rising segment of the trajectory during each penetration truly represents the interaction force, while the remaining portion of the signal arises from oscillations following penetration. The control output (actuation voltage) is shown in Fig. 6.34, where one can see that feedback is in action to suppress the disturbance caused by penetration.

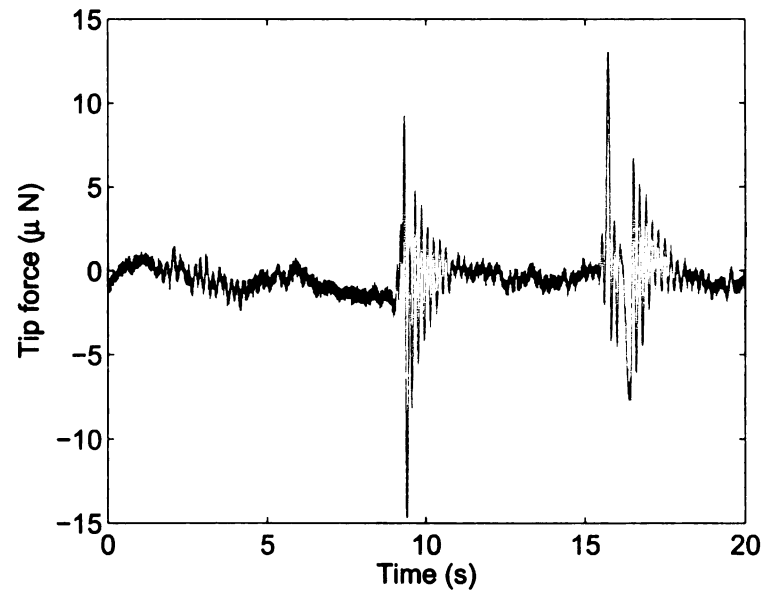
Note that the end-effector displacement z_2 predicted by the PVDF bending sensor alone (Fig. 6.33(a)) does not capture the true displacement d when the end-effector interacts with objects. To obtain the true displacement, one can combine the bending sensor output z_2 and the force sensor output F :

$$d = z_2 + F/k, \quad (6.31)$$

where k is the stiffness of the force-sensing beam. For our prototype, $k = 0.067$ N/m. Fig. 6.35 compares the end-effector displacement obtained from (6.31) and that observed by the laser sensor, which shows that indeed the end-effector position can be monitored by



(a)



(b)

Figure 6.33: Experimental results on bending feedback control with tip force measurement. (a) Displacement of the end-effector estimated based on the integrated PVDF bending sensor alone; (b) PVDF force sensor output.

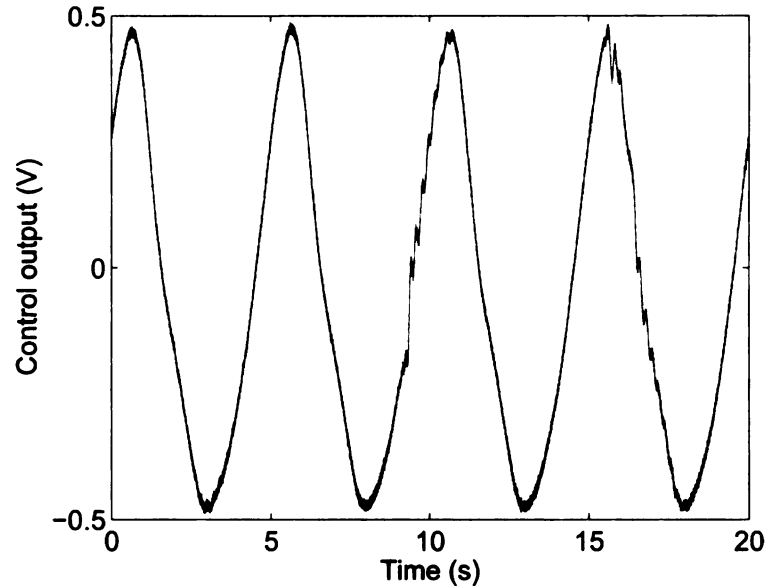


Figure 6.34: Actuation voltage generated by the feedback controller.

combining the integrated bending and force sensors.

6.3 Chapter Summary

In this chapter, a novel scheme was proposed for implementing integrated sensors for an IPMC actuator, to achieve sensing of both the bending displacement output and the force output. In the first design, an IPMC is bonded with a PVDF sensing film in a single-mode sensing configuration. The stiffening effect and the electrical feedthrough coupling are investigated. In the second design, two thin PVDF films are bonded to both sides of an IPMC beam to measure the bending output, while a passive beam sandwiched by two PVDF films is attached at the end of IPMC actuator to measure the force experienced by the end-effector. The differential configuration adopted in both sensors has proven critical in eliminating feedthrough coupling, rejecting sensing noises induced by thermal drift and EMI, compensating asymmetric tension/compression responses, and maintaining structural stability of the composite beams. For the first time, feedback control of IPMC has been

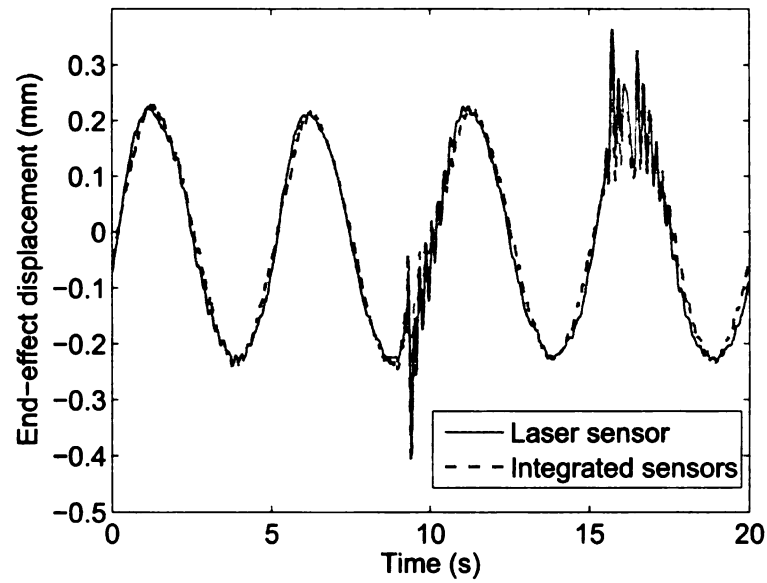


Figure 6.35: Estimation of true end-effector displacement by combining the integrated bending and force sensors, and its comparison with the laser sensor measurement.

successfully demonstrated using only integrated sensors, showing that one can simultaneously regulating/tracking the bending displacement and monitoring the force output (or vice versa).

Chapter 7

Monolithic Fabrication of Ionic Polymer Metal Composite Actuators Capable of Complex Deformations

This chapter is organized as follows. The fabrication process for MDOF IPMC actuators is presented in Section 7.1. In Section 7.2 we investigate the change of stiffness and swellability of Nafion films caused by the ion-exchange process. The performance of fabricated artificial pectoral fins is characterized in Section 7.3. Finally, concluding remarks are provided in Section 7.4.

7.1 Fabrication Process

In this section, we outline the overall fabrication flow first and then discuss the individual steps in more details. Fabrication of an artificial pectoral fin is taken as an example. As illustrated in Fig. 7.1, the major process steps include:

- **(a):** Create an aluminum mask on Nafion with e-beam deposition, which covers the intended IPMC regions;

- **(b):** Etch with argon and oxygen plasmas to thin down the passive regions;
- **(c):** Remove the aluminum mask and place the sample in platinum salt solution to perform ion-exchange. This will stiffen the sample and make the following steps feasible;
- **(d):** Pattern with photoresist (PR), where the targeted IPMC regions are exposed while the passive regions are protected;
- **(e):** Perform the second ion-exchange and reduction to form platinum electrodes in active regions. To further improve the conductivity of the electrodes, 100 nm gold is sputtered on the sample surface;
- **(f):** Remove PR and lift off the gold on the passive areas. Soften the passive regions with HCL treatment (to undo the effect of step (c));
- **(g):** Cut the sample into a desired shape.

7.1.1 Aluminum mask deposition

Since plasma will be used to selectively thin down the passive areas of the Nafion film, the first step is to make an aluminum mask to protect the active areas from being etched. Two shadow masks made of transparency films are used to cover both sides of the Nafion film, in such a way that the passive areas are covered and the active areas are exposed. The sample is then put into an e-beam deposition system, where aluminum can be deposited at room temperature. Aluminum films of 200 nm thick are deposited on both sides of the Nafion film. When the transparency masks are removed, the aluminum masks stay on the active regions and the sample is ready for plasma etching.

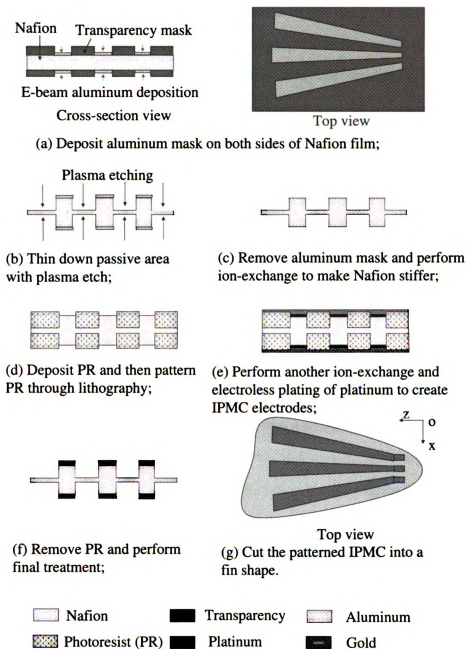


Figure 7.1: The process flow for monolithic fabrication of an MDOF IPMC actuator.

7.1.2 Plasma etching

Plasma treatment has been used for roughening the Nafion surface to increase the capacitance of IPMC [51]. In this research, we use plasma to thin down the passive areas in the MDOF IPMC actuator. The plasma etching system used in this research is Plasmaquest Model 357. Experiments have been conducted to study the etching rates with different recipes of gas sources. The etching rates with different recipes are shown in Table 7.1.

Table 7.1: Plasma etching with different recipes.

No.	Ar	O ₂	RF power	Microwave power	Etching rate
<i>R1</i>	20 sccm	30 sccm	70 W	300 W	0.28 $\mu\text{m}/\text{min}$
<i>R2</i>	0 sccm	50 sccm	70 W	300 W	0.22 $\mu\text{m}/\text{min}$
<i>R3</i>	50 sccm	30 sccm	70 W	300 W	0.51 $\mu\text{m}/\text{min}$

It can be seen that the combination of oxygen and argon plasmas can achieve a higher etching rate than using the oxygen plasma alone. The oxygen plasma performs chemical etching, which can oxidize the polymer and break Nafion into small molecules. The higher oxygen flow rate, the higher etching rate but also the higher temperature on the Nafion film. We have found that too strong oxygen plasma will damage the film because of overheating. The argon plasma performs physical etching with high-speed, heavy argon ions. It can remove the small molecules created by the oxygen plasma and roughen the Nafion surface, which creates larger contact area for the oxygen plasma and thus accelerates the chemical etching. The combination of oxygen and argon plasmas can achieve a high etching rate with a low resulting temperature, which is critical to maintaining the original properties of Nafion. In this research, the recipe *R3* is adopted.

After several hours of plasma etching, the passive areas are thinned down to the desired value. Then the sample is boiled in 2 N hydrochloride acid solution at 90 °C for 30 minutes to remove the aluminum mask and to remove impurities and ions in Nafion. After that, the membrane is further boiled in deionized (DI) water for 30 minutes to remove acid. Fig. 7.2 shows the Scanning Electron Microscope (SEM) picture of a selectively etched Nafion

sample, where the thinnest region is $48\ \mu\text{m}$ (down from the original $225\ \mu\text{m}$). The etched sidewall is almost vertical (the angle is 88°). To roughen the active areas, the sample is treated with plasma for 5 minutes. This roughening process can enlarge the metal-polymer contact areas, which enhances the actuation performance of IPMC [51].

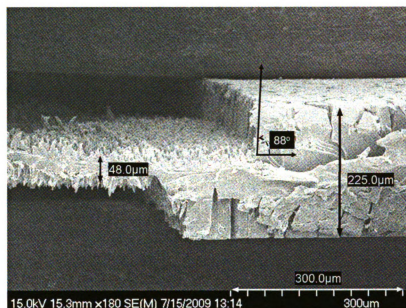
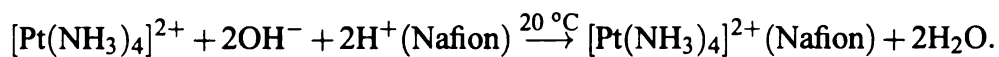


Figure 7.2: SEM picture of a plasma-etched Nafion film.

7.1.3 Stiffening treatment

It is difficult to perform lithography on a pure Nafion film because Nafion swells in the developer, which usually contains water and organic solvent, and the swelling force can easily destroy the photoresist pattern. To address this challenge, we perform an ion-exchange process to impregnate Nafion with large platinum complex ions ($\text{Pt}(\text{NH}_3)_4^{2+}$). Usually, this ion-exchange process is used to absorb platinum complex ions for electroless platinum plating [78]. However, we have discovered that, after the ion-exchange, the Nafion film becomes stiffer and virtually non-swellaible in water or acetone, which makes lithography and the subsequent patterned electroless plating possible.

To perform ion-exchange, 25 ml of aqueous solution of tetraammine-platinum chloride $[\text{Pt}(\text{NH}_3)_4]\text{Cl}_2$ (2 mg Pt/ml) is prepared with 1 ml of ammonium hydroxide solution (5%) to neutralize. The sample is immersed into the solution at room temperature for one day. The formula of reaction is



The impact of stiffening treatment will be studied in detail in Section 7.2.

7.1.4 Patterning of Nafion surface

AZ 9260 positive photoresist is selected to create thick PR patterns to protect the passive areas of the actuator from electroless platinum plating. We spin-coat PR at 1000 rpm to get 17 μm thick film and then bake it in oven at 90 $^\circ\text{C}$ for 2 hours. Since the Nafion film alone is not rigid enough for spin-coating and it is easy to deform when baked in oven, an aluminum frame is used to support and fix the Nafion film (25 mm by 25 mm), as shown in Fig. 7.3. UV light with power density of 20 mw/cm^2 is used to expose the sample with the pattern mask for 105 seconds. After the sample is exposed, the PR is developed with AZ 400K developer.

7.1.5 Electroless platinum plating and gold sputtering

The electroless platinum plating process is used to create thick platinum electrodes on the active areas, which results in strong bonding between the metal and the polymer. Three steps are taken for this process. First, another ion-exchange is performed to absorb more platinum complex ions. Second, the sample is put into a bath with DI water at 40 $^\circ\text{C}$. Third, we add 1 ml of sodium borohydride solution (5 wt% NaBH_4) into the bath every 10 minutes and raise the bath temperature up to 60 $^\circ\text{C}$ gradually. After 30 minutes of reduction, about 10 μm thick platinum electrodes will grow on the surface of the active

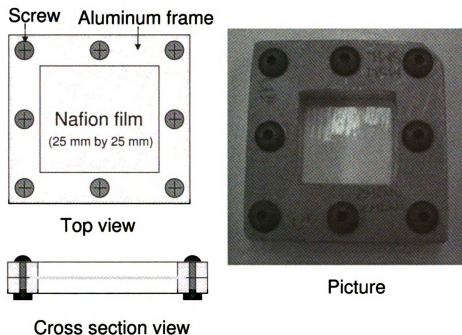
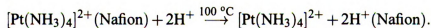


Figure 7.3: Nafion film fixed by an aluminum frame.

areas. To further improve the electrode conductivity, 100 nm thick gold is sputtered on both sides of the sample. The surface resistance can be reduced by half with this gold-sputtering step. Since PR patterns are still on the surface, the passive areas are protected. When the PR is removed with acetone, the gold on the passive areas will be lifted off.

7.1.6 Final membrane treatment

After electroless plating, the Pt complex ions in active regions are reduced to platinum metal. But the Pt complex ions in the passive regions are still there, which makes the passive regions stiff. To facilitate 3-D deformation, we need to undo the effect of step (c) to replace the Pt complex ions with H^+ . This can be achieved by simply boiling the sample in 2N hydrochloride (HCL) acid [50]. The formula of reaction is



After the sample becomes flexible, it is put into sodium or lithium ion solution (1 N) for one day to exchange H^+ with Na^+ or Li^+ ions, to enhance actuation of IPMCs. A fabricated IPMC membrane is shown in Fig. 7.4.

7.2 Impact of Stiffening Treatment

Stiffening treatment is an important step in fabrication of MDOF IPMC actuators. In this section, we study the impact of the ion-exchange process on the stiffness and swellability of Nafion films, and its implication in lithography and the overall fabrication process.

7.2.1 Stiffness change

The experimental setup for the stiffness measurement is shown in Fig. 7.5. The film is fixed at one end by a clamp. A load cell (GS0-10, Transducer Techniques) is mounted on a moving stage (U-SVRB-4, Olympus), which can be manipulated by hand to generate smooth horizontal motion. When the stage is moved, the load cell pushes the Nafion film to bend, and the restoring force at the tip of the film is measured. A laser displacement sensor (OADM 20I6441/S14F, Baumer Electric) is used to measure the corresponding tip displacement. The resolution of the laser sensor is $20\text{ }\mu\text{m}$ and the resolution of the load cell is 0.05 mN. The setup is placed on an anti-vibration table (LW3048B-OPT, Newport). A dSPACE system (DS1104, dSPACE) is used for data acquisition. The spring constant of the Nafion film is calculated as

$$k = \frac{F}{d},$$

where F and d are the tip force and the tip displacement, respectively.

We have measured the stiffness of Nafion-117 ($183\text{ }\mu\text{m}$) and Nafion-1110 ($240\text{ }\mu\text{m}$) before and after the ion-exchange process. The ion-exchanged Nafion films are dried in air before the experiments. Fig. 7.6 shows the force and displacement data for each case,

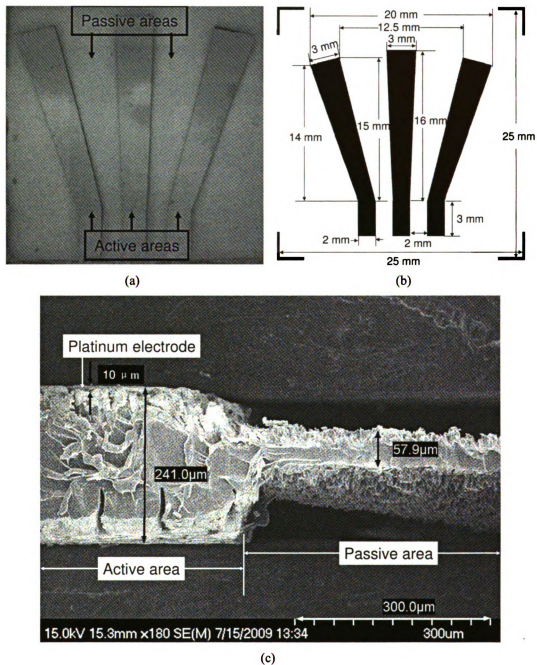


Figure 7.4: Patterned IPMC membrane. (a) Top view picture; (b) planar dimensions of the membrane; (c) SEM picture of the cross section.

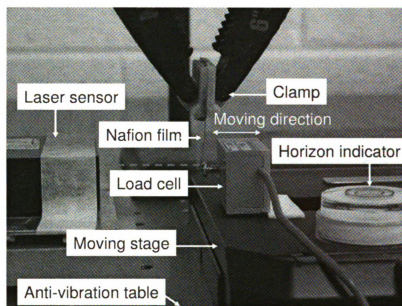


Figure 7.5: Experimental setup for measuring the stiffness of a Nafion film.

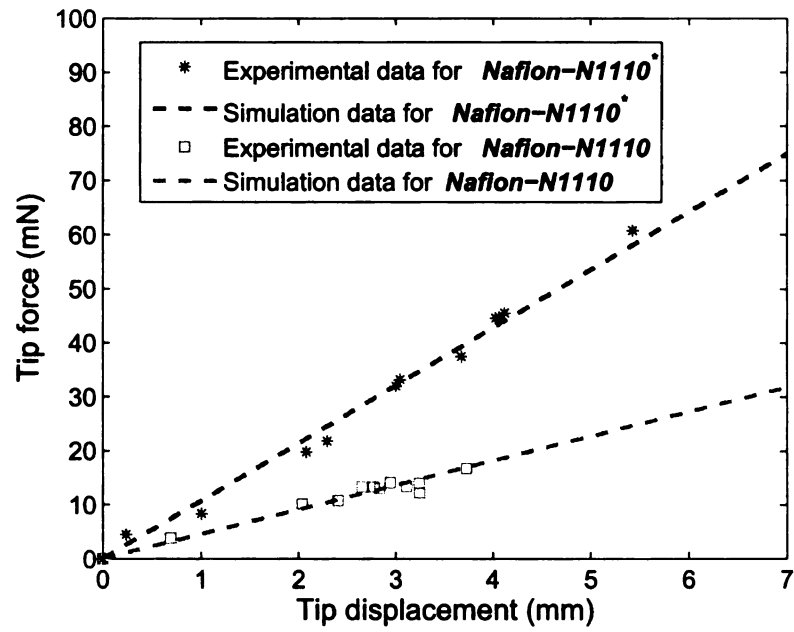
together with the results using linear fitting. The spring constant of the cantilever film is

$$k = \frac{YWT^3}{4L^3},$$

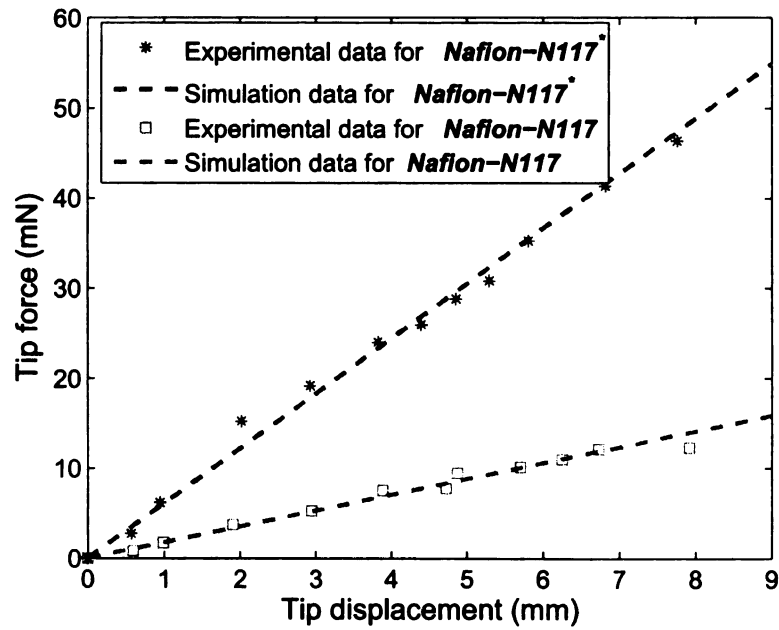
where Y , W , L , and T are the Young's modulus, width, length, and thickness of the Nafion film, respectively. Based on the measured spring constant and dimension parameters, we can calculate the Young's modulus. Table 7.2 shows the spring constant, dimensions, and Young's moduli of the Nafion films. It can be seen that the stiffness of an ion-exchanged Nafion film increases by about 2-3 times, compared to that of pure Nafion.

Table 7.2: Spring constant, dimensions, and Young's moduli of the Nafion films in stiffness testing. The ion-exchanged films are identified with an asterisk.

	k	W	L	T	Y
<i>Nafion - 117</i>	1.7 N/m	26 mm	20 mm	183 μ m	355 Mpa
<i>Nafion - 117*</i>	6.1 N/m	26 mm	19 mm	183 μ m	1.05 Gpa
<i>Nafion - N1110</i>	4.5 N/m	25 mm	20 mm	254 μ m	354 Mpa
<i>Nafion - N1110*</i>	10.7 N/m	25 mm	21 mm	254 μ m	966 Mpa



(a)



(b)

Figure 7.6: Results of stiffness measurement. (a) Nafion-N1110; (b) Nafion-117.

7.2.2 Swelling capacity change

We have further investigated the swelling capacity of Nafion before and after the ion-exchange step. Four samples as listed in Table 7.3 have been tested. Measurements are taken in the following steps. First, the surface areas of the samples in the dry condition are measured. Second, the samples are immersed in water for 5 minutes and then taken out for surface area measurement. Third, the samples are dried with paper towel and in air before being immersed in acetone. After 5 minutes, the samples are taken out of acetone and their surface areas are measured again. Table 7.3 shows the percentages of surface area change comparing to the original size, for the four samples, after being soaked in water and in acetone, respectively.

Table 7.3: Surface area changes of Nafion films in water and acetone. The ion-exchanged films are identified with an asterisk.

	With water	With acetone
<i>Nafion – 117</i>	+19.1%	+59.4%
<i>Nafion – 117*</i>	+0.7%	+0.8%
<i>Nafion – N1110</i>	+20.1%	+55.9%
<i>Nafion – N1110*</i>	+1.2%	+1.6%

It can be seen that while pure Nafion can expand by about 20% and 60% when soaked in water and in acetone, respectively, ion-exchanged Nafion experiences only 1-2% expansion under the same conditions. In other words, ion-exchanged Nafion has very low swellability in solvents, which is important in lithography based patterning of the film. One possible reason for the significantly reduced swelling capacity is that the film becomes stiffer and the swelling force is unable to enlarge the volume of the film. But the precise explanation of the phenomenon requires further study.

7.2.3 Impact of ion-exchange on lithography

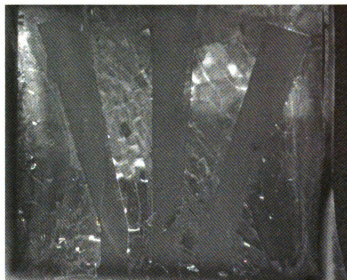
The impact of ion-exchange process on lithography has been investigated. First, we performed lithography on pure Nafion. When the sample was put into the developer, the film swelled and the PR patterns were destroyed by the swelling force, as shown in Fig. 7.7(a). Then we performed lithography on ion-exchanged Nafion. The patterning result was sharp, as shown in Fig. 7.7(b). It thus has demonstrated that the lithography of Nafion can be dramatically improved by the stiffening treatment using ion-exchange.

7.3 Characterization of Fabricated Artificial Fins

7.3.1 Characterization method

We have characterized the performance of fabricated MDOF IPMC actuators on producing sophisticated shape change. To capture the deformation, one may use multiple laser sensors to detect the bending displacement of active areas [43]. However, when the actuator generates large, complex deformation, some laser sensors can lose measurements. This approach is also expensive. Another approach is to use a CCD camera to capture the video of the actuator movement and then use image processing to extract the actuator movement [17].

The experimental setup we use to characterize MDOF IPMC actuators is shown in Fig. 7.8. The fabricated IPMC membrane is cut into a pectoral fin shape and its base is fixed by a multi-electrode clamp. The dimensions of the pectoral fin is shown in Fig. 7.8. To minimize the contact resistance, gold foils (0.1 mm thick) are used to make the contact electrodes. A CCD camera (Grasshopper, Point Grey Research) is oriented toward the edge of the fin. Sinusoid voltage inputs of the same amplitude and frequency but different phases are generated by the dSPACE system and applied to individual IPMC regions. The tip bending displacements of active areas are detected using the image edge detector (Vision



(a)



(b)

Figure 7.7: Lithography results. (a) With pure Nafion; (b) with ion-exchanged Nafion.

Assistant 8.5, National Instruments).

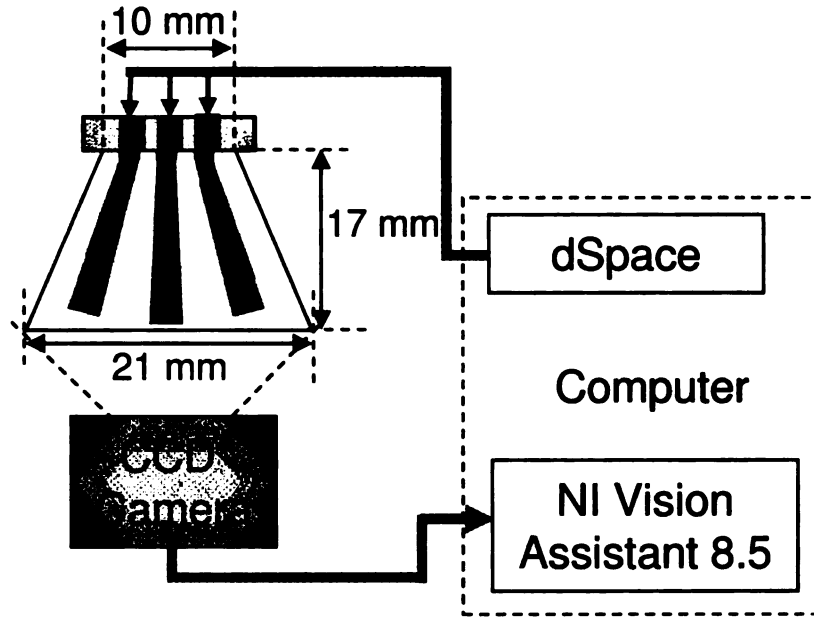


Figure 7.8: Experimental setup for characterizing MDOF IPMC actuators.

7.3.2 Demonstration of twisting and cupping

Actuation experiments are first conducted in air. The phase differences between the actuation signals applied to the three IPMC regions could be arbitrary. Since the goal here is to demonstrate sophisticated deformation and not to optimize the control input, we have restricted ourselves to the following particular class of phase patterns: the top IPMC leads the middle IPMC in phase by ϕ , while the bottom IPMC lags the middle IPMC in phase by ϕ . For such a phase pattern, we call it *phase ϕ* in short.

With all three IPMCs receiving inputs of the same phase (i.e., 0° phase), the fin generates bending. As this is not surprising (a single IPMC produces bending), we will not present the detailed results on bending here. An example of twisting is shown in Fig. 7.9, where the artificial fin has the same Nafion thickness, $85 \mu\text{m}$, in the active and passive areas. The voltages applied are sinusoidal signals with amplitude 3.0 V, frequency 0.3 Hz,

and phase 90° . The actuator clearly demonstrates a twisting motion. In order to quantify the twisting deformation, we define the twisting angle θ , which is formed by the line connecting the tips of top and bottom IPMCs with the vertical line m-n, as illustrated in Fig. 7.10(a). Note that the tip displacements d_1 , d_2 , d_3 of the IPMC regions are extracted from the video. Fig. 7.10(b) shows the time trajectories of the displacements and the corresponding twisting angle. The twisting angle achieved is 16° peak-to-peak, showing promise in robotic fish applications.

We have also verified the actuator's capability to generate the cupping motion. Fig. 7.11(a) illustrates the definition of the cupping angle α , formed by the two lines connecting the tip of the middle IPMC to the tips of the top and bottom IPMCs. Fig. 7.11(b) shows the trajectory of the cupping angle for the same sample mentioned above, where the actuation voltages have amplitude 3.0 V, frequency 0.3 Hz, and phase 180° .

7.3.3 Impact of the thickness in passive and active areas

To study the effects of thicknesses in active areas and passive areas on the actuation performance, we have fabricated 5 samples with different thicknesses in active areas and passive areas. Table 7.4 shows the thicknesses of the MDOF IPMC actuators. All actuators have the same planar dimensions as specify in Fig. 7.4(b). To compare the actuation performance of actuators with different thicknesses in the active areas, we have fabricated three samples ($S1$, $S2$, $S5$), where each sample has the same thickness in its active and passive areas. They are fabricated from Nafion-1110, Nafion-117, and Nafion-1135, respectively. To study the effects of different thickness in passive areas, we have fabricated three samples ($S2$, $S3$, $S4$) with the same thickness in the active areas ($170\ \mu\text{m}$) but different thicknesses in the passive areas.

The twisting angles generated by different samples with 0.3 Hz, 3 V and 90° phase voltage signals are shown in Fig. 7.12. From Fig. 7.12(a), for samples with uniform thickness, the thinner the sample is, the larger the deformation. This can be explained by that, under

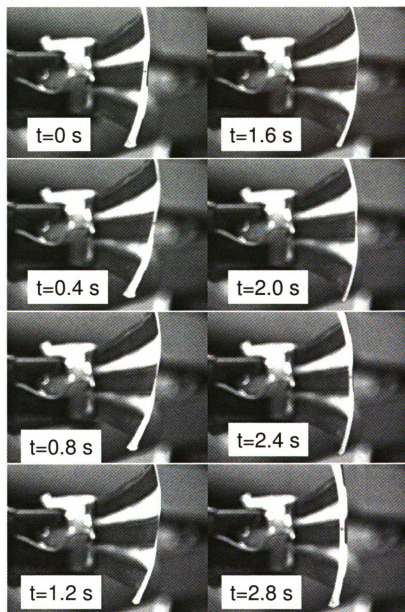


Figure 7.9: Snapshots of an actuated MDOF IPMC actuator, demonstrating the twisting motion.

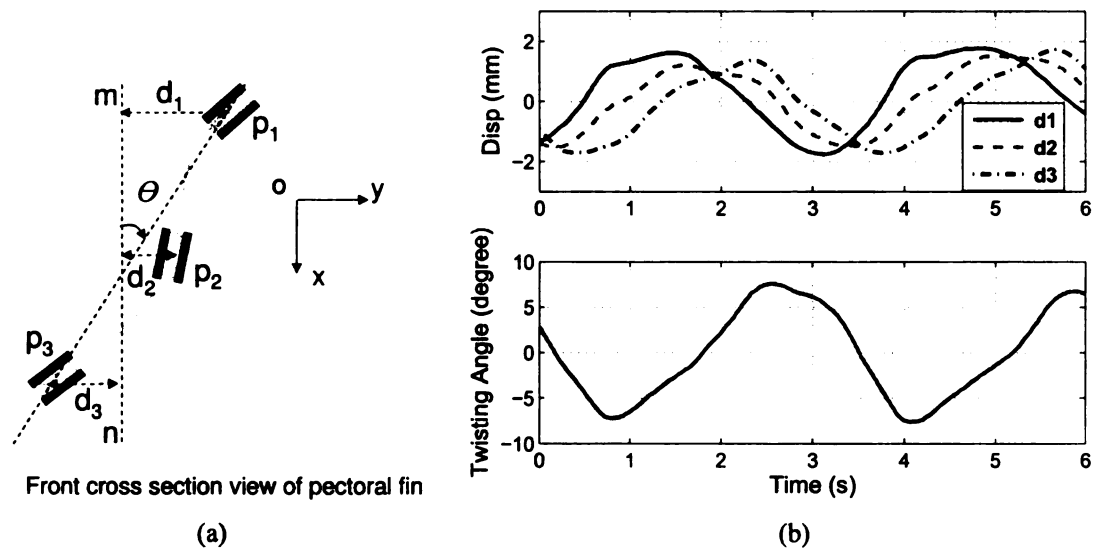


Figure 7.10: (a) Definitions of the tip displacements and the twisting angle; (b) trajectories of the tip displacements and the twisting angle corresponding to the voltage inputs as in Fig. 7.9.

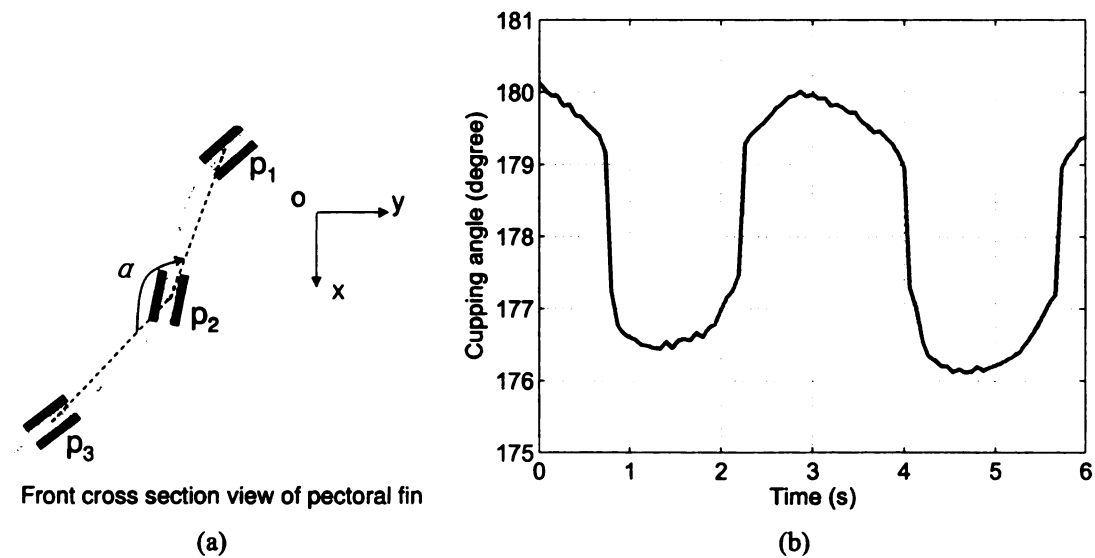


Figure 7.11: (a) Definition of the cupping angle; (b) the trajectory of the cupping angle for a sample with $85 \mu\text{m}$ thickness in both active and passive areas (voltages: 3 V, 0.3 Hz, 180°).

Table 7.4: Thicknesses of MDOF IPMC actuators.

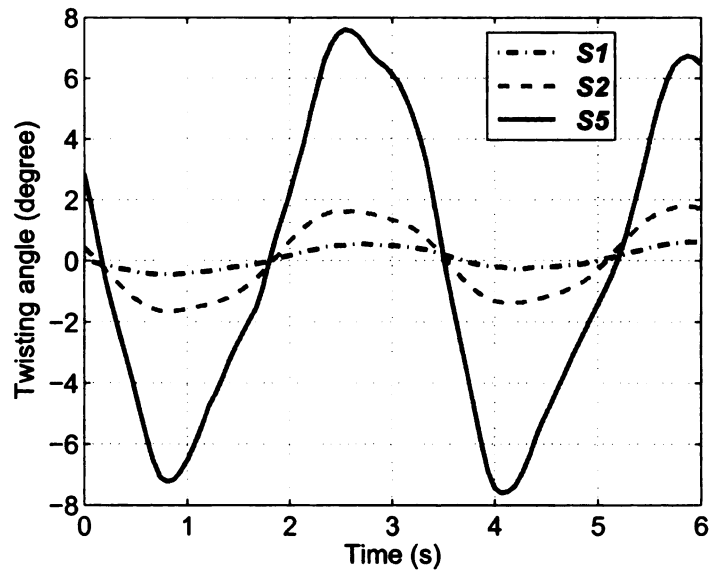
	Thickness in active area	Thickness in passive area
<i>S1</i>	240 μm	240 μm
<i>S2</i>	170 μm	170 μm
<i>S3</i>	170 μm	120 μm
<i>S4</i>	170 μm	60 μm
<i>S5</i>	85 μm	85 μm

the same voltage, a thinner sample experiences higher electrical field, and that a thinner sample is more compliant. From Fig. 7.12(b), it can be seen that for samples with the same thickness in active areas, with thinner passive regions, the deformation gets larger under the same voltage inputs. This has thus provided supporting evidence for our approach of modulating mechanical stiffness through plasma etching.

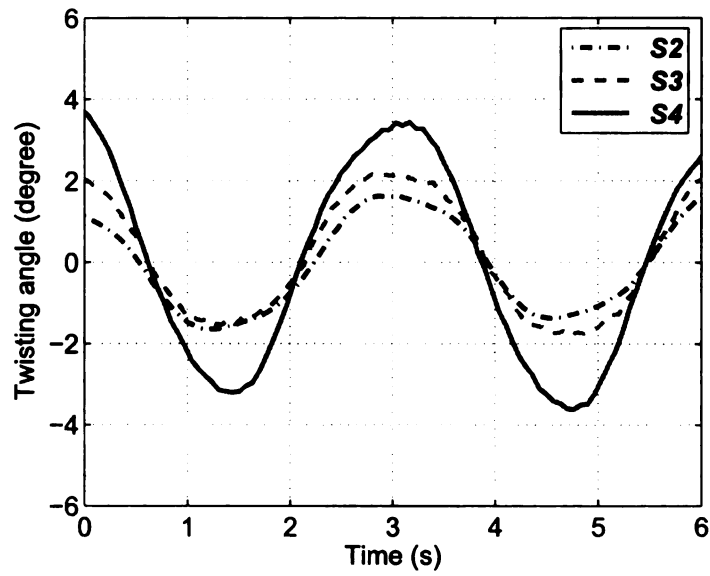
7.3.4 Impact of actuation signals

We have further experimented with actuation signals with different phases and amplitudes. Table 7.5 shows all the actuation signals we have used in the experiments. We have selected *S1* and *S5* as the test samples. All the signals have the same frequency 0.3 Hz. To study the effects of phase on the actuation performance, the voltage signals from *Control #1* to *Control #5* have the same amplitude (3 V) but different phases. To understand the performance of an MDOF IPMC actuator under different voltage levels, the voltage signals from *Control #5* to *Control #7* have the same phase (90°) but different amplitudes.

Fig. 7.13(a) shows the twisting angle of *S1* actuated under different voltage levels but with the same phase and frequency. While as expected, the higher the voltage, the larger the twisting, the gain in deformation does not appear to be linearly growing with the voltage level. Such nonlinearities will be examined in our future work. Fig. 7.13(b) shows the twisting angle of *S5* actuated by the same voltage amplitude but different phases. From the figure, 90° appears to be the best phase to generate the twisting motion, the reason of which



(a)



(b)

Figure 7.12: Twisting angles generated by different samples with 0.3 Hz, 3 V and 90° phase sinusoid voltage signals. (a) MDOF IPMC actuators with different thickness in both active areas and passive areas; (b) MDOF IPMC actuators with the same thickness in active areas (170 μm) but different thicknesses in passive areas.

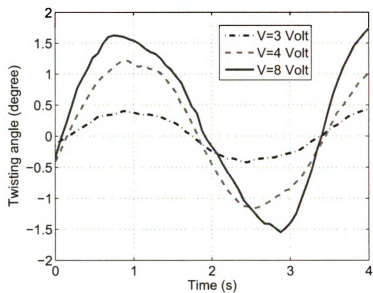
Table 7.5: Actuation signals.

	Frequency	Amplitude	Phase
<i>Control #1</i>	0.3 Hz	3 V	180°
<i>Control #2</i>	0.3 Hz	3 V	120°
<i>Control #3</i>	0.3 Hz	3 V	60°
<i>Control #4</i>	0.3 Hz	3 V	0°
<i>Control #5</i>	0.3 Hz	3 V	90°
<i>Control #6</i>	0.3 Hz	4 V	90°
<i>Control #7</i>	0.3 Hz	8 V	90°

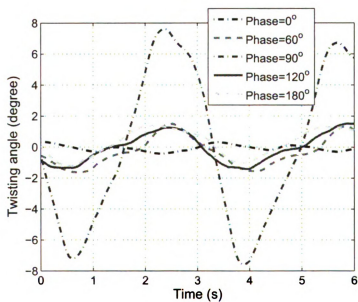
will be explored in our future modeling work.

7.3.5 DPIV study on MDOF IPMC actuation in water

In the interest of robotic fish applications, we have also conducted preliminary study of underwater operation of the MDOF IPMC actuators. Digital Particle Image Velocimetry (DPIV) system is used to observe fluid motion generated by the actuator. In a DPIV system, small particles are dispersed in a fluid and a laser sheet is created in the fluid to illuminate the particles. Processing of images taken in quick successions can reveal the movement of particles and provide information about the flow fluid. We have tested sample *S5* in water, by applying voltage signals (4 V, 0.3 Hz, and 90° phase) to the actuator. Fig. 7.14(a) shows the snapshots of the MDOF IPMC actuation in water. Fig. 7.14(b) shows the velocity field of the water around the actuator. It demonstrates that the MDOF IPMC actuator can make 3-D deformation in water and can generate some interesting flow patterns around it. The connections between the flow patterns and the actuator deformations are a subject of future investigation.



(a)



(b)

Figure 7.13: (a) $S1$ actuated by voltage signals with different amplitudes but the same frequency (0.3 Hz) and phase (90°); (b) $S5$ actuated by voltage signals with the same amplitude (3 V) and frequency (0.3 Hz) but different phases.

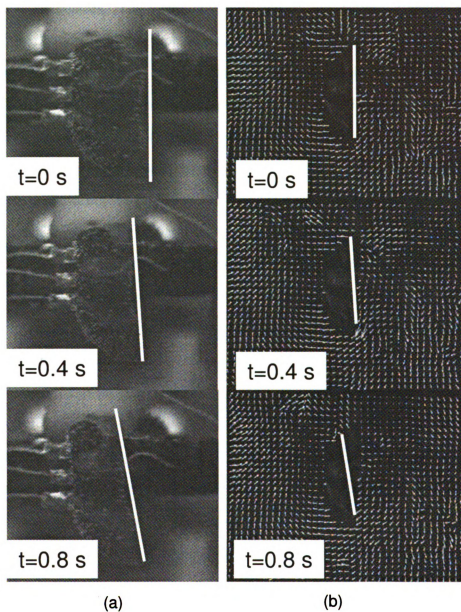


Figure 7.14: DPIV study of MDOF IPMC actuator operating in water. (a) Actuation of the actuator in water (the edge of the actuator is highlighted); (b) Velocity field of the fluid.

7.4 Chapter Summary

In this chapter we have presented a new process flow for monolithic, batch-fabrication of MDOF IPMC actuators. The methodology effectively incorporates standard techniques for IPMC fabrication and lithography-based micromachining processes. The actuator consists of multiple IPMC islands coupled through a passive membrane. The size and shape of each IPMC island are defined through photolithography and thus the approach is scalable. A key innovation in the developed process is to stiffen the Nafion film through an ion-exchange step, which virtually eliminates swelling in solvents and enables successful patterning. Tailoring the thickness and thus the rigidity of the passive area is another novel aspect of the proposed fabrication method. The fabrication method has been applied to manufacture prototypes of biomimetic fins, with demonstrated capability of producing complex deformation modes such as twisting and cupping.

The prototypes fabricated in this work have dimensions of centimeters because of our interest in biomimetic actuation for robotic fish applications. The developed fabrication process, however, can be directly applied to produce microscale devices since it is based on microelectromechanical systems (MEMS) processes. We also note that, while commercially available Nafion films have been used as the base material in our work, the approach can be easily extended to Nafion membranes obtained through casting, and to other types of ion-exchange membranes (e.g., Flemion).

Future work includes understanding and modeling of MDOF IPMC actuators, by extending the authors prior work [21] on modeling of IPMC beams. The interactions between the active IPMC regions and the passive regions will be a focus of study. We will also investigate systematically the hydrodynamics in underwater operation of such MDOF IPMC actuators using combination of analytical modeling, computational fluid dynamics (CFD) modeling, and DPIV studies, and explore the use of these actuators in biomimetic robotic fish.

Chapter 8

Conclusions and Future Work

8.1 Conclusions

In this work, a systems perspective has been taken to address the challenges in realizing IPMC-based smart microsystems. To obtain a faithful and practical mathematical model for IPMC, we have developed a physics-based, control-oriented modeling approach for IPMC sensors and actuators. The effects of distributed surface resistance have been considered in the models. The models are amenable to model reduction, geometrically scalable, and practical in real-time control. The actuation model of IPMC has been applied to the modeling of robotic fish propelled by IPMC, which has further validated the modeling approach. Since traditional sensors cannot be embedded easily into bio/micro systems, we have developed a compact sensing scheme for IPMC. We have further developed a process for monolithic fabrication for IPMCs capable of generating complex deformations. Artificial pectoral fins are fabricated and characterized, which have demonstrated bending, twisting, and cupping motions.

8.2 Future Work

Future work can be pursued in the following three directions. First, the fabrication of the artificial pectoral fins can be improved through enhanced lithography and electrode plating techniques. The analysis of DPIV results for the pectoral fins will be another integral part of this work, which can lead to the control strategies for the fin in robotic fish applications. Second, it will be interesting to extend the developed planar fabrication technology to 3-dimensional fabrication technology which can be used in microfabricating more complex bio-inspired IPMC materials, such as artificial lateral lines. The lateral line will have multiple micro IPMC sensing hairs standing on the substrate to sense fluid flow. Third, nonlinear models are necessary when a relatively high voltage is applied and a large deformation is generated. Many nonlinearities such as hysteresis, nonlinear elasticity of the polymer, and nonlinear capacitance of IPMC are involved in IPMC. Model-based nonlinear control should be explored to effectively control IPMC in applications involving large deformations.

Appendix A

Appendix for Chapter 2

A.1 Derivation of impedance model (2.31)

From (2.28) and (2.29),

$$\begin{aligned} i_p(z, s) &= \frac{\phi(h, z, s)}{h} \frac{sW \kappa_e \gamma(s) (s + K)}{(\gamma(s)s + K \tanh(\gamma(s)))} \\ &= \left(\frac{V(s)}{2} - \int_0^z \frac{r'_1}{W} i_s(\tau, s) d\tau - \frac{r'_2}{W} i_p(z, s) \right) \theta(s), \end{aligned}$$

where the second equality is from (2.27) and (2.34). This results in

$$i_p(z, s) = \left(\frac{V(s)}{2} - \int_0^z \frac{r'_1}{W} i_s(\tau, s) d\tau \right) \frac{\theta(s)}{1 + r_2 \theta(s)}. \quad (\text{A.1})$$

From (2.26) and (2.30), one obtains

$$\begin{aligned} i_k(z, s) &= \frac{\phi(h, z, s) - \phi(-h, z, s) + 2i_p(z, s)r'_2/W}{R'_p/W} \\ &= \frac{2\phi(h, z, s) + 2i_p(z, s)r'_2/W}{R'_p/W} \\ &= \frac{2W}{R'_p} \left(\frac{V(s)}{2} - \int_0^z \frac{r'_1}{W} i_s(\tau, s) d\tau \right), \end{aligned} \quad (\text{A.2})$$

where the last equality is from (2.27).

Combining (2.25), (A.1), (A.2), one gets

$$-\frac{\partial i_s(z,s)}{\partial z} = \frac{A(s)V(s)}{2} - B(s) \int_0^z i_s(\tau,s) d\tau, \quad (\text{A.3})$$

where $A(s)$ and $B(s)$ are as defined in (2.32) and (2.33).

Eq. (A.3) is an integro-differential equation for i_s . To solve this equation, we introduce the unilateral Laplace transform for functions of the length coordinate z . The new Laplace variable will be denoted as p since s has already been used for the transform of time functions. For instance, the transform of $i_s(z,s)$ will be defined as

$$I_s(p,s) \triangleq \int_0^\infty i_s(z,s) e^{-pz} dz.$$

Now perform the Laplace transform with respect to the z variable on both sides of (A.3). Using properties of Laplace transforms, one gets

$$pI_s(p,s) - i_s(0,s) = -\frac{A(s)V(s)}{2} \frac{1}{p} + B(s) \frac{I_s(p,s)}{p}. \quad (\text{A.4})$$

Solving for $I_s(p,s)$, one obtains

$$I_s(p,s) = \frac{p}{p^2 - B(s)} i_s(0,s) - \frac{1}{p^2 - B(s)} \frac{A(s)V(s)}{2}, \quad (\text{A.5})$$

which can be rewritten through partial fraction expansion as:

$$\begin{aligned} I_s(p,s) = & \frac{A(s)V(s)}{2} \left(\frac{q_1(s)}{p - \sqrt{B(s)}} + \frac{q_2(s)}{p + \sqrt{B(s)}} \right) \\ & + i_s(0,s) \left(\frac{0.5}{p - \sqrt{B(s)}} + \frac{0.5}{p + \sqrt{B(s)}} \right), \end{aligned} \quad (\text{A.6})$$

with

$$q_1(s) = -\frac{1}{2\sqrt{B(s)}}, \quad q_2(s) = \frac{1}{2\sqrt{B(s)}}.$$

The surface current $i_s(z, s)$ is then obtained from (A.6) using the inverse Laplace transform of $I_s(p, s)$:

$$i_s(z, s) = i_s(0, s) \cosh\left(\sqrt{B(s)}z\right) - \frac{A(s)V(s)}{2\sqrt{B(s)}} \sinh\left(\sqrt{B(s)}z\right). \quad (\text{A.7})$$

Using the boundary condition $i_s(L, s) = 0$, one obtains:

$$i_s(0, s) = \frac{V(s)A(s) \tanh\left(\sqrt{B(s)}L\right)}{2\sqrt{B(s)}}. \quad (\text{A.8})$$

Appendix B

Appendix for Chapter 4

B.1 Derivation of $M(L, s)$, $F_c(L, s)$, $F_d(z, s)$ in Section 4.2.3

Based on the principle of replacement in Section 4.2.3, one gets, for $0 \leq z \leq L$,

$$M_{\text{IPMC}}(z, s) = \int_z^L F_d(\tau)(\tau - z) d\tau + F_c(L, s)(L - z) + M(L, s).$$

At $z = L$, one gets

$$M(L, s) = M_{\text{IPMC}}(L, s),$$

which is (4.23). Then one takes the derivative with respect to z on both sides of (4.22):

$$\begin{aligned} \frac{\partial M_{\text{IPMC}}(z, s)}{\partial z} &= \int_z^L \frac{\partial (F_d(\tau)(\tau - z))}{\partial z} d\tau - F_c(L, s) \\ &= - \int_z^L F_d(\tau) d\tau - F_c(L, s). \end{aligned} \tag{B.1}$$

Letting $z = L$ in (B.1), one gets

$$F_c(L, s) = - \frac{\partial M_{\text{IPMC}}(z, s)}{\partial z} \Big|_{z=L} = 0.$$

Finally, Eq. (4.22) is obtained by taking the derivative with respect to z on both sides of (B.1).

B.2 Derivation of $H_{fi}(s)$

With (4.22), (4.21), and definitions of a, b, c in (4.27) and (4.28), Eq. (4.24) can be written as

$$f_{1i}(s) = \frac{V(s)}{M_i} \int_0^L (a \cosh(cz) - b \sinh(cz)) \varphi_i(z) dz + \frac{M(L, s) \varphi_i'(L)}{M_i}. \quad (\text{B.2})$$

Denote

$$f_{di} = \int_0^L (a \cosh(cz) - b \sinh(cz)) \varphi_i(z) dz. \quad (\text{B.3})$$

Then (B.2) can be written as:

$$f_i(s) = \frac{V(s)}{M_i} f_{di} + \frac{M(L, s) \varphi_i'(L)}{M_i}. \quad (\text{B.4})$$

With definition of $\varphi_i(z)$ in (4.15), Eq. (B.3) can be written as:

$$f_{di} = \int_0^L \begin{pmatrix} a (\cosh(cz) \cosh(\lambda_i z) - \cosh(cz) \cos(\lambda_i z)) - \\ \beta_i a (\cosh(cz) \sinh(\lambda_i z) - \cosh(cz) \sin(\lambda_i z)) \\ - b (\sinh(cz) \cosh(\lambda_i z) - \sinh(cz) \cos(\lambda_i z)) \\ + \beta_i b (\sinh(cz) \sinh(\lambda_i z) - \sinh(cz) \sin(\lambda_i z)) \end{pmatrix} dz$$

$$= \int_0^L \left(\begin{array}{l} a \left(\begin{array}{l} \cosh(cz + \lambda_i z) + \cosh(cz - \lambda_i z) \\ -\cosh(cz + j\lambda_i z) - \cosh(cz - j\lambda_i z) \end{array} \right) - \\ \beta_i a \left(\begin{array}{l} \sinh(cz + \lambda_i z) - \sinh(cz - \lambda_i z) \\ +j \sinh(cz + j\lambda_i z) - j \sinh(cz - j\lambda_i z) \end{array} \right) \\ -b \left(\begin{array}{l} \sinh(cz + \lambda_i z) + \sinh(cz - \lambda_i z) \\ -\sinh(cz + j\lambda_i z) - \sinh(cz - j\lambda_i z) \end{array} \right) + \\ \beta_i b \left(\begin{array}{l} \cosh(cz + \lambda_i z) - \cosh(cz - \lambda_i z) \\ +j \cosh(cz + j\lambda_i z) - j \cosh(cz - j\lambda_i z) \end{array} \right) \end{array} \right) dz. \quad (\text{B.5})$$

After integrating (B.5), we get

$$f_{di} = \frac{(a-b)(a_L + b_L - c_L - d_L) - \beta_i(a-b)(a_L - b_L + jc_L - jd_L)}{-\beta_i(a-b)(a_L - b_L + jc_L - jd_L)}, \quad (\text{B.6})$$

where a_L , b_L , c_L , and d_L are defined in (4.29) and (4.30). With (4.23) and (B.6), Eq. (B.4) can be written as

$$f_{1i}(s) = \frac{V(s)}{2M_i} \left(\begin{array}{l} (a-b)(a_L + b_L - c_L - d_L) \\ -\beta_i(a-b)(a_L - b_L + jc_L - jd_L) \end{array} \right) + \frac{\alpha_0 W K k_e (\gamma(s) - \tanh(\gamma(s)))}{(s\gamma(s) + K \tanh(\gamma(s)))} \frac{\phi_i'(L)V(s)}{(1 + r_2 \theta(s)) \cosh(cL)}. \quad (\text{B.7})$$

Then one can obtain the transfer functions (4.26) from (B.7).

B.3 Derivation of Actuation Model for Hybrid Tail

With (4.24), Eq. (4.39) can be written as

$$f_{2i}(s) = f_{1i}(s) + \frac{F_{\text{tail}}(s) \varphi_i(L_0) + M_{\text{tail}}(s) \varphi_i'(L_0)}{M_i}. \quad (\text{B.8})$$

With (4.25), (4.37), Eq. (B.8) can be written as

$$f_{2i} = H_{fi}(s) V(s) - \frac{M_s}{M_i} \left[\begin{aligned} & \left[\varphi_i'(L_0) k_a + \varphi_i(L_0) k_b \right] w'(L_0, s) \\ & + \left[\varphi_i'(L_0) k_b + \varphi_i(L_0) k_c \right] w(L_0, s) \end{aligned} \right]. \quad (\text{B.9})$$

The general coordinate $q_{2i}(s)$ is

$$q_{2i}(s) = Q_i(s) f_{2i}(s). \quad (\text{B.10})$$

Then with (B.9) and (B.10), Eq. (4.14) can be written as

$$w(z, s) = \sum_{i=1}^{\infty} \varphi_i(L_0) Q_i(s) H_{fi}(s) V(s) - \sum_{i=1}^{\infty} \frac{M_s \varphi_i(L_0) Q_i(s)}{M_i} \left[\begin{aligned} & \left[\varphi_i'(L_0) k_a + \varphi_i(L_0) k_b \right] w'(L_0, s) \\ & + \left[\varphi_i'(L_0) k_b + \varphi_i(L_0) k_c \right] w(L_0, s) \end{aligned} \right]. \quad (\text{B.11})$$

From Eq. (4.31), Eq. (B.11) can be written as

$$w(z, s) = H_1(s) V(s) - \sum_{i=1}^{\infty} \frac{M_s \varphi_i(L_0) Q_i(s)}{M_i} \left[\begin{aligned} & \left[\varphi_i'(L_0) k_a + \varphi_i(L_0) k_b \right] w'(L_0, s) \\ & + \left[\varphi_i'(L_0) k_b + \varphi_i(L_0) k_c \right] w(L_0, s) \end{aligned} \right], \quad (\text{B.12})$$

and with (4.32), the slope can be written as

$$w'(z, s) = H_{1d}(s)V(s) - \sum_{i=1}^{\infty} \frac{M_s \phi_i'(L_0) Q_i(s)}{M_i} \left[\begin{aligned} & \left[\phi_i'(L_0) k_a + \phi_i(L_0) k_b \right] w'(L_0, s) \\ & + \left[\phi_i'(L_0) k_b + \phi_i(L_0) k_c \right] w(L_0, s) \end{aligned} \right]. \quad (\text{B.13})$$

With the definition of $A_s, E_s, B_s, C_s, F_s, J_s$ in (4.42)-(4.46), one can write (B.12) and (B.13) by

$$w(L_0, s) = A_s V(s) - B_s w'(L_0, s) - C_s w(L_0, s), \quad (\text{B.14})$$

$$w'(L_0, s) = E_s V(s) - F_s w'(L_0, s) - J_s w(L_0, s). \quad (\text{B.15})$$

Solving (B.14) and (B.15) for $w(L_0, s)$ and $w'(L_0, s)$ gives

$$\begin{aligned} w(L_0, s) &= \frac{(1 + F_s) A_s - B_s E_s}{(1 + C_s)(1 + F_s) - B_s J_s} V(s), \\ w'(L_0, s) &= \frac{(1 + C_s) E_s - A_s J_s}{(1 + C_s)(1 + F_s) - B_s J_s} V(s). \end{aligned}$$

Then one can obtain the transfer functions (4.40) and (4.41).

Appendix C

Appendix for Chapter 5

C.1 Proof of Proposition 1

Proof. Define

$$\chi(p) = \frac{p}{a} - \frac{b}{a^2} \ln\left(\frac{a}{b}p + 1\right) - k, \quad p > -\frac{b}{a}. \quad (\text{C.1})$$

Let's start with the case when $k > 0$. Because $\chi(0) = -k < 0$, $\chi(p)$ is continuous in $(-\frac{b}{a}, +\infty)$ and

$$\lim_{p \rightarrow +\infty} \chi(p) = +\infty > 0, \quad \lim_{p \rightarrow -\frac{b}{a}} \chi(p) = +\infty > 0,$$

there exist $p_1 \in (-\frac{b}{a}, 0)$, $p_2 \in (0, +\infty)$ such that $\chi(p_1) = 0$ and $\chi(p_2) = 0$. Since

$$\chi'(p) = \frac{p}{ap + b}, \quad (\text{C.2})$$

with $p > -\frac{b}{a}$, we can get $\chi'(p) > 0$ when $p > 0$ and $\chi'(p) < 0$ when $0 > p > -\frac{b}{a}$. So $\chi(p)$ is monotonically increasing in $(0, +\infty)$, and monotonically decreasing in $(-\frac{b}{a}, 0)$. Then p_1 and p_2 should be unique. When $k = 0$, and $\chi(0) = 0$, then $p_1 = p_2 = 0$. \square \square

C.2 Derivation of Eq. (5.17)

Define $D \triangleq p_2 - p_1$. Eq. (5.12) can then be written as $V = \frac{D}{b}$. From Fig. 5.4,

$$\frac{p_2 - p_1}{\eta_2 - \eta_1} = a, \quad (\text{C.3})$$

where η_1 and η_2 are the η -coordinates corresponding to p_1 and p_2 , respectively, in Fig. 5.4.

Eq. (C.3) implies

$$\frac{D}{\frac{b}{a^2} \left(\ln \left(\frac{a}{b} p_2 + 1 \right) - \ln \left(\frac{a}{b} p_1 + 1 \right) \right)} = a. \quad (\text{C.4})$$

With $p_2 = D + p_1$ and (C.4), one can solve p_1 in terms of D ,

$$p_1 = \begin{cases} \frac{D}{\frac{a}{b} D - 1} - \frac{b}{a}, D > 0 \\ 0, D = 0 \end{cases}. \quad (\text{C.5})$$

When $D \rightarrow 0$, with l'Hospital's rule,

$$\lim_{D \rightarrow 0} \left(\frac{D}{\frac{a}{b} D - 1} - \frac{b}{a} \right) = \lim_{D \rightarrow 0} \left(\frac{1}{\frac{a}{b} - \frac{a}{b} D} \right) - \frac{b}{a} = 0.$$

So p_1 is still a continuous function of D . Since

$$\frac{b}{a^2} \ln \left(\frac{a}{b} p_1 + 1 \right) = \frac{p_1}{a} - k, \quad (\text{C.6})$$

from (C.5), one can get

$$\frac{b}{a^2} \ln \left(\frac{a}{b} \left(\frac{D}{\frac{a}{b} D - 1} - \frac{b}{a} \right) + 1 \right) = \frac{1}{a} \left(\frac{D}{\frac{a}{b} D - 1} - \frac{b}{a} \right) - k. \quad (\text{C.7})$$

Since $D = bV$, one can get Eq. (5.17) from Eq. (C.7). Note that with l'Hospital's rule,

$$\lim_{V \rightarrow 0} \left(\frac{aV}{e^{aV} - 1} \right) = \lim_{V \rightarrow 0} \left(\frac{a}{ae^{aV}} \right) = 1 ,$$

one gets

$$\lim_{V \rightarrow 0} \left(\frac{b}{a^2} \left(\frac{aV}{e^{aV} - 1} - \ln \left(\frac{aV}{e^{aV} - 1} \right) - 1 \right) \right) = 0 .$$

So k is a continuous function of V .

BIBLIOGRAPHY

- [1] K. Abdelnour, E. Mancina, S. D. Peterson, and M. Porfiri. Hydrodynamics of underwater propulsors based on ionic polymer metal composites: A numerical study. *Smart Materials and Structures*, 18:085006:1–11, 2009.
- [2] B. J. Akle, M. D. Bennett, and D. J. Leo. High-strain ionomeric-ionic liquid electroactive actuators. *Sensors and Actuators A*, 126:173–181, 2006.
- [3] Barbar J. Akle. *Characterization and Modeling of the Ionomer-Conductor Interface in Ionic Polymer Transducers*. PhD thesis, Virginia Polytechnic Institute and State University, 2005.
- [4] G. Alici, G. Spinks, N. N. Huynh, L. Sarmadi, and R. Minato. Establishment of a biomimetic device based on tri-layer polymer actuators\propulsion fins. *Bioinspiration & Biomimetics*, 2:S18–S30, 2007.
- [5] P. V. Alvarado and K. Youcef-Toumi. Design of machines with compliant bodies for biomimetic locomotion in liquid environments. *Journal of Dynamic Systems, Measurement, and Control*, 128:3–13, 2006.
- [6] Mart Anton, Andres Punning, Alvo Aabloo, Madis Listak, and Maarja Kruusmaa. Towards a biomimetic EAP robot. In *Proc. of Towards the Autonomous Mobile Robots*, pages 1–7, 2004.
- [7] G. A. Baker and P. Graves-Morris. *Padé Approximants*. Cambridge University Press, New York, 1996.
- [8] Y. Bar-Cohen. Electroactive polymers as artificial muscles - capabilities, potentials and challenges. In Y. Osada, editor, *Handbook on Biomimetics*, pages 1–13 (Chapter 8). NTS Inc., 2000.
- [9] Y. Bar-Cohen. *Electroactive Polymers as Artificial Muscles - Capabilities, Potentials and Challenges*. Handbook on Biomimetics. NTS Inc., 2000.
- [10] Y. Bar-Cohen. Electric flex. *IEEE Spectrum*, 41(6):29–33, 2004.

- [11] M. D. Bennett and D. Leo. Ionic liquids as stable solvents for ionic polymer transducers. *Sensors and Actuators A: Physical*, 115:79–90, 2004.
- [12] C. Bonomo, L. Fortuna, P. Giannone, S. Graziani, and S. Strazzeri. A model for ionic polymer metal composites as sensors. *Smart Materials and Structures*, 15:749–758, 2006.
- [13] C. Bonomo, L. Fortuna, P. Giannone, S. Graziani, and S. Strazzeri. A nonlinear model for ionic polymer metal composites as actuators. *Smart Materials and Structures*, 16:1–12, 2007.
- [14] C. Bonomo, C. Del Negro, and L. Fortuna S. Graziani. Characterization of IPMC strip sensorial properties: Preliminary results. In *Proceedings of the 2003 International Symposium on Circuits and Systems*, volume 4, pages IV–816– IV–819, 2003.
- [15] Frdric Boyer, Mathieu Porez, and Wisama Khalil. Macro-continuous computed torque algorithm for a three-dimensional eel-like robot. *IEEE Transactions on Robotics*, 22(4):763–775, August 2006.
- [16] Paola Brunetto, Luigi Fortuna, Salvatore Graziani, and Salvatore Strazzeri. A model of ionic polymer-metal composite actuators in underwater operations. *Smart Materials and Structures*, 17(2):1–12, 2008.
- [17] G. Del Bufalo, L. Placidi, and M. Porfiri. A mixture theory framework for modeling the mechanical actuation of ionic polymer metal composites. *Smart Materials and Structures*, 17:045010:1–14, June 2008.
- [18] Z. Chen, Y. Shen, N. Xi, and X. Tan. Integrated sensing for ionic polymer-metal composite actuators using PVDF thin films. *Smart Materials and Structures*, 16(2):S262–S271, 2007.
- [19] Z. Chen, X. Tan, and M. Shahinpoor. Quasi-static positioning of ionic polymer-metal composite (IPMC) actuators. In *Proceedings of the IEEE/ASME International Conference on Advanced Intelligent Mechatronics*, pages 60–65, Monterey, CA, 2005.
- [20] Z. Chen, X. Tan, A. Will, and C. Ziel. A dynamic model for Ionic Polymer-Metal Composite sensors. *Smart Materials and Structures*, 16(4):1477–1488, 2007.
- [21] Zheng Chen and Xiaobo Tan. A control-oriented and physics-based model for ionic polymer-metal composite actuators. *IEEE/ASME Transactions on Mechatronics*, 13(5):519–529, 2008.
- [22] C.K. Chung, P.K. Fung, Y.Z. Hong, M.S. Ju, C.C.K. Lin, and T.C. Wu. A novel fabrication of ionic polymer-metal composites (IPMC) actuator with silver nano-powders. *Sensors and Actuators B: Chemical*, 117:367–375, November 2006.
- [23] R. V. Churchill. *Operational Mathematics*. McGraw-Hill, New York, 3rd edition, 1972.

- [24] R. W. Clough and J. Penzien. *Dynamics of Structures*. McGraw-Hill, 1993.
- [25] B. E. Conway. *Electrochemical Supercapacitors Scientific Fundamentals and Technological Applications*. Springer, 1999.
- [26] H. Darcy. *Les Fontaines Publiques de la Ville de Dijon*. Dalmont, Paris, 1856.
- [27] P. G. de Gennes, K. Okumura, M. Shahinpoor, and K.J. Kim. Mechanoelectric effects in ionic gels. *Europhysics Letters*, 50(4):513–518, 2000.
- [28] Deniz Dogruer, Joonsoo Lee, Woosoon Yim, KwangJ Kim, and Doyeon Kim. Fluid interaction of segmented ionic polymerCmetal composites under water. *Smart Materials and Structures*, 16:S220–S226, 2007.
- [29] J.J. Dosch, D.J. Inman, and E. Garcia. A self-sensing piezoelectric actuator for collocated control. *Journal of Intelligent Material Systems and Structures*, 3:166–185, 1992.
- [30] Y. Fang, T. J. Pence, and X. Tan. Nonlinear elastic modeling of differential expansion in trilayer conjugated polymer actuators. *Smart Materials and Structures*, 17:065020, 2008.
- [31] Y. Fang, X. Tan, Y. Shen, N. Xi, and G. Alici. A scalable model for trilayer conjugated polymer actuators and its experimental validation. *Materials Science and Engineering: C*, 28(3):421–428, 2008.
- [32] K. Farinholt and D.J. Leo. Modeling of electromechanical charge sensing in ionic polymer transducers. *Mechanics of Materials*, 36:421–433, 2004.
- [33] Kevin M. Farinholt. *Modeling and Characterization of Ionic Polymer Transducers for Sensing and Actuation*. PhD thesis, Virginia Polytechnic Institute and State University, 2005.
- [34] Guo-Hua Feng and Ri-Hong Chen. Improved cost-effective fabrication of arbitrarily shaped μ IPMC transducers. *Journal of Micromechanics and Microengineering*, 18(1):015016:1–9, January 2008.
- [35] F. E. Fish and G. V. Lauder. Passive and active flow control by swimming fishes and mammals. *Annual Review of Fluid Mechanics*, 38:193–224, 2006.
- [36] G. F. Franklin, J. D. Powell, and A. Emami-Naeini. *Feedback Control of Dynamic Systems*. Pearson Education, Inc., Upper Saddle River, NJ, 5th edition, 2006.
- [37] J. M. Gere and S.P. Timoshenko. *Mechanics of Materials*. PWS Publishing Company, Boston, MA, fourth edition, 1997.
- [38] P.E. Grimshaw, J.H. Nussbaum, and A.J. Grodzinsky. Kinetics of electrically and chemically induced swelling in polyelectrolyte gels. *Journal of Chemical Physics*, 93:4462–4472, 1990.

- [39] S. Guo, T. Fukuda, and K. Asaka. A new type of fish-like underwater microrobot. *IEEE/ASME Transactions on Mechatronics*, 8(1):136–141, 2003.
- [40] H. Hu, J. Liu, I. Dukes, and G. Francis. Design of 3D swim patterns for autonomous robotic fish. In *Proceedings of the 2006 IEEE/RSJ International Conference on Intelligent Robots and Systems*, pages 2406–2411, Beijing, China, 2006.
- [41] J.-H. Jeon, I.-K. Oh, J.-H. Han, and S.-W. Lee. Development of bio-mimetic patterned IPMC actuators with multiple electrodes. *Key Engineering Materials*, 334-335:1005–1008, 2007.
- [42] Jin-Han Jeon and Il-Kwon Oh. Selective growth of platinum electrodes for MDOF IPMC actuators. *Thin Solid Films*, 517:5288–5292, 2009.
- [43] Jin-Han Jeon, Sung-Won Yeom, and Il-Kwon Oh. Fabrication and actuation of ionic polymer metal composites patterned by combining electroplating with electroless plating. *Composites Part A: Applied Science and Manufacturing*, 39:588–596, 2008.
- [44] Norihiro Kamamichi, Masaki Yamakita, Kinji Asaka, and Zhi-Wei Luo. A snake-like swimming robot using IPMC Actuator//Sensor. In *Proceedings of the IEEE Conference on Robotics and Automation*, pages 1812–1817, Orlando, Florida, May 2006.
- [45] R. Kanno, A. Kurata, S. Tadokoro, T. Takamori, , and K. Oguro. Characteristics and modeling of ICPF actuator. In *Proceedings of the Japan-USA Symposium on Flexible Automation*, pages 219–225, 1994.
- [46] R. Kanno, S. Tadokoro, T. Takamori, and M. Hattori. Linear approximate dynamic model of IPMC (ionic conducting polymer gel film) actuator. In *Proceedings of the IEEE International Conference on Robotics and Automation*, pages 219–225, Minneapolis, MN, 1996.
- [47] B. Kim, D. Kim, J. Jung, and J. Park. A biomimetic undulatory tadpole robot using ionic polymer-metal composite actuators. *Smart Materials and Structures*, 14:1579–1585, 2005.
- [48] B. Kim, J. Ryu, Y. Jeong, Y. Tak, B. Kim, and J.-O. Park. A ciliary based 8-legged walking micro robot using cast IPMC actuators. In *Proceedings of IEEE International Conference on Robots and Automation*, pages 2940–2945, 2003.
- [49] K. J. Kim and M. Shahinpoor. Ionic polymer-metal composites: II. manufacturing techniques. *Smart Materials and Structures*, 12:65–79, 2003.
- [50] Kwang J. Kim and Mohsen Shinpoor. A novel method of manufacturing three-dimensional ionic polymer-metal composites (IPMCs) biomimetic sensors, actuators, and artificial muscles. *Polymer*, 43:797–802, November 2002.
- [51] Seong Jun Kim, In Taek Lee, and Yong Hyup Kim. Performance enhancement of IPMC actuator by plasma surface treatment. *Smart Materials and Structures*, 16(1):N6–N11, January 2007.

- [52] G. V. Lauder, E. J. Anderson, J. Tangorra, and P. G. A. Madden. Fish biorobotics: Kinematics and hydrodynamics of self-propulsion. *Journal of Experimental Biology*, 210:2767–2780, 2007.
- [53] G. V. Lauder and E. G. Drucker. Morphology and experimental hydrodynamics of fish fin control surfaces. *IEEE Journal of Oceanic Engineering*, 29(3):556–571, 2004.
- [54] G. V. Lauder and P. G. A. Madden. Learning from fish: Kinematics and experimental hydrodynamics for roboticists. *International Journal of Automation and Computing*, 4:325–335, 2006.
- [55] K.-M. Lee, Z. Wei, and Z. Zhou. Modeling by numerical reduction of modes for multivariable control of an optical-fiber draw process. *IEEE Transactions on Automation Science and Engineering*, 3:119–130, 2006.
- [56] M. J. Lighthill. Aquatic animal propulsion of high hydromechanical efficiency. *Journal of Fluid Mechanics*, 44:265–301, 1970.
- [57] Pin Lu and K.H. Lee. An alternative derivation of dynamic admittance matrix of piezoelectric cantilever bimorph. *Journal of Sound and Vibration*, 266:723–735, 2003.
- [58] E. Mbemmo, Z. Chen, S. Shatara, and X. Tan. Modeling of biomimetic robotic fish propelled by an ionic polymer-metal composite actuator. In *Proceedings of the IEEE International Conference on Robotics and Automation*, pages 689–694, 2008.
- [59] S. McGovern, G. I Alici, V. T. Truong, and G. Spinks. Finding NEMO (Novel Electromaterial Muscle Oscillator): A polypyrrole powered robotic fish with real-time wireless speed and directional control. *Smart Material and Structures*, 18:095009:1–10, 2009.
- [60] Measurement Specialties. *Piezo Film Sensors Technical Manual*. Hampton, VA, 1998.
- [61] P. Meissner, B. Kogel Amd F. Riemenschneider, H. Halbritter, S. Jatta, M. Maute, and M. C. Amann. Tunable long-wavelength VCSELs using a moveable mirror membrane. In *Proceedings of the 18th Annual Meeting of the IEEE Lasers and Electro-Optics Society*, pages 324–325, 2005.
- [62] Kristi A. Morgansen, Benjamin I. Triplett, and Daniel J. Klein. Geometric methods for modeling and control of free-swimming fin-actuated underwater vehicles. *IEEE Transactions on Robotics*, 23(6):1184–1199, December 2007.
- [63] S. Nemat-Nasser. Micromechanics of actuation of ionic polymer-metal composites. *Journal of Applied Physics*, 92(5):2899–2915, 2002.
- [64] S. Nemat-Nasser and J. Li. Electromechanical response of ionic polymer-metal composites. *Journal of Applied Physics*, 87(7):3321–3331, 2000.

- [65] K. Newbury. *Characterization, Modeling, and Control of Ionic Polymer Transducers*. PhD thesis, Virginia Polytechnic Institute and State University, Blacksburg, Virginia, 2002.
- [66] K. M. Newbury and D. J. Leo. Electromechanical modeling and characterization of ionic polymer benders. *Journal of Intelligent Material Systems and Structures*, 13:51–60, 2002.
- [67] Kenneth M. Newbury and Donald J Leo. Linear electromechanical model for ionic polymer transducers - part I: model development. *Journal of Intelligent Material Systems and Structures*, 14:333–342, 2003.
- [68] K. Oguro, Y. Kawami, and H. Takenaka. Bending of an ion-conducting polymer film-electrode composite by an electric stimulus at low voltage. *Journal of Micromachine Society*, 5:27–30, 1992.
- [69] J. J. Pak, J. Kim, S. W. Oh, J. H. Son, S. H. Cho, S.-K. Lee, J.-Y. Park, and B. Kim. Fabrication of ionic-polymer-metal-composite (IPMC) micropump using a commercial nafion. In Y. Bar-Cohen, editor, *Smart Structures and Materials 2004: Electroactive Polymer Actuators and Devices (EAPAD)*, *Proceeding of SPIE*, pages 272–280, 2004.
- [70] R. Pelrine, R. Kornbluh, Q. Pei, and J. Joseph. High-speed electrically actuated elastomers with strain greater than 100%. *Science*, 287(5454):836–839, February 2000.
- [71] S. D. Peterson, M. Porfiri, and A. Rovardi. A particle image velocimetry study of vibrating ionic polymer metal composites in aqueous environments. *IEEE/ASME Transactions on Mechatronics*, 2009. In press.
- [72] E. Popov. *Mechanics of Materials*. Prentice-Hall, Englewood Cliffs, NJ, 2 edition, 1976.
- [73] Maurizio Porfiri. Charge dynamics in ionic polymer metal composites. *Journal of Applied Physics*, 104(10):104915, November 2008.
- [74] A. Punning, M. Kruusmaa, and A. Aabloo. Surface resistance experiments with IPMC sensors and actuators. *Sensors and Actuators A*, 2007. in press.
- [75] R. C. Richardson, M. C. Levesley, M. D. Brown, J. A. Hawkes, K. Watterson, and P. G. Walker. Control of ionic polymer metal composites. *IEEE/ASME Transactions on Mechatronics*, 8(2):245–253, 2003.
- [76] John Elie Sader. Frequency response of cantilever beams immersed in viscous fluids with applications to the atomic force microscope. *Journal of Applied Physics*, 84(1):64–76, 1998.

- [77] Takahisa Sakakibara, Hiroaki Izu, Tatsuya Kura, Wataru Shinohara, Hiroshi Iwata, Seiichi Kiyama, and Shinya Tsuda. Development of high-voltage photovoltaic micro-devices for an energy supply to micromachines. In *Proceedings of IEEE 5th International Symposium on Micro Machine and Human Science*, pages 71–76, Nagoya, Japan, 1994.
- [78] M. Shahinpoor and K. J. Kim. The effect of surface-electrode resistance on the performance of ionic polymer-metal composite (IPMC) artificial muscles. *Smart Materials and Structures*, 9:543–551, 2000.
- [79] M. Shahinpoor and K.J. Kim. Ionic polymer-metal composites: I. Fundamentals. *Smart Materials and Structures*, 10:819–833, 2001.
- [80] M. Shahinpoor and K.J. Kim. Ionic polymer-metal composites: IV. Industrial and medical applications. *Smart Materials and Structures*, 14:197–214, 2005.
- [81] Y. Shen, U. C. Wejinya, N. Xi, M. S. Buckley, C. A. Pomeroy, and D. N. Arhosti. Force measurement and mechanical characterization of living *Drosophila* embryos for human medical study. *Journal of Engineering in Medicine*, 221(2):99–112, 2007.
- [82] Y. Shen, N. Xi, U.C. Wejinya, and W.J. Li. High sensitivity 2-D force sensor for assembly of surface MEMS devices. In *Proceedings of IEEE/RSJ International Conference on Intelligent Robots and Systems*, pages 3363–3368, Sendai, Japan, 2004.
- [83] M. Siripong, S. Fredholm, Q.A. Nguyen, B. Shih, J. Itescu, and J. Stolk. A cost-effective fabrication method for ionic polymer-metal composites. In V. Bharti, Y. Bar-Cohen, Z.Y. Cheng, Q. Zhang, and J. Madden, editors, *Electroresponsive Polymers and Their Applications*, volume 889 of *MRS Symposium Proceedings*, pages 0889–W04–03, Warrendale, PA, 2006.
- [84] E. Smela. Conjugated polymers for biomedical applications. *Advanced Materials*, 15(6):481–494, 2003.
- [85] S. Tadokoro, S. Yamagami, T. Takamori, , and K. Oguro. Modeling of nafion-pt composite actuators (ICPF) by ionic motion. In Yoseph Bar-Cohen, editor, *Smart Structures and Materials 2000: Electroactive Polymer Actuators and Devices (EAPAD)*, *Proceedings of SPIE*, volume 92-102, pages 92–102, 2000.
- [86] X. Tan, D. Kim, N. Usher, D. Laboy, J.Jackson, A.Kapetanovic, J. Rapai, B. Sabadus, and X. Zhou. An autonomous robotic fish for mobile sensing. In *Proceedings of the IEEE/RSJ International Conference on Intelligent Robots and Systems*, pages 5424–5429, Beijing, China, 2006.
- [87] J. Tangorra, P. Anquetil, T. Fofonoff, A. Chen, M. Del Zio, and I. Hunter. The application of conducting polymers to a biorobotic fin propulsor. *Bioinspiration & Biomimetics*, 2:S6–S17, 2007.

- [88] Michael S. Triantafyllou and George S. Triantafyllou. An efficient swimming machine. *Scientific American*, 272:64, 1995.
- [89] S. Tung, B. Maines, F. Jiang, and T. Tsao. Transonic flow separation control by MEMS sensors and actuators. In *Proceedings of 39th AIAA Aerospace Sciences Meeting & Exhibit*, Reno, NV, 2001. AIAA Paper 2001-0123.
- [90] Steve Tung, Scott R Witherspoon, Larry A Roe, Al Silano, David P Maynard, and Ned Ferraro. A MEMS-based flexible sensor and actuator system for space inflatable structures. *Smart Materials and Structures*, 10(6):1230–1239, December 2001.
- [91] E. Voltera and E. C. Zachmanoglou. *Dynamics of Vibrations*. Charles E. Merrill Books, Inc., 1965.
- [92] Y. Xiao and Bhattacharya. Modeling electromechanical properties of ionic polymers. In *Smart Structures and Materials 2001: Electroactive Polymer Actuators and Devices (EPAD)*, *Proceedings of SPIE*, volume 4329, pages 292–300, 2001.
- [93] Sung-Weon Yeom and Il-Kwon Oh. A biomimetic jellyfish robot based on ionic polymer metal composite actuators. *Smart Materials and Structures*, 18:085002:1–10, June 2009.
- [94] W. Yim, J. Lee, and K. J. Kim. An artificial muscle actuator for biomimetic underwater propulsors. *Bioinspiration & Biomimetics*, 2:S31–S41, 2007.
- [95] Junzhi Yu, Long Wang, and Min Tan. Geometric optimization of relative link lengths for biomimetic robotic fish. *IEEE Transactions on Robotics*, 23(2):382–386, April 2007.
- [96] Side Zhao and Junku Yuh. Experimental study on advanced underwater robot control. *IEEE Transactions on Robotics*, 21(4):695–703, August 2005.
- [97] J. W. L. Zhou, H.-Y. Chan And T. K. H. To, K. W. C. Lai, and W. J. Li. Polymer MEMS actuators for underwater micromanipulation. *IEEE/ASME Transactions on Mechatronics*, 9(2):334–342, 2004.
- [98] Kemin Zhou. *Essentials of Robust Control*. Prentice Hall, Upper Saddle River, New Jersey, 1998.

MICHIGAN STATE UNIVERSITY LIBRARIES



3 1293 03062 9079